

THE INFLUENCE OF ACOUSTIC OVER-EXPOSURE  
ON CENTRAL AUDITORY PROCESSING

Thesis submitted for the degree of  
Doctor of Philosophy at the University of Leicester

By

Deborah Marie Linley BSc MSc

Department of Neuroscience, Psychology and  
Behaviour

2017

## The Influence of acoustic over-exposure on central auditory processing

Deborah Marie Linley

It is well established that exposure to loud sounds causes deafness by damaging the cochlea, however less is known about the effects of acoustic over-exposure (AOE) on the auditory pathway in the brain. Neurons of the lateral superior olive (LSO) located in the superior olivary complex (SOC) are amongst the first to receive binaural input, with excitatory input from the ipsilateral ear, and inhibitory input from the contralateral ear, via the medial nucleus of the trapezoid body (MNTB). This enables interaural level difference processing which is an important mechanism of sound localisation.

I have examined synaptic and intrinsic excitability of mouse LSO neurons using an *in vitro* brain slice preparation. Kv3 voltage-gated K<sup>+</sup> channels contribute to intrinsic excitability and AP (action potential) repolarisation in the MNTB, yet little is known of their role in the LSO. I have shown expression of Kv3.1 and Kv3.3 (but absence of Kv3.2 and Kv3.4) and assessed their contribution to outward currents using whole cell patch clamp from wildtype and knockout mice. In contrast to the MNTB, the LSO require Kv3.3 for fast AP firing, suggesting that these subunits have specific physiological roles in these nuclei. At the synaptic level, I observed rapid acceleration of decay kinetics during the first 2 postnatal weeks.

Following AOE, LSO neurons showed little change in intrinsic excitability, although MNTB neurons became more excitable with reduced AP thresholds. Measurement of auditory brainstem responses (ABRs) gives an *In Vivo* assessment of hearing. Early ABR waves were delayed and reduced in amplitude after AOE. This deficit was compensated, so that the amplitude and latency of wave IV were indistinguishable from control mice, again demonstrating plasticity in the auditory brainstem. By examining both synaptic and intrinsic excitability, I have identified complimentary mechanisms which underlie hearing loss and compensation following sound over-exposure.

## Acknowledgements

I would like to thank Ian Forsythe for guiding me through this project, and giving me this opportunity in the first place. Thanks to the rest of the lab, past and present (Sheri, Amy, Bea, Sarah, Josh, Michelle, Jon), in particular Jim Sinclair and Emanuele Schiavon who helped me learn to patch, and were very patient with me!

Thanks to Mike Mulheran and Margaret Barnes Davies for being part of my committee, and to the former for helping to set up and calibrate the sound exposure equipment. Thanks to Neil Ingham for setting up the ABR equipment. Thanks to the DBS staff, in particular Hayley and Penny.

Finally, I am grateful to Nick, my long-suffering partner! Thank you for your endless support.

## Declarations

Throughout this thesis, I have declared any work not performed exclusively by myself.

Below is a summary:

- Dr Haresh Selvaskand performed qRT PCR on NMDAR subunits and AMPAR subunits in the LSO before and after acoustic over-exposure.
- Susan Robinson performed qRT PCR on each Kv3 subunit in SOC tissue & validated Kv3.1 and Kv3.3 antibodies using knockout mice.
- Dr Joshua Smalley helped with western blotting and confocal imaging.
- NMDAR mediated EPSCs from LSO neurons recorded by Dr Nadia Pilati (n=7) were merged with my own dataset.

## Contents

<b>1</b>	<b>Introduction</b>	<b>18</b>
<b>1.1</b>	<b>The physiology of the afferent auditory system</b>	<b>19</b>
	Sound transduction to the ear	19
	The cochlea transduces frequency specific sound information	19
	Innervation of hair cells	24
	Sound transduction to the brain	25
<b>1.2</b>	<b>Function of binaural hearing</b>	<b>26</b>
	Monoaural spectral cues	26
	Cocktail Party effect	27
	Horizontal localisation	28
	Interaural time differences (ITDs)	28
	Interaural level difference (ILDs)	29
<b>1.3</b>	<b>The structure and function of the superior olivary complex</b>	<b>29</b>
	The medial superior olive extracts ITD cues for sound localisation	30
	Identifying cells of the LSO	30
	Binaural Inputs to the LSO enable ILD processing	31
	The MNTB acts as a fast acting inverting relay	33
<b>1.4</b>	<b>The developing auditory system</b>	<b>35</b>
	Outer & middle ear	35
	Organ of Corti	36
	Afferent inputs to the MNTB	36
	LSO circuits	37
<b>1.5</b>	<b>Synaptic transmission in the LSO</b>	<b>39</b>
	Glutamate receptors in the SOC	40
	NMDARs in the auditory system	41
<b>1.6</b>	<b>The role of potassium channels in the auditory system</b>	<b>43</b>
	Kv1 provides temporal precision in the auditory brainstem	44
	Kv1 in the MNTB	45
	Kv3 channels mediate fast action potential firing	46
<b>1.7</b>	<b>Effects of acoustic over-exposure in the cochlea</b>	<b>48</b>
<b>2</b>	<b>Methods</b>	<b>51</b>
<b>2.1</b>	<b>Origins of mouse strains</b>	<b>51</b>
	CBA/Ca strain provide a mouse model of normal hearing	51
	Transgenic mouse colonies	52

<b>2.2</b>	<b>Brain slice preparation &amp; maintenance .....</b>	<b>55</b>
	Brain removal and slicing process .....	55
	Slice maintenance and recording chamber .....	57
<b>2.3</b>	<b>Whole Cell Patch Clamp .....</b>	<b>59</b>
	Patch clamp rig apparatus .....	59
	Visual identification of LSO and MNTB neurons: .....	59
	Process of breaking into a cell .....	59
	Estimation of Liquid Junction Potential:.....	62
	Leak Subtraction .....	64
	Current clamp recording: .....	64
	Recording EPSCs and IPSCs from LSO principal neurons.....	65
<b>2.4</b>	<b>Hearing assessment Using The Auditory Brainstem Response (ABR) .....</b>	<b>67</b>
	ABR equipment:.....	68
	Calibration of ABR equipment:.....	68
	Anaesthetic regime.....	70
	Positioning of subdermal needles .....	72
	Recording ABRs: .....	73
	Analysis of ABR recordings .....	73
<b>2.5</b>	<b>Acoustic over-exposure (AOE) procedure .....</b>	<b>75</b>
	Acoustic over-exposure delivery .....	75
<b>2.6</b>	<b>Statistical analysis of electrophysiological data .....</b>	<b>75</b>
<b>2.7</b>	<b>Identifying Kv3 subunit expression in the SOC using Immunohistochemistry</b>	
	<b>76</b>	
	Preparation of brain sections .....	76
	Antibody test matrix using different fixation conditions: .....	77
	Blocking the tissue to avoid non-specific staining .....	77
	Antibody application .....	78
<b>2.8</b>	<b>Comparing Kv3 subunit protein levels using western Blotting .....</b>	<b>79</b>
	Dissection of LSO Tissue .....	79
	Protein extraction:.....	80
	Gel Casting .....	83
	Gel electrophoresis.....	84
	Electrophoretic transfer .....	85
	Blocking to avoid non-specific binding.....	85
	Addition of primary and secondary antibodies:.....	86
	Imaging western blot.....	87

<b>2.9</b>	<b>Identification of transgenic mice using PCR .....</b>	<b>88</b>
	DNA extraction .....	88
	Amplification of DNA using polymerase chain reaction (PCR) .....	89
	Identification of WT and KO DNA using Gel Electrophoresis .....	91
	Breeding of transgenic mice .....	91
<b>3</b>	<b>Synaptic currents of the LSO .....</b>	<b>93</b>
<b>3.1</b>	<b>Identifying LSO principal and LOC neurons .....</b>	<b>94</b>
	LSO principal and LOC neurons exhibit different voltage activated currents .....	94
	LSO principal and LOC neurons exhibit different AP characteristics .....	99
	Single-spiking and multi-spiking principal neuron AP characteristics are not significantly different .....	101
	LOC neurons exhibit significantly larger and slower APs .....	102
<b>3.2</b>	<b>Synaptic currents of LSO principal neurons.....</b>	<b>106</b>
	LSO principal neurons exhibit both EPSCs and IPSCs .....	106
	AMPA EPSC and glycinergic IPSC decay time constants show developmental acceleration.....	110
	NMDAR EPSC decay $\tau$ exhibits developmental acceleration.....	112
	NMDAR EPSCs show rapid, irreversible run-down in amplitude over time.....	114
<b>3.3</b>	<b>Discussion .....</b>	<b>118</b>
	LSO principal neurons and LOC neurons have distinct voltage activated currents and AP characteristics:.....	118
	EPSCs and IPSCs show developmental acceleration of decay tau .....	120
	NMDAR mediated EPSCs exhibit rapid acceleration upon maturation .....	122
	NMDAR EPSCs exhibit rapid, irreversible run-down of EPSC amplitude .....	123
	Summary.....	125
<b>4</b>	<b>Intrinsic excitability in the auditory brainstem: Kv3 in the LSO and MNTB .....</b>	<b>126</b>
	Kv3.1 and Kv3.3 mRNA dominate in the SOC.....	126
	Kv3.1 and Kv3.3 protein is present across the whole SOC.....	127
	Establishing optimum conditions for Kv3.2 and Kv3.4 antibodies.....	132
	Kv3.2 and Kv3.4 Ab staining is inconclusive in the SOC .....	136
	LSO neurons exhibit intrinsic leak .....	139
	Experimental set-up for measuring Kv3 currents .....	141
	Establishing criteria for measuring Kv3 mediated currents .....	142
	Kv3 channels mediate ~half the total outward $K^+$ current in the LSO and MNTB .....	146
	In the MNTB, Kv3 currents are mediated by Kv3.1 and Kv3.3, in contrast, for the LSO Kv3.3 mediates the majority of Kv3 currents.....	148
	Kv3.3 accelerates AP firing in the LSO .....	150
	AP characteristics from Kv3.1 and Kv3.3 deficient mice .....	152
	Kv3.1 and Kv3.3 protein is upregulated in knockout mice.....	157

<b>4.1 Discussion .....</b>	<b>160</b>
Both Kv3.1 and Kv3.3 are utilized by the MNTB .....	161
Kv3.1 as a target for drug therapy.....	162
Kv3.3 is vital for fast AP firing in the LSO .....	163
SCA13 impairs sound localisation.....	164
Kv3.1 is down-regulated in the cerebellum of Kv3.1 KO mice, but upregulated in the LSO .....	165
Summary.....	166
<b>5 The Effect of Acoustic over-exposure on intrinsic and synaptic excitability in the auditory brainstem.....</b>	<b>167</b>
<b>5.1 MNTB: The effect of AOE on intrinsic excitability.....</b>	<b>168</b>
MNTB: AOE converts neurons from a single-spiking to multi-spiking phenotype.....	168
MNTB: AP Half width is accelerated following AOE .....	172
MNTB: $I_H$ current is unaffected by AOE.....	174
MNTB: Amplitude of APs are unaltered by AOE .....	174
MNTB: AP threshold was lowered following AOE, however RMP and AHP remain unaffected .....	177
MNTB: Assessing low voltage activated currents .....	177
<b>5.2 LSO: The effect of AOE on intrinsic excitability .....</b>	<b>181</b>
LSO: AOE does not alter the AP firing pattern .....	181
LSO: $I_H$ current is unaffected by AOE.....	181
LSO: AOE does not affect AP half width or amplitude .....	184
<b>5.3 LSO: The effect of AOE on synaptic excitability .....</b>	<b>188</b>
AMPA EPSCs slow following AOE .....	188
AOE accelerates rise-time of NMDAR EPSCs in the LSO, but does not alter decay tau.....	192
<b>5.4 Discussion .....</b>	<b>195</b>
MNTB: Neurons show hyper-excitability following AOE.....	195
Assessing LVA currents in the MNTB.....	196
Possible mechanisms of diminished Kv1 activity .....	197
Central hyper-excitability following AOE .....	199
MNTB: AP half width accelerates following AOE .....	200
Synaptic plasticity in the MNTB: LTP cannot be induced.....	200
Intrinsic excitability of the LSO: Resting membrane potential is more negative following AOE .....	201
Synaptic excitability of the LSO: .....	202
AMPA mediated EPSC decay tau is slowed following AOE .....	202
LSO: NMDAR EPSCs rise-time is accelerated following AOE .....	203
Summary.....	204
<b>6 The effect of AOE on evoked auditory brainstem responses (ABRs) .....</b>	<b>205</b>

<b>6.1</b>	<b>AOE significantly raises ABR thresholds.....</b>	<b>206</b>
	ABR thresholds are raised at all frequencies tested, except 6 kHz.....	206
<b>6.2</b>	<b>Effect of AOE on ABR wave amplitude.....</b>	<b>211</b>
	Amplitude of wave I is reduced following AOE .....	211
	Wave IV shows compensatory increase in amplitude following AOE.....	213
	Tone-pip evoked ABRs show a reduction of ABR wave amplitude at higher frequencies following AOE .....	217
<b>6.3</b>	<b>Effect of AOE on ABR wave latency .....</b>	<b>224</b>
	AOE slows latency of ABR waves.....	224
	AOE delays ABR waves in high frequency regions .....	229
<b>6.4</b>	<b>Discussion .....</b>	<b>234</b>
	Hearing thresholds are significantly elevated following AOE .....	234
	Absolute vs relative measurements of ABR amplitude.....	236
	AOE causes a reduction in wave I amplitude .....	237
	Following AOE ABR wave amplitude is centrally compensated.....	239
	Latency of wave I is delayed following AOE .....	240
	Central compensation of ABR latency.....	241
	Summary.....	241
<b>7</b>	<b>Final Summary .....</b>	<b>242</b>
<b>7.1</b>	<b>Future work.....</b>	<b>246</b>
<b>8</b>	<b>Appendix.....</b>	<b>250</b>
<b>8.1</b>	<b>Basic theoretical principals of whole cell patch clamp.....</b>	<b>250</b>
	The phospholipid bilayer enables the establishment of concentration gradients .....	250
	Series resistance and capacitance.....	252
	RC circuit.....	255
<b>8.2</b>	<b>Calibration of noise exposure equipment.....</b>	<b>257</b>
<b>8.3</b>	<b>Western blot image analysis .....</b>	<b>262</b>

## List of Tables

Table 2.1 Composition of 'normal aCSF' and 'slicing aCSF' .....	53
Table 2.2 Patch pipette solution composition.....	53
Table 2.3 Criteria and conditions for patch clamping neurons .....	63
Table 2.4 List of materials used for recording ABRs in mice .....	74
Table 2.5 Primary antibodies .....	78
Table 2.6 Secondary antibodies for immunohistochemistry.....	79
Table 2.7 RIPA buffer composition .....	82
Table 2.8 Lower gel buffer composition .....	86
Table 2.9 Upper gel buffer composition .....	86
Table 2.10 Tris-Glycine stock X10 .....	86
Table 2.11 Electrode buffer composition .....	86
Table 2.12 Transfer buffer composition .....	87
Table 2.13 TBST (X10) composition .....	87
Table 2.14 Secondary antibodies for western blotting .....	87
Table 2.15 Primer sequences for Kv3.1 and Kv3.3 PCR .....	89
Table 2.16 List of reagents used for PCR reaction mix .....	90
Table 2.17 PCR cycles for Kv3.1 and Kv3.3 .....	90
Table 3.1 There is no difference between single-spiking and multi-spiking LSO principal neurons for all parameters measured.....	101

## Table of Figures

Figure 1.1 The peripheral auditory system.....	21
Figure 1.2 The cochlea is tonotopically organised.....	22
Figure 1.3 Cross-sectional view of the human cochlea .....	23
Figure 1.4 Mechanisms of sound localisation.....	27
Figure 1.5 The LSO receives bilateral input and is tonotopically arranged .....	33
Figure 1.6 Kv channel $\alpha$ subunit structure .....	44
Figure 2.1 Mouse brain removal and slice preparation.....	54
Figure 2.2 Brain slice maintenance chamber.....	58
Figure 2.3 Process of sealing and breaking into a cell .....	61
Figure 2.4 Whole cell voltage clamp recording from a mouse MNTB neuron .....	63
Figure 2.5 Offline linear leak subtraction of an LSO I/V .....	66
Figure 2.6 Recording postsynaptic currents in the LSO .....	67
Figure 2.7 Establishing the hearing threshold of mouse using ABR.....	69
Figure 2.8 Schematic of free-field ABR testing.....	71
Figure 2.9 Placement of sub-dermal electrodes for ABR .....	72
Figure 2.10 Dissection of LSO tissue for western blot .....	81
Figure 2.11 Generation of BSA standard curve (protein assay) .....	83
Figure 2.12 Visualising DNA bands of Kv3.1 and Kv3.3 .....	92
Figure 3.1 Voltage clamp: Identifying LSO principal and LOC neurons by their voltage activated currents .....	95
Figure 3.2 Voltage clamp: $I_A$ current in LOC neurons requires hyperpolarising pre-pulse .....	97
Figure 3.3 Current clamp: LSO principal and LOC neurons exhibit different AP firing patterns.....	98
Figure 3.4 LSO distribution plot of different neuron types .....	100
Figure 3.5 Amplitude of LOC APs are significantly larger than LSO principal neurons. ....	103
Figure 3.6 AP half widths are shorter in LSO principal neurons compared to LOC. ....	104
Figure 3.7 Comparison of LSO principal and LOC neuron characteristics .....	105
Figure 3.8 EPSCs and IPSCs can be recorded from LSO principal neurons .....	107
Figure 3.9 AMPAR EPSCs and NMDAR EPSCs can be blocked using pharmacology.....	109

Figure 3.10 EPSC and IPSC decay time constants undergo developmental acceleration to <1 ms at P17.....	111
Figure 3.11 NMDAR EPSCs exhibit acceleration of decay $\tau$ following hearing onset...	113
Figure 3.12 NMDAR EPSCs show a rapid, irreversible decrease in amplitude over time .....	115
Figure 3.13 Run-down in amplitude is not caused by increased SR, and is not prevented by calcium buffering .....	117
Figure 4.1 Kv3.1 and Kv3.3 mRNA dominate in the SOC .....	127
Figure 4.2 Verifying specificity of Kv3.1 and Kv3.3 Abs using knockout mice .....	128
Figure 4.3 Kv3.1 and Kv3.3 protein is present across the whole SOC .....	130
Figure 4.4 High magnification view of Kv3.1 and Kv3.3 in the MNTB and LSO .....	131
Figure 4.5 Kv3.1 is located in MNTB cell membranes, but is only present in LSO neuropil .....	132
Figure 4.6 Test Matrix for Kv3.2 Ab. ....	134
Figure 4.7 Test Matrix for Kv3.4 Ab .....	135
Figure 4.8 There is little Kv3.2 staining in the MNTB and LSO .....	137
Figure 4.9 Kv3.4 staining in the SOC appears non-specific.....	138
Figure 4.10 LSO principal neurons exhibit intrinsic leak, and have near identical $K^+$ conductance as MNTB neurons following leak subtraction .....	140
Figure 4.11 Wash-off period for TEA is ~15 minutes.....	143
Figure 4.12 TEA has most effect during the first 3 minutes of perfusion .....	145
Figure 4.13 Kv3 channels contribute ~half outward $K^+$ current in the LSO and MNTB	147
Figure 4.14 In the MNTB, Kv3 current is mediated by both Kv3.1 and Kv3.3; in the LSO, Kv3.3 mediates the majority of Kv3 current.....	149
Figure 4.15 Kv3.1 has no impact on AP half width in the LSO .....	151
Figure 4.16 LSO: AP amplitude in CBA/Ca, Kv3.1 KO and Kv3.3 KO mice.....	153
Figure 4.17 Action potential threshold in the MNTB and LSO.....	154
Figure 4.18 MNTB: AP amplitude is unaltered in Kv3.1 and Kv3.3 KO mice .....	155
Figure 4.19 AHP is reduced in the LSO of Kv3.3 KO mice .....	156
Figure 4.20 LSO: Kv3.1 and Kv3.3 are upregulated in KO mice .....	158
Figure 4.21 Cerebellum: Kv3.1 is down-regulated in Kv3.3 KO mice .....	159

Figure 5.1 MNTB: AOE converts neurons from a single-spiking to a multi-spiking phenotype.....	170
Figure 5.2 MNTB: Multi-spiking neurons show high spiking rates with increased current injection .....	171
Figure 5.3 MNTB: AP half width accelerates following AOE.....	173
Figure 5.4 MNTB: Hyperpolarising sag is not affected by AOE.....	175
Figure 5.5 MNTB: AP amplitude is not affected by AOE.....	176
Figure 5.6 AP threshold is lowered following AOE, however RMP and AHP remain unaffected.....	179
Figure 5.7 MNTB: Measuring low voltage threshold currents following AOE.....	180
Figure 5.8 LSO: Single-spiking neurons do not convert to a multi-spiking phenotype following AOE.....	182
Figure 5.9 LSO: AOE does not affect hyperpolarising sag in the LSO .....	183
Figure 5.10 LSO: AP half width is not altered by AOE.....	184
Figure 5.11 LSO: There is no change in AP amplitude following AOE .....	186
Figure 5.12 LSO: RMP is reduced following AOE .....	187
Figure 5.13 LSO: AOE slows AMPAR EPSC decay time constant.....	190
Figure 5.14 LSO: Comparison of my AMPAR EPSC data set to published results.....	191
Figure 5.15 LSO: NMDAR EPSC rise-time is accelerated following AOE, yet decay kinetics are unaffected. ....	194
Figure 6.1 Click ABR threshold is significantly higher following AOE .....	209
Figure 6.2 Following AOE, ABR thresholds were raised across frequencies $\geq 12$ kHz..	210
Figure 6.3 Wave I: Amplitude is reduced following AOE.....	212
Figure 6.4 Wave III: Amplitude is reduced following AOE.....	214
Figure 6.5 Wave IV: Following AOE, amplitude recovers to control values (as measured .....	215
Figure 6.6 Following AOE, wave IV amplitude is greater than wave III.....	216
Figure 6.7 Mean tone-pip (frequency specific) ABRs in control and AOE treated mice .....	219
Figure 6.8 Tone-pip evoked ABRs show a reduced dynamic range following AOE.....	220
Figure 6.9 Wave I: Absolute amplitude is reduced following AOE at mid to high frequency ranges .....	221

Figure 6.10 Wave III: Absolute amplitude is low and variable in both control and AOE treated mice.....	222
Figure 6.11 Wave IV: Absolute amplitude is reduced following AOE at higher frequencies only.....	223
Figure 6.12 Wave I: Latency is prolonged following AOE .....	225
Figure 6.13 Wave III: Latency is prolonged to a lesser extent than wave I following AOE .....	226
Figure 6.14 Wave IV: Relative latency is unchanged by AOE .....	227
Figure 6.15 Wave I is delayed to a greater extent than subsequent waves .....	228
Figure 6.16 Wave I: Absolute latency is prolonged following AOE at all frequencies tested (12:30 kHz).....	230
Figure 6.17 Wave I: Relative latency is prolonged at high frequencies (30 kHz) .....	231
Figure 6.18 Wave IV: Absolute latency is prolonged only at high frequencies (30 kHz) .....	232
Figure 6.19 Wave IV: Relative latency is unaffected by AOE.....	233
Figure 8.1 The phospholipid membrane acts as a capacitor .....	251
Figure 8.2 Whole cell configuration can be represented by a simple RC circuit .....	254
Figure 8.3 Equivalent circuit for whole cell patch configuration.....	256
Figure 8.4 Analysing the output of the acoustic over-exposure (AOE) set-up.....	259
Figure 8.5 Average power spectrum of broadband noise generator .....	261
Figure 8.6 Analysing the density of western blot bands .....	264

## Abbreviations

**ABR:** Auditory brainstem response

**aCSF:** Artificial cerebral spinal fluid

**AHP:** Afterhyperpolarisation

**AMPAR:**  $\alpha$ -amino-3-hydroxy-5-methyl-4-isoxazolepropionic acid receptor

**AOE:** Acoustic over-exposure

**AP:** Action potential

**APS:** Ammonium persulfate

**AVCN:** Anteroventral cochlear nucleus

**BDNF:** Brain-derived neurotrophic factor

**BM:** Basilar membrane

**BMLDs:** Binaural masking level differences

**CF:** Characteristic frequency

**CN:** Cochlear nucleus

**CNQX:** 6-cyano-7-nitroquinoxaline-2,3-dione

**CNS:** Central nervous system

**D-AP5:** D-2-amino-5-phosphonopentanoic acid

**DCN:** Dorsal cochlear nucleus

**ddH<sub>2</sub>O:** Double distilled water

**DG:** Dentate gyrus

**DMSO:** Dimethyl sulfoxide

**DNLL:** Dorsal nucleus of the lateral lemniscus

**DPOAEs:** Distortion product otoacoustic emissions

**DTX-I:** Dendrotoxin-I

**E:I:** Excitatory:inhibitory

**EAM:** External auditory meatus

**EDTA:** Ethylenediaminetetraacetic acid

**EPSC:** Excitatory postsynaptic current

**EPSCG:** Excitatory postsynaptic conductance

**EPSP:** Excitatory postsynaptic potential

**FFT:** Fast Fourier transform

**GABAR:**  $\gamma$ -aminobutyric acid receptor

**GBCs:** Globular bushy cells

**GluA1-4:** Glutamate receptor subunit, AMPA subtype: 1-4

**GluN1-2:** Glutamate receptor subunit, NMDA subtype 1, 2 a-d.

**GlyR:** Glycine receptor ion channel

**Gly $\alpha$ 1-4:** Glycine receptor alpha subunit 1–4

**GM:** Genetically modified

**HCN:** Hyperpolarisation-activated cyclic nucleotide-gated

**HP:** Holding potential

**HRP:** Horseradish peroxidase

**HVA:** High voltage activated

**I<sub>A</sub>:** A-type current

**IC:** Inferior colliculus

**I<sub>H</sub>:** Hyperpolarisation activated current

**IHCs:** Inner hair cells

**ILD:** Interaural level difference

**IPSC:** Inhibitory postsynaptic currents

**ITD:** Interaural time difference

**K2P:** Two-pore potassium channel

**Kir:** Inwardly rectifying potassium channel

**KO:** Knockout

**Kv1.1 etc.:** Voltage-gated potassium family 1, member 1

**LNTB:** Lateral nucleus of the trapezoid body

**LOC:** Lateral olivocochlear

**LSO:** Lateral superior olive

**L-type:** Long lasting – type

**LVA:** Low voltage activated

**mEPSC:** Miniature excitatory postsynaptic current

**MET:** Mechano-electric transducer

**MGB:** Medial geniculate body

**MNTB:** Medial nucleus of the trapezoid body

**MOC:** Medial olivocochlear

**MSO:** Medial superior olive

**NBQX:** 2,3-dihydroxy-6-nitro-7-sulfamoyl-benzo[f]quinoxaline-2,3-dione

**NIHL:** Noise induced hearing loss

**NMDAR:** *N*-methyl-D-aspartate receptor

**NO:** Nitric oxide

**OHCs:** Outer hair cells

**OoC:** Organ of Corti

**P1 etc.:** Postnatal day 1

**PBS-T:** Phosphate buffered saline tween-20

**PCR:** Polymerase chain reaction

**PFA:** Paraformaldehyde

**PIP<sub>2</sub>:** Phosphatidylinositol 4,5-bisphosphate

**PSC:** Postsynaptic current

**PSP:** Postsynaptic potential

**PVCN:** Posteroventral cochlear nucleus

**qRT PCR:** Quantitative reverse transcription PCR

**RIPA:** Radioimmunoprecipitation

**RMP:** Resting membrane potential

**SBC:** Spherical bushy cell

**SGNs:** Spiral ganglion neurons

**SOC:** Superior olivary complex

**SPL:** Sound pressure level

**SPN:** Superior pons nuclei

**SR:** Series resistance

**Tau,  $\tau$ :** EPSC decay time-constant

**TB:** Trapezoid body

**TBST:** Tris-buffered saline, 0.1% Tween 20

**TEA:** Tetraethylammonium

**TEMED:** Tetramethylethylenediamine

**TM:** Tympanic membrane

**TrKB:** Tropomyosin receptor kinase B

**WCC:** Whole cell capacitance

**WT:** Wildtype

# 1 INTRODUCTION

---

It is well established that acoustic over-exposure (AOE) can damage the hair cells of the cochlea within the inner ear. However, little is known about the effects of AOE further up the auditory pathway. Here, I will examine the effects of AOE on the lateral superior olive (LSO), located within the superior olivary complex (SOC) in the brainstem. I have chosen the LSO because it is one of the first groups of neurons in the brain to receive input from both ears, by way of ipsilateral excitatory glutamatergic input and contralateral glycinergic input via the medial nucleus of the trapezoid body (MNTB) (Galambos et al., 1959, Boudreau and Tsuchitani, 1968, Tsuchitani and Boudreau, 1969, Tollin, 2003). Thus, both excitatory postsynaptic currents (EPSCs) and inhibitory postsynaptic currents (IPSCs) can be recorded from LSO neurons. Coincidental inhibitory and excitatory input to the LSO enable interaural level difference (ILD) processing, an important mechanism of sound localisation (Tollin, 2003).

Throughout this thesis, I will explore the intrinsic and synaptic excitability of LSO neurons with and without AOE using whole cell patch clamp in mouse brainstem slices containing the SOC. I shall then compare this with the intrinsic excitability of MNTB neurons (with and without AOE). A key determinate of normal intrinsic excitability in the ascending auditory pathway are Kv3 channels (voltage-gated K<sup>+</sup> channels) which enable rapid AP firing. Here I will assess the contribution of Kv3 current to total outward K<sup>+</sup> conductance in the MNTB and LSO, and find which Kv3 subunits (Kv3.1:Kv3.4) mediate this current.

I have chosen a mouse model to carry out my project because they are well characterised, easy to breed and of relatively low cost to maintain. Furthermore, due to the small head size of a mouse, they must rely on ILD cues, and thus have large well-defined LSOs (Ollo and Schwartz, 1979, Kuwabara and Zook, 1992). The lab also have many transgenic strains including Kv3.1 knockout (KO) and Kv3.3 KO mice, which helped determine Kv3 channel subunit composition in the LSO and MNTB.

Finally, I have measured auditory brainstem responses (ABRs) to establish hearing thresholds of the mice before and after AOE. This technique also offers a broader view of the ascending auditory brainstem pathway *in vivo*, providing information about speed of transmission, and levels of excitability.

### **Project aims:**

- Establish normal synaptic and intrinsic excitability of the LSO, and record any developmental changes.
- Find which Kv3 subunits (Kv3.1:Kv3.4) contribute to Kv3 mediated current in the LSO and MNTB.
- Assess the effect of AOE on synaptic and intrinsic excitability in the LSO and MNTB.
- Measure changes following AOE *in vivo* using the ABR method.

## 1.1 THE PHYSIOLOGY OF THE AFFERENT AUDITORY SYSTEM

### Sound transduction to the ear

Sound waves are the mechanical oscillation of the medium in which it propagates (air, water etc.). In order to perceive sound, sound waves first enter the external auditory meatus (EAM) via the pinna, the shape of which acts to amplify particular frequencies of sound within the speech range (Grothe et al., 2010). From here, sound waves travel towards the tympanic membrane (TM) and cause it to vibrate. This vibration causes movement of the ossicular chain in the middle ear, which is comprised of three small bones (malleus, incus and stapes) (fig 1.1). The ossicular chain acts as a compound lever by multiplying the force applied at the TM. This is to overcome the impedance mismatch between the air filled middle ear (low impedance) and the fluid filled inner ear (high impedance) (Helmholtz, 1877, Brenkman et al., 1987).

### The cochlea transduces frequency specific sound information

The inner ear consists of the semi-circular canals (involved in balance) and the cochlea, which is a spiral shaped bony structure (fig 1.2). The cochlea contains three fluid filled compartments: scala vestibuli, scala tympani and scala media (fig 1.3) (Lewis Tilney, 1983). The scala media (middle) is separated from the scala vestibuli (top) by

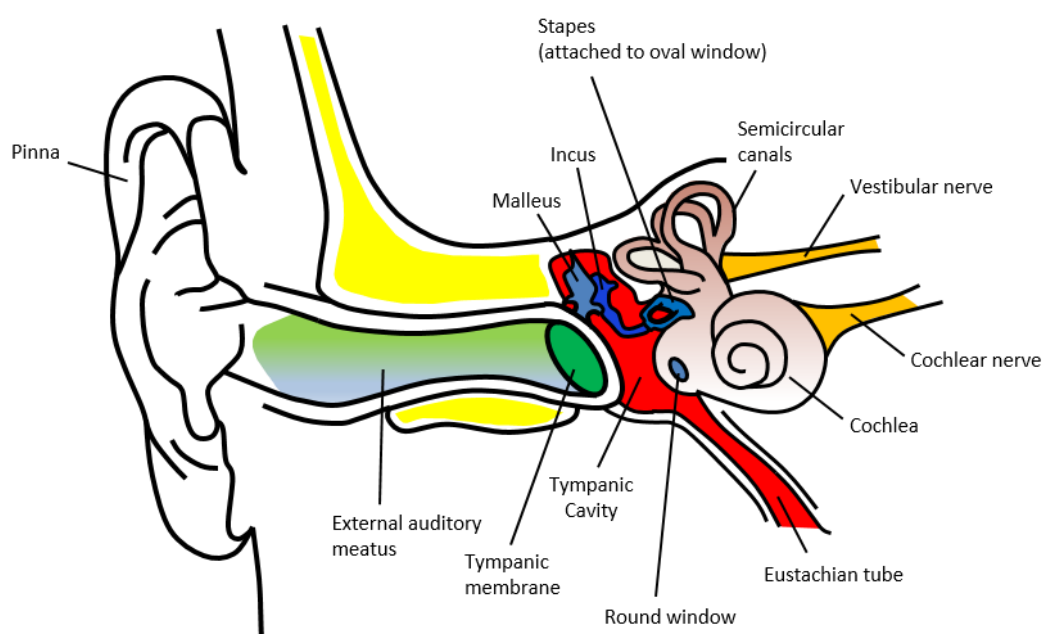
Reissner's membrane, and from the scala tympani (bottom) by the basilar membrane (BM). The fluid that fills the scala media, termed endolymph, is high in  $K^+$  and low in  $Na^+$ , whilst the fluid that fills both the scala tympani and scala vestibuli (perilymph) is rich in  $Na^+$  and low in  $K^+$  &  $Ca^{2+}$ . The scala tympani and scala vestibule meet at the apical end of the cochlea at a small opening called the helicotrema, and thus form one continuous duct (Musiek, 2006).

Vibration transmitted from the middle ear to the oval window causes a travelling wave along the BM. This occurs due to pressure differences between the different fluid filled compartments in the cochlea, which sets the BM into oscillation when it receives vibration from the middle ear. The travelling wave propagates along the BM, and deposits most energy at a frequency specific location, after which the wave abruptly disappears. Low frequency sound waves cause maximal displacement at the broad, floppy apex, and high frequency sound waves cause maximal displacement at the stiffer narrow base (Békésy, 1944) (fig 1.2). Mapping of frequency by spatial position is known as tonotopy, and is maintained through the ascending auditory pathway (Lauter et al., 1985).

The BM supports the Organ of Corti (OoC), which is responsible for converting vibration into electrical impulses (mechanotransduction) to be sent to the brain for processing. Here lie the sensory hair cells, of which there are two types: outer hair cells (OHCs), also known as the cochlear amplifier, and inner hair cells (IHCs), which perform mechanotransduction (Opstal, 2016). The human cochlea contains around 12000 OHCs, which are arranged in three rows along the BM. They act to boost amplitude and increase frequency selectivity of low level sounds by actively contracting and relaxing, thus stimulating adjacent IHCs (Ruggero et al., 1992). There are far less IHCs (3,500) in the cochlea, which are arranged in a single row, and act to convert the vibrations of the BM into action potentials (APs) (LeMasurier & Gillespie, 2005). IHCs have mechanosensory bundles which lie underneath tectorial membrane, each of which consist of around 300 stereocillia (Lewis Tilney, 1983). The vibration of the BM creates a shearing motion between the reticular lamina and the tectorial membrane, displacing the tip links of the IHC stereocillia. This allows cations (mainly  $K^+$ ) to flow

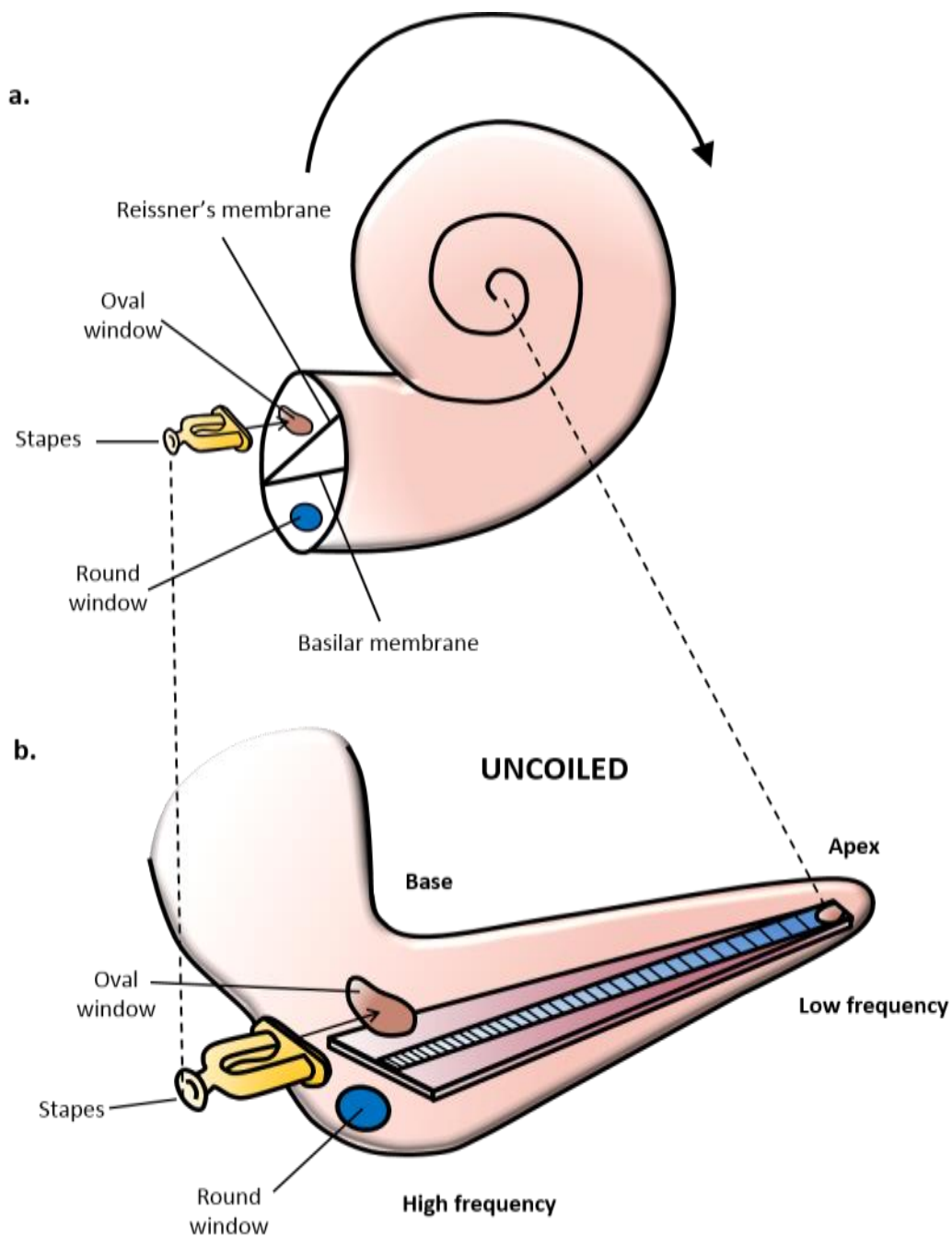
down their electrochemical gradient through non-specific ion channels, termed mechano-electric transducer (MET) channels, depolarising the IHCs in the process (Ricci and Fettiplace, 1998, Fettiplace, 2009). Depolarisation activates L-type voltage-gated  $\text{Ca}^{2+}$  channels (Platzter et al., 2000), allowing  $\text{Ca}^{2+}$  to enter the hair cell (Moser and Beutner, 2000), triggering glutamate release (Kataoka and Ohmori, 1994, Glowatzki and Fuchs, 2002) from the synaptic ribbon synapses at the basal end of the cell.

*Figure 1.1 The peripheral auditory system*



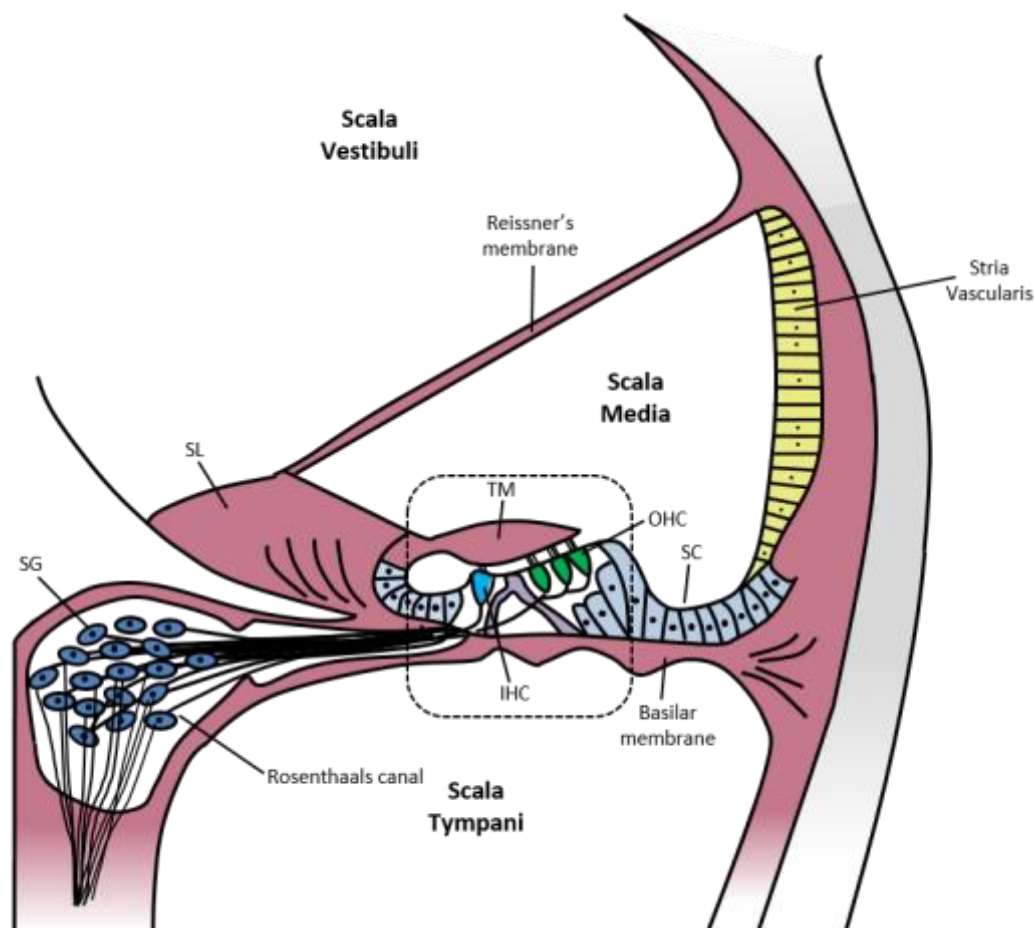
**Fig 1.1. The peripheral auditory system.** Diagram of the peripheral auditory system showing the outer, middle and inner ear. The outer ear consists of the pinna, external auditory canal and tympanic membrane. The middle ear consists of the ossicles (malleus, incus, and stapes), tympanic cavity, and the Eustachian tube, which connects the middle ear to the nasopharynx. The inner ear is composed of the cochlea and semicircular canals, auditory nerve and vestibular nerve. Figure redrawn from Chittka, L et al (2005).

Figure 1.2 The cochlea is tonotopically organised



**Fig 1.2. The cochlea is tonotopically organised** **a.** Diagram of the human cochlea. The ossicles in the middle ear amplify and transmit vibrations to the bony, spiral shaped cochlea via the oval window. This results in a travelling wave along the basilar membrane. **b.** Schematic diagram of the cochlea uncoiled. Low frequency sounds cause the travelling wave to deposit most energy at the apical end of the basilar membrane, whilst high frequency sounds cause maximal displacement towards the base of the basilar membrane. Figure is redrawn and adapted from Bear (2006).

Figure 1.3 Cross-sectional view of the human cochlea



**Fig 1.3. Cross-sectional view of the human cochlea.** Diagram representing the morphology of the membranous labyrinth. The scala media (middle) is separated from the scala vestibuli (top) by Reissner's membrane, and from the scala tympani (bottom) by the basilar membrane (BM). The scala media contains  $K^+$  rich endolymph, maintained by the action of the stria vascularis (SV) whilst  $Na^+$  rich perilymph fills both the scala tympani and scala vestibule. The BM supports a single row of inner hair cells (IHCs), 3 rows of outer hair cells (OHCs) and supporting cells (SC), with the tectorial membrane (TM) resting above projecting from the spiral limbus (SL). IHCs are innervated by afferent bipolar spiral ganglion (SG) neurons, the cell bodies of which are located in Rosenthal's canal. Figure is redrawn from Hurley et al. (2007).

### Innervation of hair cells

IHCs are innervated by afferent bipolar spiral ganglion neurons (SGNs), the cell bodies of which are located in Rosenthal's canal (fig 1.3). Each cell body has a peripheral process which synapses with IHCs, and a central process, which projects into the auditory nerve, and ultimately terminates with cells of the cochlear nucleus (CN) (Nayagam et al., 2011). The auditory nerve is formed of afferent nerve fibers of which there are two types:

- Type I fibers: Large diameter & myelinated, bipolar,
- Type II fibers: small & unmyelinated, pseudomonopolar

Type I fibers form approximately 95% of the afferent nerve fibers and innervate IHCs (Spoendlin, 1972, Dannhof and Bruns, 1993), whilst type II fibers receive input from OHCs (Berglund and Ryugo, 1987, Liberman et al., 1990). Many type I neurons may innervate a single IHC, in contrast, a single type II neuron may synapse with several different OHCs. The function of type I neurons is to rapidly propagate auditory information from the ear to the brain, whilst type II neurons have recently been implicated in driving medial olivocochlear (MOC) mediated suppression of OHC movements (Froud et al., 2015).

Both hair cell types are also innervated differently by efferent nerve fibers arising from the olivocochlear bundle, allowing higher centres to modulate sound processing performed at the periphery. There exists two main types of olivocochlear neurons, both of which originate in the SOC of the brainstem. Lateral olivocochlear (LOC) neurons arise from the LSO, and their axons synapse with afferent type I fiber dendrites directly beneath IHCs (Guinan, 2006). In contrast, MOC fibers arise from the medial superior olive (MSO) and synapse directly with OHCs.

LOC neurons can be further subdivided into two groups: intrinsic and shell neurons (Vetter and Mugnaini, 1992). Each group utilizes different neurotransmitters, with intrinsic neurons primarily cholinergic and shell neurons dopaminergic (Darrow et al., 2006) although a wide variety of other neurotransmitters have also been implicated

(Eybalin, 1993). Both are unmyelinated, and consequently have very slow conduction (Groff and Liberman, 2003). LOC fibers (not cell bodies) are notoriously difficult to record from or electrically stimulate due to their size, however the properties of LOC neurons have been studied by indirect activation via the inferior colliculus (IC), which either enhanced or reduced activity of the auditory nerve (Groff and Liberman, 2003). Given the differences in neurotransmitters between shell and intrinsic LOC neurons, it may be that one group causes excitation of the auditory nerve and another causes inhibition, allowing further control over the output of the auditory nerve. Another proposed function of LOC neurons is as a mechanism to protect against acoustic trauma by reducing the afferent output of the type I spiral ganglion neurons in response to damaging levels of sound. Lesioning LOC neurons in mice led to increased hearing thresholds as measured by the auditory brainstem response (ABR) following AOE. In addition, LOC innervation could help balance binaural sensitivity, as unilateral lesioning of LOC neurons caused an imbalance of ipsilateral and contralateral output (measured by ABRs), potentially undermining sound localisation mechanisms (Darrow et al., 2007).

In contrast, MOC axons are myelinated, and the majority cross the midline to innervate the contralateral cochlea (Warr, 1975). MOC innervation hyperpolarises OHCs, resulting in decreased OHC electromotility, and thus reduced amplification of adjacent IHCs. Consequently, the overall afferent output from the cochlea is reduced (Elgoyhen et al., 2001, Elgoyhen et al., 1994, Brown and Nuttall, 1984). MOC innervation is thought to act as a neuroprotective mechanism against excessive noise (Maison and Liberman, 2000, Maison et al., 2013), and is also thought to preserve upper limits of firing in background noise, to 'unmask' signals of interest (Guinan, 2006).

### Sound transduction to the brain

The auditory nerve is the final structure of the auditory periphery. Beyond the cochlea, ipsilateral ascending auditory nerve fibers synapse with the CN, located in the brainstem. The CN can be divided into three nuclei: the anteroventral cochlear nucleus (AVCN) the posteroventral cochlear nucleus (PVCN) and the dorsal cochlear nucleus (DCN). Auditory nerve fibers entering the CN first bifurcate, with one branch synapsing

with an AVCN cell, and the other branch bifurcating once more and innervating both the PVCN and DCN (Rhode, 1991). This is one of the first of many instances of parallel processing in the ascending auditory pathway, where a single nerve fiber provides input to different cell types, enabling simultaneous processing of different aspects of the signal from a single input.

Some AVCN fibers synapse with nuclei of the SOC, which is the first point in the ascending auditory where there is bilateral representation of acoustic input. Other AVCN, DCN and PVCN fibers cross the midline and synapse with the contralateral IC, using separate fiber tracts, which together form the lateral lemniscus (LL). In contrast, other fibers of the CN do not cross the midline, but instead synapse directly with the dorsal nucleus of the lateral lemniscus (DNLL), whose fibers project to the ipsilateral IC. Thus, the IC receives information from both contralateral and ipsilateral ears (binaural). The next structure in the ascending auditory pathway is the medial geniculate body (MGB), followed finally by the auditory cortex, where we perceive the sound (Moller, 2006).

## 1.2 FUNCTION OF BINAURAL HEARING

Fast and accurate localisation of sound is important for most animals, to find a mate, escape predators, or even to catch their next prey. In many sensory systems, location of a stimuli involves direct mapping onto sensory cells e.g. light activates cells of the retina. However, in the auditory system, only sound frequency is directly mapped onto the auditory pathway (tonotopy) (Tsuchitani and Boudreau, 1966, Tollin and Henning, 1998). In order to localise sound, the auditory system must identify differences in the soundwaves, caused by the physical interactions of the soundwave and the ear and/or head. There are several mechanisms of sound localisation that the auditory system utilizes, most of which depend on binaural hearing.

### Monoaural spectral cues

The pinna and concha change the spectral shape of the sound entering the EAM, dependent on its origin. Here, without binaural comparison, the ear can pick up

directional cues in the vertical plane, and determine whether a sound originates from the front or back (fig 1.4, a) (Musicant and Butler, 1984).

### Cocktail Party effect

Binaural hearing enables us to pick out speech amongst competing auditory stimuli, known as the 'cocktail party effect', which is impaired in those with unilateral deafness (Durlach et al., 1981). The cocktail party effect can be partly explained by binaural masking level differences (BMLDs) (Kuyper, 1972, Jiang et al., 1997). Here, if the phase of the signal of interest is different at each ear compared to the noise, this implies the signal and the noise originate from different locations, helping to distinguish the signal from the background noise.

Figure 1.4 Mechanisms of sound localisation

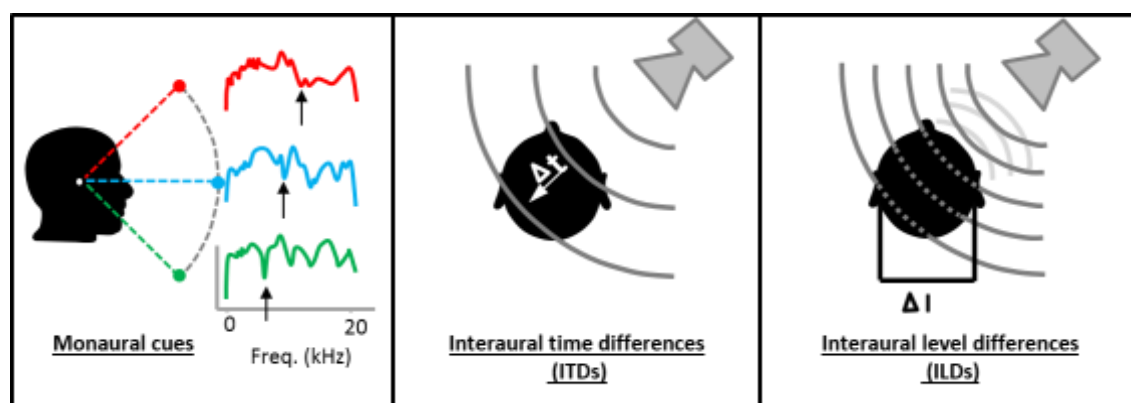


**Fig 1.4. Mechanisms of sound localisation. a. Monaural cues.** The interaction of the sound waves with the head and the pinna alters the spectral shape of the sound arriving at the tympanic membrane, which provides directional cues in the vertical plane. The central notch indicated by the black arrow shifts to high frequencies when shifted from  $-45$  degrees below the azimuth to  $+45$  degrees above the azimuth. **b. Interaural time differences (ITDs)** is the difference in the arrival time ( $\Delta t$ ) of the sound wave at the two ears provides sound source localisation cues in the horizontal plane. **c. Interaural level differences (ILDs)** provide location cues in the horizontal plane due to differences in amplitude ( $\Delta I$ ) in sound arriving at the two ears. This is due to the reflection and refraction of sound waves from the head known as the head shadowing effect. Figure is redrawn and adapted from Grothe et al., 2010.

### Horizontal localisation

This refers to localisation of a sound source from left to right. The origin of our understanding can be traced back to the work of Lord Rayleigh in the late 19<sup>th</sup> century. He observed that left to right locations of a sound source could be discriminated by human participants across a wide range of frequencies using tuning forks. Sounds could be localised due to the 'head shadow effect', where sound waves reflect and refract around the head, resulting in reduced sound level entering the contralateral ear. However this theory did not explain how low frequency sounds are located, which have longer wavelengths that can simply bend around the head. Rayleigh proposed that low frequency sounds were localised by differences in the phase of sound entering each ear.

This theory of azimuthal sound localisation became known as the 'duplex theory', where high frequency sounds are localised by ILDs and low frequency sounds are localised by interaural time differences (ITDs).

### Interaural time differences (ITDs)

ITDs arise from the difference in length that sound must travel in order to reach each ear, which varies systematically with source azimuth (fig 1.4, b). For example, if a sound source is at 90° azimuth to one ear, the time it takes to reach the other ear will be much longer, as the distance to the other ear is greater. However, if a sound source is located directly in front of the head, the time it takes to reach each ear is equal. Thus, ITDs differ depending on the location of the sound source. The difference in the time it takes the sound waves to reach each ear is directly proportional to head size (Masterton et al., 1967). In humans this is up to 700  $\mu$ s, in small rodents this can be as little as 40  $\mu$ s (Wightman FL). Threshold for detection of ITDs in humans (i.e. the smallest ITD needed to successfully locate a sound) is 10 -20  $\mu$ s (R.G. Klumpp, 1956, J. Zwislocki, 1956, Brughera et al., 2013). Low frequency sounds are predominantly localised using ITDs, with the lowest threshold for pure tone stimuli (i.e. most sensitivity) at 0.7 - 1 kHz.

If we do not hear the onset of the sound, such as with a continuous tone, how do we compare timing differences between each ear? This is achieved by comparing the phase of the sound wave entering each ear. For this to work, one cycle of the sound wave must be longer than the distance between the two ears. For example, for a 200 Hz sound, one cycle covers 172 cm, which is much larger than the ~20 cm between our ears. Thus, if the sound enters the ears at azimuth 90° (right), the peak of the sound wave will take 0.6 msec to reach the left ear. This processing breaks down at frequencies above ~ 2 kHz. This is because at high frequencies, one cycle of the wave is smaller than the distance between the two ears. Here, the phase of the wave can no longer give information about the ITDs. Instead, ILD processing is used to locate higher frequency sounds (Bear, 2006).

#### Interaural level difference (ILDs)

ILDs provide location cues by determining the relative difference in volume between the two ears (Rayleigh, 1907, Middlebrooks and Green, 1991). ILDs arise because the head obstructs soundwaves, which instead reflect and refract around the head, resulting in a loss in amplitude of sound reaching the contralateral ear, known as the 'head shadow effect' (fig 1.4, c). This can produce large differences in volume in sound reaching each ear, of up to 20 dB at 4 kHz, and 35 dB at 10 kHz (Middlebrooks et al., 1989, Shaw, 1974). The detection threshold is around 1 dB (Mills, 1960, Hafter et al., 1977). ILD processing cannot be used to locate low frequency sounds (<2 kHz), because sound waves at these frequencies can diffract around the head, resulting in matching intensity at the two ears.

In summary, low frequency sounds (20 – 2000 Hz) are located using ITD processing, after which ILD processing is used to locate high frequency sounds (2000 – 20 000 Hz). Together these two processes form the duplex theory of sound location (Bear, 2006).

### 1.3 THE STRUCTURE AND FUNCTION OF THE SUPERIOR OLIVARY COMPLEX

When considering possible sites where ILD cues and ITD cues could first be extracted, scientists first looked at sites in the auditory pathway that receive input from both ears. The SOC is the first structure of the ascending auditory pathway to receive

binaural input (Boudreau and Tsuchitani, 1970). This enables the comparison of sound entering each ear by extracting cues such as differences in timing (ITDs) and sound levels (ILDs) to form the basis of sound localisation. The SOC comprises of several different nuclei: the LSO, the superior paraolivary nuclei (SPN), which is involved in gap detection (Kopp-Scheinflug et al., 2011), the MSO, and the MNTB.

#### The medial superior olive extracts ITD cues for sound localisation

The first model of how ITD cues could be extracted came from Jeffress (1948) who proposed 'hard-wired delay lines' theory based on coincidence detection. Here it is proposed APs arising from each ear must propagate down secondary fibers, which are spatially organized to branch and innervate tertiary cells at various points along its length. Each of these cells, termed 'coincidence' detectors, are innervated bilaterally, and will only fire an AP if they receive bilateral input at the same time. This spatial organisation can be used to detect ITDs, as each cell is tuned to a particular ITD, due to differences in conduction time.

Whilst the Jeffress model corresponds well to the organisation of the avian nucleus laminaris (Koppl and Carr, 2008, Overholt et al., 1992, Carr and Konishi, 1990), there exists debate over its relevance to the equivalent structure in mammals (MSO) (Manley GA et al., 2004, Duncan and Fritzsche, 2012). Here, MSO neurons also receive an inhibitory input from both the lateral nucleus of the trapezoid body (LNTB), and the MNTB, which is unaccounted for in the 'hard delay lines' model. The role of this inhibition is currently debated, and has led to new enquiries of how ITDs are extracted in mammals (Brand et al., 2002, Joris and Yin, 2007).

#### Identifying cells of the LSO

The LSO is located bilaterally in the SOC (fig 1.5) and is easily recognised in most mammals due its characteristic 'S' shape in the coronal plane (Boudreau and Tsuchitani, 1968). Morphological studies have shown the LSO contains multiple cell types. Reitzel and Friauf (1998) investigated the morphology of the rat LSO neurons (P4-P36) using intracellular dye injections into lightly fixed brainstem slices, and were able to identify seven classes of neuron. The two major cell types found were bipolar

neurons and multipolar neurons. Other less numerous cell types included small multipolar cells, bushy cells, banana-like cells, unipolar cells and marginal cells. In contrast, electrophysiological experiments performed in rats have revealed only two main neuronal types: LSO principal and LOC neurons (Adam et al., 2001, Adam et al., 1999a, Barnes-Davies et al., 2004, Sterenborg et al., 2010). Each group can be identified by their distinct electrophysiological characteristics. LSO principal neurons respond to depolarising current injections with either a single AP (single-spiking), or a train of APs (multi-spiking), (Barnes-Davies et al., 2004, Sterenborg et al.) as recorded from brainstem slices from rats and mice respectively. Both single and multi-spiking APs are time locked to the stimulus onset. This is in contrast to LOC neurons, which have a multi-spiking AP firing pattern, and exhibit a delay before the first elicited AP upon depolarisation, and thus are often termed 'delay neurons' in earlier literature (Adam et al., 1999a).

Principal neurons and LOC neurons also display markedly different responses under voltage clamp. LOC neurons show a fast transient outward  $K^+$  current ( $I_A$ ) current in response to depolarising voltage steps, whilst principal neurons (both single and multi-spiking) do not. Conversely, when hyperpolarised, LSO principal neurons show a slowly activating inward current  $I_H$ , which is mediated by hyperpolarisation-activated cyclic nucleotide-gated (HCN) channels, whilst LOC neurons do not show any  $I_H$  when hyperpolarised. LOC neurons also exhibit significantly slower EPSCs and IPSCs than those measured in principal neurons, and have higher input resistance and less negative resting membrane potentials (RMPs) (Sterenborg et al., 2010).

#### **Binaural Inputs to the LSO enable ILD processing**

LSO principal neurons receive excitatory glutamatergic input from the ipsilateral (AVCN) spherical bushy cells and inhibitory glycinergic input from the contralateral AVCN globular bushy cells, via the MNTB (fig 1.5) (Glendenning et al., 1985, Cant and Casheday, 1986, Kandler and Friauf, 1995, Smith et al., 1993). The LSO then sends an excitatory projection to the contralateral IC, and an inhibitory projection to the ipsilateral IC (Saint Marie et al., 1989, Glendenning et al., 1992, Oliver et al., 1995).

LSO principal cells are termed excitatory inhibitory (E:I) cells due to receiving both excitatory and inhibitory inputs (Boudreau and Tsuchitani, 1968). The excitability of the LSO neurons is determined by the levels of excitatory and inhibitory input received, which in turn depends on the position of the sound source on the azimuth. Thus, integration of excitatory and inhibitory inputs from each ear enables the extraction of ILD cues. This has been demonstrated experimentally in cats, by presenting localisation cues along the azimuth through earphones, whilst recording extracellular responses from single LSO cells. High discharge rates were found for the ipsilateral azimuth, and low discharge rates were found for the contralateral azimuth, consistent with the hypothesis that LSO cells are E:I, and because of this, can detect ILDs (Tollin and Yin, 2002a, Tollin and Yin, 2002b). Furthermore, behavioural studies have shown lesions to primary afferents or cell bodies of the LSO disrupts localisation performance in ferrets and cats respectively (Kavanagh and Kelly, 1992, Masterton et al., 1967).

The extraction of ILD cues is performed in a frequency specific manner by LSO neurons, thus maintaining the tonotopy of the auditory pathway. Both the ipsilateral and contralateral inputs, with high characteristic frequency neurons are located in the medioventral region and the lower CF neurons located more dorsolateral in the LSO (Tsuchitani and Boudreau, 1966, Tollin and Henning, 1998) (fig 1.5).

Figure 1.5 The LSO receives bilateral input and is tonotopically arranged

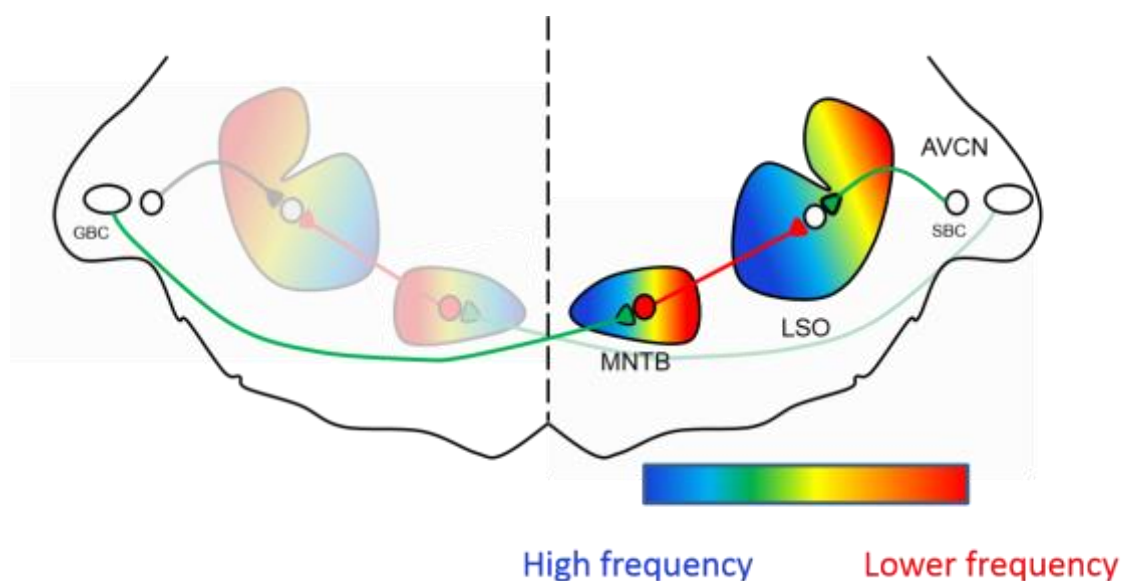


**Fig 1.5. The LSO receives bilateral input and is tonotopically arranged.** Diagram of a coronal section of the brainstem showing SOC circuitry. LSO neurons receive bilateral inputs from both ears. Input from the ipsilateral ear is via the spherical bushy cells (SBCs) of the anteroventral cochlear nucleus (AVCN), and is glutamatergic and excitatory (green). Input from the contralateral AVCN globular bushy cells (GBCs) is glycinergic and inhibitory (red) due to the additional synapse with the ipsilateral MNTB. The colour bar indicates tonotopic organisation. Overall, the LSO is sensitive to high frequency sounds. Higher characteristic frequency neurons are located in the medioventral region and the lower CF neurons located more dorsolateral in the LSO.

#### The MNTB acts as a fast acting inverting relay

The MNTB is located bilaterally in the SOC, ventromedial to the MSO. Golgi studies have shown it contains three distinct cell types: principal, elongate and stellate cells (Morest, 1968). Principal neurons have large, round somata of 15-20  $\mu\text{m}$ , with short distal dendrites, which are only sparsely innervated (Smith et al., 1998). The main input to the MNTB arises from axons of globular bushy cells (GBCs) in the AVCN (or to a lesser extent the PVCN), which cross the midline and synapse 1:1 with contralateral principal cells of the MNTB (Thompson and Schofield, 2000, Kuwabara et al., 1991). This giant synapse was first discovered by Hans Held (1893) who noted the large end terminus of the synapse resembled the calyx of a flower and thus it was named the Calyx of Held. Properties of the other less numerous cell types (elongate and stellate)

are less well understood. For the remainder of the document, references to the MNTB refer to MNTB principal neurons.

Input from the AVCN to the MNTB is excitatory and glutamatergic (Banks and Smith, 1992, Forsythe and Barnes-Davies, 1993) (fig 1.5). The MNTB then acts as a neural relay, sending glycinergic inhibitory projections to multiple targets of the ascending auditory system including the SPN, nuclei of the LL, and both the MSO and LSO (Thompson and Schofield, 2000).

The MNTB is therefore important for accurate ILD processing in the LSO, whose excitability depends on coincidental E:I inputs it receives. The contralateral input to the LSO has further to travel, and has an extra synapse (MNTB) compared to the ipsilateral input. Thus, the MNTB must be able to rapidly propagate APs to ensure simultaneous arrival of E:I inputs to the LSO (Grothe et al., 2010). This is aided by the large, myelinated GBCs, and sheer size of the Calyx of Held, which has many release sites, estimated to be between 300-700 (Taschenberger et al., 2002, Dondzillo et al., 2010, Satzler et al., 2002). This means the calyx can release over 100 vesicles in response to a single AP (Borst and Sakmann, 1996) to generate an extremely large excitatory postsynaptic conductance (EPSC) of 100 -300 nS (Johnston et al., 2009), which rapidly depolarises the membrane.

Intensity of a sound has long been believed to be coded via spike rate (Micheyl et al., 2013). This requires the MNTB to be able to produce a wide range of AP firing, to encode subtle ILDs. Indeed, many other neurons in sensory systems change their AP firing rate in response to differing stimulus input. For example neurons of the visual cortex increase AP firing rates when presented with visual stimuli that is of greater contrast (Albrecht and Hamilton, 1982). This has also been demonstrated in the auditory system, where neurons exhibit increased firing levels with increased sound intensity, such as those in the IC (Irvine and Gago, 1990). During a sound presentation, AP firing rates in the MNTB can reach up to 800 Hz from a spontaneous frequency of ~30 Hz in rodents (Kopp-Scheinflug et al., 2008). At frequencies beyond their AP firing capabilities, MNTB neurons phase lock to every other wave at the same phase (Wang

et al., 1998). Output from the MNTB is closely linked to its input due to the 1:1 relationship of the CN input, with one AP generated in the GBC generating one AP in the MNTB. In addition to robust AP firing, MNTB neurons maintain the tonotopic gradient of the CN, with neurons encoding high frequencies found in the medial MNTB and low frequency neurons located in more lateral regions (fig 1.5) (Sommer et al., 1993).

Inhibitory inputs from the MNTB to LSO principal neurons may be more complex than originally thought. Jalabi et al (2013) found that glycinergic innervation of the SOC was maintained in mice lacking the MNTB. Furthermore, interaural level discrimination was only subtly undermined in the absence of the MNTB. Whether this is a true representation of another inhibitory pathway in the SOC in wild type mice, or a compensatory pathway specific to MNTB KO mice is unknown.

#### 1.4 THE DEVELOPING AUDITORY SYSTEM

Much of the *in vivo* evidence presented so far has been performed on adult animals, however the *in vitro* evidence, such as whole cell patch clamping has mostly been performed on adolescent animals, presumably because the neurons are easier to visualise. This approach assumes that the auditory system is the same in both young and adult animals. However, more recently it has emerged that the developing auditory system undergoes a large degree of synaptic reorganisation before reaching maturity.

##### Outer & middle ear

The outer ear is comprised of the pinna, EAM and TM. Embryonically, the outer and middle ear forms from the first and second pharyngeal arches. The EAM develops from the first pharyngeal arch, which forms a meatal plug (Nishimura and Kumoi, 1992). During development, breakdown of the cells within the middle of the plug causes a hollow 'cul-de-sac' tube to emerge lined with ectodermal cells which creates the EAM. The EAM first opens at P10 in most mouse strains, allowing sound waves to pass through to the TM, (Mikaelian, 1965).

The most prominent feature of the middle ear are the ossicles, which are constructed from neural crest cells from the mesenchyme of the first and second pharyngeal arches (James Byron Snow, 2009). A mature functioning middle ear is necessary to overcome the impedance mismatch between the air-filled middle ear and the fluid filled cochlea. The TM reaches adult size in C57BL/6J mice at 15-20 days, and the ossicles have reached full length by just 10 days (Huangfu and Saunders, 1983). Studies have measured TM velocity across a range of frequencies using BALB/c mice at different ages, which showed lower levels of velocity at younger age groups (P10 and P12), which reached maturity by P17.5 (Doan et al., 1994). Thus, in rodents it seems the middle ear does not fully mature until ~ P17.

### Organ of Corti

A large degree of synaptic development occurs within the OoC before birth. In mice, hair cells first become post-mitotic at embryonic day 11.5 – 14.5. This occurs first at the apical end of the cochlea and spreads to the basal end (Matei et al., 2005). By the time of birth, both IHC and all three row of OHCs are innervated by SGNs. Following birth, development and refinement of the hair cells and their afferent and efferent inputs continues. Maturation of hair cells and the neurons that innervate them is thought to be driven by innate spontaneous  $Ca^{2+}$  mediated APs (Marcotti et al., 2003, Kros et al., 1998, Brandt et al., 2003) which trigger exocytosis. Mature innervation of IHCs and OHCs are reached by P12 and P20 respectively (Bulankina and Moser, 2012).

### Afferent inputs to the MNTB

The neural connections from the CN to the SOC are already present at birth (Hoffpauir et al., 2010), and undergo a large degree of synaptic pruning and refinement in the following weeks. For example, in rats, immature calyces of Held have a different morphology to mature calices of held. Immature calices of held have several long thin collaterals, which innervate adjacent MNTB neurons. Pruning of these collaterals begins 1 week before hearing onset (Hoffpauir et al., 2010). Both the number and length of the immature processes reduce with age. In rodents, the mature morphology of the calyx is reached about 1 week following hearing onset, when it becomes chalice shaped, and terminates onto a single MNTB neuron (Kandler and Friauf, 1993, Wimmer et al., 2006, Ford et al., 2009). Changes in morphology begins before hearing

onset (P12 in rats) suggesting that refinement of the calyx of held does not rely on acoustic stimuli (Kandler and Friauf, 1993). Indeed, congenitally deaf mice have normal synaptic transmission at the calyx, and similar morphology (Oleskevich et al., 2004, Youssoufian et al., 2005, Youssoufian et al., 2008).

How do differences in the immature MNTB affect its function? MNTB neurons in mature rats are able to follow high frequency trains (Wu SH, 1993), however younger rats (P8 – P11) are unable to follow high frequency trains (1kHz), only managing discharge rates of up to 200 Hz. In the rat, the most dramatic postnatal changes occur between the onset of hearing (P12) to the opening of the eyes (P14) (Oliver and Fakler, 1999). Upon maturation in rodents, presynaptic APs are narrowed (Taschenberger and von Gersdorff, 2000), NMDAR EPSCs are reduced (Taschenberger and von Gersdorff, 2000, Futai et al., 2001, Joshi and Wang, 2002) & AMPAR EPSCs are accelerated (Bellingham et al., 1998, Lawrence and Trussell, 2000). Immunohistochemistry has shown it is likely there is a developmental shift in AMPAR subunits from GluA1 to GluA4 (Joshi et al., 2004). This change is associated with acceleration of EPSCs, which are crucial for fast synaptic transmission in the MNTB (Yang et al., 2011).

### LSO circuits

Mature LSO principal neurons receive both ipsilateral glutamatergic excitatory input (AVCN-LSO) and contralateral glycinergic input (MNTB – LSO), which are needed for ILD processing (Tollin, 2003). This input is carefully arranged, so that each principal cell receives bilateral input arising from the same tonotopic location from both ears. Here, I will discuss how these bilateral innervations develop to fulfil their function as ILD detectors.

Anterograde tracing studies in rats have shown that bilateral inputs to the LSO are present pre-natally at just E18 (4 days before birth) (Kandler and Friauf, 1993, Kil et al., 1995, Sanes and Rubel, 1988). Furthermore, electrophysiological recordings (*in vitro*) have shown both ipsilateral and contralateral evoked PSPs are functional around birth in gerbils and rats (Sanes, 1993, Kandler and Friauf, 1995). Thus, the LSO has functional

input about 2 weeks prior when it is needed at hearing onset, which is around (P12-P14), when the external ear canal opens in rats and gerbils (Kandler et al., 2002).

**MNTB – LSO synapse** Surprisingly, contralateral evoked PSPs in the LSO are initially depolarising in early development (E18 & P4), but switch to mature hyperpolarising PSPs by P8 (Kandler and Friauf, 1995). Thus, immature LSO principal neurons receive bilateral excitatory input. During the first postnatal week, co-release of GABA, glycine and glutamate are thought to drive developmental refinement and pruning of the MNTB-LSO synapse, which are initially widely branched (Gillespie et al., 2005, Kandler et al., 2009b). By ~P14 there is a switch to glycine dominance (Kullmann et al., 2002, Kotak et al., 1998), although GABA spillover has been shown to excite nearby pre-synaptic MNTB neurons beyond P14 (Weisz et al., 2016).

How do glycine and GABA, neurotransmitters associated with an inhibitory hyperpolarising action cause depolarising PSPs? Immature LSO neurons maintain a high intracellular  $\text{Cl}^-$  concentration, setting the  $E_{\text{Cl}}$  at positive relative to the RMP (Kakazu, 2000, Ehrlich et al., 1999). Consequently, activation of GABA/glycine receptors causes  $\text{Cl}^-$  to flow out of the cell, down its electrochemical gradient, depolarising the cell. This is enough to trigger AP firing in the LSO, which suggests contralateral depolarising currents do not merely exist to prevent inhibition, but are an excitatory input in their own right (Ehrlich et al., 1999). Indeed, refinement of MNTB/LSO synapses is activity dependent, where cochlea ablation, or blockade of glycine receptors results in immature, widely branched MNTB axon terminals (Sanes and Takacs, 1993, Sanes et al., 1992).

Following the first postnatal week, glycinergic input to the LSO converts from a depolarising response, to a hyperpolarising response (Kandler and Friauf, 1995). This is due to increased activity of KCC2 (an outward  $\text{Cl}^-$  transporter), which causes a gradual negative shift of  $E_{\text{Cl}}$ , rendering intracellular  $\text{Cl}^-$  levels low (Kakazu et al., 1999). This switch to a hyperpolarising contralateral input to the LSO coincides with the maturational changes of the neuronal connections, such as strengthening and silencing of synapses (Kandler et al., 2009a, Hirtz et al., 2012). Thus, could it be the transition

from depolarisation to hyperpolarisation which causes maturation and refinement of the LSO inputs? Surprisingly, when this switch to hyperpolarisation was prevented using KCC2 knockdown mice, there was no change in the development and maturation of the MNTB-LSO or the CN-LSO synapses (Lee et al., 2016). Therefore, it may not be the change itself, but the presence of depolarising currents in perinatal animals that drives maturation of the LSO synapses.

### **AVCN-LSO synapse**

There has been little investigation into the development of the ipsilateral AVCN-LSO pathway. It is known that, unlike the MNTB-LSO pathway, stimulation of ipsilateral fibers at any age evokes depolarising excitatory postsynaptic potentials (EPSPs) in the LSO (*rat in vitro*), whose amplitude increased at higher stimulus intensities, indicating multiple synapses (Kandler and Friauf, 1995). In the same study, EPSPs were totally blocked by application of 6-cyano-7-nitroquinoxaline-2,3-dione (CNQX), suggesting they are not NMDAR mediated (Kandler and Friauf, 1995). However, more recent evidence demonstrates both the MNTB-LSO and AVCN-LSO pathways in the first postnatal week contain functional postsynaptic GluN2B containing NMDARs (Case et al., 2011, Case and Gillespie, 2011). Indeed, a population of extrasynaptic LSO NMDARs can be activated by both the contra and ipsilateral inputs, and are thought to allow 'cross talk' between the developing MNTB-LSO and AVCN LSO (Alamilla and Gillespie, 2011). It thought the AVCN-LSO pathway also undergoes extensive synaptic pruning (like the MNTB-LSO pathway) to ensure the synapses remain tonotopically aligned (Kandler et al., 2009b).

In summary, whilst many neuronal connections are already in place at birth, the auditory system is not yet mature, and must undergo significant refinement of neuronal connections, and further development of the outer and middle ear.

## **1.5 SYNAPTIC TRANSMISSION IN THE LSO**

The LSO receives both glutamatergic excitatory input from the ipsilateral ear, and glycinergic inhibitory synaptic input from the contralateral ear, the kinetics of which must be matched to enable accurate ILD processing (Tollin, 2003, Park et al., 1996b).

Throughout this thesis, I have assessed AOE mediated changes to EPSCs in the LSO. It has already been confirmed that AOE does not alter IPSCs (Pilati et al., 2016). I shall therefore discuss the glutamate receptors responsible for excitatory synaptic transmission in the LSO.

### Glutamate receptors in the SOC

Glutamate receptors can be divided into two major classes: Ionotropic and metabotropic. Several ionotropic glutamate receptors have been identified:  $\alpha$ -amino-3-hydroxy-5-methyl-4-isoxazolepropionic acid (AMPA), *N*-methyl-D-aspartate (NMDA) and kainate receptors (Dingledine et al., 1999, Lodge, 2009). All are composed of four large transmembrane subunits (>900 residues), which together form a pore through which ions can pass (Traynelis et al., 2010). The LSO and MNTB have been found to possess both AMPARs and NMDARs, which can be blocked by the addition of the antagonists CNQX and d-AP5 respectively (Stereberg, 2011).

### AMPARs mediate fast EPSCs in the LSO, crucial for ILD processing

AMPARs mediate the majority of fast glutamatergic synaptic transmission in the central nervous system. They are composed of four subunits: GluA1 GluA2, GluA3 and GluA4, each encoded from the same gene, which together can form homo or heteromeric channels (Perfilova and Tyurenkov, 2016). Each subunit has an extracellular N terminus and an intracellular C terminus. The ligand-binding domain is located on the N-terminal (region S1 and S2) (Geiger et al., 1995, Hollmann et al., 1994, Dingledine et al., 1999). Subunit composition, splice variants and mRNA editing can produce AMPARs with diverse functions (Borges and Dingledine, 1998).

AMPAR subunits exist as two different splice variants, flip and flop, in which only a few amino acids are changed in the C terminal end of the loop (Hollmann and Heinemann, 1994, Sommer et al., 1990). Although the difference between the flip and flop splice variants are only minor, there are dramatic changes in desensitization kinetics between the two. For example, the flop variant of AMPAR subunits GluA2, GluA3 and GluA4 desensitize three times faster than their flip counterparts, however recovery from desensitization is much slower (Quirk et al., 2004, Mosbacher et al., 1994). The auditory brainstem predominantly expresses the flop splice variant (Schmid et al., 2001).

$\text{Ca}^{2+}$  permeability is controlled via the posttranscriptional editing of the GluA2 subunit, which changes a single amino acid from glutamine (Q) to arginine (R) (Washburn et al., 1997, Hollmann and Heinemann, 1994, Geiger et al., 1995). This occurs at the TMII region, and is termed the Q/R site. The 'Q' variant is  $\text{Ca}^{2+}$  permeable, whilst the 'R' variant is not. Most AMPARs in the brain are impermeable to  $\text{Ca}^{2+}$ , and are associated with slow kinetics (Wright and Vissel, 2012). In contrast, the auditory brainstem expresses AMPARs with high  $\text{Ca}^{2+}$  permeability which is associated with rapid synaptic transmission (Ravindranathan et al., 2000) needed for accurate ILD processing (Tollin, 2003). For example, Geiger et al (1995) have shown that rat MNTB AMPARs are highly permeable to  $\text{Ca}^{2+}$ , and have rapid desensitization and deactivation kinetics. In the LSO, Caicedo et al (1998) reported moderate glutamate induced cobalt uptake via  $\text{Ca}^{2+}$  permeable non-NMDARs in the mature auditory system in rats.

Finally, subunit composition of AMPARs can alter the kinetics of the response. Expression of GluA3 flop and GluA4 flop subunits, and post transcriptional suppression of GluA2 results in fast kinetics observed in the auditory system. Specifically, the MNTB is dominated by GluA4 (not GluA3), where removal of GluA4 (transgenic mouse) resulted in much slower EPSCs and mEPSCs (but not in a GluA3 KO mouse) (Yang et al., 2011).

#### NMDARs in the auditory system

NMDARs are ionotropic glutamate receptors located throughout the central nervous system (CNS), whose activity is critical for regulating developmental plasticity, learning and memory in the brain (Kerchner and Nicoll, 2009). Like other glutamate receptors, NMDARs are composed of 4 subunits, each of which have an extracellular N terminus and an intracellular C terminus, that together form a heteromer surrounding a central pore. All NMDAR complexes contain the subunit GluN1, whilst there are four GluN2 subunits (GluN2A-D) each a product of a different gene (Vyklícky et al., 2014). Different GluA2 subunits in combination with an obligatory GluN1 subunit generate a large number of NMDARs with different properties. For example, NMDARs containing GluN2A have fast response kinetics, where EPSCs last tens of milliseconds, whilst those

that contain GluN2B have much slower kinetics, mediating EPSCs lasting hundreds of milliseconds (Sanchez et al., 2015). In addition, different splice variations of GluN1 exist, through differential splicing of mRNA which encodes either the N terminus or the C terminus of the subunit, thus expanding variety of NMDAR functionality in the brain.

Unlike most AMPARs, NMDARs are highly permeable to  $\text{Ca}^{2+}$  (as well as  $\text{K}^+$  and  $\text{Na}^+$ ) (Lynch et al., 1983, Malenka et al., 1988). Furthermore, they are blocked at resting membrane potential by extracellular  $\text{Mg}^{2+}$  (Nowak et al., 1984, ChesnoyMarchais and Barthe, 1996). This voltage dependent block is relieved only upon sufficient depolarisation of the neuron, such as when AMPARs are activated by a release of glutamate caused by a train of APs arriving at the pre-synaptic terminal. As well as glutamate, NMDARs require glycine to act as a co-agonist, which must bind to the GluN1 subunit, whilst glutamate binds to the GluN2 subunit to enable activation of the channel (Kleckner and Dingledine, 1988, Hirai et al., 1996, Cummings and Popescu, 2015).

Once activated,  $\text{Ca}^{2+}$  is able to flow down its electrochemical gradient into the neuron, and trigger signaling cascades which activate a wide range of post synaptic functions, such as long term potentiation (LTP) by activation of CaMKII and phosphorylation of the GluA2 AMPA receptor subunit (Lisman et al., 2012) .

Fast temporally precise encoding of sound in the auditory system is dependent on AMPARs (Trussell, 1998, Parks, 2000), whereas activation of NMDARs results in a slow time-course EPSP, which act in concert with the fast AMPAR to form a dual component response to glutamate release (Forsythe and Westbrook, 1988). In rats, within the first 2 postnatal weeks, NMDARs in hair cells are composed of GluN1 and GluN2A as well as afferent and efferent fibers (Knipper et al., 1997). It is thought their presence contributes to activity dependent maturation of the cochlea. Maturation is accompanied a reduction in GluN1 and GluN2A, and an increase in GluN2B-D. The role of NMDARs in mature IHC-SGC synapse is not direct glutamatergic transmission. They are instead thought to be involved in regulating AMPARs. Indeed, surface AMPARs in

cultured mouse auditory neurons were reduced upon application of NMDAR agonist (Chen et al., 2007).

## 1.6 THE ROLE OF POTASSIUM CHANNELS IN THE AUDITORY SYSTEM

There are a huge number of genes (around 40) dedicated to  $K^+$  channels, from ~12 families (Johnston et al., 2010). Typically,  $K^+$  channels in vertebrates are tetrameric, with 4  $\alpha$  subunits arranged as a ring, forming a highly selective pore through which  $K^+$  can flow. Elaboration of this structure through differences in subunit composition,  $\beta$  subunits and accessory proteins provide a large diversity of properties and functions of  $K^+$  channels (Johnston et al., 2010). RMP is primarily dictated by leak channels: inwardly rectifying  $K^+$  (Kir) channels (Hibino et al., 2010), and outwardly rectifying tandem 2 pore  $K^+$  channels (K2P) (Enyedi and Czirjak, 2010). Here I will focus on voltage-gated potassium channels, which act to repolarise APs, and their role within the auditory system. These channels are major controllers of excitability, whose properties shape the AP firing phenotype of neurons, depending on the type and composition of channels present. The Kv family can be divided into several subfamilies on the basis of sequence similarity and function. Four of these subfamilies (Kv1:Kv4) are composed of 4 pore forming  $\alpha$  subunits, with auxiliary cytoplasmic  $\beta$  subunits, which can regulate the properties of the channel (Isom et al., 1994). Each  $\alpha$  subunit is composed of 6 transmembrane segments (fig 1.6) (Doyle et al., 1998). Subunits from the same subfamily can come together to form heteromeric channels (Isacoff et al., 1990, Ruppersberg et al., 1990).

Kv4 channels (present in the LOC neurons) generate A-type ( $I_A$ ) current upon depolarisation, but require prior hyperpolarisation to activate (Leijon and Magnusson, 2014, Hille, 2001). Here, I will focus on the roles of Kv1 and Kv3 in the auditory brainstem.

Figure 1.6 Kv channel  $\alpha$  subunit structure

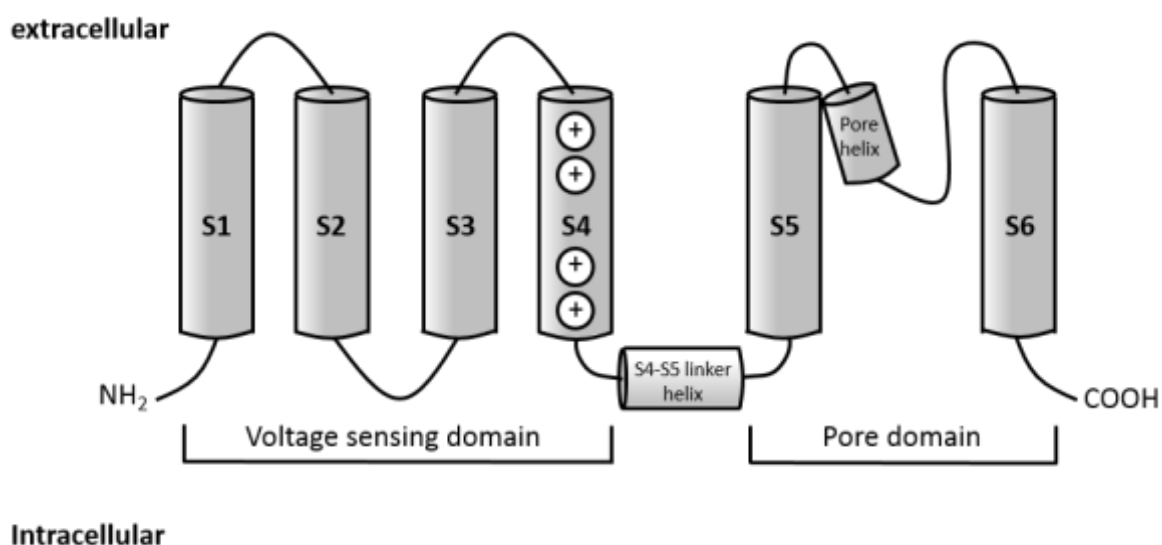


**Fig 1.6. Kv channel  $\alpha$  subunit structure.** Schematic representation of Kv  $\alpha$  subunit structure. 6 transmembrane segments create two functional domains: voltage-sensing (S1-4) & pore domain (S5-6)

### Kv1 provides temporal precision in the auditory brainstem

There are seven members of the Kv1 family (Kv1.1-Kv1.7) which are found widely in many areas of the brain and body, and act to regulate AP firing in nerve and muscle tissue (Hille, 2001). Kv1 channels are low voltage activated (LVA) with fast kinetics, and will activate after only small depolarisation close to RMP (Johnston et al., 2010). Kv1 are found throughout the auditory system. and act to limit AP firing, so that only one AP, rather than a train of APs, occurs in response to a single depolarising input, thus reducing temporal summation (Oertel, 1983). This is essential in the auditory system for detecting sound localisation cues (Trussell, 1999). Indeed, deletion of the *Kcna1* gene in mice (which codes for Kv1.1) lowers behavioural sensitivity to small changes in sound location, but has no effect on hearing level thresholds (Allen and Ison, 2012b). Furthermore, single unit recordings from LSO neurons in Kv1.1 KO mice showed the ILD function was skewed towards the ipsilateral ear, thus undermining ILD processing, and resulted in auditory deficits similar to those experienced by mice with monoaural hearing (Karcz et al., 2011, Karcz et al., 2015).

## Kv1 in the MNTB

The MNTB expresses LVA  $K^+$  currents, which are blocked by addition of dendrotoxin-I (DTX I) (Brew and Forsythe, 1995b), an antagonist which acts specifically against Kv1.1, Kv1.2 and Kv1.6. Immunohistochemistry has revealed Kv1.1, Kv1.2 and Kv1.6 protein is present in the MNTB, with comparatively low levels of Kv1.3 and Kv1.4. Kv1.1 and Kv1.2 form heteromeric channels in the somatic and axonal regions, whilst Kv1.6/Kv1.1 heteromers are located in the soma only (Dodson et al., 2002).

What is the function of Kv1 in the MNTB? MNTB neurons receive a large EPSP courtesy of the giant Calyx of Held. The EPSP has a fast AMPAR mediated component, but also a slower NMDAR component (Forsythe and Barnes-Davies, 1993). The presence of the slow NMDAR mediated current would cause multiple firing in the absence of Kv1 (Brew and Forsythe, 1995b). It is Kv1 mediated current which acts to prevent multiple firing, by opposing the depolarisation of the slow NMDAR component. Single AP firing is maintained by Kv1.2 containing channels (Kv1.1 and Kv1.2 heteromer) in the first 20  $\mu\text{m}$  of the axon (Clark et al., 2009, Dodson et al., 2002) a key site of spike initiation (Stuart and Sakmann, 1994). Indeed, blocking Kv1 using DTX I causes MNTB neurons to switch from single-spiking neurons, to multi-firing neurons (Dodson et al., 2002). Similarly, mice lacking Kv1.1 showed hyper-excitability and reduced LVA currents in the MNTB (Brew et al., 2003a).

The majority of the work discussed in relation to Kv1 has been performed on rodent brain slices *in vitro*, but do these observations apply *in vivo*? *In vivo* single unit recordings from both the axonal endings of VCN bushy cells (calyces of held) and MNTB neurons were performed in Kcna1 null mice (lack Kv1.1) (Kopp-Scheinflug et al., 2003). KO mice showed increased jitter in the CN calyces and AP failures in the MNTB in response to high frequency sound stimulation, thus reducing the capacity for processing temporal information. In contrast to *in vitro* studies, which have shown an increase in excitability in response to current injection (Brew et al., 2003b, Brew and Forsythe, 1995b, Smart et al., 1998, Gittelmann and Tempel, 2006), evoked APs *in vivo* were significantly lower in KO mice in response to mid-high sound intensities. What is the reason for this discrepancy between *in vivo* and *in vitro* findings? *In vitro*, AP

recording in response to depolarising current injection reflects only intrinsic excitability of the neuron being recorded, however *in vivo* recordings reflect both the intrinsic excitability, but also the balance of excitatory and inhibitory inputs to the neuron itself. Kopp-Scheinflug et al (2003) postulated that increased inhibition *in vivo* reduced AP firing, which would not be detected *in vitro*. An alternative reason was contributed by Gittelman et al (2006), who postulated that during high stimulation rates, the membrane is depolarised sufficiently to inactivate voltage-gated Na<sup>+</sup> channels, and thus decrease AP firing.

### Kv3 channels mediate fast action potential firing

Kv3 channels are high voltage activated channels (HVA), which require voltages only achieved during APs to open. This has been demonstrated *in vitro* using HEK293 cells transfected with Kv3.1 or Kv1.1 cDNA, which were voltage clamped to mimic a pair of APs recorded from a neocortical neuron. Here, Kv3 mediated current does not appear until the AP has reached its peak, unlike Kv1 current, which is first seen during the rising phase of the AP (Rudy et al., 1999). Kv3 channels rapidly activate and deactivate to produce APs of brief duration, which quickly repolarize the neuron, and limit the refractory period, enabling high frequency firing. Because of this, they are usually found where there is a need for rapid AP firing, such as the hippocampus, basal ganglia, neo cortex and auditory nuclei (Weiser et al., 1994a).

Kv3 antagonists have proven useful in confirming the properties of Kv3 channels on high frequency repetitive firing neurons. Kv3 channels can be blocked by addition of tetraethylammonium (TEA) or 4-aminopyridine (4-AP), which have IC50 values of ~200 μm and 0.02-0.5 mM respectively (Rudy and McBain, 2001). Application of 1 mM TEA has been shown to broaden APs and disrupt fast spiking of interneurons in response to a sustained depolarising current in mouse neocortical slices (Erisir et al., 1999). Interestingly, whilst the overall steady state firing pattern was lower following application of TEA, the first few AP spikes were unaffected, suggesting that one way Kv3 channels act to mediate high frequency firing is by reducing Na<sup>+</sup> channel inactivation.

There are 4 Kv3 genes (KCN1-4) which produce 4 Kv3 subunits (Kv3.1, Kv3.2, Kv3.3 and Kv3.4) present in both rodents and humans (Rudy and McBain, 2001). Whilst Kv3.1-Kv3.3 are abundant in the (CNS), Kv3.4 is only present in a few neurons in the brain, and is mostly found in skeletal muscle and sympathetic nerves (Weiser et al., 1994a). Kv3 channels are able to form heteromeric channels with other members of the same subfamily. Moreover, co-immunoprecipitation studies have shown Kv3 channels exist as heteromers in many areas of the CNS including the neocortex and cerebellum (Chow et al., 1999, Tansey et al., 2002).

All four can undergo alternative splicing, which produces 13 known isoforms with different intracellular C-terminal sequences (Kv3.1a-Kv3.1b, Kv3.2a-Kv3.2d, kv3.3a-kv3.3d and Kv3.4a-Kv3.4c) (McIntosh et al., 1998). When expressed in a heterologous system, the currents mediated by the different isoforms are indistinguishable (Vega-Saenz de Miera E et al., 1994). This begs the question, why have so many different isoforms if the currents they mediate are the same? Evidence has shown alternate splicing of Kv3 subunits may instead serve to traffic channels to different subcellular locations (Ozaita et al., 2002).

### **Kv3 in the auditory brainstem**

The auditory system relies upon the ability to fire APs at high frequencies in order to faithfully encode sound frequency and level, and to extract sound localisation cues (Tollin, 2003). The MNTB for example is capable of firing phase locked APs at over 600 Hz (Wu and Kelly, 1993). Neurons of the auditory system, particularly the MNTB, have become models for investigating Kv3 properties in native neurons, due to their rapid firing properties, and high levels of Kv3 expression. Indeed, MNTB neurons lose their ability to fire high frequency APs when Kv3 channels are blocked by addition of TEA (Wang et al., 1998). Currently the subunit composition of Kv3 subunits in the SOC are unconfirmed, and will be explored in chapter 4.

## 1.7 EFFECTS OF ACOUSTIC OVER-EXPOSURE IN THE COCHLEA

Noise induced hearing loss (NIHL) is a major, preventable form of hearing loss, and is therefore a major public health issue (Sliwinska-Kowalska and Davis, 2012). Following acoustic injury, hearing thresholds recover exponentially over the next few weeks (Miller JD, 1963), and can either recover fully (temporary threshold shift) or stabilize at an elevated level (permanent threshold shift). NIHL can be generated by exposure to a single, very intense sound, such as an explosion, or by exposure to loud sounds over a longer period of time, such as working in a factory (Spoendlin and Brun, 1973). Permanent threshold shifts are caused by damage of the hair cells and/or the mechanosensory bundle by excessive mechanical stress (Slepecky, 1986) and/or hair cell death via metabolic stress (Henderson et al., 2006).

Many studies have attempted to examine the effect of acoustic trauma on the cochlea, using rat and mouse models, by subjecting them to varying levels of sound at different intensities. In humans, hearing thresholds are measured using a behavioural audiogram, which measures the quietest sound the respondent can hear across a range of frequencies. This type of assessment in mice and rats is not possible, and so other non-invasive methods are used to assess the extent of hearing damage, such as the auditory brainstem response (ABR) (see chapter 2, section 2.4 for explanation) or distortion product otoacoustic emissions (DPOAEs). DPOAEs provide a measure of OHC function, whose motility mechanically amplifies movement of the BM and generates a low frequency sound in the process. When two primary tones are presented to a normal ear, healthy functioning OHCs produce DPOAEs, which are reflected back through the middle ear and TM to be measured at the EAM (Shera and Guinan, 1999).

Differences in AOE protocols, whether that be the length of exposure or stimulus type (pure tone, broadband etc.) can lead to varying levels of damage to the cochlea, and determine whether hearing thresholds return to normal, or remain permanently elevated. For example, Wang (2002) found that delivery of 95 dB SPL octave band noise (8-16 kHz) for two hours in CBA/CaJ mice led to a temporary hearing loss, which returned to near normal levels two weeks following the acoustic insult. Exposure at levels over 100 dB SPL led to a permanent hearing threshold shift, the severity of

which correlated with the intensity of the sound delivered, resulting in ABR thresholds beyond 80dB SPL in mice exposed to the highest intensity sound (116 dB SPL).

Light microscopic histopathology analysis from the same mice found that exposure at high levels (>100 dB) initially caused swollen nuclei in the OHCs, which led to selective loss of OHCs in the two weeks following the acoustic insult, and permanent hearing loss. Similarly stereocilia of the IHCs were damaged at slightly higher levels of noise at >106 dB SPL. Supporting cells were also affected such as the Henson cells, and at higher intensity sounds (116 dB SPL), the reticula lamina was ruptured when examined within the first 24 hours of AOE, causing cellular debris in the scala media (Wang et al., 2002).

Further studies have focused on the effect of mild/moderate trauma designed to induce temporary hearing loss in the cochlea. Kujawa and Liberman (2009) found that delivery of 100 dB SPL for two hours (8-16 kHz) to mice caused a temporary hearing threshold shift, as well as temporary OHC dysfunction (as measured by ABR and DPOAEs respectively). Interestingly, whilst both DPOAE and ABR thresholds recovered after two weeks, suprathreshold ABR amplitudes, especially in high frequency regions (32 kHz), were significantly reduced, indicating neuronal loss in the high frequencies, despite full recovery of OHCs.

Confocal images of immunostained mouse cochlea confirmed no loss of hair cells (OHCs or IHCs), or damage to the stereocillia up to a year post-exposure. Yet, as predicted by the reduction in suprathreshold ABRs, within just 24 hours post AOE, roughly half the IHC ribbon synapses had disappeared, along with the afferent postsynaptic fibers that contacted them. It was previously thought that permanent hair cell injury led to cochlear terminal loss. In fact, it appears the synaptic connections between IHCs and SGNs show irreversible losses, even when hair cells exhibit full recovery (Kujawa and Liberman, 2009, Furman et al., 2013, Liberman et al., 2015). This synaptopathy has been termed 'hidden hearing loss', and is likely to degrade suprathreshold auditory processing because it appears to target low spontaneous firing fibers (Liberman et al., 2015, Furman et al., 2013). This cannot be detected by conventional audiometry, and could account for 5-15% of patients who seek

audiological help for hearing difficulties, yet have normal hearing thresholds using standard audiometry (Hind et al., 2011).

Whilst much is known about the effect of AOE in the periphery, much less is known about the effect of AOE on further up the ascending auditory pathway. Emerging evidence has provided insight into changes in central mechanisms following acoustic trauma. Throughout this thesis, I will build upon this work, and assess how AOE changes the intrinsic and synaptic excitability in the SOC of the auditory brainstem.

## 2 METHODS

---

The aim of this thesis is to explore the intrinsic and synaptic excitability of the LSO, and assess how damaging levels of sound may alter these properties. In this chapter, I shall first describe the origins of the mouse strains and transgenic mice, which were used for all the experiments presented in this thesis. Next, the process of mouse brain removal, slicing and maintenance is detailed. Brainstem slices containing the LSO were then subject to whole cell patch clamping to measure ionic and synaptic conductance. I shall describe how cell types were identified, the process of breaking into the cells, the different types of recordings (e.g. voltage clamp, current clamp etc.) and any offline corrections to the data.

Prior to culling, the hearing of mice was assessed both before and after AOE, using the auditory brainstem response (ABR). Here, the process of obtaining ABRs is detailed, along with and the procedure to deafen the mice by AOE. Next, the immunohistochemistry protocol is described, which was used to localise Kv3 channel subunits in the mouse auditory brainstem. This is followed by the western blotting protocol, employed to assess any changes in Kv3 channel subunits between control (CBA/Ca) and KO mice. Finally, the polymerase chain reaction (PCR) protocol is detailed, which was used to identify the genotype of mice within the transgenic colonies.

### 2.1 ORIGINS OF MOUSE STRAINS

All animal experiments were performed in accordance with the UK Animals (Scientific Procedures) Acts of 1986 and 2012 using personal license (PIL) number 40/2689, under project license 60/4363. Mouse colonies were maintained by The University of Leicester Biomedical Science Division and kept under controlled conditions, fed on a standardized diet, and kept on a twelve-hour light/dark cycle. These studies were conducted using 3 strains of mice:

#### **CBA/Ca strain provide a mouse model of normal hearing**

CBA/Ca mice were chosen because they have 'good hearing' in the first year of life (Ohlemiller et al., 2010) in contrast to C57 which show an accelerated age-related

hearing loss (Henry and Chole, 1980). The colony founders were acquired from Harlan (UK) with further breeding pairs supplied by Charles River (UK). CBA/Ca mice are an inbred strain, thus reducing genetic variability compared to an outbred strain.

#### Transgenic mouse colonies

The original Kv3.1 null mice were generated by Joho et al (Ho et al., 1997) at The University of California, and we subsequently acquired them from Professor L. Kaczmarek, University of Yale. We have backcrossed the original strain onto our control strain of mice (CBA/Ca), to enable comparison of findings.

The Kv3.3 null mice strain were originally generated by Joho et al (Espinosa et al., 2001), and later acquired from Professor Brian Robertson at The University of Leeds. This colony was also backcrossed onto our control CBA/Ca strain by The University of Leicester Biomedical Science Division.

Mice were used both for *in vivo* (ABR, AOE) and *in vitro* experiments (whole cell patch clamping, immunohistochemistry, western blotting). The *in vitro* experiments required mice to be culled and the brain removed either for 1) embedding in OCT (immunohistochemistry) or 2) slicing using a vibratome (whole cell patch clamping, western blotting). The slicing procedure to prepare brainstem slices for whole cell patching is detailed next. The process of brain removal prior to slicing was also used for both immunohistochemistry and western blotting protocols.

*Table 2.1 Composition of 'normal aCSF' and 'slicing aCSF'*

Substance	Conc. in normal aCSF (mM)	Conc. Low Na <sup>+</sup> slicing aCSF (mM)
NaCl	125	0
KCl	2.5	2.5
Glucose	10	10
Sucrose	0	250
NaH <sub>2</sub> PO <sub>4</sub>	1.25	1.25
Na pyruvate	2	0
Myo-inositol	3	0
Ascorbic acid	0.5	0.5
NaHCO <sub>3</sub>	26	26
CaCl <sub>2</sub>	2	0.1
MgCl <sub>2</sub>	1	4

**Table 2.1** Composition of 'normal aCSF' and 'slicing aCSF'. Slicing aCSF contains low sodium and low magnesium to prevent excitotoxicity, osmolality is maintained by substituting sucrose for NaCl.

Osmolality = 310 - 320 mOsm/L

*Table 2.2 Patch pipette solution composition*

Substance	Conc. In normal patch solution (mM)	Patch pipette solution containing caesium chloride (mM)
KCl	32.5	0
HEPES	10	5
EGTA	5	5
MgCl <sub>2</sub>	1	1
Kgluconate	97.5	0
CsCl	0	130

**Table 2.2** Patch pipette solution composition. All experiments used 'normal' patch solution, unless otherwise specified. Patch solution containing caesium chloride was used when recording postsynaptic currents. Osmolality = 280 - 300 mOsm/L

Figure 2.1 Mouse brain removal and slice preparation

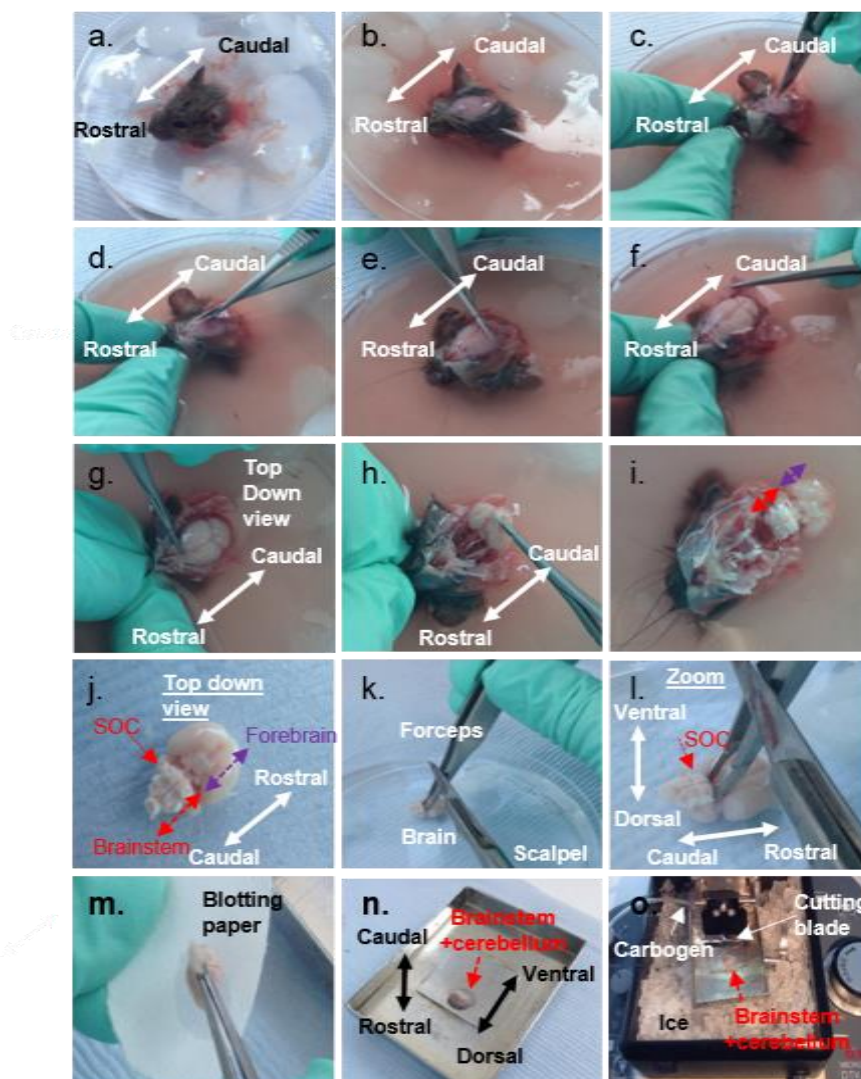


**Fig 2.1. Mouse brain removal and slice preparation.** **a.** The head was removed with singular rapid cut using a scalpel blade, and placed into partially frozen low sodium slicing aCSF. **b.** Skin removal via scalpel blade. **c.** A hole was made at the top of the skull using scalpel blade tip. **d.** Fine scissors were inserted into the hole, and rostral & caudal cuts were made along the midline **e.** A lateral cut using fine scissors. **f.** The skull was prised back using forceps to reveal brain underneath. **g.** Top-down view of the brain, showing severance of the olfactory bulbs, using fine scissors. **h.** The brain is tilted caudally, so that the ventral side faces upwards. **i.** Remaining nerves are severed, and the brain freed from the skull via severing the spinal cord, red arrow denotes the brainstem, purple arrow denotes the cerebrum. **j.** Top down view of the brain, rested on its dorsal side, the lateral plane where the SOC is located is labelled in red. **k.** Forceps are placed between the cerebrum and the brainstem + cerebellum at a 45° angle, to act as a guide for a singular transverse cut using a scalpel blade. **l.** A zoomed in version of image k, showing the separation of cerebrum and brainstem + cerebellum. **m.** The brainstem + cerebellum was then lifted via the spinal cord end using forceps and blotted on the cut side to removed excess aCSF. **n.** The brainstem + cerebellum was then mounted to the cutting plate using superglue, with the ventral side facing towards the cutting blade. **o.** Slicing aCSF is added to the cutting plate, and is fixed in place on vibratome, and supplied with carbogen (95% O<sub>2</sub>: 5% CO<sub>2</sub>).

## 2.2 BRAIN SLICE PREPARATION & MAINTENANCE

Rapid, and careful preparation of brain slices is essential for experimental success when patch clamping. Here, I describe the slicing procedure used to produce healthy mouse brainstem slices containing the SOC.

### Brain removal and slicing process

Mice aged P7 to P27 from CBA/Ca, Kv3.1, Kv3.3 strains were decapitated using a surgical blade (Swann Morten, no 26), and the head immediately submerged in partially frozen low Na<sup>+</sup> 'slicing' artificial cerebral spinal fluid (aCSF) (fig 2.1, a). Slicing aCSF had been bubbled with carbogen (95% O<sub>2</sub> and 5% CO<sub>2</sub>) prior to use, ensuring a pH of 7.4 (see table 2.1 for details of aCSF composition). The skin overlying the skull was removed immediately using the scalpel blade (fig 2.1, b). A small incision was then made in the centre of the sagittal suture using the tip of the scalpel, between the two parietal bones of the skull, allowing the access of small fine scissors (fig 2.1, c). A rostral cut using the scissors was then made between the parietal bones, extending through the frontal bone between the eye sockets, and a caudal cut continuing through the interparietal bone and occipital bone towards the spinal cord (fig 2.1, d). Scissors were directed towards the surface throughout, to avoid damaging the brain tissue underneath. Following this, lateral cuts were made along the parietal bones (fig 2.1, e), perpendicular to the original dissection, thus creating four distinct areas of skull which could be prised away using forceps, to reveal the brain underneath (fig 2.1, f). The olfactory bulbs were then severed (fig 2.1, g), freeing the brain at the rostral end, allowing the forebrain to be carefully tilted caudally (whilst still submerged in ice-cold slicing aCSF), so that the ventral side of the brain faced upwards (fig 2.1, h). Remaining nerve connections and blood vessels were cut using fine scissors, each time freeing the brain and revealing more of the ventral side of the brainstem (fig 2.1, i). When the ventral side of spinal cord came into view, this was severed using scissors, and the whole brain removed from the skull of the mouse (still submerged in slicing aCSF) (fig 2.1, j).

To separate the brainstem and cerebellum from the forebrain, the brain was rested on its dorsal side, and forceps pushed between the forebrain and cerebellum and held at

a 45° angle. A scalpel blade was then used to make a single transverse cut, using the forceps as a guide, separating the brainstem and cerebellum from the forebrain (fig 2.1, k and l). The cerebellum was left intact to anchor the brainstem during the slicing process. To mount the brainstem ready for slicing, a small drop of superglue (approx. 6mm diameter, spread thinly) was placed on the cutting plate of a DTK-1000 Microslicer (Dosaka, Kyoto, Japan). The brain was then lifted via the spinal cord using forceps and quickly blotted using filter paper, to absorb excess aCSF (fig 2.1, m). The brainstem was then placed on top of the glue, with the cut side facing down and the spinal cord facing upwards, and was orientated so that the ventral side of the brain containing the (SOC) faced towards the cutting blade (fig 2.1, n). The brainstem was then gently pushed down using a gloved finger, to ensure good adhesion of the tissue to the cutting plate, which was then fixed in place within the microslicer. Ice-cold slicing aCSF was then poured into the chamber, and supplied with carbogen during the slicing process, to maintain pH 7.4. Ice directly underneath the cutting tray ensured the aCSF bathing the brainstem remained cool during the slicing process (tissue remains firmer and easier to slice at low temperatures) (fig 2.1, o).

Initially, thick coronal slices were taken, by raising the cutting plate platform by up to 1mm, with more caution taken thereafter (thinner slices) when approaching the 7<sup>th</sup> cranial nerve. These slices were quickly discarded, by pushing them behind the blade using a needle, to avoid interfering with subsequent slicing. The emergence of the 7<sup>th</sup> nerve at the ventral side of the brainstem indicates the arrival of the SOC, and was used as a cue to start collecting 150 or 200 µm slices. Typically, three to four slices were collected and individually transferred to a custom-made chamber containing normal aCSF (table 2.1) using a modified Pasteur pipette (cut to a diameter of 8mm). Slices were incubated in the chamber for 50 minutes, and maintained at 36°C, by partial immergence in a water bath. The chamber was supplied with 95% O<sup>2</sup>/5% CO<sup>2</sup> to keep a pH of 7.4 (fig 2.2).

### Slice maintenance and recording chamber

Following incubation at 36°C, the custom-made chamber containing the slices was removed from the water bath and allowed to cool to room temperature. For recording, one slice at a time was transferred to the recording chamber, mounted on the stage of a Zeiss Axioskop microscope. The recording chamber was continuously perfused with normal aCSF (gassed with 95% O<sub>2</sub>, 5% CO<sub>2</sub> at 1 ml min<sup>-1</sup>). The aCSF was held in a 100 ml conical flask at room temperature, and drawn through tubing from the flask to the recording chamber using a peristaltic pump (Gilson Minipuls 3, R8 medium flow pump head). The aCSF was heated via a Peltier device immediately prior to entering the recording chamber, so that temperature was 35±1 °C at the position of the brain slice in the recording chamber. Temperature was monitored using an electronic thermometer. If temperature deviated from 35±1°C, the custom-built control unit for the Peltier device was manually adjusted to change the temperature of the aCSF entering the recording chamber. The slice was held down using a 'harp'; a thin piece of platinum, bent into a horseshoe shape with thin horizontal nylon strings secured by superglue. The slice was first viewed on low magnification using differential interface contrast (DIC) optics with a 4x, (0.10) Zeiss Achroplan objective to visualise the SOC. Cells of the LSO or MNTB were then visualised on high magnification, using a 63 X (0.9) Zeiss Achroplan water immersion objective. For image acquisition, a charge coupled device (CCD) camera (KP-M2RP, Hitachi) using WinTV software (Hauppauge Computer Works) was used.

Figure 2.2 Brain slice maintenance chamber

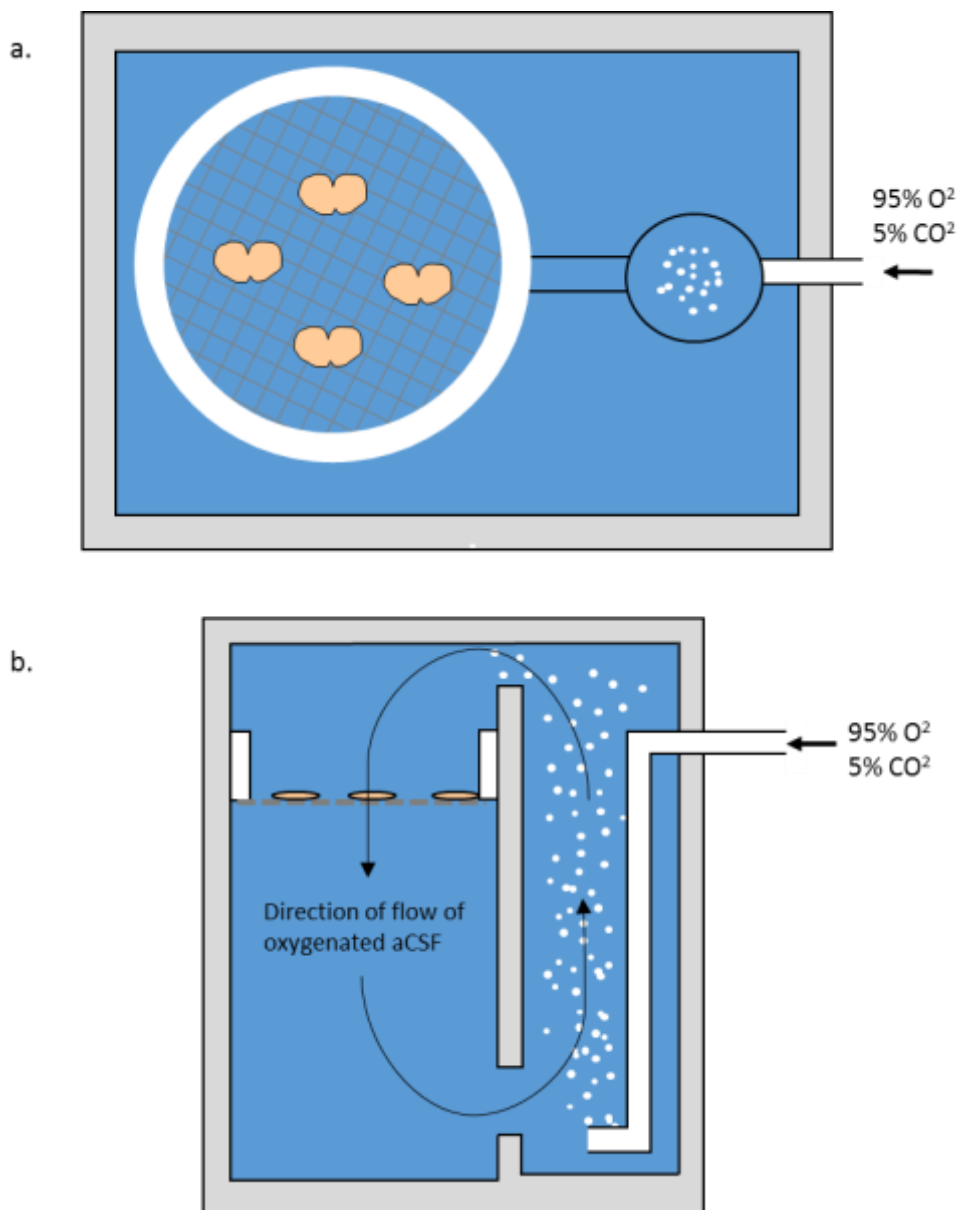


**Fig 2.2. Brain slice maintenance chamber.** **a.** Birds-eye view of the custom-built chamber filled with normal aCSF. The chamber contains two cylindrical spaces set within a Perspex box, joined together at the bottom by a 1.5 cm diameter tunnel. The larger chamber (left) contains a custom-built removable circular Perspex ring, set 2 cm down from the top of the chamber, to which nylon mesh is glued. This is where the brain slices are laid flat following slicing. **b.** Cross section of the chamber. Carbogen (95% O<sub>2</sub>, 5% CO<sub>2</sub>) enters the chamber via plastic tubing in the smaller chamber (right), which is blocked at the end by silicone rubber, and finely perforated with a needle, allowing small bubbles of carbogen to enter the larger chamber where the brain slices sit. Fine bubbles rise to the top of the smaller chamber, creating a gentle flow of aCSF, which pushes down on the slices, keeping them in pressed against the mesh, and well oxygenated.

## 2.3 WHOLE CELL PATCH CLAMP

Basic theoretical principals underpinning whole cell patch clamp can be found in the appendix (chapter 8, section 8.1).

### Patch clamp rig apparatus

Whole cell patch recordings were made using a Multiclamp 700B (Molecular Devices, Sunnyvale, CA, USA), Digidata 1322a (Molecular Devices) and pClamp 10 software (Molecular Devices). Data were sampled at 50 KHz, and filtered at 10 kHz. Thin walled borosilicate glass capillaries (GC150F-7.5, Harvard Apparatus Ltd, Edenbridge, UK) were pulled to form patch pipettes (resistance 2-5M $\Omega$ ) using a two stage vertical puller (Narishige, Digitimer Research Instruments). Before use, patch pipettes were injected with intracellular patch solution using a non-metallic syringe needle (Microfil, World Precision Instruments). Patch pipettes were then inserted and secured in the recording head-stage, which in turn was mounted onto a PatchStar Micromanipulator (Scientifica, UK). (For details of the patch pipette solutions see table 2.2). Caesium chloride patch pipette solution was used to measure postsynaptic currents and 'normal' patch solution was used for all other whole cell patch clamp experiments shown.

### Visual identification of LSO and MNTB neurons:

The LSO could be identified on the slice on low magnification due to its characteristic 'U' shape (often depicted as an 's' shape in rats), and proximity to the 7<sup>th</sup> nerve on the ventral side of the slice. Once the microscope was aligned over the LSO, the objective was switched to high magnification. LSO principal cells could be identified by their 'fusiform' shape (Stereberg et al., 2010). Cells of the MNTB were identified by their large round, clustered appearance, and their position above to the lateral pyramidal tracts on the ventral side of the brainstem.

### Process of breaking into a cell

Patch pipettes were lowered into the bath, and positive pressure applied, by injecting around 2ml of air using a 5ml syringe. This created a jet of intracellular solution from the end of the patch pipette, preventing blockage by any material that may be floating

in the recording bath (e.g. fragments of brain tissue, dust etc.) The amplifier was then set to voltage clamp mode. A repetitive 20ms 5mV test pulse was then applied, enabling the amplifier to automatically calculate the resistance of the pipette (typically 2-5 MOhms). Automatic pipette offset was then used to 'zero' the amplifier.

Following pipette offset, the pipette was lowered down onto the cell of interest. When the patch pipette reached just above the cell, a further 2ml of positive pressure was applied using the 5ml syringe. The pipette was slowly lowered onto the cell, until the positive pressure from the pipette caused a dimple to appear on the cell (see fig 2.3 a). The pipette was repositioned if necessary, to the outer edge (still keeping a slight dimple), to prevent the electrode digging into the membrane. If the pipette was positioned too far towards the centre of the cell, this usually caused the nucleus of the cell to become lodged in the patch pipette upon whole cell configuration.

Pressure was then gradually released using a mouth pipette, so that the cell membrane was slowly drawn towards the tip of the patch pipette. When the cell membrane reached the pipette, pressure was released entirely, and very gentle suction applied to encourage a gigaseal to form. The holding potential was then immediately set to -60mV, to match the voltage inside the cell, and prevent a sudden depolarisation of the cell upon breakthrough. The formation of a gigaseal could be monitored by observing the currents measured in response to the continuous 5 mV test pulse. Due to the high resistance ( $>G\Omega$ ), the seal test amplitude was very low (appearing as a flat line), as current is inversely proportional to resistance (fig 2.3, b). Once a gigaseal was achieved, quick sharp suction was applied via the mouth pipette to break into the cell, forming a whole cell configuration (fig 2.3, c). Transient capacitance currents and series resistance were then compensated for at 70% (fig 2.3, d).

Figure 2.3 Process of sealing and breaking into a cell

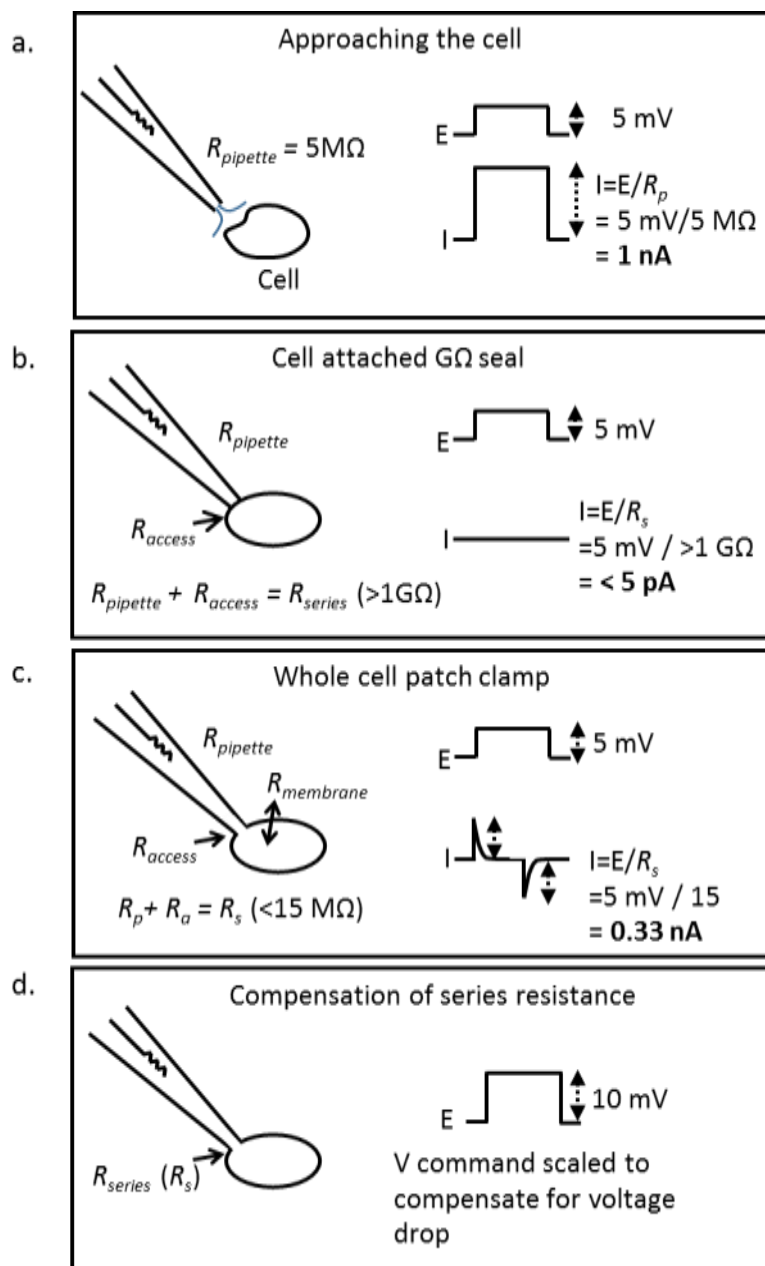


**Fig 2.3. Process of sealing and breaking into a cell.** **a.** Approaching the cell. Positive pressure is applied to the cell, forming a dimple on the cell surface. A constant seal test of 5 mV is delivered ( $E$ ) and the currents measured ( $I$ ), which are inversely proportional to the pipette resistance ( $R_{pipette}$ ). **b.** Cell attached  $\text{G}\Omega$  seal. The positive pressure is released, and gentle suction applied, drawing the membrane to the pipette, until the series resistance  $R_s$  reaches  $>1\text{G}\Omega$ . **c.** Whole cell patch clamp. Sharp suction is applied via a mouth pipette, allowing electrical access inside the cell. Capacitive transients can be seen in response to the 5 mV seal test. **d.** To overcome the voltage drop across the pipette due to series resistance, the voltage command must be scaled up. Figure is adapted from [www.axolbio.com](http://www.axolbio.com).

Using pClamp software, various pre-programmed protocols were then employed, in either voltage clamp or current clamp. Fig 2.4 shows a simple I/V recorded from an MNTB neuron. Here, the cell was held at a holding potential of -90mV for 150 ms followed by 10 mV steps up to +40mV, before returning to -90mV (fig 2.4, b) and the resulting currents recorded (fig 2.4, a).

$I_K$  first becomes measurable at -60mV and increases with further depolarisation because: 1. More channels open and 2. The electrochemical driving force on  $K^+$  increases. In other words, the difference between the membrane potential and the equilibrium potential for  $K^+$  increases (fig 2.4, c).  $I_{Na}$  first becomes increasingly negative (inward) as membrane potential becomes more positive due to depolarisation of opening the voltage dependent  $Na^+$  channels.  $Na^+$  flows down its concentration gradient into the cell, however, as the holding potential increases, the difference in electrical potential causes  $Na^+$  to flow out of the cell (fig 2.4, c) (Hille, 2001). Criteria and conditions for patch clamp recordings are shown in table 2.3.

#### **Estimation of Liquid Junction Potential:**

Differences in the composition between the intracellular patch solution and the extracellular aCSF causes a potential difference across the interface between the pipette tip and the bath. The reason why junction potentials develop is because of the difference in mobility of the ions across the interface, in particular the difference in motility between  $Na^+$  and  $K^+$  ions.  $K^+$  ions have high mobility (relative mobility = 1.00) compared to  $Na^+$  (0.682). Thus,  $K^+$  ions in the intracellular patch solution flow down their electrochemical gradient into the aCSF faster than  $Na^+$  ions flow from the aCSF into the patch pipette. This causes a voltage drop across the patch pipette, estimated to be -11.4 mV using offline calculations

([http://web.med.unsw.edu.au/phbsoft/LJP\\_Calculator.htm](http://web.med.unsw.edu.au/phbsoft/LJP_Calculator.htm)). Membrane potentials have not been corrected for this throughout the thesis.

Figure 2.4 Whole cell voltage clamp recording from a mouse MNTB neuron

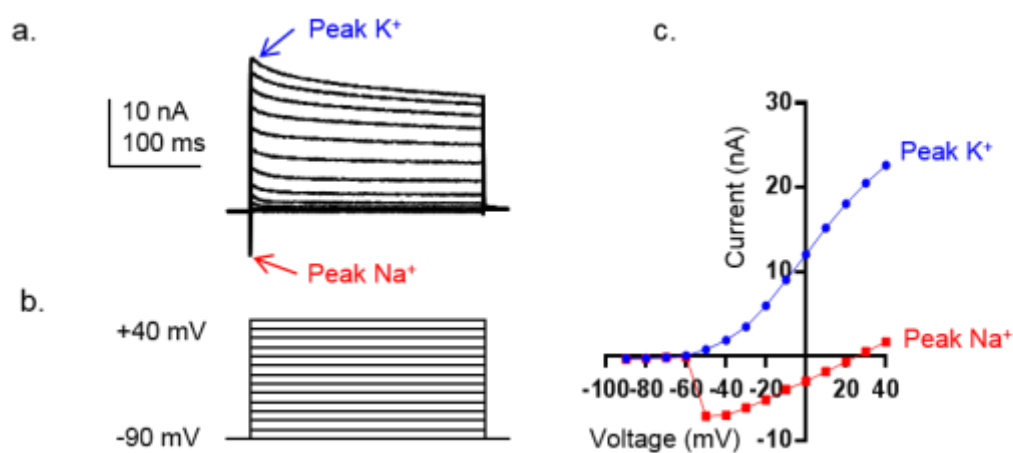


**Fig 2.4. Whole cell voltage clamp recording from a mouse MNTB neuron.** **a.** The family of currents observed using whole cell patch clamp, with peak outward  $K^+$  current (blue) and peak inward  $Na^+$  current (red) highlighted. **b.** The voltage clamp protocol: 10 mV steps were applied between 90 mV and +40 mV. **c.** Current-voltage ( $I/V$ ) relationship for peak  $I_{Na}$  (red) and peak  $I_K$  (blue). Holding potential before voltage clamp protocol = -60 mV.

Table 2.3 Criteria and conditions for patch clamping neurons

<b>Series resistance</b>	$\leq 15$ MOhm (unless specified)
<b>Holding potential (current clamp) at -60 mV</b>	$\leq -450$ pA
<b>Compensation of series resistance and capacitance</b>	70%
<b>Perfusion rate of aCSF into recording chamber</b>	$1 \text{ ml min}^{-1}$
<b>Temperature of aCSF</b>	$35^\circ\text{C} \pm 1^\circ\text{C}$

### Leak Subtraction

Leak current can be defined as a voltage independent, non-inactivating current. It is largely due to the summation of  $K^+$  leak through Kir channels, K2P channels and HCN channels, as well as leak of ions through membrane disruption. This current sums with the amplitude of voltage-gated outward currents (with the exception of Kir channels which are blocked at higher voltages by  $Mg^{2+}$ ) (Hibino et al., 2010), and HCN channels, which are only activated at voltages negative to  $\sim -50$  mV (Chen et al., 2015). Leak currents can be identified by their inward linear I/V relationship at negative holding potentials, typically  $< -70$  mV, where no voltage activated channels are open; after which they merge with voltage-gated channel mediated current at higher holding potentials. Offline linear leak subtraction was performed by determining the slope of the leak current measured at  $-90$ ,  $-80$  and  $-70$  mV, using the equation  $y=mx+c$ . The slope of the leak current was then subtracted from current recorded at each membrane potential ( $-90$  to  $+40$  mV). If performed correctly, the recalculated I/V relationship shows no inward current at negative holding potentials, with reduced outward current which is proportional to the amount of initial leak (see fig 2.5).

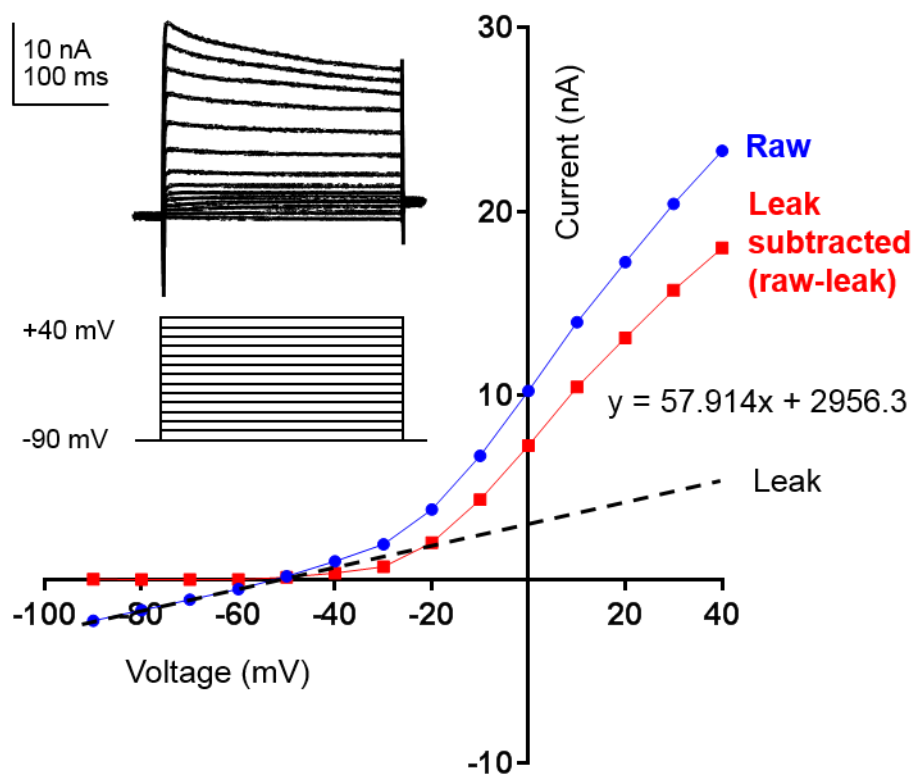
### Current clamp recording:

Current clamp measures the membrane potential of a neuron in response to injection of current. First, the MultiClamp amplifier software was set to  $I=0$ , where no current was passed into the cell and a gap-free protocol was loaded. The amplifier was then set to current clamp mode, and the gap-free protocol activated to show the membrane potential in real time. Current was then injected to set the membrane potential to either  $-50$ ,  $-60$  or  $-70$  mV, enabling a comparison of amplitude and AP threshold between cells. A current clamp protocol was then employed, and the changes in membrane potential recorded. Recordings were rejected if the holding current at  $-60$  mV exceeded  $-450$  pA (unless specified).

### Recording EPSCs and IPSCs from LSO principal neurons

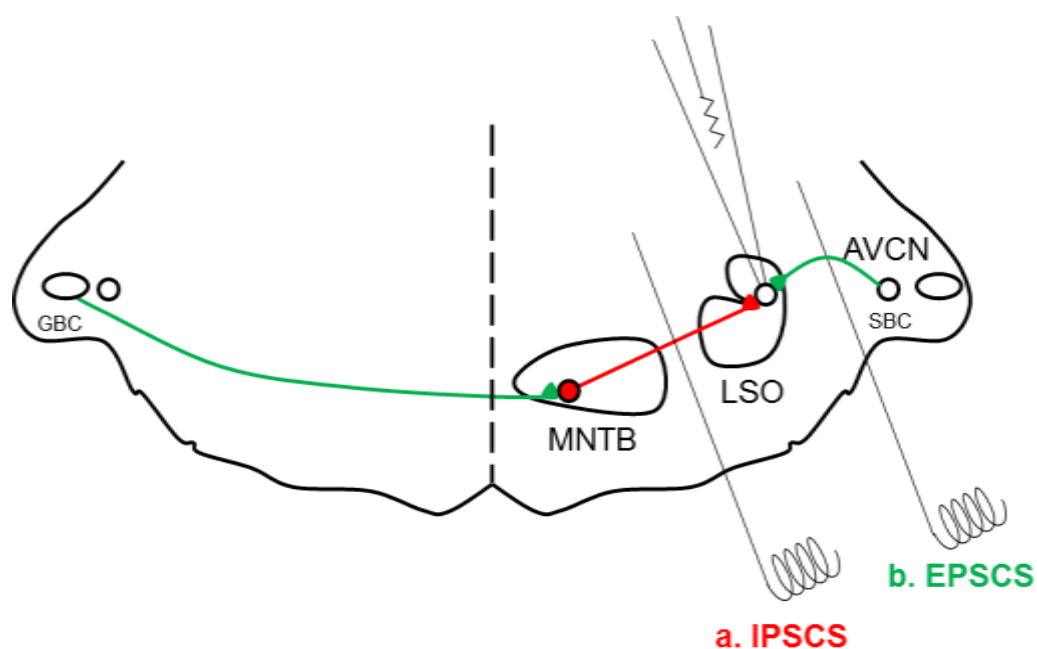
LSO principal neurons receive both ipsilateral glutamatergic input, and contralateral glycinergic input via the MNTB. This enables both EPSCs and IPSCs to be recorded from the same cells. To help clamp the cells, caesium chloride was used in the intracellular pipette solution (table 2.2) to block voltage-gated K<sup>+</sup> channels. EPSCs were recorded by placing a custom built stimulating electrode between the ipsilateral aVCN and LSO, whilst IPSCs were measured by placing the stimulating electrode between fibers of the ipsilateral MNTB and LSO (fig 2.6). Stimulation pulses of 20  $\mu$ s duration (0.1 - 99V), at frequency 0.25 Hz were applied using a constant voltage isolated stimulator, (Digitimer Ltd, model DS 2A). EPSCs were pharmacologically isolated by perfusing the slice with aCSF containing 10 $\mu$ M bicuculline (Sigma Aldrich, cat no. 14340) and 1 $\mu$ M strychnine (Sigma Aldrich), with the addition of either 10 $\mu$ M NBQX (Tocris, cat no. 0373) or 20 $\mu$ M d-AP5 (Tocris, cat no. 0106) to isolate NMDAR or AMPAR mediated EPSCs respectively. IPSCs were isolated with 10 $\mu$ M NBQX and 20 $\mu$ M d-AP5, with the addition of 10 $\mu$ M bicuculline to measure glycinergic IPSCs only. The drugs were kept as frozen stock aliquots at -20°C, with strychnine and d-AP5 dissolved in ddH<sub>2</sub>O (1mM and 20mM respectively), whilst bicuculline and NBQX were dissolved in dimethyl sulfoxide (DMSO) (Sigma Aldrich), both at 10mM. Aliquots were defrosted on the day of each experiment, and diluted to the desired concentration in normal aCSF.

Figure 2.5 Offline linear leak subtraction of an LSO I/V



**Figure 2.5. Offline linear leak subtraction of an LSO I/V.** 10 mV current steps were applied between -90 and +40 mV and the subsequent currents recorded. An I/V plotting the peak  $K^+$  currents is plotted in blue, and the linear leak current is denoted by the dashed black line, with the slope of the leak given above ( $y=mx+c$ ). Using  $y = mx+c$ , the leak was subtracted from the raw I/V at each holding potential (-90 to +40 mV), to give the leak subtracted I/V (red). Inset: raw current traces (upper left) and voltage clamp protocol (lower left). Holding potential = -60 mV.

Figure 2.6 Recording postsynaptic currents in the LSO



**Figure 2.6. Recording postsynaptic currents in the LSO.** Schematic diagram of the SOC showing the ipsilateral excitatory input (green) to the LSO arising from the spherical bushy cells (SBC) in the anteroventral cochlear nucleus (AVCN). The same cell receives contralateral inhibitory input via the MNTB, which acts as a neural relay, converting the excitatory input from the globular bushy cells (GBC) in the contralateral AVCN, to an inhibitory projection to the LSO (red). **a.** When recording IPSCs, the stimulating electrode is placed over the inhibitory fibers between the MNTB and LSO. **b.** When recording EPSCs, the stimulating electrode is placed over the excitatory fibers between the ipsilateral AVCN and the LSO.

#### 2.4 HEARING ASSESSMENT USING THE AUDITORY BRAINSTEM RESPONSE (ABR)

The auditory brainstem response (ABR) consists of synchronous auditory evoked potentials recorded via sub-dermal electrodes in the scalp. The ABR is composed of waves, in response to a brief click (broadband stimulus) or single tone-pip (frequency specific stimulus). The mouse ABR is composed of 5 waves lasting < 8ms post stimulus onset, each reflecting the neural activity of different populations of neurons in the ascending auditory brainstem. In the mouse they correspond to the activity of the 1) Auditory Nerve, 2) Cochlear nucleus, 3) SOC and 4) Lateral lemniscus/inferior colliculus (Melcher et al., 1996).

Through many repetitions of the sound stimuli, ABRs can be averaged to decrease the noise floor, thus increasing the accuracy of auditory thresholds obtained. Hearing threshold was taken as lowest sound level to elicit clear and recognizable waveforms (see fig 2.7). As well as providing information on how well the mouse can hear, ABRs show the speed of neurotransmission and/or possible location of any possible damage in the ascending auditory pathway, through analysis of the amplitude and latency of the ABR waves.

#### ABR equipment:

All equipment used for ABR recordings was sourced from Tucker-Davies Technologies (TDT) and was set up and calibrated by Dr Neil Ingham from The Wellcome Trust Sangor Institute. Thus, our system is an amended/simplified version of the ABR system outlined in their 2011 paper (Ingham et al., 2011). See table 2.4 for complete list of ABR equipment.

#### Calibration of ABR equipment:

The ABR equipment was set-up as outlined in figure 2.8. Before the first ABR recordings of the day, calibration of the sound delivery system was performed. This was achieved using a PCB microphone pre-amplifier (model 426B03) with a 1/4" pre-polarized condenser microphone. This is connected to the TDT MA3 Stereo microphone amplifier, through a PCB Battery Powered Signal Conditioner (model 480C020). To perform calibration, the microphone was positioned where the mouse's head would usually lie (20 cm at 0° to the speaker), within a sound attenuated booth, and 500 msec noise bursts were presented 10 times. The MA3 amplifier then amplifies the signal at 40 dB gain, which is then digitized at a sample rate of 100 kHz by the RP2.1 processor. Each response is then subject to a fast fourier transform (FFT), converting the signal from the time domain, to the frequency domain. The average FFT is then analysed by the custom software on the PC to produce an equalization curve. This was then used to digitally generate ABR stimuli that are presented at a known sound pressure level, and remain consistent across all frequencies. This is achieved by converting the digitized signal generated by the PC custom software to an analogue signal using the RP2.1 processor at a sample rate of 100 kHz. The PA5 programmable

attenuator then attenuates the analogue waveform to produce the desired sound pressure level according to the calibration/equalization curve (see fig 2.8).

Figure 2.7 Establishing the hearing threshold of mouse using ABR

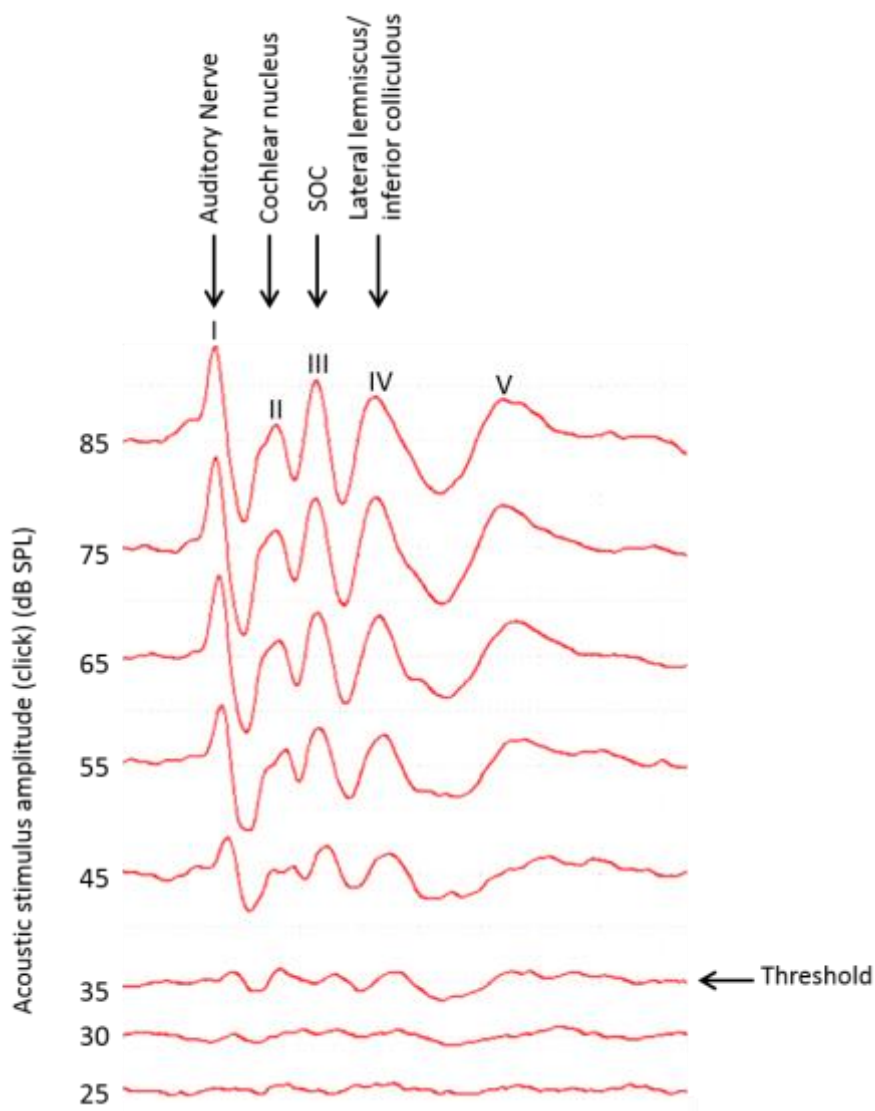


**Fig 2.7. Establishing the hearing threshold of mouse using ABR.** ABRs in response to click stimuli ranging from 25 to 85 dB SPL are plotted (some traces have been removed for clarity). Waves are labelled I – V, with corresponding neuronal generators of each wave labelled above. All waveforms shown are the average of 512 repetitions. Hearing threshold can be defined as the lowest level at which any wave (I – V) is clearly visible, with an absent response 5 dB SPL below. At 35 dB SPL, there are clear waves present, however below this at 30 dB SPL, there are no distinctive waves are present, thus 35 dB SPL is taken as threshold.

### Anaesthetic regime

CBA/Ca mice (P17-P32) were anaesthetised intraperitoneally using a combination of Fentanyl (0.15mg/kg), Fluanisone (5mg/kg) (trade name Hypnorm, Vetapharma), and Midazolam (trade name Hypnovel, Roche) (2.5 mg/kg), diluted two fold with sterilized water for more accurate dosing. Effectiveness of the anaesthetic was determined by the loss of the pedal reflex. If the mouse showed signs of waking up, no more than two 25% top ups of the original dose could be administered on the advice of the NACWO and vet associated with the central research facility (University of Leicester). Sufficient depth of anaesthesia is necessary to reduce myogenic noise during the recordings, and ensure the mouse cannot feel the subdermal needle insertion. Liquid eye gel containing 2 mg/g Carbomer, with Cetrimide was then applied to each eye, to prevent drying of the cornea during the procedure. 100 µl saline warmed to 37°C was injected subcutaneously, to prevent dehydration during the ABR.

Figure 2.8 Schematic of free-field ABR testing

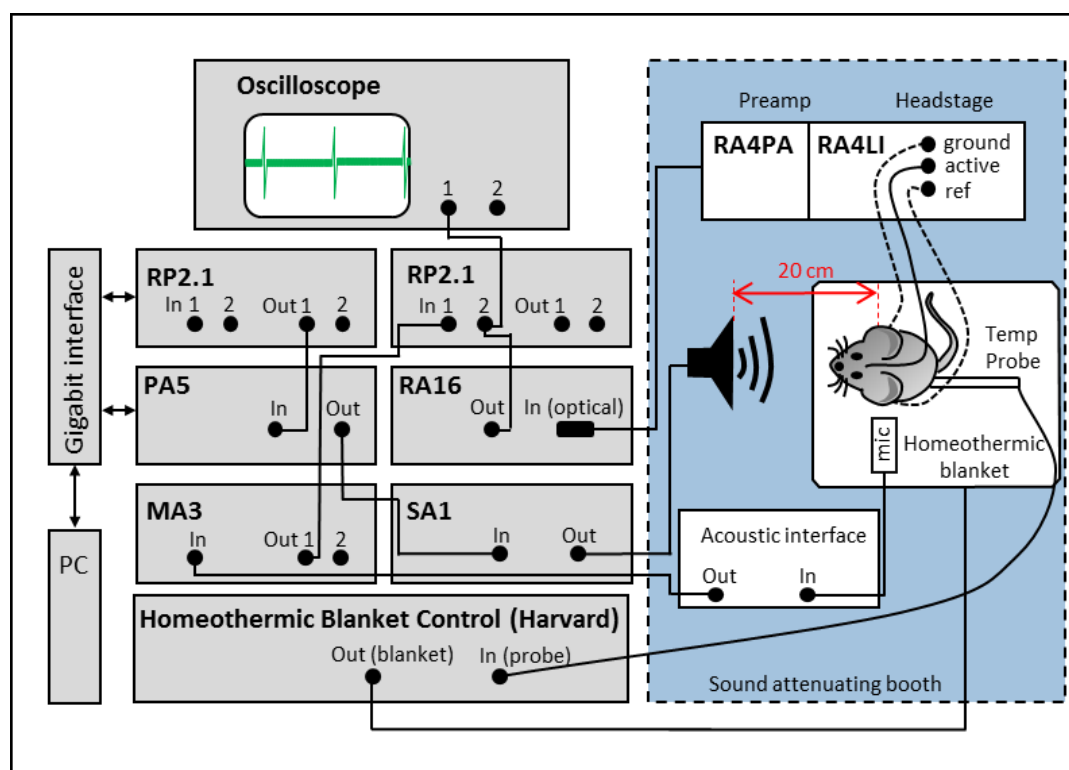


**Fig 2.8. Schematic of free-field ABR testing.** **Daily calibration:** the microphone was positioned where the mouse's head would usually lie, at  $0^\circ$  to the speaker, from which ten 500 ms white noise bursts are delivered. The microphone inputs to the battery powered acoustic interface (PCB Signal Conditioner, model 480C020). The signal is then amplified by 40 dB by the MA3 amplifier, and is digitized at a sample rate of 100 kHz by the RP2.1 processor. The signal is then returned to the PC, with custom TDT software, which produces an equalization curve. **ABR recording:** A mouse is shown within the sound attenuated booth 20 cm from the leading edge of the speaker and the mouse's interaural axis. Digital acoustic signals produced by TDT custom software on the PC are converted to an analogue signal by the RP2.1 processor. The signal is then attenuated by the PA5 programmable attenuator to produce the desired sound pressure level according to the calibration/equalization curve. Acoustic stimuli is delivered to the mouse via the speaker, and the evoked responses from the mouse are captured by the subdermal electrodes. This inputs to the RA4LI head-stage, which digitizes the signal. The signal is then amplified by the RA4PA pre-amplifier, filtered by the RA16 Medusa Basestation, and is then sampled at 100 kHz by the RP2.1 processor, before returning to the PC, via a gigabit interface. **Maintaining body temperature:** Temperature was constantly monitored via a probe directly underneath the mouse, which inputs to a homeothermic blanket control unit (Harvard), adjusting the blanket temperature accordingly, to maintain  $37^\circ\text{C}$ . **Monitoring myogenic noise:** An oscilloscope (Hewlett Packard, 54603B) was used to constantly monitor the myogenic noise of the mouse. Subdermal electrodes were positioned to produce minimal electrical noise, so that the trace remained flat and interspersed by the QRS complex of the mouse heartbeat. Noise on the oscilloscope trace indicates myogenic movement, perhaps from insufficient anaesthetic depth. Figure is adapted and redrawn from Ingham (2011).

### Positioning of subdermal needles

Once sufficient depth of anaesthesia was achieved (as confirmed by loss of pedal reflex) the mouse was placed within a sound attenuated booth, on a thermostatic heating blanket (37°C), in an unrestrained prone position, nose forward, at a calibrated distance from the speaker (20 cm). The heating blanket prevents hypothermia, and is important not only for the well-being of the mouse, but for the accuracy of ABR recordings, as decreased metabolic rate can artificially raise auditory thresholds (Ingham et al., 2011). Subdermal electrodes were then inserted as shown in figure 2.9. The active electrode was inserted into the vertex of the mouse, the ground and reference electrodes were inserted in the patch of bare skin behind the right and left pinna respectively.

*Figure 2.9 Placement of sub-dermal electrodes for ABR*

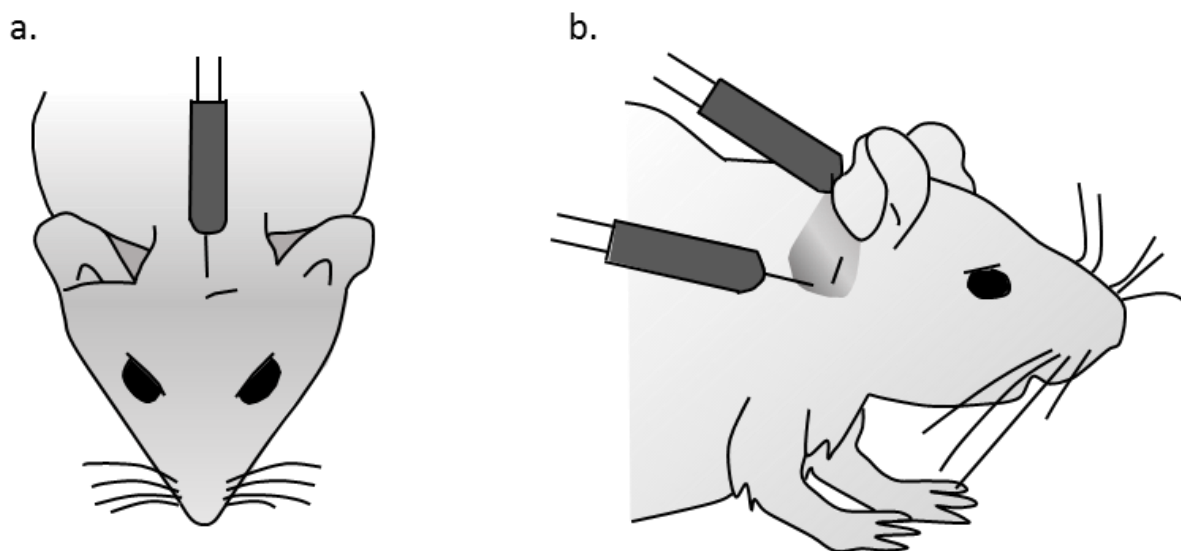


**Fig 2.9. Placement of sub-dermal electrodes for ABR.** a. Active electrode positioned on the vertex. b. Reference/earth electrode inserted behind each ear. Figure redrawn from Ingham et al (2011).

### Recording ABRs:

ABRs were evoked by click stimuli, with 10  $\mu$ s duration, or tone-pips (6, 12, 18, 24, 30 kHz, 1 ms rise time and fall time, 5 ms duration). Both were generated using a Tucker Davies Technologies SA1 Stereo power amplifier, and delivered through a Sound Transducer (CTS Type 341) with a repetition rate of 42.6/s. The stimuli were presented in decreasing frequency order, in 5 dB steps from 0 dB SPL to 85 dB SPL (512 repetitions for each). The electrode signals from the mouse in response to the acoustic stimuli are converted from analogue to digital via the RA4LI, then amplified by the RA4PA. The signal was then returned to the RA16 basestation, which filtered the digitized signal, and was then sampled at a rate of 100 Hz by the RP2.1 and sent to the PC with custom TDT software (see fig 2.11). Throughout recording, an oscilloscope (Hewlett Packard, 54603B) was used to monitor myogenic activity. If the oscilloscope read-out was deemed too noisy, this could be a sign of insufficient anaesthetic depth, at which point, the experiment was stopped and a top-up anaesthetic administered. If poor signal to noise continued following anaesthetic top-up, the experiment was abandoned due to muscle movement obscuring the relatively small tone-pip ABR signals, resulting in artificially raised thresholds. Interestingly, myogenic activity rarely altered click ABR thresholds, yet could significantly raise tone-pip evoked ABR thresholds. This may be because click stimuli activate the whole BM, and thus produce a large robust response, compared to smaller tone-pip evoked ABRs, produced by small, frequency specific regions of the BM.

### Analysis of ABR recordings

Custom TDT software was used to analyse ABR traces produced in response to click or frequency specific stimuli at different levels (0 – 85 dB SPL, in 5 dB steps). The software allows the user to label the peak of each wave (P1, P2, P3 and P4) and label each trough (N1, N2, N3 and N4). The amplitude of each wave (e.g. wave I = P1-N1) is then given for each of the ABR traces at each level (0 – 85 dB SPL). The time onset of each peak is also determined, allowing comparison of the latency of each peak between control and noise exposed mice.

*Table 2.4 List of materials used for recording ABRs in mice*

Male or Female CBA/Ca mice ( $\geq$ P17)
Anaesthetic: Fentanyl (0.15mg/kg), Fluanisone (5mg/kg) and Midazolam (2.5 mg/kg)
Liquid eye gel containing 2 mg/g carbomer, with cetrimide;
Sound-attenuating chamber
Homeothermic heating blanket (to prevent hypothermia in the mouse)
<b>Stimulus generation and calibration equipment including:</b>
PCB microphone pre-amplifier (model 426B03) with a 1/4" pre-polarized condenser microphone
PCB Battery Powered Signal Conditioner (model 480C020)
TDT MA3 Stereo microphone amplifier
Sound Transducer (CTS Type 341; RS Components part no. 172-7712)
BNC and other connector cables
RP2.1 Enhanced Real-time processor
PA5 Programmable Attenuator
SA1 Stereo Amplifier
0.5ml disposable syringes with needle (for injection; BD Plastipak)
<b>Response-processing equipment (Tucker-Davis Technologies) including:</b>
Needle electrodes (Chalgren Enterprises, cat. no. 112-812-48-TP; disposable low-profile EEG needle electrodes)
Low-Impedance Recording Head-stage/Preamplifier (RA4LI + RA4PA)
RA16 Medusa Base Station
RP2.1 Enhanced Realtime processor
BNC and other connector cables
Personal computer (PC), housing TDT gigabit interface, TDT driver software and bespoke averager software
Digital Oscilloscope (Hewlett Packard, 54603B)

**Table 2.4.** List of materials used for recording ABRs in mice. Table is adapted from Ingham (2011).

## 2.5 ACOUSTIC OVER-EXPOSURE (AOE) PROCEDURE

Mice were subject to AOE (whilst under anaesthetic) to temporarily raise auditory thresholds across most frequencies, by applying 105-110 dB SPL of broadband noise (5-50 kHz) within a sound attenuated booth. Details of calibration of noise exposure delivery equipment can be found in the appendix (chapter 8, section 8.2).

### Acoustic over-exposure delivery

Immediately following the ABR procedure, the mice were placed on a thermostatic heating blanket (37°C) within a sound attenuated booth, in an unrestrained prone position, nose forward, at a calibrated distance from the speaker (20 cm). In cases where ABR was not performed, mice were anaesthetised and given a subcutaneous saline injection as for the ABR procedure, and placed in the booth once sufficient anaesthetic depth was achieved. The speaker delivered a broadband noise (5-50 kHz) at 105 -110 dB SPL for 2 hours. The mice were checked every 5-10 minutes through a window built into the sound attenuated booth, to ensure they were breathing normally, and remained under anaesthetic. The project licence does not require the procedure to be performed under anaesthetic, however this helps keep the mice static, at the correct distance from the speaker, and is (likely) less stressful for the mice. Following the noise procedure, mice were removed from the booth, and allowed to recover. Once consciousness had been regained (e.g. pedal reflex, self-righting, attempts to walk), mice were ear snipped for identification purposes, and placed back in the home cage.

## 2.6 STATISTICAL ANALYSIS OF ELECTROPHYSIOLOGICAL DATA

Data were analysed using the software package GraphPad Prism 6 and SPSS statistics 22. Data are plotted as mean  $\pm$  SEM, with n being specified as: voltage clamp, n = neurons recorded from at least 3 animals (unless specified), ABR: n = animal. Data was first tested for equality of variance (via Levene's test), and the appropriate statistical test applied. Unpaired t tests were used when comparing 2 groups (with Welch's correction in cases of unequal variance). When comparing 3 or more groups ANOVA was used with post-hoc analysis: One-way = Tukey post hoc testing, Two-way = pairwise comparisons. In cases of unequal variance, one-way ANOVA was conducted

using Games Howell post hoc testing, and two-way ANOVAs were replaced by multiple t-tests with Sidak Holm corrections for multiple comparisons. Statistical significance was concluded when  $P \leq 0.05$ .

## 2.7 IDENTIFYING Kv3 SUBUNIT EXPRESSION IN THE SOC USING IMMUNOHISTOCHEMISTRY

Kv3 channels are a key determinate of normal intrinsic excitability in auditory pathway, however subunit composition in the SOC is currently unconfirmed. I used immunohistochemistry to assess the Kv3 subunit composition in the SOC. Next, I will describe how I prepared brain slices, validated Kv antibodies and performed immunohistochemistry staining.

### Preparation of brain sections

Brainstems were removed from mice, as described in section 2.2, and immediately frozen in moulds containing OCT embedding matrix (LAMB Thermo Fisher Scientific) using hexane cooled in dry ice. Brainstems were orientated with the cut end facing the bottom of the mould and the spinal cord facing upwards. Samples were kept at  $-80^{\circ}\text{C}$  until required.  $12\mu\text{M}$  sections were obtained using a cryostat (Thermo Cryostar NX50, Thermo Fisher Scientific), and were mounted onto polysine slides (Thermo Scientific, Art No J2800AMNZ), and stored at  $-20^{\circ}\text{C}$ . Cresyl violet staining was performed on every 15<sup>th</sup> slide, and the presence of the LSO and MNTB confirmed via visual inspection under the microscope.

For hippocampal sections, the brain was removed as before, however a  $90^{\circ}$  cut was made to separate the hippocampus and brainstem from the forebrain. The forebrain was then frozen in OCT embedding matrix as above, orientated with the cut end (caudal) facing the bottom of the mould, and the rostral end facing upwards. Confirmation of hippocampus was made via visual inspection (without microscope) due to its large size.

### Antibody test matrix using different fixation conditions:

To establish the optimal conditions for the new antibody four fixation conditions were applied simultaneously on CBA/Ca mouse brain tissue. These were: 1) 4% paraformaldehyde (PFA), 2) 4% PFA + antigen retrieval, 3) Methanol, 4) No fixation.

To control for non-specific staining from the primary antibody, KO tissue was used where available. Specificity of the secondary antibody was assessed using a slide lacking primary antibody. The different fixation conditions were timed carefully so that all slides were washed in phosphate buffered saline tween-20 (PBS-T) for the same amount of time, before blocking solution was applied.

4% PFA: Slides were submerged in pre-cooled 4% PFA at 4°C for 10 minutes. Slides were then removed into glass schiffedeckers (Thermo Scientific) containing pre-cooled (4°C) 1XPBS/1% Triton (PBS-T) for 3 X 10 min washes (replacing the PBS-T for each wash).

4% PFA + Antigen retrieval: Slides were submerged in pre-cooled 4% PFA at 4°C for 10 min, then removed for 3 X 10 min washes in PBS-T (as in '4% PFA' condition). Antigen retrieval was then performed by submerging the slides in preheated (90°C) 10mM citric acid (pH 6) for 20 mins on a temperature controlled hotplate. Slides were then removed to glass schiffedeckers containing room temperature PBS-T.

Methanol: Slides were placed in pre-cooled 9% methanol for 10 minutes, and then washed for 3 X 10 mins in PBS-T (cooled to 4°C).

No Fix: Slides were washed for 3 X 10 mins in PBS-T (cooled to 4°C).

### Blocking the tissue to avoid non-specific staining

All slides were then dried around the sections using tissue, and an ImmEdge hydrophobic barrier pen (Vector Labs UK) used to draw vertical lines, approximately 2 cm apart either side of the brain section. This created a barrier to hold approximately 150µl of blocking or antibody solution. Slides were then flooded with blocking solution (composition per ml: 100µl 10% bovine serum albumin (BSA), 100µl goat serum

(Vector Labs) 800µl 1xPBS/0.1% triton), and left at room temperature in a covered humidity chamber flooded with dd H<sub>2</sub>O for 60 minutes.

### Antibody application

Blocking solution was removed from the slides (poured off), and primary antibody diluted in blocking solution applied. A list of primary antibodies used and their dilutions can be found in table 2.5. On some occasions, two different primary antibodies raised in different species (e.g. Anti Kv3.3, Alomone, rabbit, and anti-Kv3.1, Neuromab, mouse) were added to the same slides. Slides were then incubated overnight in a humidity chamber at 4°C. The following day, 3X10 min washes using PBS-T cooled to 4°C were performed, followed by incubation with secondary antibody diluted 1:1000 in blocking solution (table 2.6). Secondary antibody was chosen to match the animal the primary antibody was raised (e.g. antibody raised in a mouse requires an anti-mouse secondary antibody). On occasions where two different primary antibodies had been applied, secondary antibodies that fluoresce at different wavelengths (488 nm and 546 nm) were chosen, to allow visualisation of two different proteins of interest on the same slide. Samples were subsequently DAPI stained (Invitrogen, 5mg/ml diluted in PBS-T) for 5 minutes on a shaking platform (covered to prevent photo bleaching) and subject to 3 X 5 min washes in PBS-T. Slides were then dried, cover slipped (Vector Hard Set Mounting Medium, Vector Labs H-1400) and imaged using a fluorescence microscope (Leica DM2500).

*Table 2.5 Primary antibodies*

<b>Primary antibodies</b>				
<b>Antibody target</b>	<b>Host species</b>	<b>Mono/polyclonal?</b>	<b>Supplier</b>	<b>Dilution</b>
Kv3.1b	Mouse	Monoclonal	Neuromab	1:1000
Kv3.2	Rabbit	Polyclonal	Alomone	1:500
Kv3.3	Mouse	Monoclonal	Neuromab	1:3000
Kv3.4	Mouse	Monoclonal	Neuromab	1:500

Table 2.6 Secondary antibodies for immunohistochemistry

<b>Secondary antibodies</b>						
Name	Excitation Peak (nm)	Emission Peak (nm)	Host species	Target species	Supplier	Dilution
Alexo Fluor 488	493	519	Goat	Mouse	Molecular Probes	1:1000
Alexo Fluor 546	556	576	Goat	Rabbit	Molecular Probes	1:1000
Alexo Fluor 488	493	519	Goat	Rabbit	Molecular Probes	1:1000
Alexo Fluor 546	556	576	Goat	Mouse	Molecular Probes	1:1000

## 2.8 COMPARING KV3 SUBUNIT PROTEIN LEVELS USING WESTERN BLOTTING

A preliminary investigation was performed using western blots to assess levels of Kv3.1 and Kv3.3 subunits in the LSO and cerebellum of Kv3.1 KO, Kv3.3 KO and CBA/Ca mice.

### Dissection of LSO Tissue

Mouse brains from either CBA, Kv3.1 KO or Kv3.3 KO mice (age P14-P16, male or female) were removed into partially frozen slicing aCSF and mounted onto a cutting plate ready for slicing (as described previously in section 2.2). Upon the emergence of the 7<sup>th</sup> nerve at the ventral side of the brainstem, a 1 mm slice was cut and immediately removed to a dish containing cooled slicing aCSF under a dissection microscope. Using a small blade with a small curved cutting edge (size 15, Swann Morton) a straight incision was made along the 7<sup>th</sup> nerve. Following this, a second incision was made, originating halfway between the 7<sup>th</sup> nerve and the midline on the ventral edge of the slice (fig 2.10). The tissue containing the LSO was then removed to an Eppendorf tube, and immediately frozen, by immersing the tube in dry ice. This was then repeated for the opposite LSO.

The remaining cerebellar tissue on the cutting plate was cut at the same level as the brainstem slice using the vibratome blade, and frozen in the same manner. All samples were kept at -80°C until ready for protein extraction.

**Protein extraction:**

To extract protein from LSO, MNTB or cerebellar brain tissue, the following protocol was used:

- Make Lysis buffer by dissolving 1X tablet of complete, mini, EDTA free protease inhibitor and 1X tablet phosSTOP (both SigmaAldrich) in 10 ml Radioimmunoprecipitation assay buffer (RIPA) buffer (table 2.7).
- Pool LSO samples or MNTB samples in 1.5 ml Eppendorf tubes (3-4 per tube) and add 50  $\mu$ l fresh lysis buffer (4°C) to each. Cerebellar samples do not need pooling, and require 300  $\mu$ l fresh lysis buffer adding to each.
- Immediately homogenize samples to a smooth consistency, then sonicate to break down any insoluble tissue, whilst keeping samples cool over ice.
- Store samples 4°C for 30 minutes.

Figure 2.10 Dissection of LSO tissue for western blot

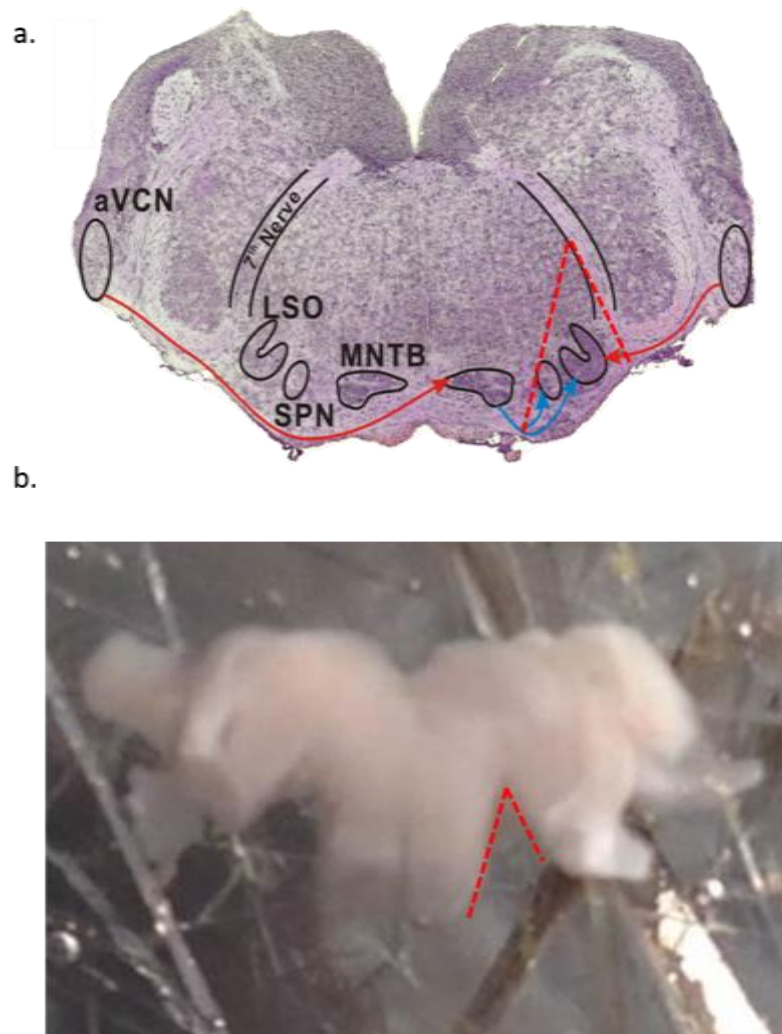


**Fig 2.10. Dissection of LSO tissue for western blot.** **a.** Example brainstem section (12  $\mu$ m) with visible landmarks of the LSO, MNTB and 7<sup>th</sup> nerve (as labeled). Red dashed lines correspond to the dissected area in part b. **b.** 1mm brainstem slice containing the LSO. An incision was made along the 7<sup>th</sup> nerve, and halfway between the midline and the 7<sup>th</sup> nerve, as indicated by red dashed lines. Tissue was immediately removed to an Eppendorf tube, and snap frozen using dry ice.

Table 2.7 RIPA buffer composition

RIPA Buffer	Formula Weight	(final conc for 1X)	Qty
Tris HCL	157.6	50mM	788mg
NaCl	58.44	150mM	876.6mg
Triton X100	-	1%	1ml
SDS	-	0.1%	100mg or 1ml 10% stock
Sodium deoxycholate	-	0.5%	500mg

Table 2.7 RIPA buffer composition. Final volume = 100 ml (using dd H<sub>2</sub>O), pH 7.6.

To calculate the amount of protein in each sample, a Bradford protein assay was conducted using the following protocol:

- Line cuvettes up on workbench and fill with 1 ml Bradfords reagent (Thermo Fisher Scientific). The no. of cuvettes needed = 6 (for standard curve) + no. samples to be tested.
- To generate a standard curve, add bovine serum albumin (BSA) (Sigma) to the first 6 cuvettes to create either 0, 3, 6, 9, 12 or 15 µg/ml BSA.
- Immediately following this add 1ul of sample to each subsequent cuvette (1 sample per cuvette). It is important the protein reaction for the standards and unknown samples are started at the same time because absorbance changes in a time dependent manner.
- Mix the contents of each cuvette by covering with (gloved) thumb and inverting

Measure the absorbance a spectrophotometer (Eppendorf BioPhotometer) at 596nm in quick succession. The absorbance of the known protein concentrations (0, 3, 6, 9, 12 and 15 µg/ml) were used to generate a standard curve, with protein concentration on the x axis, and absorbance (nm) plotted on the y axis (fig 2.16).

To calculate the amount of protein in the sample cuvettes, a linear regression line was fitted to the curve, with the y intercept set to 0. This gives the equation of  $y=mx+c$ , where m (the gradient of the line) is shown. This equation can then be rearranged as  $y/m = x$ , where y = measured absorbance (nm), m=gradient of linear regression line

and  $x$  = protein concentration ( $\mu\text{g/ml}$ ). As  $y$  and  $x$  are known,  $x$  can then be calculated, to give the protein concentration within each sample cuvette.

Figure 2.11 Generation of BSA standard curve (protein assay)

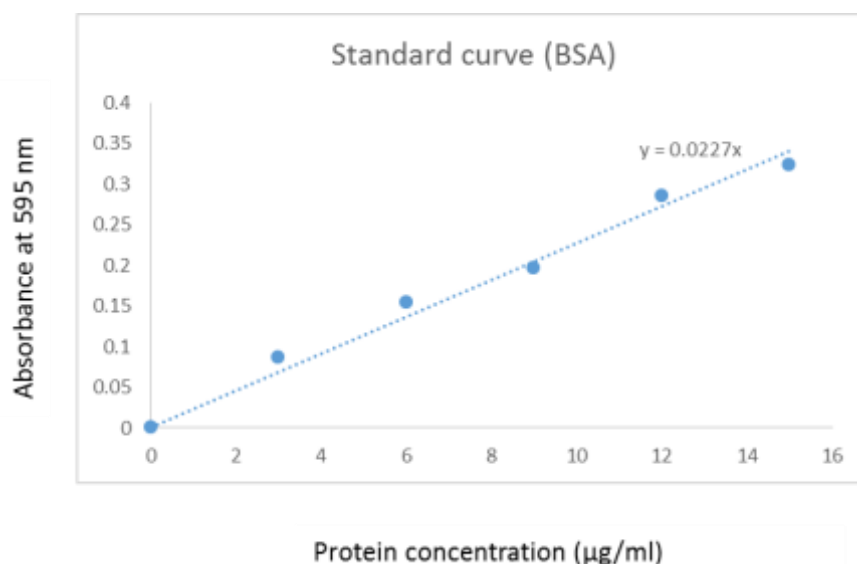


**Fig 2.11. Generation of BSA standard curve (protein assay).** Curve generated by plotting known concentrations of BSA (0, 3, 6, 9, 12, 15  $\mu\text{g/ml}$ ) on the x axis against absorbance measured at 595nm. A linear regression line is shown (intercept at 0), and the gradient of the line is displayed.

It is important the amount of protein loaded in each lane in a western blot is equal, so that any differences detected on the final blot are not due to unequal loading of protein. Sample protein was normalized to the sample containing the least amount of protein, by dilution with 2X sample buffer (BioRad). All samples were then diluted 1:1 by adding the same amount of 2X sample buffer as the volume in each tube. Samples were then incubated at  $95^{\circ}\text{C}$  for 5 minutes to denature the proteins ready for SDS-PAGE, then allowed to cool, and stored at  $-20^{\circ}\text{C}$ .

### Gel Casting

To examine proteins of interest in a sample, it is necessary to separate them by molecular weight. A gel with two layers: a stacking layer above, and a resolving layer below is required to separate the proteins through electrophoresis. The stacking layer is composed of larger sized pores which enable the protein to migrate and become 'stacked' at the interface between the two gels. Thus, protein entering the resolving

layer starts at the same level. The resolving gel then separates the protein based on its molecular weight, with low molecular weight proteins moving faster through the gel.

To cast the gels the following protocol was used:

- For a 10% resolving gel, add 10 ml acrylamide, 180  $\mu$ l 10% APS stock (ammonium persulfate) and 24  $\mu$ l Tetramethylethylenediamine (TEMED) (all Thermo Fisher Scientific) and 12.3ml distilled water to 5 ml of lower gel buffer (see table 2.8) immediately before addition to 1.5 ml casting plates using an automatic pipette dispenser.
- Add a layer of isopropanol (approx. 0.5cm) on top of the lower gel buffer whilst the gel polymerizes, to help ensure a smooth, even edge to the resolving gel, and eliminate air bubbles.
- When the resolving gel is set, pour off the isopropanol, and push blotting paper between the casting plates to remove excess.
- Prepare the stacking gel by adding 12.38 ml distilled water, 2.5 ml acrylamide, 100  $\mu$ l APS (10% stock) and 20  $\mu$ l TEMED to 5 ml upper gel buffer (see table 2.9)
- Immediately fill casting plates to the top with the stacking gel using an automatic pipette dispenser.
- Insert a horizontal comb, and leave to set.

### Gel electrophoresis

Proteins were separated by size by gel electrophoresis using the following protocol:

- Remove protein samples from the freezer and warm to approx. 85°C.
- Once set, place gel casts in an electrophorator containing electrode buffer (see table 2.11), making sure the buffer completely covers the gel.
- Carefully remove the comb
- Load 5  $\mu$ l molecular weight ladder (Kaleidoscope, Biorad) into the first well, and the samples in each subsequent well.
- Load empty wells with 1 X loading buffer.
- Electrophorese at 60 V until the loading dye reaches the resolving gel, and then at 140 V thereafter for approx. 3 hours, or until the loading dye front has run off the gel.

### Electrophoretic transfer

To transfer the protein from the gel to a membrane, the following protocol was used:

- To create a 'transfer sandwich', soak sponge (same size as the gel) in transfer buffer (4°C) (see table 2.12), and add to support grid, to form the base.
- Soak filter paper (cut to the same dimensions of the gel) in transfer buffer to form the next layer of the sandwich
- Lay the gel on top of the filter paper, followed by a nitrocellulose membrane
- To complete the sandwich layer filter paper, and then sponge (both soaked in transfer buffer).
- Secure the transfer sandwich, by pushing each side of support grid together, and lock in place.
- Place vertically in an electroblotting tank (Criterion, Biorad) between the stainless steel electrodes with the nitrocellulose membrane positioned between the gel and the positive electrode. Fill with pre-cooled transfer-buffer (4°C).
- Place an ice-pack in the tank, to mitigate the heat produced in the transfer
- Set to 40 V, and leave overnight.
- The following day, increase the voltage to 90 V for the last 30 mins of transfer.

### Blocking to avoid non-specific binding

- Switch off the power supply and open the transfer sandwich.
- Discard the gel, and add the nitrocellulose to a tray containing ponceau (Sigma) for approximately 5 seconds to visualise protein bands for confirmation of a successful transfer.
- Rinse the membrane with Tris-buffered saline, 0.1% Tween 20 (TBST) (see table 2.13) (approx. 2 X 10 ml rinses or until all ponceau is removed).
- Place the membrane in 5% milk blocking solution (2 g skimmed milk powder (Sigma) in 40 ml TBST).
- Leave for 1 hour on a rocking platform, then rinse 5 times in TBST (10 ml per rinse)

Addition of primary and secondary antibodies:

- Dilute primary antibody (table 2.5) in TBST.
- Add primary antibody to the tray containing the membrane, and leave to incubate for 1 hour at 4°C on a platform rocker.
- Rinse membranes 7 times in TBST (10 ml per rinse)
- Dilute secondary antibodies conjugated to horseradish peroxidase (HRP) 1:1000 in TBST add to the membrane, and incubate for 1 hour on a rocking platform (table 2.14).

*Table 2.8 Lower gel buffer composition*

Lower gel buffer	Formula weight	(final conc for 1X)	qty
Tris HCL	157.6	1.5	59.1g
SDS		0.4%	10ml of 10% stock

**Table 2.8 Lower gel buffer composition.** Final volume = 250 ml. pH = 8.8.

*Table 2.9 Upper gel buffer composition*

Upper gel buffer	Formula weight	(final conc for 1X)	qty
Tris HCL	157.6	1.5M	7.88g
SDS	-	0.4%	4 ml of 10% stock

**Table 2.9 Upper gel buffer composition.** Final volume = 100 ml.

*Table 2.10 Tris-Glycine stock X10*

Tris-Glycine stock X10	Formula weight	(final conc for 10X)	qty
Tris HCL	157.6	250mM	78.7g
Glycine	75.06	1920mM	288g

**Table 2.10 Tris-Glycine stock X10.** Final volume = 2 litres (with dd H<sub>2</sub>O). pH to 8.5.

*Table 2.11 Electrode buffer composition*

Electrode buffer	Formula weight	(final conc for 1X)	Qty
Tris HCL	157.6	25mM	100 ml of 10X Tris-Glycine stock
Glycine	75.06	192mM	
SDS	10% stock	0.1%	10ml of 10% stock

**Table 2.11. Electrode Buffer Composition.** Final volume = 1litre (with dd H<sub>2</sub>O). pH to 8.3.

Table 2.12 Transfer buffer composition

Transfer Buffer	Formula weight	(final conc for 1X)	Qty
Tris HCL	157.6	25mM	100 ml of 10X Tris-glycine stock
Glycine	75.06	192mM	
Methanol		20%	200 ml methanol

Table 2.12 Transfer buffer composition. Final volume = 1 litre (with dd H<sub>2</sub>O).

Table 2.13 TBST (X10) composition

TBS-T (10X)	Formula weight	Final conc (for 1X)	Qty
Tris-Hcl	157.6g	20mM	31.5 g
NaCl	58.44g	137mM	80g
Tween	-	0.1%	10ml

Table 2.13. TBST (X10) composition. pH to 7.6. Final volume = 1 litre (with dd H<sub>2</sub>O).

Table 2.14 Secondary antibodies for western blotting

Secondary antibodies					
Name	Host species	Target species	Supplier	Cat. No.	Dilution
Anti-mouse IgG peroxidase antibody	Goat	Mouse	Sigma	A8924	1:1000
Anti-Rabbit IgG peroxidase antibody	Goat	Rabbit	Sigma	A6154	1:1000

### Imaging western blot

Conjugation of HRP to the secondary antibody enables chemiluminescent detection when combined with enhanced chemiluminescence (ECL) (West PICO chemiluminescent from Pierce, cat. No. 34080). ECL is kept as two components; a stable peroxide solution, and a luminol solution, which were mixed at a ratio of 50:50 immediately before addition to the membrane, and left to incubate for two minutes.

Membranes were then removed from the ECL ready for imaging using a FUJI LAS 4000 multipurpose CCD camera system.

Image J software can be used to calculate the relative density of each band on the western blot. This can then be normalized to relative density of the loading control (tubulin). See appendix (chapter 8, section 8.3 for details).

## 2.9 IDENTIFICATION OF TRANSGENIC MICE USING PCR

It was necessary to establish the genotype of each mouse produced by the Kv3.1 and Kv3.3 colonies for both breeding and experimental purposes. To do this, DNA was extracted from ear or tail tissue of each mouse. PCR and gel electrophoresis were then used to identify if the mouse was wildtype (WT) (+/+), heterozygous (+/-) or a KO (-/-).

### DNA extraction

Ear snips were taken from pups born to either the Kv3.1 or Kv3.3 mouse colonies at around P11, and the tissue rapidly frozen, and stored in the freezer at -20°C. To extract DNA from each of the samples, the following protocol was used:

- Remove tissue sample from freezer, mix with 200µl tissue lysis buffer (TLB) (Qiagen Sciences) and 1µl proteinase K (20mg/ml) (Fisher Scientific) in 1ml Eppendorf tubes.
- Incubate at 55°C for two hours on a shaker platform, to provide optimal conditions for the enzyme to breakdown the tissue.
- Centrifuge at a speed of 14 RCF for two minutes.
- Remove supernatant and add to 200µl isopropanol (Acros Organics) to precipitate the DNA.
- Centrifuge at a speed of 14 RCF for two minutes, to form DNA pellet
- Remove supernatant and re-suspend DNA pellet 100µl Tris EDTA (TE) buffer (National Diagnostics, USA).
- Store DNA suspension at -20°C until ready for PCR.

### Amplification of DNA using polymerase chain reaction (PCR)

1µl of DNA sample was added to a mastermix in a 200µl PCR tube. Mastermix included PCR buffer (DreamTaq DNA polymerase, Thermo Fisher Scientific), forward and reverse primers specific to the sequence of interest (see table 2.15 for sequences) and ddH<sub>2</sub>O. For the Kv3.1 PCR, primers targeting both the specified WT and KO regions of DNA were included in the same mastermix. For Kv3.3, PCR reactions were performed in duplicate, with one sample containing a mastermix with primers targeting the WT region of DNA, and the same sample in a separate tube containing primers targeting the knockout region of DNA. For more information on mastermix composition, see table 2.16.

In addition, a negative control was included, which contained the PCR mastermix but no DNA. Positive controls were also provided, using DNA from mice from where the genotype was known. All samples were then placed in a thermocycler (Mastercycler EP, Eppendorf) and run through the appropriate cycle for either Kv3.1 or Kv3.3 (table 2.17). Samples were then stored at 4°C until ready for gel electrophoresis.

*Table 2.15 Primer sequences for Kv3.1 and Kv3.3 PCR*

<b>Genotyping Kv3.1 mice</b>		
<b>Primer</b>	<b>Sequence (5'-3')</b>	<b>Supplier</b>
3.1X	GAA ATC GAG AAC GTT CGA AAC GG	Sigma
3.1Y	TGA TAT TGA GGG AGT TCT TGA TG	Sigma
PPVR	CTA CTT CCA TTT GTC ACG TCC TG	Sigma
<b>Genotyping Kv3.3 mice</b>		
3.3F	GAC AGC GGT AAG ATC GTG AT	Sigma
3.3R	AAA CAC AGA CGC TTG AGC TC	Sigma
NeoF	TCC ATT TGT CAC GTC CTG CA	Sigma

**Table 2.15 Primer sequences for Kv3.1 and Kv3.3 PCR.** List of primer sequences used in PCR reactions for targeting both knockout (-) and wildtype (+) regions of DNA in Kv3.1 and Kv3.3 mice

Table 2.16 List of reagents used for PCR reaction mix

<b>Kv3.1 mastermix</b>	<b>Kv3.3 mastermix (Wildtype)</b>	<b>Kv3.3 mastermix (Knockout)</b>
5µl DreamTaq Green PCR mastermix	5µl DreamTaq DNA polymerase	5µl DreamTaq DNA polymerase
0.5µl primer 3.1X (10µM)	0.5µl primer 3.3F (10µM)	0.5µl primer 3.3 NeoF (10µM)
0.5µl primer 3.1Y (10µM)	0.5µl primer 3.3R (10µM)	0.5µl primer 3.3R (10µM)
0.5µl primer PPVR (10µM)	3 µl dd H <sub>2</sub> O	3 µl dd H <sub>2</sub> O
2.5µl dd H <sub>2</sub> O		

**Table 2.16 List of reagents used for PCR reaction mix for Kv3.1, Kv3.3 wildtype (+/+) and Kv3.3 knockout (-/-).** Each mix contains DreamTaq Green PCR mastermix, primers specific to the DNA region of interest (forward and reverse) and ddH<sub>2</sub>O.

Table 2.17 PCR cycles for Kv3.1 and Kv3.3

<b>Kv3.1 PCR cycle</b>	
<b>Temperature (°C)</b>	<b>Time</b>
94	5 minutes
94	30 seconds
57	30 seconds
72	30 seconds
} 35 cycles	
72	5 minutes
<b>Kv3.3 PCR cycle</b>	
<b>Temperature (°C)</b>	<b>Time</b>
94	5 minutes
94	30 seconds
57	30 seconds
72	1 minute
} 35 cycles	
72	5 minutes

**Table 2.17 PCR cycle for Kv3.1 and Kv3.3 samples.** PCR samples from Kv3.1 mice were first heated to 94°C for 5 minutes. This was followed by 35 cycles of denaturation (94°C, 30 secs), annealing (57°C, 30 secs) and elongation (72°C, 30 secs). Finally, the samples were held for a 5 minute period at 72°C. Kv3.3 PCR cycle is similar, however during the 35 cycles, the elongation period (72°C) is extended to 1 minute.

### Identification of WT and KO DNA using Gel Electrophoresis

PCR products were electrophoresed to enable separation and identification of WT and KO bands using the following protocol:

- Cast a gel containing 2% agarose and 0.01% DNA gel stain (SYBR Safe, Thermo Fisher Scientific). Insert horizontal gel combs and allow to set.
- Place in gel electrophoresis tank containing 1% Tris-acetate-EDTA (TAE) buffer (Gibco).
- Remove gel combs and load 10  $\mu$ l molecular weight ladder (100bp Hyperladder, Bioline)
- Load 10 $\mu$ l of PCR product into each subsequent well (leaving one well free between the ladder and the first sample, in case ladder spreads into the next lane)
- Electrophorese for 60 mins at 100V (Biorad Powerpac Basic)
- Visualize bands under UV light using a transilluminator (UVP, model 3UV). Acquire image using image analysis software (Launch DocITLS) (fig 2.12).

### Breeding of transgenic mice

Once the genotype of each mouse was established, new breeding pairs could be set up (at 8 weeks of age). Kv3.1 mice were bred heterozygously (+/- to +/-) with genotyping performed on subsequent litters. KO mice from the offspring (-/-) were then used for experimental purposes and heterozygous (+/-) mice formed future breeding pairs. Kv3.3 colonies were bred homozygously (-/- to -/-), with genotyping performed on the first litter born to each breeding pair, to ensure the KO (-/-) phenotype had been maintained.

Figure 2.12 Visualising DNA bands of Kv3.1 and Kv3.3

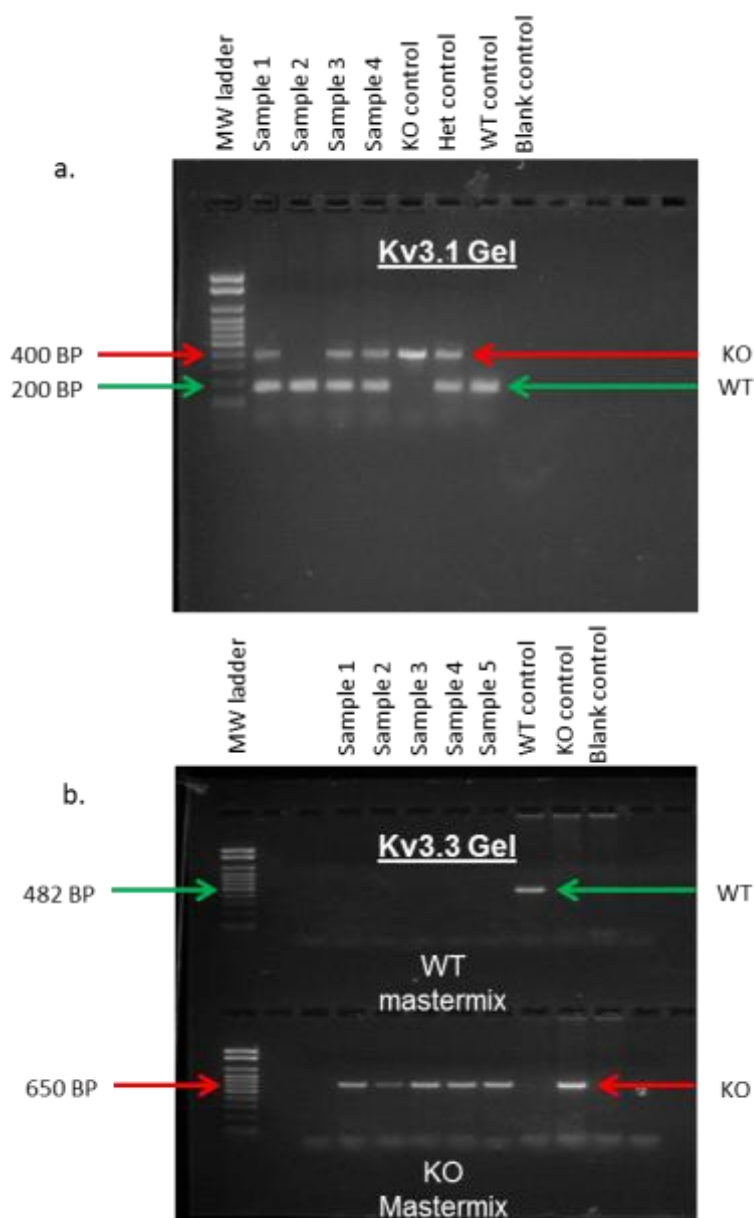


**Fig 2.12. Visualising DNA bands of Kv3.1 and Kv3.3.** **a.** Image of a gel following electrophoresis, separating Kv3.1 WT and KO PCR product by weight. Molecular weight (MW) ladder is shown on the far left. Samples were loaded into consecutive lanes, with control samples containing known WT DNA (WT control), known KO DNA (KO control) and the mastermix only (Blank) loaded into the final three lanes respectively (right). Red arrow indicates KO DNA (400 BP) and green arrow indicates WT DNA (200 BP). Both WT and KO bands in the same lane indicates the DNA originates from a heterozygous mouse. **b.** Image of Kv3.3 gel following gel electrophoresis. Samples are run in duplicate, with PCR product resulting from primers targeting Kv3.3 WT DNA run on the upper part of the gel (WT mastermix), and PCR product from targeting KO DNA (KO mastermix) shown on the lower half of the gel.

### 3 SYNAPTIC CURRENTS OF THE LSO

---

The aim of this chapter is to examine synaptic inputs to the LSO, and how their kinetics change over development. It is crucial we understand how the auditory brainstem operates normally in order to identify changes following AOE. First, it was necessary to correctly identify the 2 major cell types in the LSO: LSO principal neurons and LOC neurons, the latter of which form part of the efferent system, and are not of interest in this study. This was made possible by comparing differences in their voltage activated currents, and AP characteristics.

Both EPSCs and IPSCs can be recorded from LSO principal neurons, as they receive an ipsilateral excitatory glutamatergic input, and a contralateral inhibitory glycinergic input via the MNTB, which acts as a neural relay (Tollin, 2003). Here I have recorded both EPSCs and IPSCs in LSO principal neurons. Furthermore, I pharmacologically isolated AMPAR-mediated EPSCs and NMDAR EPSCs, and documented the developmental acceleration of decay time constant ( $\tau$ ). Finally, a rapid run-down of NMDAR EPSC amplitude was observed. I have started preliminary investigations into the cause of this run-down, to ascertain whether this was  $\text{Ca}^{2+}$  mediated.

Here, I have decided to focus solely on the LSO rather than the MNTB for a number of reasons.

1. EPSC recordings from MNTB neurons are difficult to obtain because each principal neuron receives only one excitatory input from the CN (Thompson and Schofield, 2000, Kuwabara et al., 1991), which can easily be damaged during the slicing process. Once this calycal input is damaged, EPSCs can no longer be recorded from the postsynaptic MNTB neuron. Therefore, attempting to record EPSCs from the MNTB yields a low success rate compared to the LSO, where principal neurons receive multiple excitatory inputs from the CN.
2. MNTB EPSCs have already been well characterised by the lab and published (Steinert et al., 2010).

### 3.1 IDENTIFYING LSO PRINCIPAL AND LOC NEURONS

Throughout this thesis, I have examined the effect of AOE on LSO principal neurons. The LSO also contains LOC neurons, which form part of the efferent system. Thus, it was crucial I was able to reliably distinguish between LOC and principal neurons, to avoid merging the 2 different neuronal populations.

#### LSO principal and LOC neurons exhibit different voltage activated currents

I was able to identify both LSO principal neurons and LOC neurons by comparing their electrophysiological properties, consistent with previous findings (Adams 1999, Barnes Davies 2004, Sterenborg 2011). CBA/Ca mice (age P14-P16) were culled, and brain slices prepared (as described in chapter 2, section 2.2). Neurons of the LSO were subject to whole cell patch clamp, where an I/V protocol was employed consisting of 250 ms voltage steps from -90 mV to +40 mV (10 mV steps) from a holding potential (HP) of -60 mV (fig 3.1). Here, LSO principal neurons show a sustained outward current in response to depolarising voltage steps (fig 3.1, a). There was little difference between I/Vs plotted from the instantaneous current (open circles) and currents measured 5 ms before the end (black circles). Identical analysis was performed on a representative LOC neuron (fig 3.1 b), which exhibited transient  $I_A$  current, as measured by the much greater outward  $K^+$  current amplitude of at the beginning of the voltage step (open circles) compared to the end of the voltage step (black circles).

Figure 3.1 Voltage clamp: Identifying LSO principal and LOC neurons by their voltage activated currents

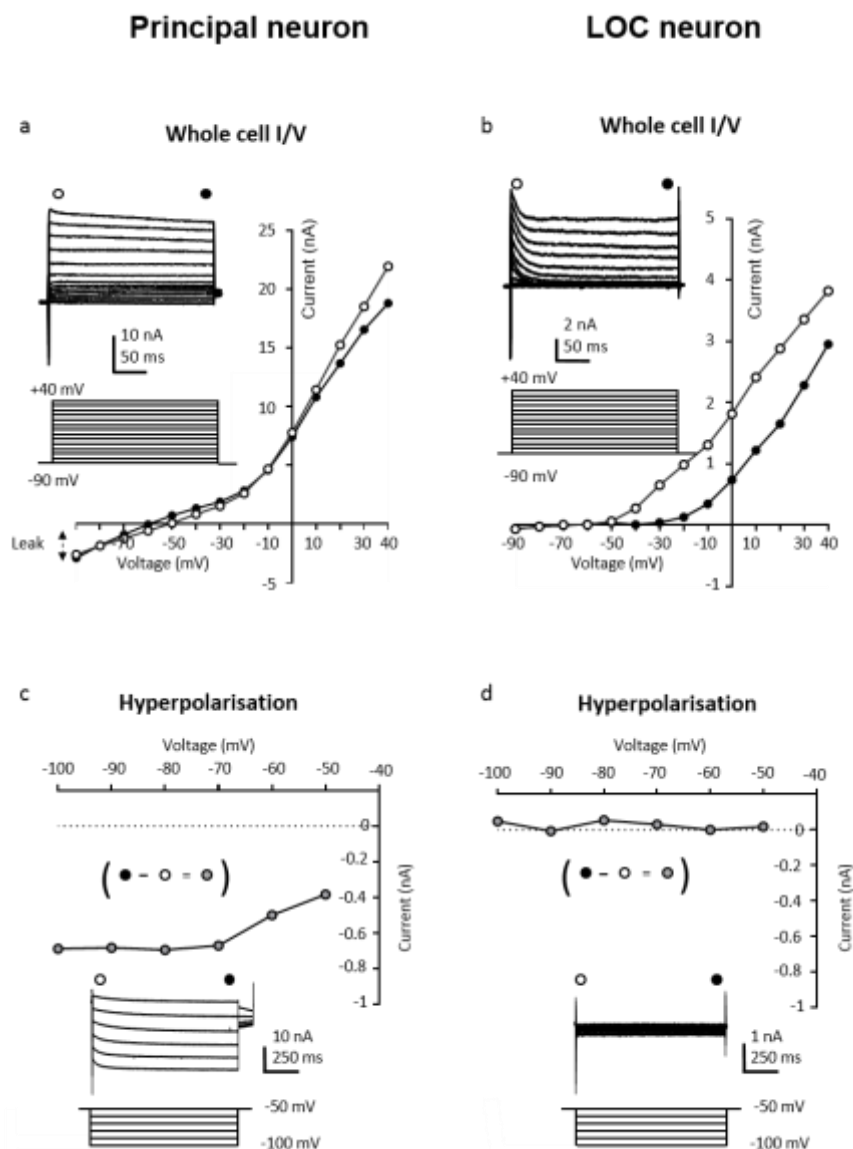


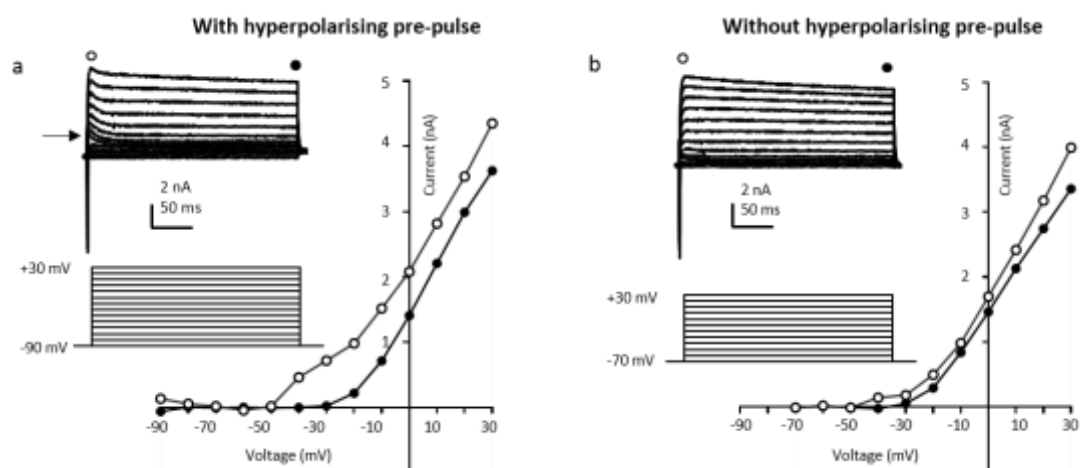
**Fig 3.1. Voltage clamp: Identifying LSO principal and LOC neurons by their voltage activated currents.** **a.** Example LSO principal neuron from CBA/Ca mouse (P15) shows a sustained outward current in response to 250 ms depolarising steps from -90mV to +40 mV (10 mV steps) (inset lower trace). The current-voltage relationship (I/V) is plotted for currents measured 5 ms from the start of the voltage steps (open circles) and 5 ms before the end of the voltage steps (black circles). **b.** Example LOC neuron from CBA/Ca mouse (P16) shows a fast transient outward current in response to the same protocol, which activates on depolarisation positive to -50 mV, consistent with  $I_A$  current. **c.** Same cell as in **a** (principal neuron), in response to hyperpolarising steps from +50 mV to -100 mV (10 mV steps).  $I_H$  is plotted by subtracting the instantaneous current (open circles) from the current measured 5 ms before the end of the voltage step (black circles), with the difference represented at grey circles. **d.** The same LOC neuron as part **b** shows no  $I_H$  current in response to hyperpolarising voltage steps (1s) from +50 mV to -100 mV. Holding potential = -60 mV.

The same neurons were subjected to hyperpolarising voltage steps from -50 mV to -100 mV (fig 3.1 c & d). Here, the difference between the instantaneous current (open circles) and current at the end of the voltage step (black circles) were represented as grey circles, and plotted at each HP (-50 mV to -100 mV, 10 mV steps). Principal neurons showed slowly activating inward current in response to hyperpolarising steps, indicative of  $I_H$ , as evidenced by the difference in current at the beginning and end of the voltage step (when  $I_H$  has turned on), which increased with further hyperpolarisation (fig 3.1, c). In contrast, the LOC neuron showed no change in inward current (fig 3.1, d), and thus lacked  $I_H$ .

How can we determine whether  $I_A$  current is present in LOC neurons, or whether we are simply measuring inactivation of other channels? Activation of  $I_A$  current requires a hyperpolarising pre-pulse (Hille, 2001). Fig 3.2 shows the voltage activated currents of an LOC neuron with (a) and without hyperpolarising pre-pulses (-90 mV) (b). With prior hyperpolarisation  $I_A$  current is observed, but removal of the hyperpolarising pre-pulses in the same cell abolishes  $I_A$  current (fig 3.2, b), rendering the outward  $K^+$  currents almost identical at the beginning and end of the voltage step.

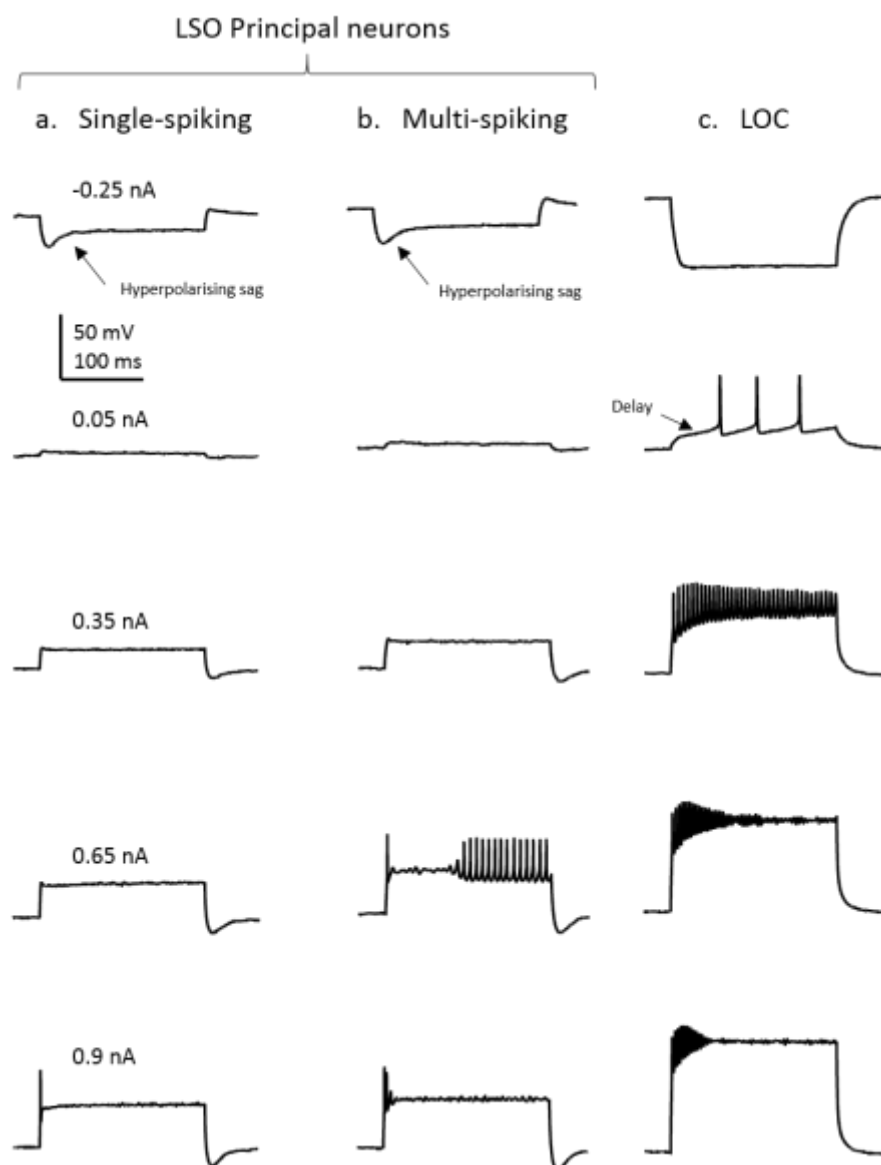
In conclusion, I can confidently identify LSO principal and LOC neurons based on their voltage activated currents. LSO principal neurons show  $I_H$  current when hyperpolarised, yet LOC neurons do not. In contrast, LOC neurons exhibit  $I_A$  current, yet principal neurons do not. Overall principal neurons have much larger voltage activated currents compared to LOC neurons, and show intrinsic leak at negative HPs, which is absent in LOC neurons.

Figure 3.2 Voltage clamp:  $I_A$  current in LOC neurons requires hyperpolarising pre-pulse



**Fig 3.2. Voltage clamp:  $I_A$  current in LOC neurons requires hyperpolarising pre-pulse.** Example LOC neuron  $I/V$  in the presence or absence of a hyperpolarising pre-pulse of -90 mV. **a.** Pre-pulse present: The voltage command consisted of a 250 ms hyperpolarising pre-pulse to -90 mV, followed by a series of depolarising steps (250 ms duration) from -70 mV to +30 mV (inset, lower traces). Raw traces show  $I_A$  current (as indicated by arrow). The current-voltage relationship ( $I/V$ ) is plotted for currents 5 ms from the start of the voltage steps (open circles) and 5 ms before the end of the voltage steps (closed circles). A fast transient outward current activates on depolarisation positive to -50 mV, consistent with  $I_A$  current. **b.** Pre-pulse absent: The same cell was subjected to the same voltage clamp protocol, however the 250 ms hyperpolarising pre-pulse was not given.

Figure 3.3 Current clamp: LSO principal and LOC neurons exhibit different AP firing patterns



**Fig 3.3. Current clamp: LSO principal and LOC neurons exhibit different AP firing patterns** Raw current clamp data from a single-spiking principal neuron (**a**), a multi-spiking principal neuron (**b**) and LOC neuron (**c**) in response to 200 ms current injection steps (-0.025 to 0.9 nA, top to bottom) from a holding potential of -60 mV. The level of current injection is indicated above each trace in **a** and also applies to **b** and **c**. A current injection of -0.25 nA causes a hyperpolarising sag in both single and multi-spiking principal neurons, as indicated by black arrows, which is absent in LOC neurons. The first AP recorded in both single-spiking and multi-spiking principal neurons (**a & b**) exhibits a rapid onset at the beginning of the depolarising current injection. LOC neurons (**c**) show delay of action potential initiation (black arrow), which reduced with increasing current injection. All subsequent figures showing APs elicited from the LSO principal neurons were recorded using the same current step protocol, from a HP of -60 mV, and a holding current which did not exceed  $\pm 450$  pA.

### LSO principal and LOC neurons exhibit different AP characteristics

APs were recorded from LSO neurons in current clamp mode using 200 ms current injection steps ranging from -0.25 to 0.9 nA (0.05 nA steps). Principal neurons can be subdivided into 2 categories: single-spiking ( $\leq 3$  APs) or multi-spiking (5 – ~100 APs). In contrast, LOC neurons are always multi-spiking. Figure 3.3 shows example raw current clamp data from a single-spiking principal neuron (a), a multi-spiking principal neuron (b) and a LOC neuron (c), in response to increasing current injection steps (top to bottom, values indicated far left).

Single-spiking principal neurons fire once at the beginning of the current injection, and maintain this single-spiking firing pattern with further depolarisation (although occasionally a second or third AP may occur at higher current injection levels). In contrast, multi-spiking principal neurons may initially fire 1 AP at the beginning of the depolarising step, and then up to ~100 APs in response to further depolarisation (fig 3.3, b). It is possible to distinguish multi-spiking LSO principal neurons and LOC neurons based on their AP firing characteristics alone. LOC neurons have a characteristic delay of onset of the first AP fired (as depicted by arrow), in contrast to principal neurons which fire at the onset on the current injection. In addition, principal neurons exhibit a hyperpolarising voltage sag (arrow) in response to -0.25 nA current injection, due to the presence of  $I_H$  current.

Figure 3.4 LSO distribution plot of different neuron types

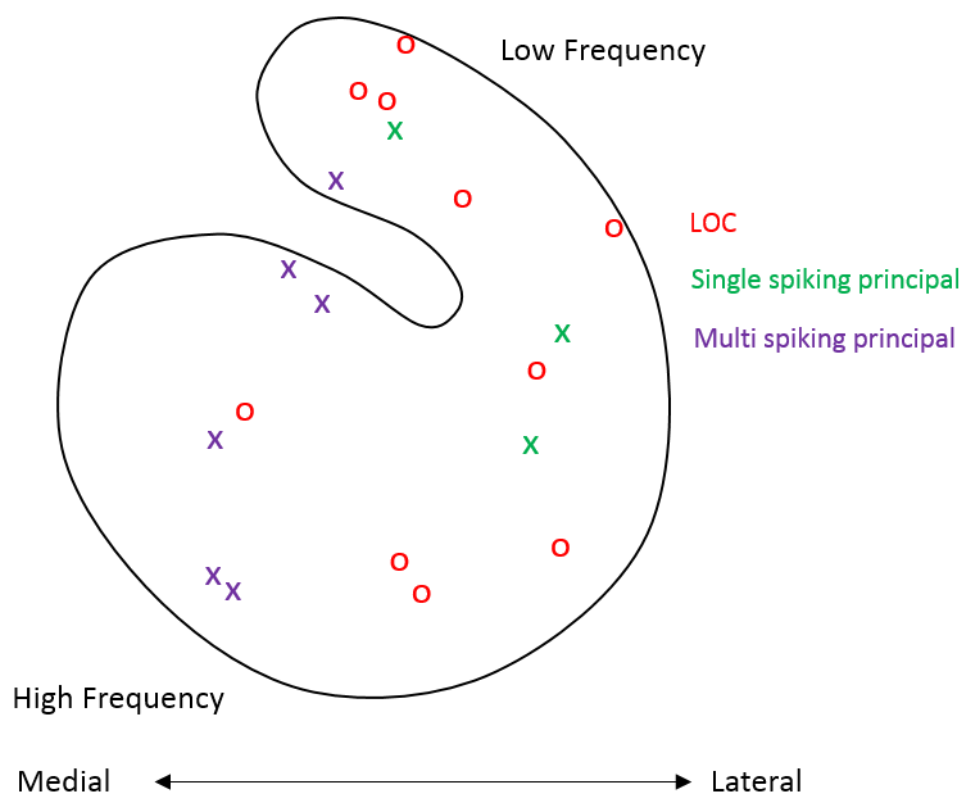


**Fig 3.4. LSO distribution plot of different neuron types** Stereotypical profile of the LSO, plotting the location of LSO single-spiking (green crosses,  $n = 3$ ), multi-spiking (purple crosses,  $n = 6$ ) and LOC neurons (red circles,  $n = 10$ ). Medial and lateral sides of the LSO and the tonotopic gradient (low frequency and high frequency) are labelled.

Next, I examined the distribution of the different neuronal types in the LSO. Figure 3.4 shows a stereotypical profile of the LSO, plotting the location of LSO single-spiking (green crosses,  $n = 3$ ), multi-spiking (purple crosses,  $n = 7$ ) and LOC neurons (red circles,  $n = 10$ ). The distribution of principal neurons concurs with previous research, where multi-spiking neurons are mostly located in the medial limb of the LSO, and single-spiking neurons are predominantly in the lateral limb (Barnes-Davies et al., 2004). In contrast, LOC neurons exhibited no obvious distribution pattern (see discussion).

Single-spiking and multi-spiking principal neuron AP characteristics are not significantly different

I compared AP characteristics and membrane properties between single-spiking and multi-spiking LSO principal neurons to establish if they could be grouped together, and found no significant differences (see table 3.1, and fig 3.5 (a) for an explanation of different measures of amplitude). Thus, going forward, I will group data recorded from these two neuron types under 'LSO principal neuron'.

*Table 3.1 There is no difference between single-spiking and multi-spiking LSO principal neurons for all parameters measured*

Measurement	LSO Principal neurons AP firing		P value * $\leq 0.05$
	Single-spiking (mean $\pm$ SEM) (n = 3)	Multi-spiking (mean $\pm$ SEM) (n = 6)	
AP absolute amplitude	5.22 $\pm$ 4.75 mV	9.33 $\pm$ 2.72 mV	0.5013
AP relative amplitude	38.72 $\pm$ 8.02 mV	44.83 $\pm$ 3.69 mV	0.5408
AP amp from baseline	66 $\pm$ 4.67 mV	69.47 $\pm$ 2.46 mV	0.5550
AP threshold	-32.88 $\pm$ 3.82 mV	-35.39 $\pm$ 2.47 mV	0.6111
AHP	-4.39 $\pm$ 2.27 mV	-6.03 $\pm$ 0.97 mV	0.5438
Whole cell capacitance	24 $\pm$ 7.5 pF	19.2 $\pm$ 1.9 pF	0.5898
RMP	-52.33 $\pm$ 1.45 mV	-53 $\pm$ 1.91 mV	0.8282

**Table 3.1** A comparison of single-spiking and multi-spiking LSO principal neurons (statistical significance tested using unpaired t-test).

### LOC neurons exhibit significantly larger and slower APs

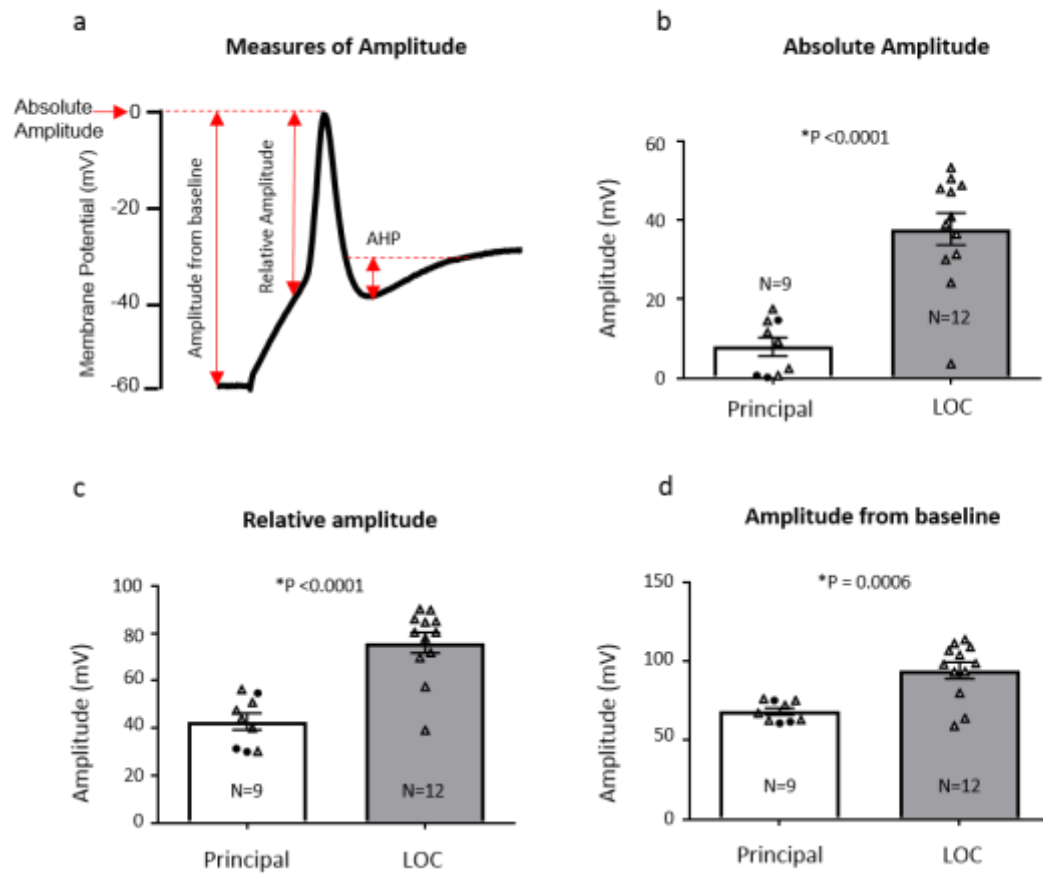
To assess whether LOC and principal neurons have different AP amplitudes, three separate measurements of amplitude were taken from the first evoked AP of each cell: absolute amplitude, relative amplitude and the amplitude from baseline (fig 3.5, a). Absolute amplitude was defined as the membrane potential at which the AP peaks, whilst relative amplitude was the difference between the membrane potential where the AP was initiated and the absolute amplitude. Amplitude from the baseline was defined as the difference between the absolute amplitude and the membrane potential before the current injection step, where the membrane potential of the neuron was held at -60 mV.

For each measure of amplitude, APs from LOC neurons had significantly larger amplitudes compared to LSO principal neurons. Specifically, absolute amplitude values for principal neurons and LOC neurons were  $7.96 \pm 2.33$  mV (mean  $\pm$  SEM),  $n = 9$  &  $37.77 \pm 4.07$  mV,  $n = 12$ ,  $P < 0.0001$  respectively (fig 3.5, b). Relative amplitude: Principal neurons =  $42.79 \pm 3.48$  mV,  $n = 9$  and LOC neurons =  $76.04 \pm 4.30$  mV,  $n = 12$ ,  $P < 0.0001$  (fig 3.5, c). Amplitude from baseline: Principal neurons =  $68.31 \pm 2.16$  mV,  $n = 9$ , LOC neurons =  $94.35 \pm 5.17$  mV,  $n = 12$ ,  $p = 0.0003$  (fig 3.5, d).

Following this, I compared the half widths of the first elicited AP between LOC neurons and LSO principal neurons (fig 3.6). Principal neurons had significantly shorter half widths compared to LOC neurons ( $0.30 \pm 0.02$  ms, (mean  $\pm$  SEM),  $n = 9$  &  $0.67 \pm 0.05$  ms,  $n = 12$ , ( $p < 0.0001$ ) respectively. RMP was also more negative in principal neurons than LOC neurons ( $-52.78 \pm 1.31$  mV, (mean  $\pm$  SEM),  $n = 11$  &  $-44.18 \pm 3.37$  mV,  $n = 9$  respectively,  $p = 0.034$  (fig 3.7 d). No differences were observed for all other parameters measured: WCC, AP threshold, afterhyperpolarisation (AHP) (fig 3.7, a, b, c).

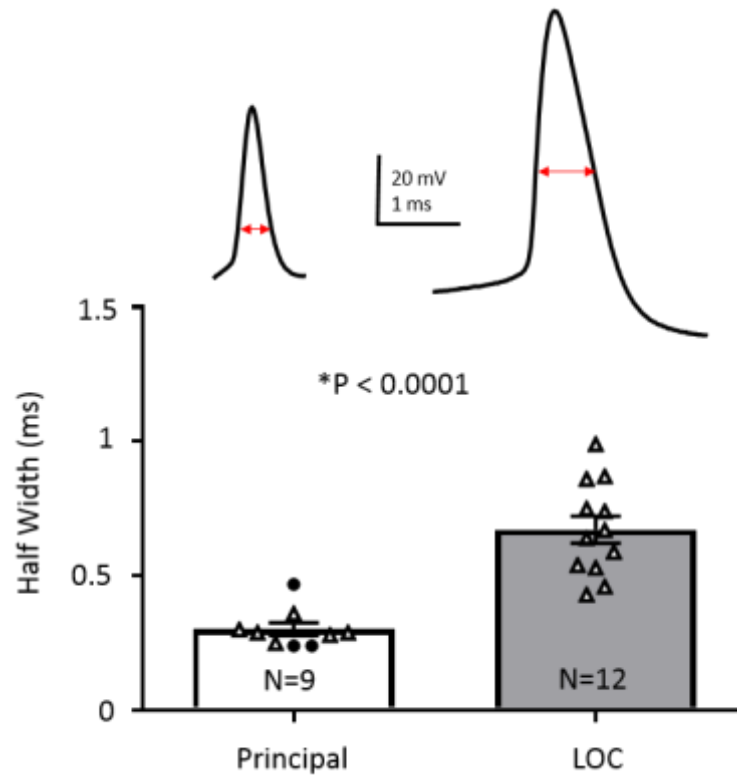
In conclusion, APs recorded from LOC neurons have larger amplitudes and longer half widths, as well as a delay of the first elicited AP. These differences are vast, and immediately enable clear identification of either a principal or LOC neurons, based on their AP characteristics alone.

Figure 3.5 Amplitude of LOC APs are significantly larger than LSO principal neurons



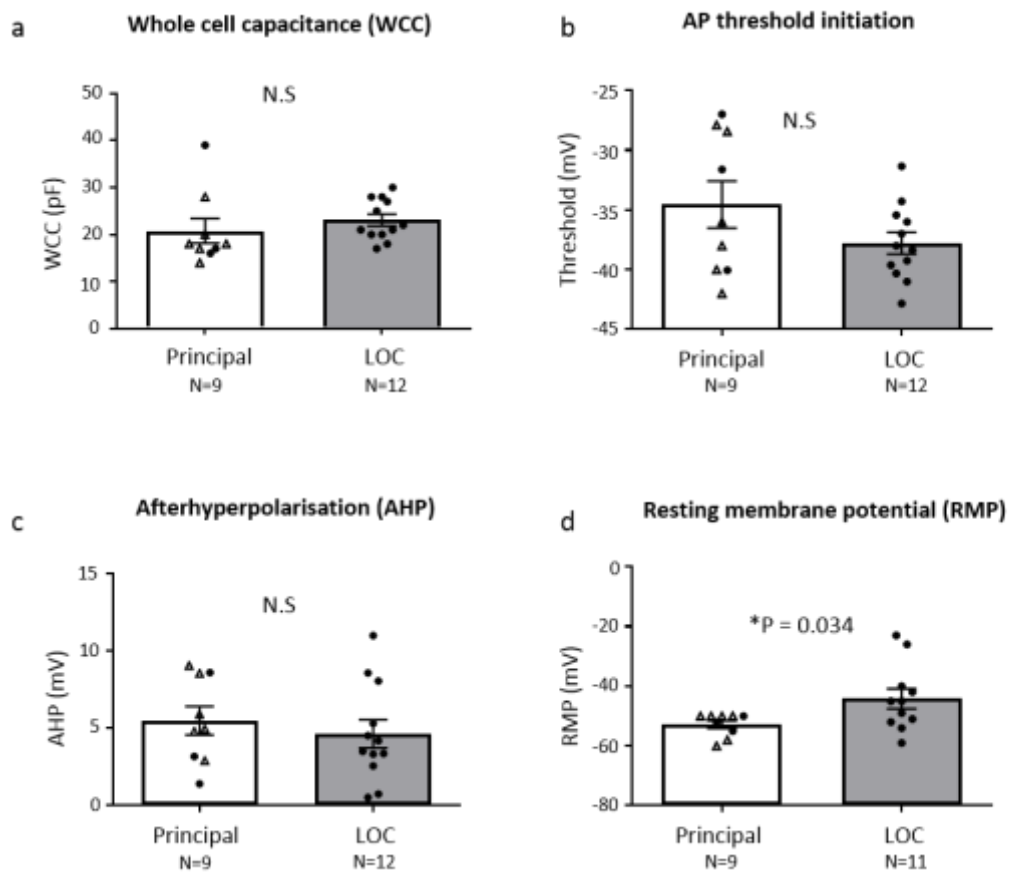
**Fig 3.5. Amplitude of LOC APs are significantly larger than LSO principal neurons** APs were recorded from LSO principal neurons and LOC neurons in CBA/Ca mice (P14-P16). **a.** Diagram of an action potential showing the different measures of amplitude. **b.** Absolute amplitude: Principal neurons =  $7.96 \pm 2.33$  mV (mean  $\pm$  SEM), (n = 9), LOC neurons =  $37.77 \pm 4.07$  mV, (n = 12),  $p < 0.0001$  (Unpaired t-test). **c.** Relative amplitude: Principal neurons =  $42.79 \pm 3.48$  mV, LOC neurons =  $76.04 \pm 4.304$  mV,  $p < 0.0001$ . **d.** Amplitude from baseline: Principal neurons =  $68.31 \pm 2.16$  mV, LOC neurons =  $94.35 \pm 5.17$  mV,  $p = 0.0006$ . Filled circles indicate single-spiking neurons, open triangles indicate multi-spiking neurons (b-d).

Figure 3.6 AP half widths are shorter in LSO principal neurons compared to LOC.



**Fig 3.6. AP half widths are shorter in LSO principal neurons compared to LOC.** APs were recorded from LSO principal neurons and LOC cells from CBA/Ca mice (P14-P16). Below: Half width of the first elicited AP was compared between principal neurons ( $n = 9$ ) and LOC neurons ( $n = 12$ ), ( $0.30 \pm 0.02$  ms, (mean  $\pm$  SEM),  $0.67 \pm 0.05$  ms, respectively,  $p < 0.0001$ , via unpaired t-test). Above: example AP traces of a principal cell and LOC cell, with red arrows showing half width (0.29 ms and 0.67 ms respectively). Filled circles indicate single-spiking neurons, open triangles indicate multi-spiking neurons.

Figure 3.7 Comparison of LSO principal and LOC neuron characteristics



**Fig 3.7. Comparison of LSO principal and LOC neuron characteristics.** The first elicited APs were compared between LSO principal neurons and LOC neurons from CBA/Ca mice (P14:P16). **a.** Whole cell capacitance (WCC): There is no significant difference in WCC between LSO principal (n = 9) and LOC neurons (n = 12) ( $20.78 \pm 2.63$  pF, (mean  $\pm$  SEM), n = 9 &  $23.08 \pm 1.25$  pF, n = 12, respectively, p = 0.4). **b.** There is no difference in AP threshold initiation (principal =  $-34.55 \pm 1.96$  mV, LOC =  $-37.78 \pm 0.92$ , p = 0.12). **c.** AHP: There is no difference in AHP (principal =  $4.78 \pm 1.33$  mV, LOC =  $4.63 \pm 0.91$  mV, p = 0.93). **d.** RMP is less negative in LOC (n=11) neurons compared to principal neurons (n=9) ( $-44.18 \pm 3.37$  mV &  $-52.78 \pm 1.31$  mV, respectively, p = 0.034). Filled circles indicate single-spiking neurons, open triangles indicate multi-spiking neurons (a-d).

### 3.2 Synaptic currents of LSO principal neurons

LSO principal neurons exhibit both EPSCs and IPSCs

Once I was able to distinguish between principal neurons and LOC neurons, I then measured EPSCs and IPSCs from LSO principal neurons. To help record EPSCs and IPSCs I blocked voltage-gated  $K^+$  channels using caesium chloride in the patch pipette (see chapter 2, table 2.2). Whilst this prevented me from recording most voltage-gated  $K^+$  conductances, I was still able to identify LSO principal neurons by measuring  $I_H$  current upon hyperpolarisation. EPSCs were recorded using a bipolar stimulating electrode placed over the fibers between the ipsilateral CN and the LSO (see chapter 2, fig 2.6 for diagram). To record IPSCs, the electrode was placed over the inhibitory fibers from the ipsilateral MNTB to the LSO. To evoke postsynaptic currents (PSCs), stimulation pulses were supplied by a constant voltage stimulator (20  $\mu$ s duration, frequency of 0.25 Hz, amplitude 0.1 - 99V). IPSCs were recorded in the presence of 10  $\mu$ M NBQX and 20  $\mu$ M d-AP5, whilst EPSCs were recorded in the presence of 1  $\mu$ M strychnine and 10  $\mu$ M bicuculline.

Fig 3.8 (a) shows postsynaptic current (PSC) amplitude plotted in response to increasing stimulation (0-15 mA). To the right are average raw data traces at each stimulation level tested. The amplitude of the PSC produces a sinusoidal response to increased current injection. Eventually PSC amplitude did not increase with higher levels of stimulation, because all the fibers synapsing with the LSO had already been recruited. Fig 3.8 (b) shows an I/V of IPSCs (HPs = -80 to +40 mV) from a representative example LSO principal neuron (P14). To the right are average raw traces from each HP tested. Similarly, Fig 3.8 (c) shows average EPSC traces from a different representative LSO principal neuron from a pre-hearing mouse (P8). The EPSCs have a fast AMPAR mediated component, and a slower NMDAR mediated component. Open circles indicate the latency at which the I/V of the fast AMPAR EPSCs were measured, and closed circles show the latency at which the I/V of NMDAR EPSCs were measured. NMDAR EPSCs have a classic non-linear I/V response due to blockage by external  $Mg^{2+}$  at negative holding potentials (Nowak et al., 1984, ChesnoyMarchais and Barthe, 1996), in contrast to AMPAR EPSCs which have a linear I/V relationship.

Figure 3.8 EPSCs and IPSCs can be recorded from LSO principal neurons

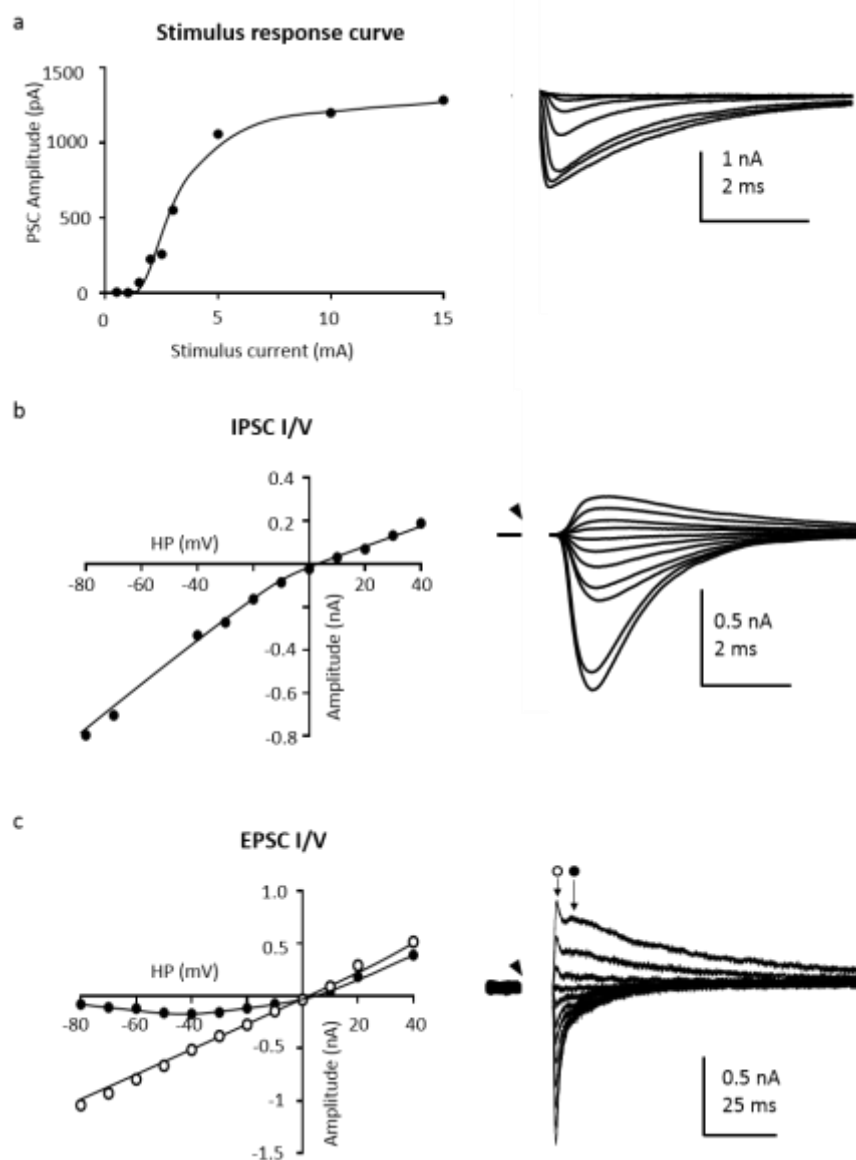


**Fig 3.8. EPSCs and IPSCs can be recorded from LSO principal neurons.** Postsynaptic currents were recorded from LSO principal neurons in response to stimulation pulses of 20  $\mu$ s duration (0.1-99V), at 0.25 Hz using a constant voltage stimulator. **a.** Left: Stimulus response curve: Amplitude of PSCs were recorded in response to increasing stimulus intensity (0-15 mA). Right: Average traces (10 sweeps) at each stimulus intensity. **b.** Left: IPSC I/V recorded in the presence of 10  $\mu$ M NBQX and 20  $\mu$ M d-AP5. Right: Average traces (10 sweeps) at each holding potential (-80 to +40 mV) (age P14) **c.** EPSC I/V recorded from a prehearing mouse (P8) in the presence of 1  $\mu$ M strychnine and 10  $\mu$ M bicuculline. AMPAR EPSCs were measured from the time point indicated by the open circle above the average traces (right) whilst NMDAR EPSCs were measured from the time point indicated by the closed circle. Stimulus artefacts have been removed throughout for clarity (indicated by arrow). All subsequent figures showing EPSCs and IPSCs were evoked from LSO principal neurons using the same stimulation protocol of 20  $\mu$ s duration (0.1-99V), at a frequency of 0.25 Hz.

The reversal potential of both IPSCs (fig 3.8, b) and EPSCs (fig 3.8, c) was  $\sim 0$ mV. The reversal potential for IPSCs would usually be  $\sim -50$  mV in LSO principal cells (Sterenborg, 2011), however caesium chloride was present in the intracellular patch solution creating symmetrical chloride levels between the patch pipette and the extracellular fluid.

In summary, both IPSCs and EPSCs can be recorded from LSO principal neurons. EPSCs are formed of both AMPAR mediated EPSCs (fast kinetics) and NMDAR EPSCs (slower kinetics), the latter of which forms a non-linear I/V due to blockage by external  $Mg^{2+}$  at negative HPs.

Next, I wanted to examine developmental changes in the decay kinetics of AMPAR EPSCs, NMDAR EPSCs and glycinergic IPSCs in LSO principal neurons. To do this, it was necessary to pharmacologically isolate the currents. Figure 3.9 (a) shows an EPSC response in the presence of  $1 \mu\text{m}$  strychnine &  $10 \mu\text{m}$  bicuculline, showing both fast AMPAR and slow NMDAR components (green). Addition of  $20 \mu\text{m}$  d-AP5 (NMDAR antagonist), abolishes the NMDAR EPSC response, isolating the fast AMPAR EPSC (purple). Further addition of  $10 \mu\text{m}$  NBQX (AMPA antagonist) (different cell) abolishes the AMPAR EPSC response (red) (3.9, b). Thus, I am able to isolate both AMPAR EPSCs and NMDAR EPSCs using specific antagonists.

Similarly, glycinergic IPSCs were isolated by  $10 \mu\text{m}$  bicuculline (GABAR antagonist), and EPSC antagonists ( $10 \mu\text{m}$  NBQX and  $20 \mu\text{m}$  d-AP5). GABAergic IPSCs were not recorded, due to the negligible amplitude of the response (Sterenborg et al., 2010).

Figure 3.9 AMPAR EPSCs and NMDAR EPSCs can be blocked using pharmacology

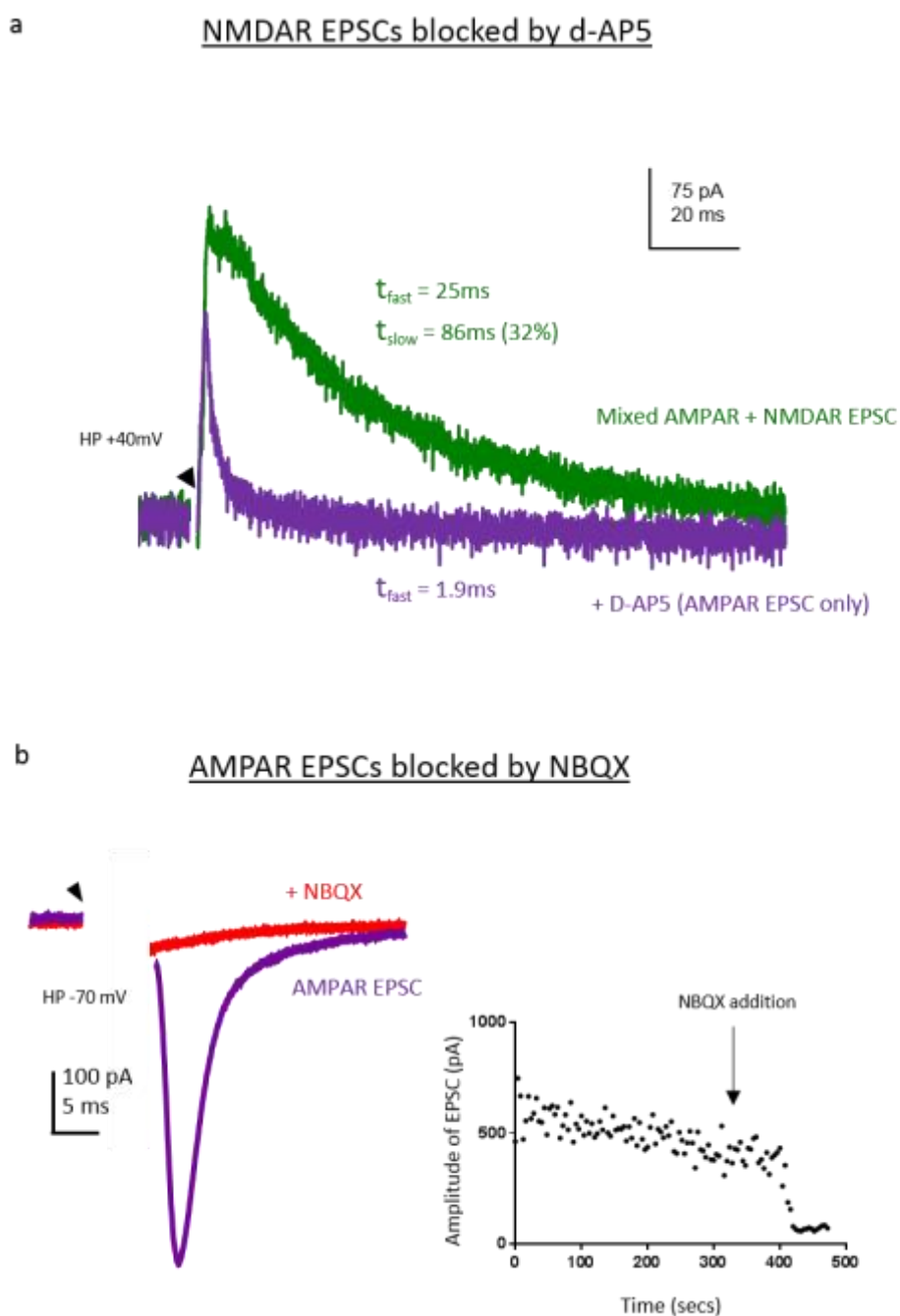


**Fig 3.9. AMPAR EPSCs and NMDAR EPSCs can be blocked using pharmacology.** Postsynaptic EPSCs were recorded from LSO principal neurons from CBA/Ca mice. **a. Green:** Average traces (5-10 sweeps) of mixed EPSCs (AMPA + NMDAR) recorded in the presence of 10  $\mu\text{m}$  bicuculline and 1  $\mu\text{m}$  strychnine (HP = +40 mV). **Purple:** Addition of 20  $\mu\text{m}$  d-AP5 blocks the NMDAR component, leaving the fast AMPAR EPSC. Mouse age = P8. **b. Left: Purple:** AMPAR EPSC recorded in the presence of 10  $\mu\text{m}$  bicuculline and 1  $\mu\text{m}$  strychnine and 20  $\mu\text{m}$  d-AP5. **Red:** Addition of 10  $\mu\text{m}$  NBQX to the same cell (AMPA antagonist) abolishes response (HP = -70 mV, mouse age = P13). Right: Amplitude of the EPSCs over time. At 316 secs, NBQX perfusion began (indicated by arrow).

AMPA EPSC and glycinergic IPSC decay time constants show developmental acceleration. Accurate ILD processing requires rapid, sub millisecond decay time constants of both AMPAR mediated EPSCs and glycinergic IPSCs in the LSO (Tollin, 2003). Previously in the lab, Dr Nadia Pilati examined the developmental acceleration of glycinergic IPSC and AMPAR EPSC decay kinetics in LSO principal neurons. Here I will compare data collected by myself under the same conditions (fig 3.10, a) to the developmental profile published by Dr Pilati (fig 3.10, b). In both instances, the mean decay tau of both glycinergic IPSCs (red) and AMPAR EPSCs (green) were recorded from mice belonging to 4 different age groups (pre-hearing (P7-9), hearing-onset (P12-15), juvenile (17-23) and young adult (>P23-36). Fig 3.10 (b) (Dr Pilati's data), shows both IPSCs and EPSCs in pre-hearing mice have slow decay kinetics ( $2.6 \pm 0.2$  ms (mean  $\pm$  SEM),  $n=10$ , and  $1.97 \pm 0.39$  ms,  $n = 10$ , respectively). IPSC and EPSC decay tau ( $\tau$ ) then converge and stabilize at  $\sim$ P17 (juvenile), ( $0.79 \pm 0.1$  ms,  $n = 7$ , and  $0.65 \pm 0.09$  ms,  $n = 5$ , respectively). Below are superimposed representative average traces of EPSCs and IPSCs for each age group, recorded at HP -70 mV.

My recordings have mirrored this trend (fig 3.10, a). I also observed slow decay  $\tau$  of IPSCs and EPSCs in pre-hearing mice ( $3.67 \pm 0.49$  ms,  $n = 3$ , and  $2.6 \pm 0.4$  ms,  $n= 7$ ) respectively. This was followed by an acceleration in EPSC decay  $\tau$  at hearing onset ( $0.85 \pm 0.08$  ms,  $n=3$ ) which stabilized through to juvenile stage (P17-P22) ( $0.80 \pm 0.04$  ms,  $n=2$ ) and beyond into young adulthood (P23-P28) ( $0.99 \pm 0.07$  ms,  $n =5$ ). An IPSC measured from a young adult mice had similar decay  $\tau$  to EPSCs measured at the same age ( $0.91$  ms,  $n=1$ ). Please note, this section serves to highlight that the recordings I have made concur with work already completed in the lab, hence low or even lack of  $n$  numbers in the case of IPSC recordings. The emphasis of chapter 5 is to examine the effect of AOE on EPSCs, at an age where EPSCs and IPSCs have converged to  $<1$ ms decay  $\tau$ , and thus have 'mature' kinetics. Here I can conclude that EPSCs and IPSCs converge to sub millisecond decay  $\tau$  by P17. Henceforth, AOE was only performed on mice aged  $\geq$  P17.

Figure 3.10 EPSC and IPSC decay time constants undergo developmental acceleration to <1 ms at P17

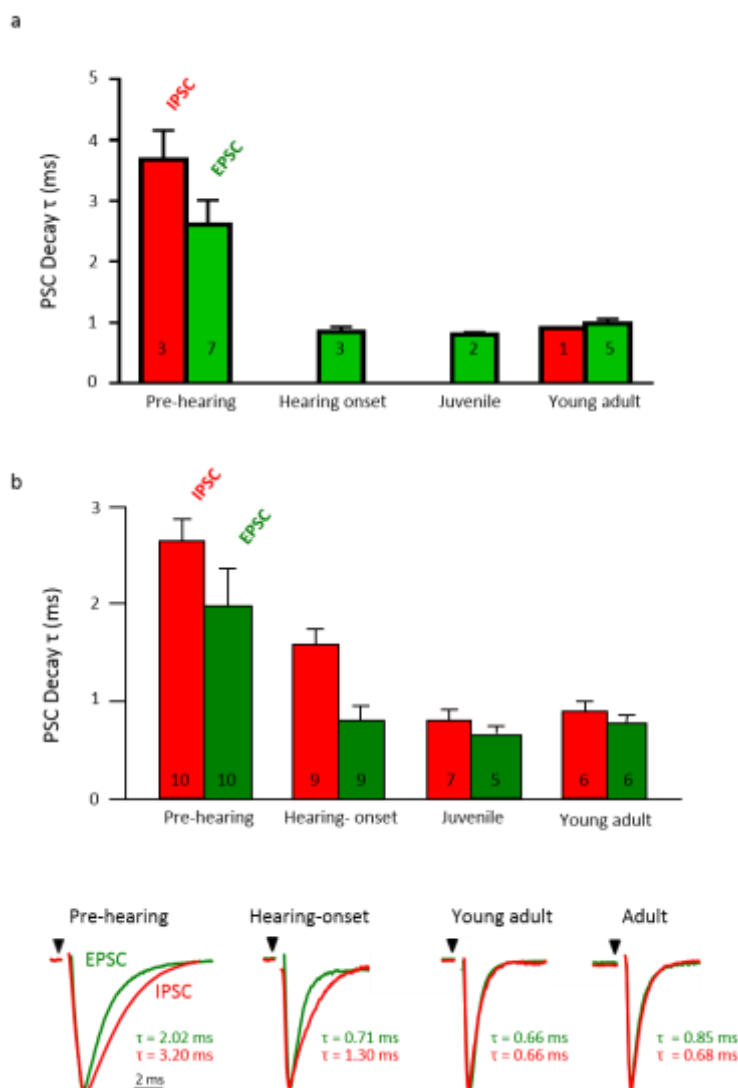


**Fig 3.10. EPSC and IPSC decay time constants undergo developmental acceleration to <1 ms at P17.** **a.** Partially complete developmental profile of decay  $\tau$  of IPSCs and EPSCs, divided into the age groups: pre-hearing (P6-P9), hearing onset (P12-P15), juvenile (P17-P22), young adult (P23-P28). PSCs were recorded in response to stimulation pulses of 20  $\mu$ s duration (0.1-99V), at 0.25 Hz using a constant voltage stimulator with a bipolar stimulator electrode placed over the MNTB (IPSCs) or over the ipsilateral CN tracts (EPSCs). Bar chart shows mean decay  $\tau$  of (5-10 sweeps), error bars: SEM. **b.** Complete developmental profile of EPSCs and IPSCs collected under the same conditions by Nadia Pilati (2016), but with CNQX substituted for NBQX. Below: Representative example average raw traces (20 sweeps) of EPSCs (green) and IPSCs (red) recorded in pre-hearing (P6), hearing onset (P13), juvenile (P22) and young adult (P23). EPSCs and IPSCs are superimposed, and have amplitude normalized. The black arrowhead indicates stimulation, and stimulus artifacts have been removed throughout for clarity. The decay time constant for each trace is indicated. All recordings were from a holding potential of -70 mV.

### NMDAR EPSC decay $\tau$ exhibits developmental acceleration

Next, I have assessed the developmental acceleration of NMDAR EPSC decay  $\tau$  in LSO principal neurons. Figure 3.11 (a) shows average EPSCs data traces (left) in response to HPs -80 mV to +40 mV (10 mV steps) from a pre-hearing CBA/Ca mouse (P8) (same data as shown in 3.8, c). In this instance, AMPAR EPSCs were not blocked by the addition of NBQX because AMPARs and NMDARs in pre-hearing mice have vastly different kinetics, with decay  $\tau$  of  $\sim 3$  ms and  $\sim 40$  ms respectively. An NMDAR EPSC IV (right) was plotted at the latency indicated by the black arrow, and showed a classic non-linear response.

LSO NMDAR EPSCs recorded from pre-hearing (P8-9) mice are slow, with the majority possessing dual decay components ( $\tau_{fast}$  and  $\tau_{slow}$ ) ( $\tau_{fast} = 44.82 \pm 5.41$  ms, (Mean  $\pm$  SEM),  $n = 8$ ,  $\tau_{slow} = 115.13 \pm 17.95$  ms,  $n = 6$ ) where  $\tau_{slow}$  contributed to  $34 \pm 9\%$  of the total amplitude. The decay  $\tau$  then underwent rapid developmental acceleration following hearing onset (fig 3.11, c), from  $\sim 40$  ms to  $\sim 3$  ms ( $\tau_{fast}$ ) by P14, and a reduction of  $\tau_{slow}$  amplitude.

By P10-P11, there is a lot of variability of  $\tau_{fast}$ , with some LSO neurons showing mature decay kinetics ( $\tau_{fast} < 20$  ms), whilst others remain slow and 'immature' ( $\tau_{fast} > 20$  ms) (3.11, d). Consequently, at age  $\geq P10$  it was necessary to block AMPAR EPSCs, to avoid contamination of the NMDAR EPSCs. Specifically, decay  $\tau$  at age P10-P11 were:  $\tau_{fast} = 27.29 \pm 9.08$  ms,  $n = 7$  &  $\tau_{slow} = 101 \pm 55.06$  ms,  $n = 6$  (fig 3.11, d), with  $\tau_{slow}$  contributing  $16 \pm 6\%$  (SEM) to the amplitude. By P14-P16 and beyond, all of the neurons displayed fast 'mature' decay kinetics ( $< 20$  ms), ( $\tau_{fast} = 3.96 \pm 1.35$  ms,  $n = 9$ ,  $\tau_{slow} = 35.72 \pm 7.75$  ms,  $n = 6$ ,  $\tau_{slow}$  contribution =  $18 \pm 7\%$ ). By P17-P19, NMDAR EPSCs remained fast ( $\tau_{fast} = 2.57 \pm 0.43$  ms,  $n = 6$ ,  $\tau_{slow} = 42.02 \pm 15.1$  ms,  $n = 4$ ), however  $\tau_{slow}$  was reduced to the limits of detectability at just  $5 \pm 2\%$  of the total amplitude. Similarly, at P23 - P25,  $\tau_{slow}$  contributed just ( $9 \pm 4\%$ ) of the total amplitude, and maintained fast decay kinetics  $\tau_{fast} = 2.58 \pm 0.37$  ms,  $n = 6$ , and  $\tau_{slow} = 28.83 \pm 8.7$  ms,  $n = 4$ .

Figure 3.11 NMDAR EPSCs exhibit acceleration of decay  $\tau$  following hearing onset

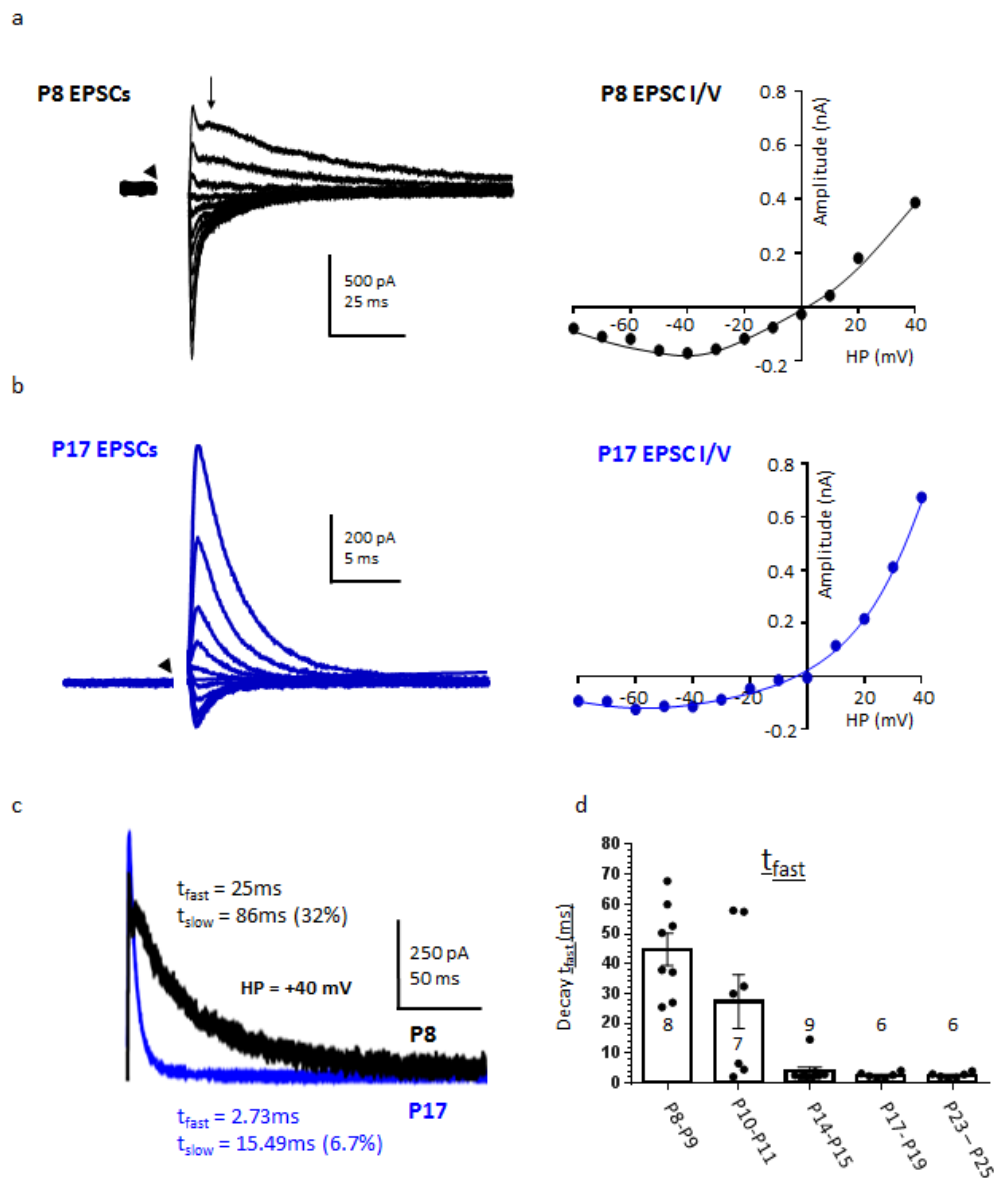


**Fig 3.11. NMDAR EPSCs exhibit acceleration of decay  $\tau$  following hearing onset. a. Right.**

Representative NMDAR EPSC I/V recorded from a pre-hearing mouse (P8) in the presence of  $1\mu\text{M}$  strychnine,  $10\mu\text{M}$  bicuculline. **Left:** Average raw traces (5-10 sweeps) at each holding potential (-80 to +40 mV, 10 mV steps). **b. Right:** Representative NMDAR EPSC I/V recorded from a juvenile mouse (P17) in the presence of  $1\mu\text{M}$  strychnine,  $10\mu\text{M}$  bicuculline &  $10\mu\text{M}$  NBQX. **Left:** Average raw traces of NMDAR EPSCs (5-10 sweeps) at each holding potential (-80 to +40 mV, 10 mV steps).

**c.** Superimposed average traces of NMDAR EPSCs recorded from a P8 mouse (black) and P17 mouse (blue) (HP = +40 mV). **d.** Developmental profile of  $\tau_{fast}$  at age groups (P8-P9), (P10-P11), (P14-P15), (P17-P19) and (P23-P25).  $\tau_{fast}$  is significantly slower in P8 – P9 mice compared to all other groups ( $p < 0.001$ ), as measured by One-way ANOVA with Games Howell post hoc testing. Filled circles indicate individual data points.

In summary, NMDARs undergo rapid acceleration in EPSC decay kinetics, so that by P14-P15 all LSO principal neurons exhibit mature kinetics of  $< 20$  ms, (although the majority were  $\sim 3$  ms). In addition, most NMDAR EPSCs have bi-exponential decay ( $\tau_{fast}$  and  $\tau_{slow}$ ), where the latter is prominent in pre-hearing mice, but is reduced to the limits of detectability by P17.

#### NMDAR EPSCs show rapid, irreversible run-down in amplitude over time

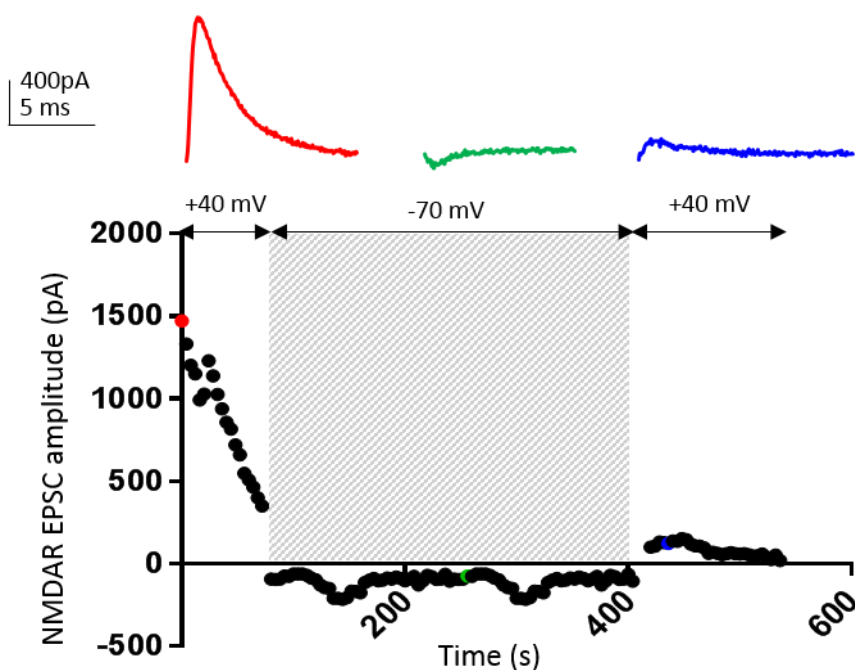
Upon whole cell configuration of LSO neurons, the neuron was held at  $-70$  mV, and stimulated at  $0.25$  Hz during pharmacological isolation of NMDAR EPSCs ( $1 \mu\text{M}$  strychnine,  $10 \mu\text{M}$  bicuculline and  $10 \mu\text{M}$  NBQX) for  $\sim 5$  minutes. The membrane potential was then increased to  $+40$  mV and NMDAR EPSCs were immediately recorded. Initially, my aim was to collect an I/V from holding potentials between  $-80$  to  $+40$  mV ( $10$  mV steps) as quickly as possible. Thus, only 5-10 sweeps were recorded at each holding potential. However, when the neuron was held for longer at  $+40$  mV, the amplitude of the NMDAR EPSCs rapidly declined in LSO principal neurons with fast 'mature' decay kinetics ( $< 20$  ms), but was absent in slow, 'immature' NMDAR EPSCs in pre-hearing mice.

Fig 3.12 shows the amplitude of NMDAR EPSCs ( $\tau_{fast} = 2.09$  ms,  $\tau_{slow} = 13.8$  (12%)) from a representative LSO principal neuron over time at different HPs ( $-40$  mV or  $-70$  mV, as indicated by horizontal arrows above, shaded area = HP  $-70$  mV). Upon stepping to  $+40$  mV, the initial amplitude of the NMDAR EPSCs was very large ( $1472$  pA) (see raw trace in red above), however within just 48 seconds, the amplitude had declined to half this value. HP was then reduced to  $-70$  mV for  $\sim 5$  mins (shaded area) and then returned to  $+40$  mV, where no recovery of the amplitude was observed. Two other LSO principal neurons tested under the same conditions also showed no recovery of amplitude (data not shown), suggesting the run-down is irreversible. Note: only cells with 'mature'  $\tau_{fast}$  of  $< 20$  ms were analysed, with a robust initial amplitude ( $> 400$  pA).

Previous studies have shown  $\text{Ca}^{2+}$  mediated run-down of NMDAR EPSCs in other cell types in the brain (see discussion). Indeed, NMDARs are permeable to  $\text{Ca}^{2+}$  themselves,

and thus  $\text{Ca}^{2+}$  mediated depression of activity can serve as a self-regulatory mechanism. Here I have performed preliminary investigations to assess whether NMDAR EPSC run-down in LSO principal neurons was mediated by  $\text{Ca}^{2+}$ . Firstly, I wanted to rule out that an increase in series resistance (SR) during recording was responsible for the run-down in NMDAR EPSC amplitude. Fig 3.13 (a) shows an NMDAR EPSC amplitude from an example LSO principal neuron. SR did not alter >20%, however it took just 60 secs to reach half the initial amplitude. Furthermore, the neuron was only stimulated once per minute (rather than 0.25 Hz), but did not slow the rate of run-down, suggesting it is not activity-dependent.

*Figure 3.12 NMDAR EPSCs show a rapid, irreversible decrease in amplitude over time*



**Fig 3.12. NMDAR EPSCs show a rapid, irreversible decrease in amplitude over time.** NMDAR EPSCs were recorded from an LSO principal neuron from a CBA/Ca mouse (P11). The neuron was held at -70 mV and stimulated at 0.25 Hz during pharmacological isolation of NMDAR EPSCs (addition of 1  $\mu\text{M}$  strychnine, 10  $\mu\text{M}$  bicuculline and 10  $\mu\text{M}$  NBQX) for ~5 mins. At time 0 on graph, the HP was increased to +40 mV and NMDAR EPSCs recorded. Below: NMDAR EPSC amplitude was plotted against time. After 80 secs, the HP was decreased to -70 mV, as indicated by horizontal arrows above. Following ~5 mins at HP -70 mV, the HP was returned to +40 mV. Above: Example raw traces taken at different time points, each example has a corresponding data point below, in a matching colour. **Red:** HP = +40 mV, amplitude = 1472 pA at 0 secs. **Green:** HP = -70 mV, amplitude = -76 pA at 256 secs. **Blue:** HP = +40 mV, amplitude = 122 pA at 436 secs.

Next, EGTA (a calcium chelator) was increased in the intracellular patch solution from 5 mM to 20 mM. Run-down of NMDAR EPSCs still occurred, however run-down times were variable compared to the 5 mM EGTA condition: **5 mM EGTA** =  $43.4 \pm 1.8$  secs (mean  $\pm$  SEM),  $n = 5$  & **20 mM EGTA** = 55 secs,  $n = 2$  (80 secs and 30 secs) (fig 3.13 b & c). EGTA is a slow acting calcium chelator, which may not act quickly enough to counter the rapid run-down of the EPSCs observed. To address this, 20 mM EGTA was substituted with the faster acting calcium buffer BAPTA (20 mM) (Adler et al., 1991). Again, run-down times in the 20 mM BAPTA condition were very inconsistent ( $76 \pm 41.1$  secs,  $n = 3$ ) (fig 3.13 c).

Here, I patched 5 neurons using high levels of calcium chelators in the pipette (20 mM EGTA & 20 mM BAPTA) to elucidate whether NMDAR EPSC run-down in LSO principal neurons is  $\text{Ca}^{2+}$  mediated. The run-down times were highly variable, and thus it remains unclear whether run-down is regulated by intracellular  $\text{Ca}^{2+}$  levels. The slowest run-down in amplitude took just 156 seconds to reach half the initial amplitude, thus it seems unlikely it is solely determined by  $\text{Ca}^{2+}$  levels. Ultimately, the experiment proved technically difficult, and produced highly variable results. For these reasons, I decided not to pursue this enquiry any further.

Figure 3.13 Run-down in amplitude is not caused by increased SR, and is not prevented by calcium buffering

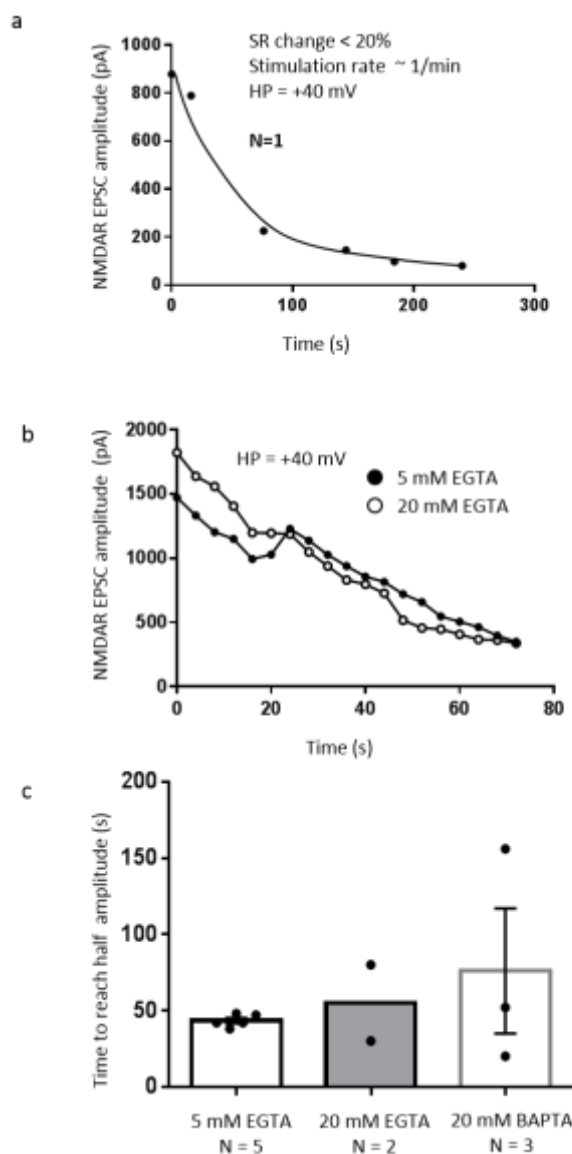


**Fig 3.13. Run-down in amplitude is not caused by increased SR, and is not prevented by calcium buffering.** NMDAR EPSCs were recorded from LSO principal neurons. The neurons were held at -70 mV during pharmacological isolation of NMDAR EPSCs (addition of 1  $\mu$ M strychnine, 10  $\mu$ M bicuculline and 10  $\mu$ M NBQX) for 3-5 mins. **a.** NMDAR EPSC amplitudes are plotted over time, using 5 mM EGTA patch solution. At time 0 on graph, the HP was increased to +40 mV whilst the cell was stimulated approx. once per min. Time to reach half initial amplitude = ~ 60 secs. SR did not alter by more than 20% during recording. Mouse age = P14. **b.** Comparison of NMDAR EPSC amplitudes over time from 2 representative LSO principal neurons, 1 recorded with 5 mM EGTA in the pipette solution (closed circles) (P11), and the other with 20 mM EGTA in the pipette solution (open circles) (P12). Neurons were stimulated at a rate of 0.25 Hz whilst being held at HP -70 mV for a minimum of 3 mins during drug application. The HP was increased to +40 mV at time 0 on the graph. Time to reach half initial amplitude for 5 mM and 20 mM EGTA conditions were 48 secs and 30 secs respectively. **c.** Comparison of NMDAR amplitude run-down between LSO neurons patched using 5 mM EGTA (left), 20 mM EGTA (middle) or 20 mM BAPTA (right) in the patch solution. Time to reach half the initial amplitude is plotted for each. 5 mM EGTA =  $43.4 \pm 1.8$  secs (mean  $\pm$  SEM), n = 5, (P10-P26), 20 mM EGTA = 55 secs, n = 2 (80 secs and 30 secs, 2 mice (P10 & P11) & 20 mM BAPTA =  $76 \pm 41.1$  secs, n = 3, (2 mice, P16). Filled circles indicate individual data points.

### 3.3 DISCUSSION

In this chapter, I have examined the synaptic excitability of LSO principal neurons in brainstem slices from normal hearing CBA/Ca mice. We must understand normal synaptic function of LSO principal neurons to identify any changes following damaging levels of noise (chapter 5). Firstly, I had to reliably distinguish LSO principal neurons from LOC neurons, the latter of which form part of the efferent system. This was possible by comparing their voltage activated currents and AP characteristics. I then recorded both IPSCs and EPSCs in LSO principal neurons, and examined the decay kinetics. The main findings were:

- AMPAR EPSCs and glycinergic IPSCs decay taus converge to sub millisecond kinetics by P17.
- NMDAR EPSCs also show developmental acceleration of decay  $\tau$  to  $\sim 2\text{-}3$  ms by  $\sim P14$ . This is faster than any other NMDAR EPSC decay  $\tau$  reported in the literature.
- NMDAR EPSCs show rapid, irreversible depression of amplitude at positive holding potentials. Preliminary results suggest this depression is not  $\text{Ca}^{2+}$  mediated.

LSO principal neurons and LOC neurons have distinct voltage activated currents and AP characteristics:

LSO principal neurons and LOC neurons can be identified by their distinct electrophysiological characteristics. Here, LSO principal neurons responded to depolarising current injections with either a single-spiking firing pattern ( $\leq 3$  APs) or a multi-spiking firing pattern (5 to  $\sim 100$  APs) consistent with previous findings (Barnes-Davies et al., 2004, Sterenborg et al., 2010). Both single and multi-spiking principal neurons have similar AP characteristics and membrane properties (table 3.1). Consequently, the 2 principal neuron types were grouped together for subsequent analysis. In contrast, LOC neurons always respond with a multi-firing AP firing pattern.

LSO principal neurons responded to depolarising current injections with APs of short half width ( $\sim 0.3$  ms), which were time locked to the stimulus onset. In contrast LOC neurons exhibit a delay before the first elicited AP, thus are often termed 'delay

neurons' in earlier literature (Adam et al., 1999b). They exhibited slower half width (0.7 ms), and larger amplitude compared to principal neurons, both of which have not been explicitly stated in the literature.

Single-spiking principal neurons are prevented from firing a train of APs due to the presence of Kv1 channels (low voltage activated  $K^+$  channels). When these channels are specifically blocked using DTX-I, LSO principal neurons revert to a multi-spiking AP firing pattern (Barnes-Davies et al., 2004). In the same study, more single-spiking neurons (and Kv1 channels) found in the low frequency lateral limb of the LSO, and more multi-spiking neurons in the medial limb (in rats) (Barnes Davies 2004). I observed a similar pattern (fig 3.4), although n numbers were low. It is postulated that high numbers of single-spiking neurons in the low frequency lateral limb is due to the need for greater temporal precision, which would help in preserving timing information (Svirskis et al., 2002).

LOC neurons can be divided into 2 subtypes: small intrinsic LOC neurons (distributed throughout the LSO) & large LOC neurons which are restricted to the outer shell of the LSO (Azeredo et al., 1999). Each utilize different neurotransmitters (Darrow et al., 2006), and may have opposing effects on excitability at its target neuron (Type I SGN neurons under IHCs) (Groff and Liberman, 2003).

Surprisingly, I have observed large LOC neurons distributed throughout the LSO (fig 3.4), as measured by WCC (fig 3.7, a). Here, I was attempting to patch LSO principal neurons, and consequently patched large LOC neurons. Thus, the WCC of LOC neurons is likely biased towards the large population of LOC neurons, as I deliberately targeted large cell bodies. This is the first time large LOC neurons have been reported to be distributed throughout the LSO, and not just in the outer shell. It is not possible to establish whether previous studies have underestimated intrinsic LOC neuron size, or whether my recordings reflect a separate population large LOC neurons. Either way, the electrophysiological properties of both large LOC neurons recorded here, and smaller intrinsic neurons from previous studies are similar, and distinct from principal neurons, enabling reliable identification.

Principal neurons and LOC neurons also display markedly different responses under voltage clamp, which have previously been documented using rats (Barnes-Davies et al., 2004, Adam et al., 1999b, Fujino et al., 1997, Adam et al., 2001) and mice (Sterenborg et al., 2010). LOC neurons show a fast transient outward  $K^+$  current ( $I_A$ ) in response to depolarising voltage steps, whilst principal neurons (both single and multi-spiking) do not (fig 3.1 a & b). Conversely, when hyperpolarised, LSO principal neurons show a slowly activating inward  $I_H$  current mediated by HCN channels, whilst LOC neurons do not (fig 3.1 c & d). In addition, I found LOC neurons have a less negative RMP of -44.18 mV (fig 3.7, d), in contrast to previous observations in rats : -64 mV for identified LOC neurons (Fujino et al., 1997) and -61 mV for 'delay' neurons (Adam et al., 1999b). However, a study performed using CBA/Ca mice by Sterenborg et al (2011) showed near identical RMP in LOC neurons (-44.5 mV), and thus the difference may be species related, or perhaps due to differences in  $Cl^-$  levels in the patch pipette solution.

In conclusion, I have shown LSO principal neurons and LOC neurons exhibit vastly different AP characteristics and voltage activated currents, enabling easy identification. These observations are consistent with previous literature. Furthermore, I have identified APs in LOC neurons are around double the amplitude and half width of LSO principal neurons APs (fig 3.6). I have also demonstrated that large LOC neurons are distributed throughout the LSO, and not just at around the outer perimeter (shell) as previously thought.

EPSCs and IPSCs show developmental acceleration of decay tau

Once I was able to reliably identify principal neurons, I recorded both IPSCs and EPSCs from LSO principal neurons. EPSCs from pre-hearing mice showed a classic dual component EPSC, composed of fast AMPAR EPSCs and slower NMDAR EPSCs (fig 3.8, c) (Forsythe and Westbrook, 1988). AMPAR EPSC and glycinergic IPSC decay  $\tau$  showed developmental acceleration, so that by P17, both were  $\leq 1$ ms (fig 3.10, a & b).

### AMPA EPSC decay tau acceleration

Age dependent acceleration of AMPAR EPSC decay  $\tau$  has previously been observed in the MNTB, where a shift from slow to fast kinetics has been attributed to a shift from GluA1 to GluA3/4 dominance (Joshi et al., 2004). Similarly, qRT PCR using mouse LSO tissue showed levels of GluA1 and GluA2 remain relatively constant from ~P7 to ~P36. However there is then a significant increase in GluA3 and GluA4 mRNA, with the latter dominating in the LSO by P17-23 (Pilati et al., 2016).

Of course, high expression of mRNA does not necessarily correlate with high expression of protein. In support of the mRNA evidence, immunohistochemistry studies in the rat SOC have revealed GluA1 and GluA2 protein were present during the first two postnatal weeks, but then rapidly declined in the third. This decline in GluA1/2 was accompanied by an increase in GluA4 (Caicedo and Eybalin, 1999, Knipper et al., 1997).

The importance of GluA4 for fast synaptic transmission in the auditory brainstem has been demonstrated using GluA4 KO mice. Yang et al (2011) found the decay  $\tau$  of AMPAR EPSCs and mEPSCs in MNTB neurons from GluA4 KO mice were significantly slower compared to WT. However, EPSCs measured from GluA3 KO mice showed a similar time course to WT. Thus, it is likely GluA4 is vital for fast synaptic transmission in nuclei of the SOC.

### IPSC decay tau acceleration

During maturation, LSO neurons lose approximately 75% of their synapses with the MNTB, whose loss is compensated by a 12 fold strengthening of remaining synapses (Kim and Kandler, 2010). In parallel, there is a shift from hyperpolarising GABA/glycinergic IPSCs to depolarising glycinergic transmission (Lim et al., 2000, Ehrlich et al., 1999). Here we observed an acceleration of IPSC kinetics from ~2-3 ms to  $\leq 1$  ms by P17. This is consistent with other reports of fast glycinergic transmission, which report decay time constants of ~1 ms (Jonas et al., 1998, Smith et al., 2000, Lu et al., 2008). The acceleration in the time constant is preceded by a change in glycine receptor subunit composition, from predominantly GlyR $\alpha$ 2 to GlyR $\alpha$ 1 in mature

animals (Becker et al., 1988, Malosio et al., 1991, Takahashi et al., 1992), the latter of which is associated with fast kinetics (Lynch, 2009).

In summary, AMPAR EPSCs and glycinergic IPSCs converge to sub-millisecond kinetics by P17. Fast matched kinetics of EPSCs and IPSCs are important for accurately encoding ILD cues (Tollin, 2003). In cases of mismatched kinetics, ILD performance is lowered (Pollak, 1988, Park et al., 1996a, Park et al., 2004). For example, in young animals (P12-P17), ILD processing is skewed towards the ipsilateral ear, where inhibition is more effective than excitation (Sanes and Rubel, 1988). Similarly, computer modelling has shown the slow kinetics and large amplitudes of IPSCs at hearing onset shift ILD function towards the ipsilateral ear (Pilati, 2016).

#### NMDAR mediated EPSCs exhibit rapid acceleration upon maturation

LSO principal neuron NMDAR EPSCs from pre-hearing (P8-9) mice show typically slow decay kinetics, with the majority exhibiting bi-exponential decay ( $\tau_{fast} = \sim 45$  ms &  $\tau_{slow} = \sim 115$  ms). EPSC I/Vs show depressed currents at negative HPs in the presence of  $[Mg^{2+}]_o$ , and currents could be abolished by addition of d-AP5, consistent with previous reports of NMDAR EPSCs (Nowak et al., 1984, ChesnoyMarchais and Barthe, 1996). Extreme acceleration of decay  $\tau$  then occurred upon maturation, so that by P14, NMDAR EPSCs decay  $\tau$  were  $\sim 2$ -3 ms ( $\tau_{fast}$ ). Moderate acceleration of NMDAR EPSCs has previously been observed in other areas of the brain, such as the thalamo-cortical synapses, which accelerate to 50 ms by P27 (Barth and Malenka, 2001). Similarly, NMDAR EPSC decay kinetics of cerebellar granule cells from WT mice accelerate from  $\tau_{fast}$  57.3 ms in (P7-P9) to  $\tau_{fast}$  35.7 ms (P21-P24) (Takahashi et al., 1996). In the same study, the slow decay component ( $\tau_{slow}$ ) was reduced from 43% (P7-P9) to 23% (P21-P24) of the total current amplitude. In my study, a more extreme reduction in the slow NMDAR EPSC decay was observed in LSO principal neurons, which was reduced from 34% (P8-P9) to just 9% (P23-P25) of the total current amplitude (fig 3.11).

In the SOC, developmental acceleration of NMDAR EPSCs has previously been reported in the MNTB in mice and rats (Steinert et al., 2010), where decay time constants accelerated to  $\sim 15$  ms upon maturation, with adult dominance of GluN2C. These were

some of the fastest NMDAR EPSCs ever published. However, the NMDAR EPSC decay kinetics observed here in the LSO are even faster, and are closer to that the GluA1 dominated AMPAR EPSCs observed in pre-hearing mice. Consequently, NMDAR EPSCs in the LSO may have been mistaken for AMPAR EPSCs previously. GluN2C dominated in the LSO following hearing onset (similar to the MNTB), which may underlie the fast kinetics observed here (chapter 5, fig 5.15, d).

In summary, NMDAR EPSC decay kinetics in LSO principal neurons undergo extreme acceleration to just 2-3 ms by P14, which is accompanied by a switch to GluN2C dominance. These are the fastest NMDAR EPSCs ever reported. Further work is needed to uncover the specific properties of the NMDARs, to uncover how they mediate EPSCs of such rapid kinetics.

#### NMDAR EPSCs exhibit rapid, irreversible run-down of EPSC amplitude

Amplitude of NMDAR EPSCs recorded from LSO principal neurons rapidly declined when held at positive HPs, so that amplitude was halved after ~45 secs (fig 3.12 & 3.13). Run-down in amplitude was not recoverable, remaining low even after 5 minutes at HP -70 mV. In contrast, run-down did not occur in NMDAR EPSCs recorded from pre-hearing mice, which have slower decay kinetics. NMDARs are permeable to  $\text{Ca}^{2+}$ , (Lynch et al., 1983, Malenka et al., 1988), and thus activity dependent run-down can limit the amount of  $\text{Ca}^{2+}$  entering the cell, and prevent excitotoxicity (Hardingham and Bading, 2010). This involves both changes in channel open probability and/or changing the number of NMDARs on the cell surface (Tong et al., 1995).

$\text{Ca}^{2+}$  mediated reduction in NMDAR activity has been observed in other areas of the brain. In SNc dopaminergic neurones, activity dependent NMDAR EPSC run-down was slowed by addition of 10 mM BAPTA ( $\text{Ca}^{2+}$  chelator) in the pipette solution (Wild et al., 2014). Similarly, here I have attempted to assess whether run-down in NMDAR EPSCs in LSO principal neurons is  $\text{Ca}^{2+}$  mediated by increasing levels of the calcium chelators EGTA (20 mM) or the faster acting BAPTA (20 mM) in the intracellular pipette solution. Preliminary results showed increased EGTA or BAPTA did not prevent run-down in amplitude (fig 3.13), although results were highly variable, and thus difficult to

interpret. Rapid run-down still occurred with high EGTA or BAPTA, suggesting it is not  $\text{Ca}^{2+}$  mediated, or only partly mediated by  $\text{Ca}^{2+}$ . Furthermore, stimulation at just once per minute (instead of 0.25 Hz) did not reduce the run-down, suggesting run-down is not activity mediated ( $n = 1$ ).

Calcium independent NMDAR-EPSC run-down has been observed in cell lines expressing GluN1/GluN2A heteromers, where tyrosine dephosphorylation reduced the number of functioning channels (Vissel et al., 2001). Similarly, GluN2B containing NMDARs undergo tyrosine dephosphorylation, reducing the number of receptors at the membrane (Zhang et al., 2008a). However, in the LSO, GluN2B mRNA levels decrease upon maturity concomitant with an increase in GluNC mRNA (chapter 5, fig 5.15). Thus, it seems likely that the rapid run-down of NMDAR EPSCs observed in mature LSO neurons is associated with a switch in subunits to GluN2C. Whilst there has been much investigation into GluN2B modulation (Roche et al., 2001, Lavezzari et al., 2004, Zhang et al., 2008b), presently little is known about GluN2C.

Clearly further work is needed to uncover the mechanisms of NMDAR EPSC run-down in LSO principal neurons, which could form the basis of an entire project. Preliminary work to uncover the mechanism by increasing calcium chelators in the patch pipette solution produced highly inconsistent results. Further experiments that could uncover the run-down mechanism include:

- Is the NMDAR run-down activity dependent? Here the run-down with and without the presence of external  $\text{Mg}^{2+}$  at HP -70 mV could be measured. NMDARs are usually blocked by external  $\text{Mg}^{2+}$  at negative HPs, thus any run-down at -70 mV would suggest NMDARs are regulated by activity.
- Is NMDAR run-down voltage dependent? Compare NMDAR run-down in  $\text{Mg}^{2+}$  free aCSF (as above) with run-down observed at +40 mV to observe whether it is voltage dependent.
- Is run-down caused by tyrosine phosphorylation? A tyrosine phosphatase blocker could be included in the patch pipette, which should slow/abolish run-down.

## Summary

Throughout this chapter, I have demonstrated I can identify LSO principal and LOC neurons based on their distinct voltage activated currents and AP characteristics. Furthermore, I have identified APs from LOC neurons have much larger amplitudes and longer half widths, both of which have not been explicitly stated in the literature. Next, I showed AMPAR EPSC and glycinergic IPSC decay kinetics converge to  $\leq 1$  ms by P17. Meanwhile, NMDAR EPSCs decay  $\tau$  showed an extreme acceleration in decay  $\tau$ , from  $\sim 45$  to 2-3 ms ( $\tau_{fast}$ ). This is faster than any NMDAR EPSCs published in the literature. Finally, I observed run-down of NMDAR EPSC amplitude in LSO principal neurons expressing NMDARs with fast 'mature' decay kinetics. I attempted to uncover whether this run-down was  $Ca^{2+}$  mediated by increasing  $Ca^{2+}$  chelators in the pipette solution, however results were highly variable and difficult to interpret.

Here, we can conclude mature decay kinetics of IPSCs and EPSCs are not reached until P17. Thus, going forward, AOE experiments were conducted mice P17 or over.

## 4 INTRINSIC EXCITABILITY IN THE AUDITORY BRAINSTEM: KV3 IN THE LSO AND MNTB

---

In the previous chapter, I examined the synaptic currents of LSO principal neurons from CBA/Ca mice under normal conditions (no prior AOE). In this chapter, I will assess normal intrinsic excitability of LSO principal and MNTB neurons. This will allow me to identify any changes following AOE (chapter 5). A key determinate of neuronal excitability are the characteristics of the voltage-gated K<sup>+</sup> channels it possesses (Hille, 2001). A major controller of excitability in the ascending auditory pathway are the Kv3 subfamily of VG K<sup>+</sup> channels (Wang et al., 1998, Macica et al., 2003, Song et al., 2005, Brown and Kaczmarek, 2011), which only activate at voltages reached when an AP is fired (~20 mV) (Rudy et al., 1999). Their fast kinetics facilitate high frequency firing, by rapidly activating and deactivating to produce APs of a brief duration and a limited refractory period (Johnston et al., 2010).

Kv3 channels are expressed throughout the ascending auditory pathway, enabling fast processing of sound information, required for ILD processing (Brown and Kaczmarek, 2011). The channels are tetrameric, and can be made up of any combination of subunits (Kv3.1:Kv3.4) including splice variants (Rudy and McBain, 2001, McIntosh et al., 1998). Whilst it is known Kv3 channels are highly expressed in the SOC, the subunit composition of the channels is unknown. Here we have used qRT PCR and immunohistochemistry to assess Kv3 subunit mRNA and protein expression in the SOC respectively. I have then recorded voltage-activated currents and APs from GM mice lacking either Kv3.1 or Kv3.3, to assess which Kv3 subunits contribute to Kv3 mediated current in both the LSO and MNTB.

### Kv3.1 and Kv3.3 mRNA dominate in the SOC

Previously in the lab, Susan Robinson performed qRT PCR on three nuclei of the SOC: MNTB, SPN and LSO extracted from a CBA/Ca mouse (P13), using antibodies (Ab) directed towards Kv3.1a, Kv3.1b, Kv3.2, Kv3.3 and Kv3.4. The results showed that Kv3.1b mRNA and Kv3.3 mRNA dominate across the whole of the SOC (MNTB, SPN and

LSO), whilst Kv3.1a, Kv3.2 and Kv3.4 levels are negligible (fig 4.1). Here, mRNA levels were normalised to the house keeping gene  $\gamma$  actin, and are expressed as percentage of total Kv3 subunit mRNA. There exist reciprocal gradients across the SOC, with relative Kv3.1 mRNA higher in the MNTB and reduced the lateral regions, whilst relative Kv3.3 mRNA is higher in the LSO, and reduced in medial regions.

Figure 4.1 Kv3.1 and Kv3.3 mRNA dominate in the SOC

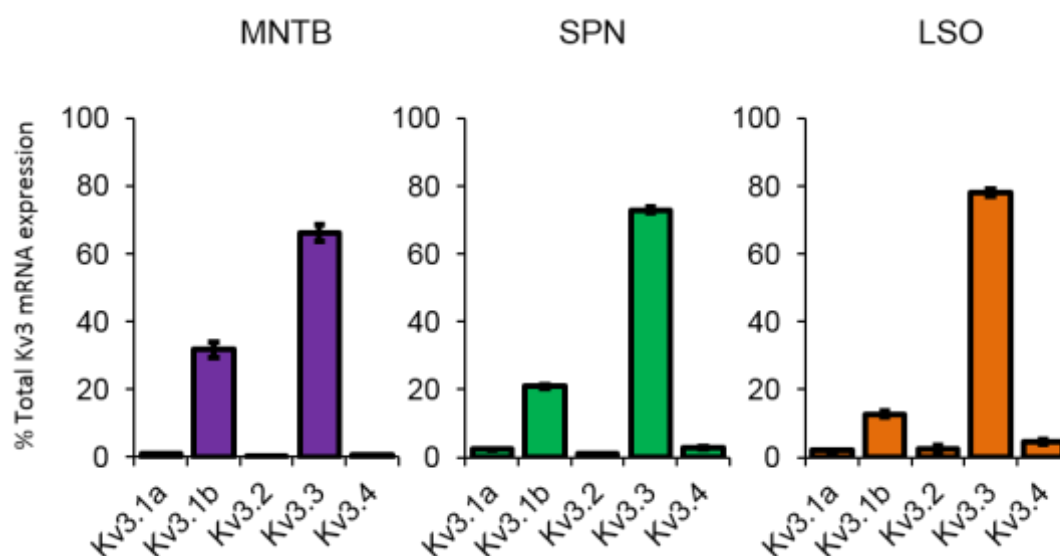


**Fig 4.1. Kv3.1 and Kv3.3 mRNA dominate in the SOC.** qRT PCR of each Kv3 subunit (Kv3.1a, Kv3.1b, Kv3.2, Kv3.3 & Kv3.4) using tissue of each nuclei of the SOC (MNTB, SPN and LSO) isolated by PALM laser microdissection from a CBA/Ca mouse (P13). Data is normalised to  $\gamma$  actin and expressed as percentage of total Kv3 subunit mRNA. Data collected and analysed by Susan Robinson.

#### Kv3.1 and Kv3.3 protein is present across the whole SOC

Immunohistochemistry was used to establish whether high levels of Kv3.1b and Kv3.3 mRNA in the SOC are translated into protein. The specificity of each antibody (Kv3.1 Ab and Kv3.3 Ab) was previously verified in the lab by Susan Robinson, using coronal sections (12  $\mu$ m) from KO mice lacking either Kv3.1 or Kv3.3 (fig 4.2). Here, Kv3.1 Ab staining (top) in the MNTB were compared between CBA/Ca (top, left) and a Kv3.1 KO mouse (top, right). Similarly, Kv3.3 Ab staining was compared in the MNTB between

CBA/Ca mice (bottom, left) and Kv3.3 KO mouse (bottom, right). Neither Ab is visible in the corresponding KO mouse. We can conclude that Kv3.1 Ab and Kv3.3 Abs are specific to their target protein.

*Figure 4.2 Verifying specificity of Kv3.1 and Kv3.3 Abs using knockout mice*

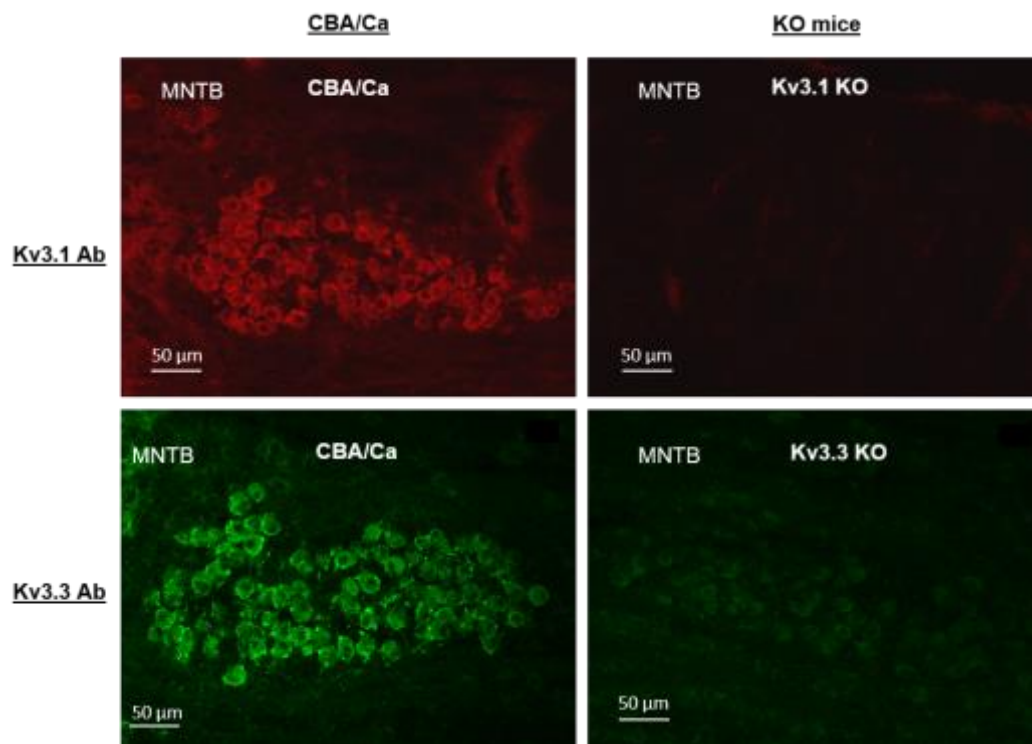


**Fig 4.2. Verifying specificity of Kv3.1 and Kv3.3 Abs using knockout mice.** Kv3.1 Abs and Kv3.3 Abs were verified in coronal sections of brainstem (12 µm) containing the MNTB from a CBA/Ca mice (left) and either Kv3.1 KO (top right) and Kv3.3 KO (bottom right). Kv3.1 Ab (dilution 1:1000) was used in conjunction with secondary antibody AlexaFluor 488 goat anti-rabbit IgG (1:1000) (red, top) whilst Kv3.3 Ab (1:3000) was used together with AlexaFluor 546 goat anti-mouse IgG (1:1000) (green, bottom). Data collected by Susan Robinson

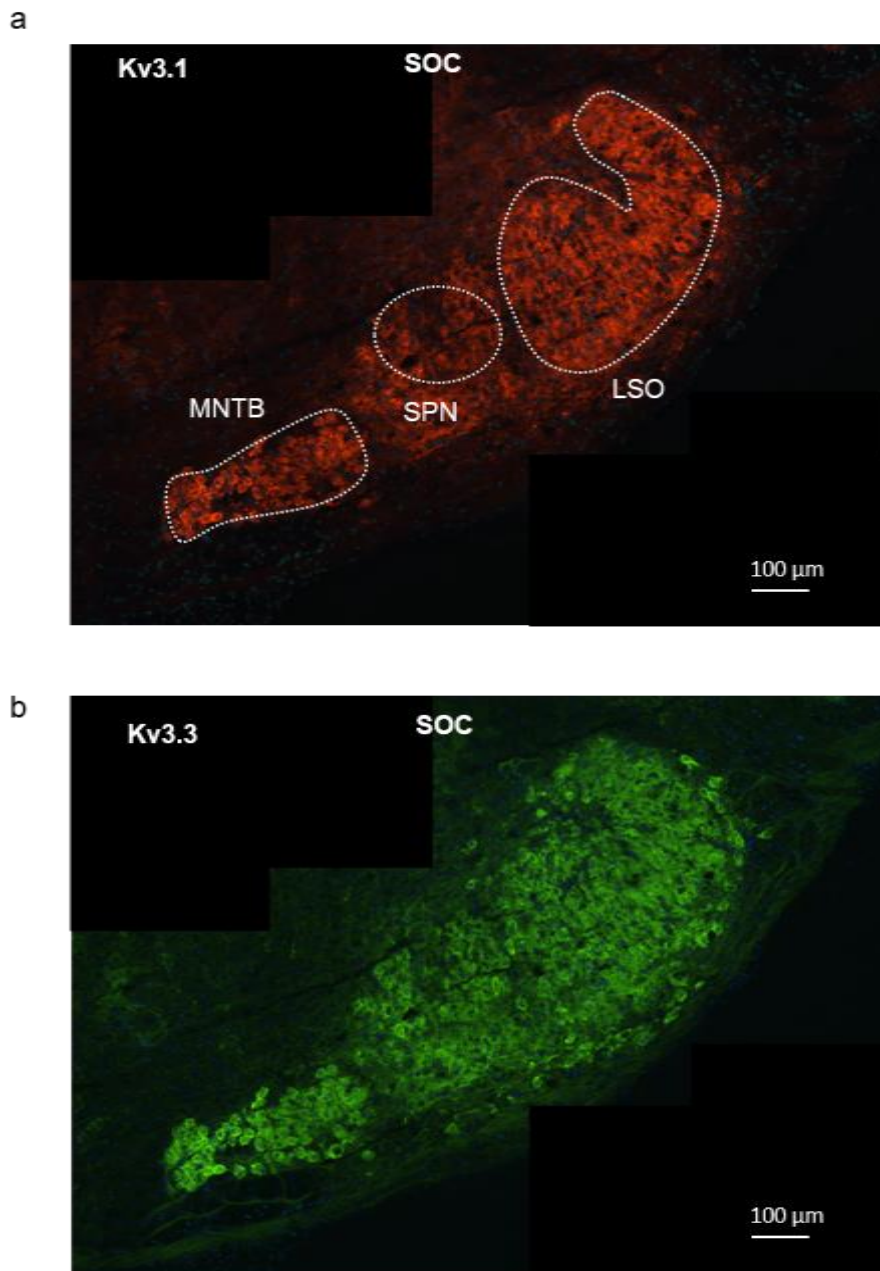
Figure 4.3 shows a representative coronal section (12  $\mu\text{m}$ ) of the SOC from a CBA/Ca mouse (P16) co-stained with Kv3.1b Ab (red) (a) and Kv3.3 Ab (green) (b). Both are stained with DAPI (blue) to visualize nuclei of the cell bodies. Kv3.1b and Kv3.3 are clearly visible in each nuclei of the SOC (LSO, SPN & MNTB), which are outlined in white dashed lines, and labelled in part (a).

The distribution of Kv3.1 and Kv3.3 at a higher magnification (X40) were then examined in both the LSO and MNTB in the same brainstem section, to determine whether the subunits are expressed at the cell membranes (a necessity for functioning Kv3 channels) (fig 4.4). Membrane staining was visualized as a brighter band of staining which defines the perimeter of the cell.

Figure 4.4 shows Kv3.1 staining (red, left) in MNTB (top) and LSO (bottom) and Kv3.3 staining (green, right) in the same area of MNTB (top) and LSO (bottom). In the MNTB, there was clear staining in the cell membranes of both Kv3.1 and Kv3.3. Likewise, in the LSO, Kv3.3 staining was observed in the cell membranes (as indicated by white arrows). In contrast, Kv3.1 does not appear to be in the cell membranes but is instead heavily prevalent in the neuropil.

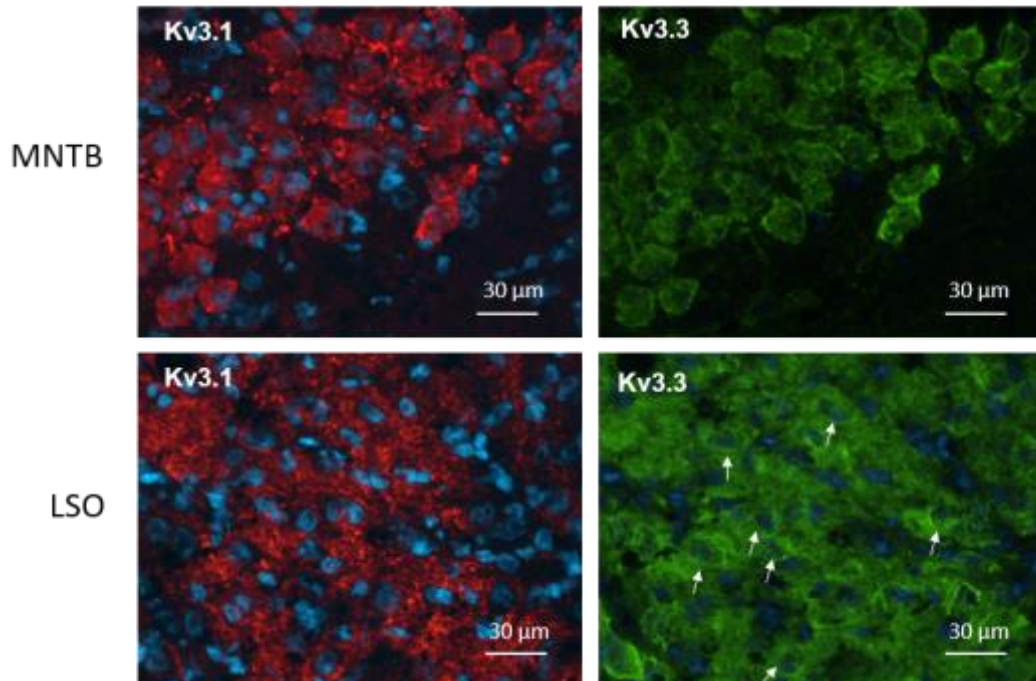
To examine the distribution of Kv3.1 in the LSO in more detail, a brainstem section from a different CBA/Ca mouse (P16) was stained using Kv3.1 Ab only, and was imaged using a confocal microscope (imaging was performed by Dr Joshua Smalley) (fig 4.5). Again, Kv3.1 clearly stains the MNTB cell bodies themselves, and possibly the calycal inputs and/or axon initial segments. However, in the LSO, it is confirmed there is no Kv3.1 staining of the LSO cell bodies, and bright staining of the neuropil.

Figure 4.3 Kv3.1 and Kv3.3 protein is present across the whole SOC



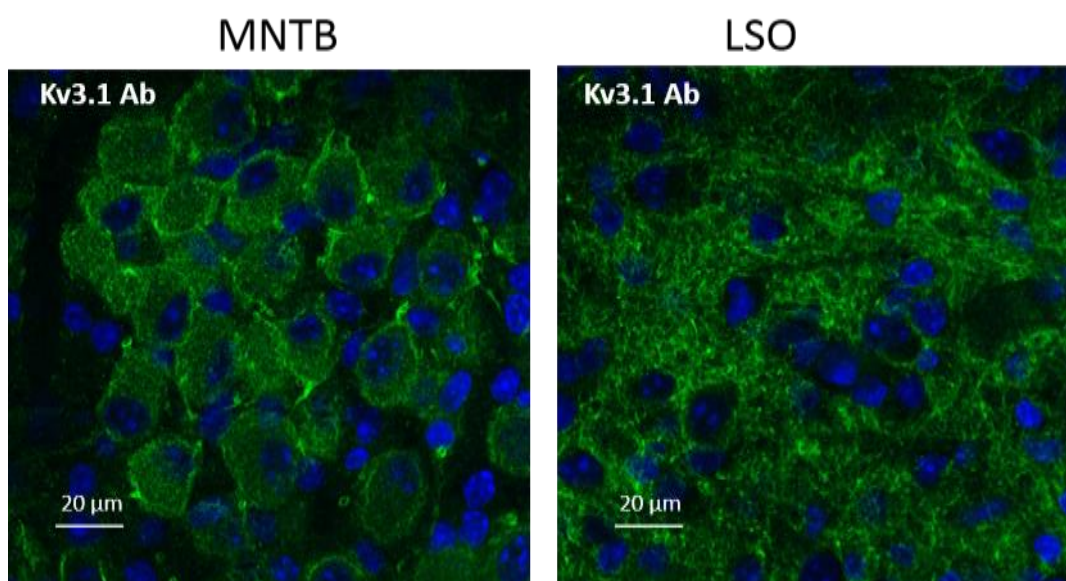
**Fig 4.3. Kv3.1 and Kv3.3 protein is present across the whole SOC.** **a.** Kv3.1 primary Ab (diluted 1:1000) was applied to 12 μm coronal sections of brainstem containing the SOC from a CBA/Ca mouse (P16). Secondary antibody = AlexaFluor 546 goat anti-mouse IgG (1:1000). Nuclei of the SOC (MNTB, SPN and LSO) are highlighted in white. **b.** Kv3.3 primary Ab (1:3000) applied to the same section as in (a). Secondary antibody: Alexafluor 488 goat anti-rabbit IgG (1:1000). DAPI staining of cell nuclei appears in blue. Each image (**a&b**) is a composite of three separate images, mounted on a black background.

Figure 4.4 High magnification view of Kv3.1 and Kv3.3 in the MNTB and LSO



**Fig 4.4. High magnification view of Kv3.1 and Kv3.3 in the MNTB and LSO.** 12  $\mu\text{m}$  coronal sections of brainstem containing the SOC from a CBA/Ca mouse (P16) were co-stained with primary Abs anti-Kv3.1 (diluted 1:1000) and anti-Kv3.3 (1:3000), with secondary Abs AlexaFluor 546 goat anti-mouse IgG (1:1000) (green) and Alexafluor 488 goat anti-rabbit IgG (1:1000) (red) respectively. High magnification images (X40) were acquired in the same areas of the LSO and MNTB, using different excitation filters to visualize either Kv3.1 or Kv3.3. DAPI staining of cell nuclei appears in blue.

*Figure 4.5 Kv3.1 is located in MNTB cell membranes, but is only present in LSO neuropil*



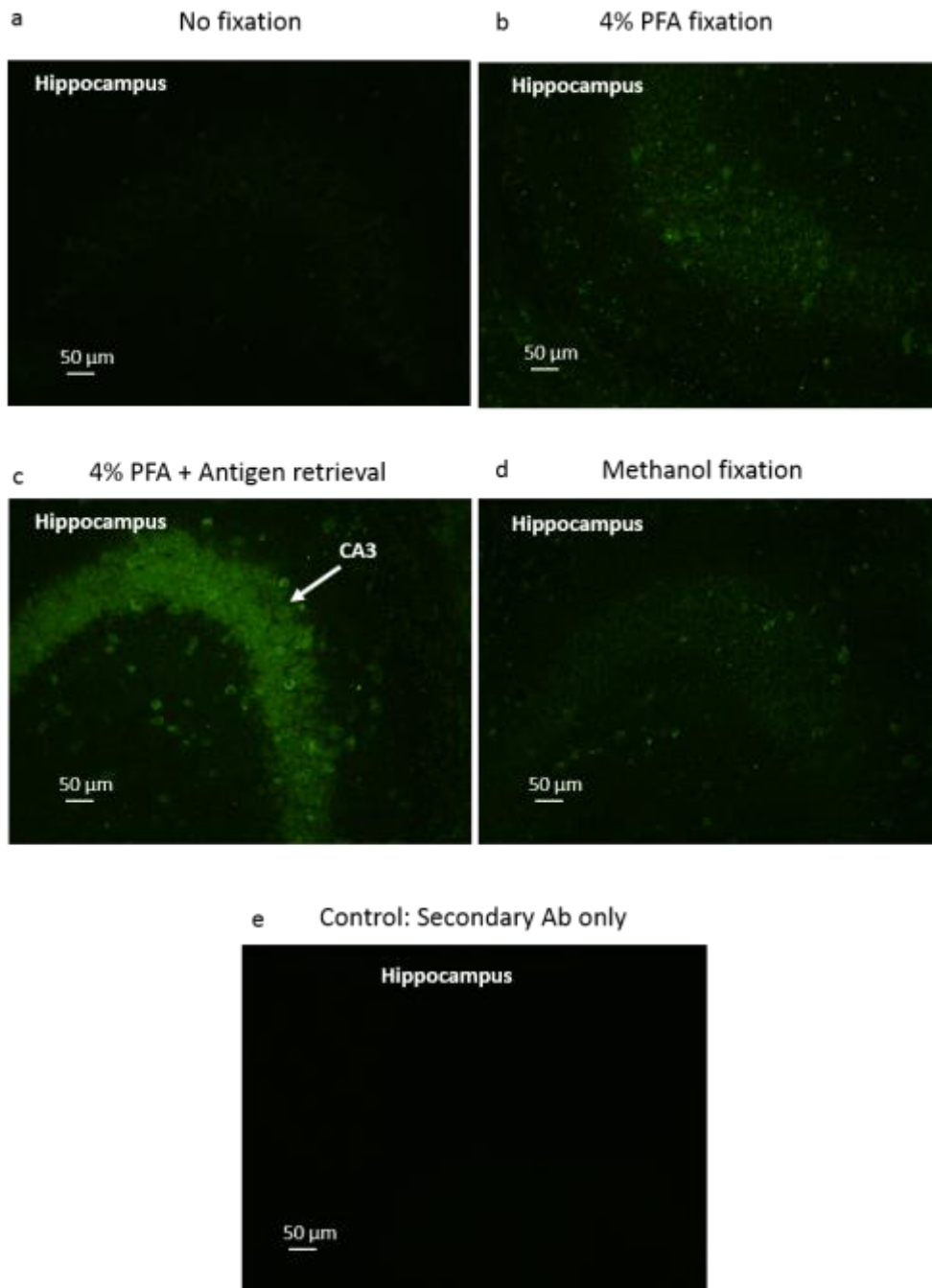
**Fig 4.5. Kv3.1 is located in MNTB cell membranes, but is only present in LSO neuropil.** Confocal images of the MNTB and LSO from the same brainstem section stained with Kv3.1 Ab (dilution 1:1000). Secondary antibody = Alexafluor 488 goat anti-mouse (1:1000). Section was taken from a CBA/Ca mouse

#### Establishing optimum conditions for Kv3.2 and Kv3.4 antibodies

It is clear both Kv3.1 and Kv3.3 protein are abundant in the SOC, as predicted by the high levels of mRNA. Despite very low levels of Kv3.2 and Kv3.4 mRNA in the SOC, it was necessary to establish whether there was any translation to protein using immunohistochemistry. Protocols for both Kv3.3 & Kv3.1 Abs have previously been established within the lab, and verified using KO mice (fig 4.2). In contrast, Kv3.2 Ab and Kv3.4 Ab were bought in new, and thus optimum test conditions for these Abs were unknown. To address this, a test matrix for each Ab was performed using adjacent coronal sections of CBA/Ca mouse brain (P15) containing the hippocampus, which is known to express both target proteins (for method see chapter 2, section 2.7). Specifically, Kv3.2 is prominent in the CA3 region, and Kv3.4 is found in the dentate gyrus (DG) (Rudy et al., 1999). Figure 4.6 shows the results of a Kv3.2 Ab test matrix, for each

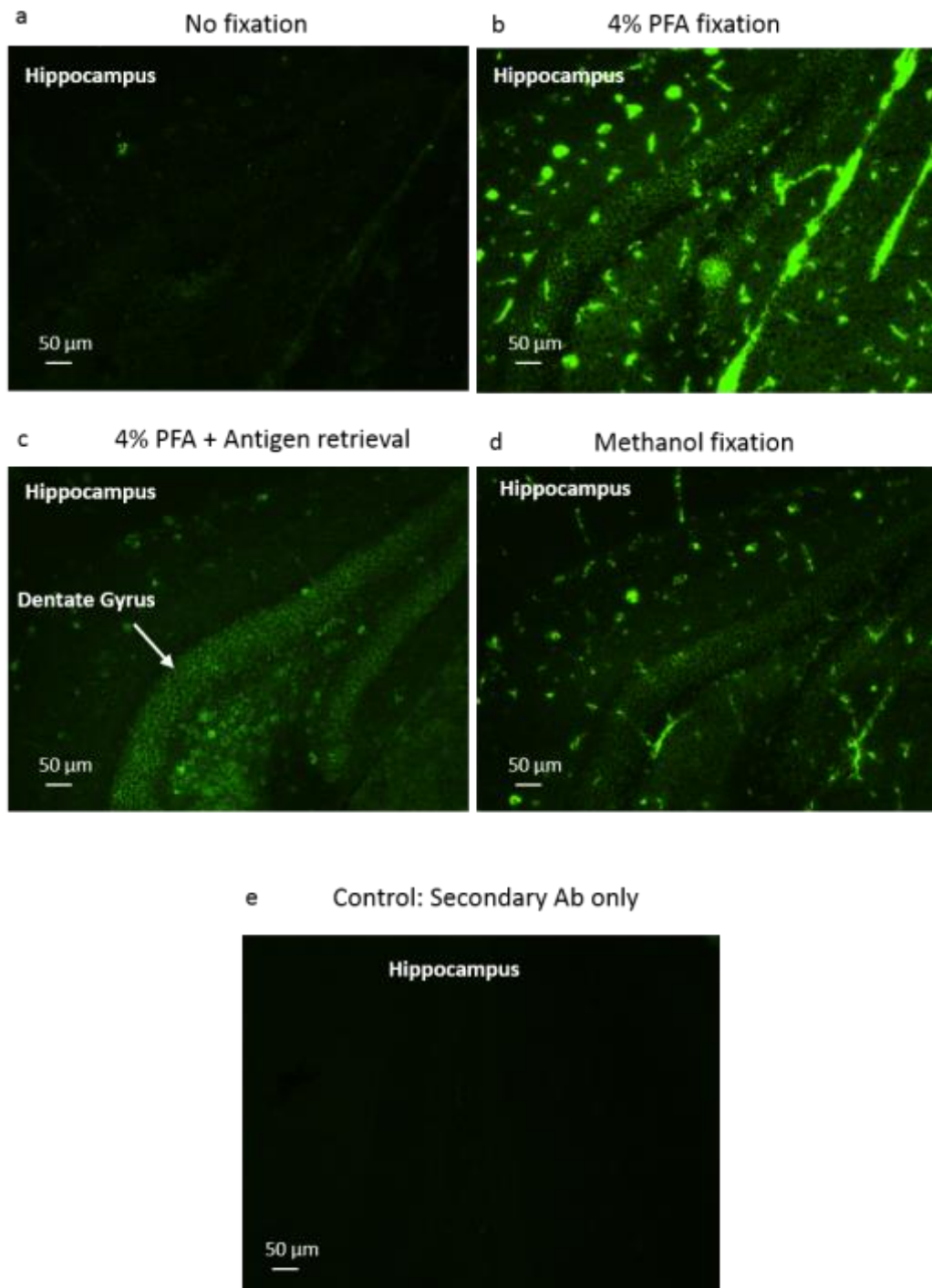
fixation condition tested: (a) no fixation, (b) 4% PFA fixation, (c) 4% PFA with antigen retrieval and (d) methanol fixation. The clearest and brightest staining for Kv3.2 could be seen when using 4% PFA fixation with antigen retrieval (fig 4.6, c). A test matrix for Kv3.4 Ab was also performed on separate adjacent sections of the hippocampus (Fig 4.7), which focused on staining of the DG. Again, 4% PFA with antigen retrieval produced the clearest staining (fig 4.7, c). Thus, going forward 4% PFA with antigen retrieval was used for both Kv3.2 and Kv3.4 Abs.

Figure 4.6 Test Matrix for Kv3.2 Ab.



**Fig 4.6. Test Matrix for Kv3.2 Ab.** Four fixation conditions were applied to adjacent coronal sections of the hippocampus (12 μm) from CBA/Ca mouse brain (P15). **a.** No fixation. **b.** 4% PFA fixation. **c.** 4% PFA + antigen retrieval. **d.** Methanol fixation. Kv3.2 Ab was diluted 1:500, and used in conjunction with secondary antibody goat-anti-rabbit IgG, Alexa Fluor 488. Images were acquired from the same position in the brain (CA3 hippocampus), with equal adjustment of brightness and contrast, to enable comparison. **e.** Secondary Ab only (no primary antibody).

Figure 4.7 Test Matrix for Kv3.4 Ab



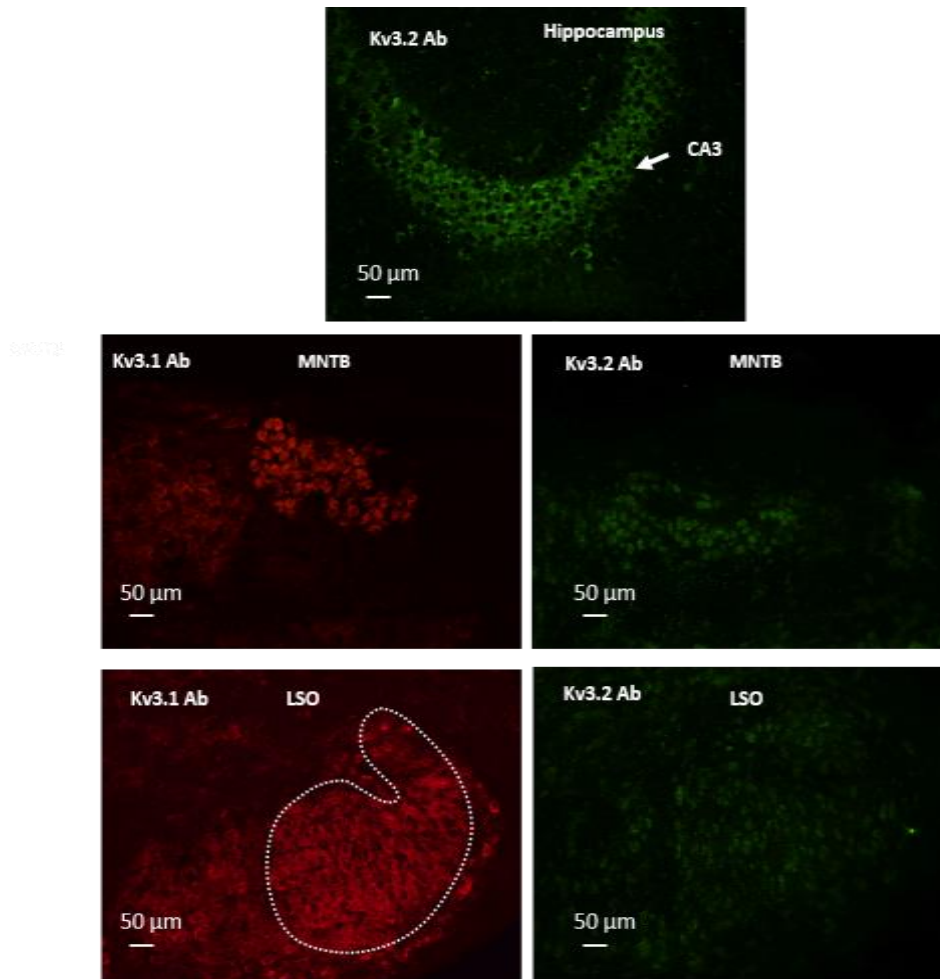
**Fig 4.7. Test Matrix for Kv3.4 Ab.** Four fixation conditions were applied to adjacent coronal sections of the hippocampus (12 μm) of CBA/Ca mouse brain (P15). **a.** No fixation. **b.** 4% PFA fixation **c.** 4% PFA + antigen retrieval. **d.** Methanol fixation. Kv3.4 Ab was diluted 1:500, and used in conjunction with secondary antibody Goat-anti-mouse IgG, Alexa Fluor 488. Images were acquired from the same position in the brain (Dentate gyrus, hippocampus), with equal adjustment of brightness and contrast, to enable comparison. **e.** Secondary Ab only (no primary antibody).

### Kv3.2 and Kv3.4 Ab staining is inconclusive in the SOC

Next, I assessed if Kv3.2 protein is expressed in the SOC. Here, I stained adjacent sections of the SOC with either Kv3.1 Ab (red) or Kv3.2 Ab (green), (fig 4.8). In addition, a section containing the hippocampus was stained with Kv3.2 to act as a positive control. Typical Kv3.1 staining was observed in the SOC, where Kv3.1 is located in the cell bodies of the MNTB (top left) but in the neuropil of the LSO (bottom left). There was some low level Kv3.2 staining of the MNTB (top right) and LSO (bottom right), however many surrounding cells outside the LSO are also visible. Here, it is difficult to interpret whether low levels of Kv3.2 protein are present in the SOC, or whether the Ab is non-specific. I suspect the latter, as Kv3.2 mRNA levels were very low in the SOC (fig 4.1). Unfortunately, there is no way to verify the antibody in a Kv3.2 KO mouse, as we do not breed these animals at this university.

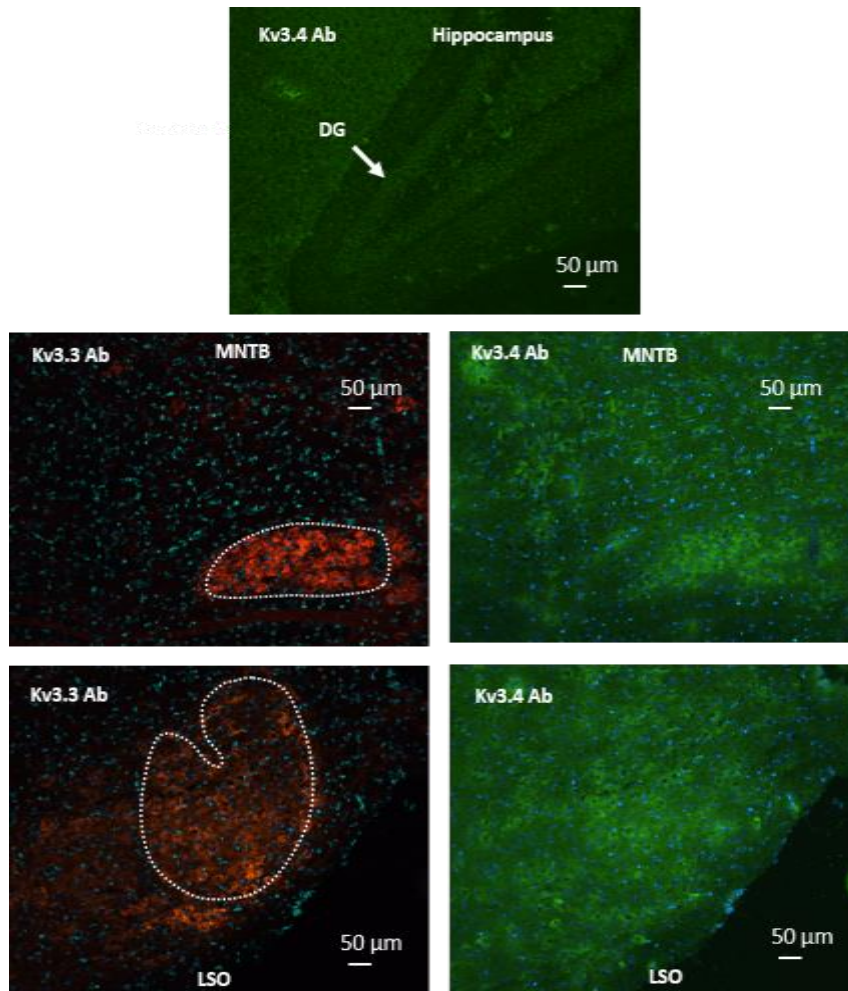
Kv3.4 expression in the SOC was then examined, this time by co-staining the same SOC sections with Kv3.3 Ab (red) and Kv3.4 Ab (green) (fig 4.9). In addition, a hippocampus section was stained at the same time with Kv3.4 Ab, to act as a positive control. Again, Kv3.3 staining is consistent with previous observations in the MNTB (top left) and the LSO, with little to no background staining. In contrast, Kv3.4 Ab in the same section shows very bright background staining, indicative of lack of specificity. Indeed, the LSO cannot be identified using Kv3.4 staining alone. I do not believe this antibody is specific to Kv3.4, and thus whilst Kv3.4 might be expressed in the SOC, it is impossible to conclude from the immunohistochemistry alone. Unfortunately, again there is no way to verify if the antibody is specific, as we cannot test the antibody using Kv3.4 KO mouse tissue and observe if there is any non-specific staining. Low Kv3.4 mRNA levels (fig 4.1) suggest Kv3.4 is not expressed in the SOC.

Figure 4.8 There is little Kv3.2 staining in the MNTB and LSO



**Fig 4.8. There is little Kv3.2 staining in the MNTB and LSO.** Adjacent coronal sections (12 μm) of brainstem containing the SOC from a CBA/Ca mouse (P16) were stained with either Kv3.1 Ab (diluted 1:1000) or Kv3.2 Ab (1:500), with secondary antibodies Alexafluor 488 goat anti-rabbit IgG (1:1000) (red, left) and AlexaFluor 546 goat anti-mouse IgG (1:1000) (green, right) respectively. At the same time, a coronal section containing the hippocampus was also stained with Kv3.2 to act as a positive control. Images of the MNTB (top row) and LSO (bottom row) were acquired using low (10 X) magnification. LSO and MNTB are highlighted by dashed white outline in each instance

Figure 4.9 Kv3.4 staining in the SOC appears non-specific



**Fig 4.9. Kv3.4 staining in the SOC appears non-specific.** Coronal sections (12  $\mu\text{m}$ ) of brainstem containing the SOC from a CBA/Ca mouse (P16) were co-stained with Kv3.3 Ab (diluted 1:3000) and Kv3.4 Ab (1:500), with secondary antibodies Alexafluor 488 goat anti-rabbit IgG (1:1000) (red, left) and AlexaFluor 546 goat anti-mouse IgG (1:1000) (green, right) respectively. At the same time, a coronal section containing the hippocampus was also stained with Kv3.4 to act as a positive control (top). Images of the MNTB (top row) and LSO (bottom row) were acquired using low (10 X) magnification. LSO and MNTB are highlighted by dashed white outline in each instance.

In summary, qRT PCR revealed Kv3.1b and Kv3.3 mRNA dominate in the SOC, in contrast to Kv3.2 and Kv3.4 mRNA which is negligible. In addition, there exist reciprocal gradients, where Kv3.1b mRNA was highest in the MNTB whilst Kv3.3 mRNA was highest in the LSO. Kv3.1 and Kv3.3 mRNA is translated into protein in all nuclei of the SOC, as shown by immunohistochemistry. In the MNTB both Kv3.1 and Kv3.3 are located in the cell membranes. In contrast, LSO neurons have Kv3.3 in the cell membranes, however Kv3.1 appears to be restricted to the neuropil. Both Kv3.2 and Kv3.4 Abs showed non-specific staining, and thus were not a reliable indicator of the presence of Kv3.2 and Kv3.4 protein in the SOC. It is possible both are present, but this cannot be confirmed by the immunohistochemistry alone. Whilst both Kv3.1 and Kv3.3 Abs were verified using KO mice, the lab do not breed Kv3.2 or Kv3.4 KO mice, and thus it was not possible to verify either the Kv3.2 nor Kv3.4 Abs for specific staining. However, given the extremely low levels of Kv3.2 and Kv3.4 mRNA present in the SOC, I believe they are not expressed in high levels, and the SOC is instead dominated by Kv3.3 and Kv3.1.

#### LSO neurons exhibit intrinsic leak

Next I examined the intrinsic excitability of LSO and MNTB in CBA/Ca mice (P14-P16) using whole cell patch clamp. Firstly I recorded I/Vs (-80 to +40 mV, 10 mV steps) from the LSO and MNTB, and compared the voltage activated currents (fig 4.10). LSO neurons show inward leak current at negative HPs (fig 4.10, c). This can be seen most clearly at negative HPs < -70 mV, where voltage activated channels are closed. It is unlikely that the leak observed in LSO neurons is due to a poor seal between the patch pipette and the cell membrane (where  $R_{leak}$  is low), as the same phenomenon is not seen in other cell types (MNTB and LOC). I therefore believe the leak is mediated by  $K^+$  leak channels (Kir and K2P). Leak currents summate with outward  $K^+$  currents at positive membrane potentials under voltage clamp. Therefore offline leak subtraction was performed as (described in chapter 2, section 2.3). Following leak subtraction,  $K^+$  currents from MNTB and LSO neurons are almost identical (fig 4.10, d).

Figure 4.10 LSO principal neurons exhibit intrinsic leak, and have near identical  $K^+$  conductance as MNTB neurons following leak subtraction

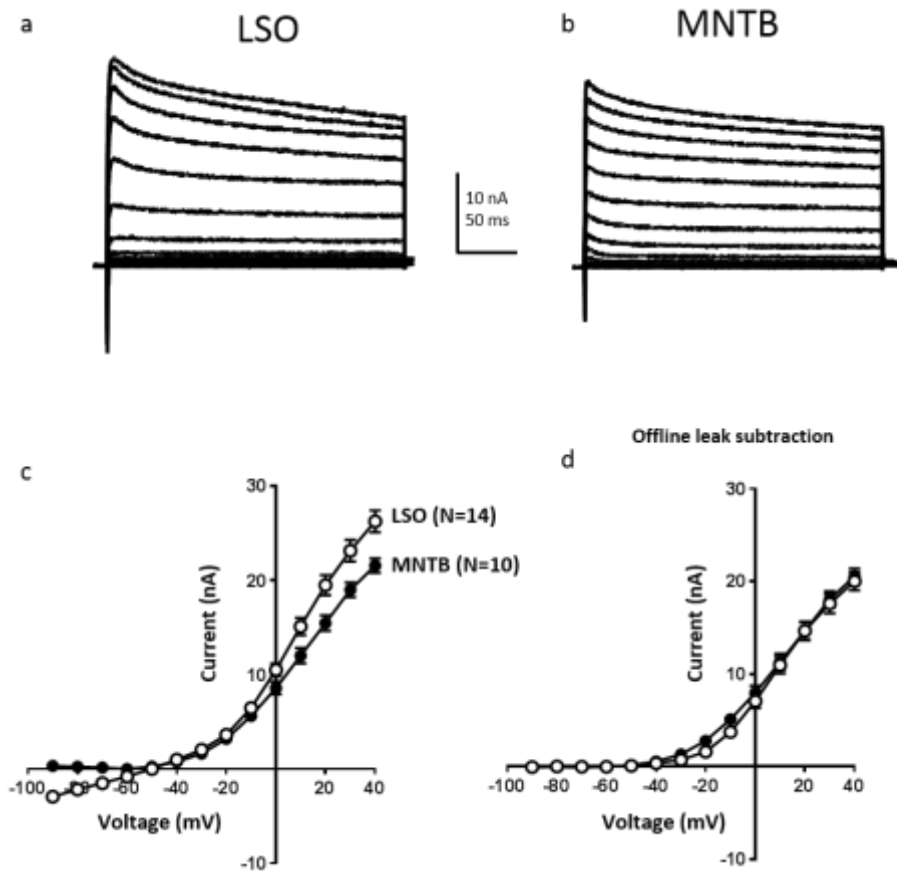


**Fig 4.10. LSO principal neurons exhibit intrinsic leak, and have near identical  $K^+$  conductance as MNTB neurons following leak subtraction.** **a.** LSO: Representative raw current traces, from voltage protocol -90 to +40 mV (10 mV steps). **b.** MNTB: Representative raw current traces (same protocol as part a). **c.** No leak subtraction: I/V recorded from either LSO (n=14) or MNTB (n=10) from CBA/Ca mice (P14-P16) (mean  $\pm$  SEM). **d.** Offline leak subtraction: Amended mean I/V of LSO and MNTB following leak subtraction. Holding potential = -60 mV.

### Experimental set-up for measuring Kv3 currents

Kv3 currents can be blocked by addition of 1mM TEA (Rudy and McBain, 2001). The remaining current is non Kv3 mediated. Thus, current after the addition of TEA can be subtracted from the initial current (immediately before TEA addition) to give the Kv3 mediated current. Here, I used a paired experiment, where an I/V was recorded in voltage clamp mode both before, and after addition of TEA. For each experiment, the following protocol was used:

- Prepare a 1mM TEA solution on the day of each experiment by dissolving TEA powder (Sigma) in normal aCSF.
- Before adding a brain slice to the recording chamber, assign normal aCSF and 1 mM aCSF separate perfusion lines (both perfuse the recording chamber of the patch clamp apparatus).

Next, it was important to prime the TEA aCSF line, to reduce the time it takes to reach the brain slice and block Kv3 channels:

- Clamp the normal aCSF line, turn on the peristaltic pump so that only TEA aCSF is drawn through the system and into the recording chamber.
- Clamp the TEA line, so no solution continues to be drawn up into the system, and open the normal aCSF line.
- After 10 minutes, the recording chamber should be flooded with normal aCSF.

Even when the TEA line is primed and closed, TEA containing aCSF can still flow slowly into the recording chamber through capillary action. To prevent this, the bubble trap through which the TEA solution must flow has a syringe attached to the top, which can be used to draw 1 ml of normal aCSF from the recording chamber into the TEA line. This creates a barrier of normal aCSF between TEA solution present in the line and the normal aCSF in the recording chamber, to prevent TEA entering the recording chamber when the TEA line is closed.

Next, to start data collection:

- Add a brainstem slice to the recording chamber.
- Upon whole cell configuration of cell (LSO or MNTB), record an I/V.
- Immediately following this open the TEA line, close the normal aCSF line, and record an I/V every subsequent minute.

#### Establishing criteria for measuring Kv3 mediated currents

Next, I needed to establish a criteria for recording Kv3 currents in the LSO or MNTB.

**Wash-off period:** Following TEA application, it is possible to wash-off TEA with normal aCSF so that other cells can be patch clamped from the same brain slice. However, the length of time to achieve total wash-off was unknown. Figure 4.11 shows the amplitude of K<sup>+</sup> currents in the MNTB at the voltage step of +40 mV over time, where an I/V was recorded once per minute following TEA application at ~30 sec. At 6 minutes, the TEA application was stopped, and the normal aCSF was perfused onto the slice. Within 15 minutes the amplitude had recovered to 'pre TEA' levels (amplitude at time 0), and thus the wash-off period was complete. Therefore, the wash-off period was established as 15 minutes.

**Series resistance criteria:** Next, it was important to establish a series resistance (SR) criteria for future recordings. During TEA application, SR can start to increase, due to factors such as cell membrane re-sealing, or cell debris blocking the patch pipette etc. An increase in SR has an inverse effect on the amplitude of currents measured after TEA application, thus potentially exaggerating the Kv3 mediated component. At the same time, it is unrealistic to dismiss every recording in which any SR change occurred. SR criteria for recordings performed upon break-through (no TEA) was set at <15 MΩ (nearly all cells were <10 MΩ). Fig 4.11 shows that although SR increased by 5.4 MΩ between time 0 and 17 minutes, amplitude at +40 mV was almost identical when SR compensation was adjusted. Thus, a criteria was set so the pre-TEA and post-TEA SR levels must be within 5 MΩ of each other.

**TEA time-course** The majority of the TEA effect on current amplitude occurred between 1-2 minutes following application. Figure 4.12 (a) shows the amplitude of currents at +40 mV recorded from both LSO and MNTB neurons before (time 0) and after 1mM TEA application (shaded grey), where an IV was recorded once per minute. Clearly, the majority of the TEA effect takes place between 0 – 3 minutes. I therefore decided the I/V used to represent non-Kv3 current should be taken 3 minutes after the start of TEA perfusion. In the event where this was not possible due to an increase in SR at this time point, the next time point (4 minutes) was used.

Figure 4.11 Wash-off period for TEA is ~15 minutes

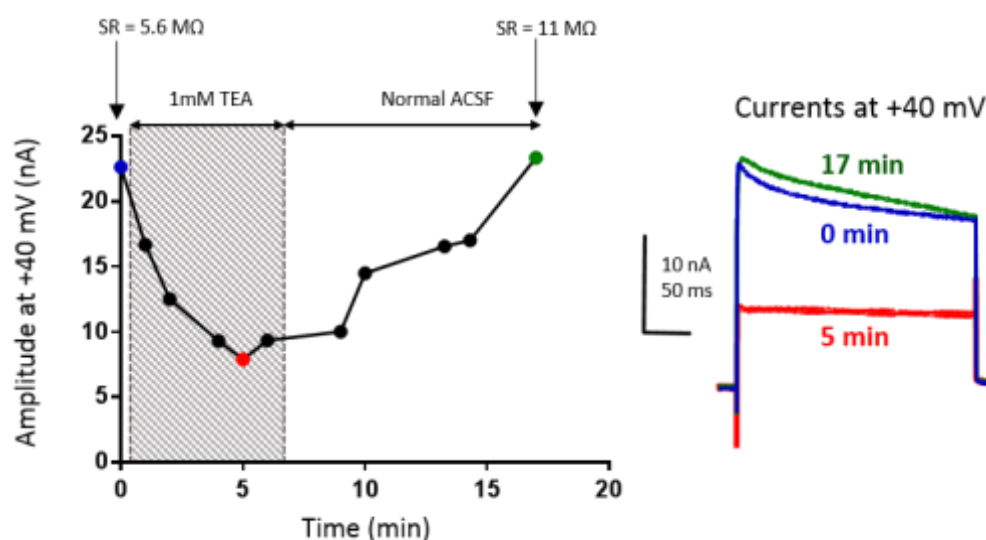


**Fig 4.11. Wash-off period for TEA is ~15 minutes.** An MNTB neuron (CBA/Ca, P15) was subject to an I/V protocol consisting of 10 mV steps depolarising steps from -90 to +40 mV, (duration 250 ms), from a holding potential of -60 mV. The amplitude of currents measured 5 ms from the start of the voltage step at +40 mV was plotted over time. Immediately following the first I/V recorded at time 0, the slices were perfused with 1 mM TEA (shaded area), and an I/V was recorded every subsequent minute. Note: Some data points are missing due to the series resistance having risen substantially. After 6 minutes, TEA perfusion was stopped, and normal aCSF perfusion resumed. Series resistance = 5.6 MΩ at the beginning and 11 MΩ at the end. **Right:** representative traces at 0 minutes (before TEA, blue), 5 mins (red) and 17 minutes (green). Each trace has a corresponding data point in a matching colour.

**Accounting for non-TEA mediated rundown of amplitude:** Non-Kv3 mediated currents are measured 3 or 4 minutes following TEA perfusion, with the assumption that any reduction in amplitude is due to blockage of Kv3 mediated K<sup>+</sup> currents. It was important to establish that current amplitude does not run-down regardless of TEA addition. Fig 4.12 (b) shows the amplitude of currents at +40 mV recorded from the LSO, where an I/V protocol was recorded every minute without TEA addition. Minimal run-down occurred, therefore the majority of run-down in amplitude following TEA addition can be attributed to the effects of blocking Kv3 channels.

Figure 4.12 TEA has most effect during the first 3 minutes of perfusion

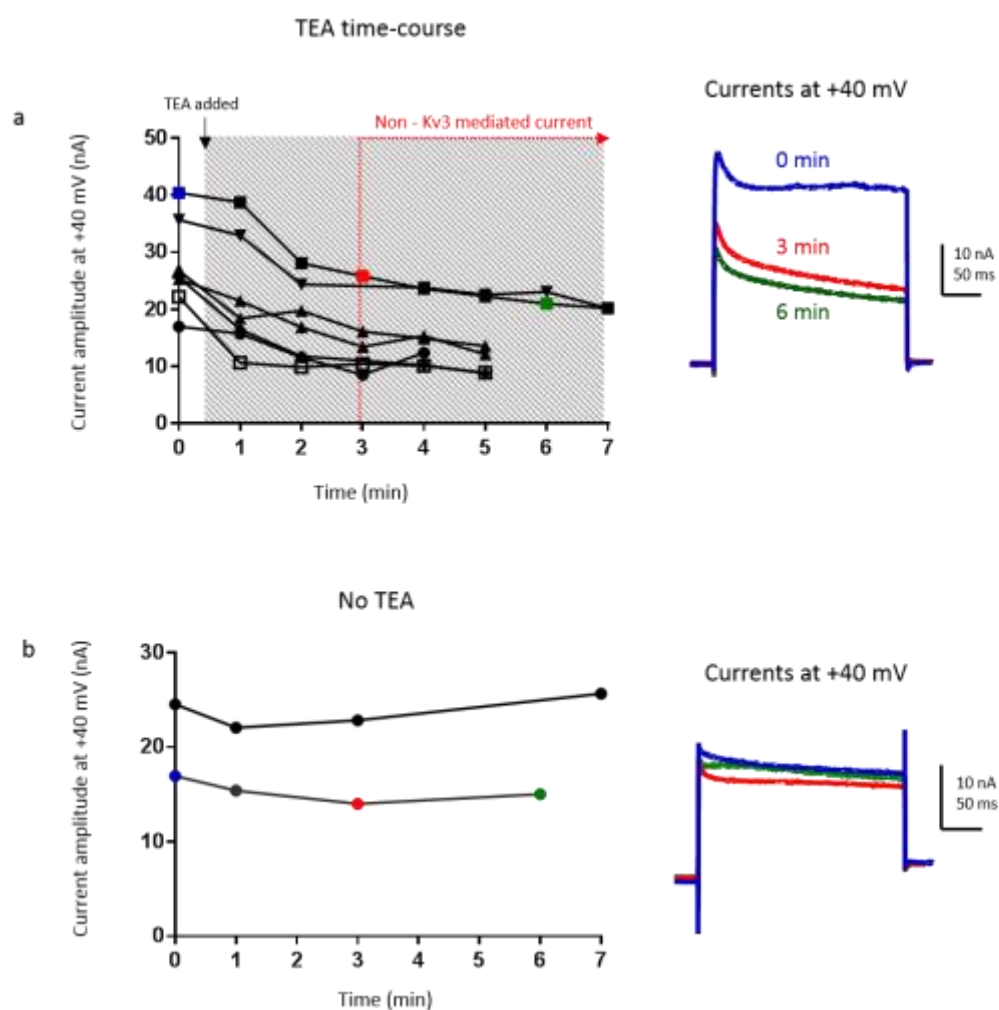


**Fig 4.12. TEA has most effect during the first 3 minutes of perfusion.** Neurons (MNTB and LSO from CBA/Ca and Kv3.3 KO mice, P14-P16) were subjected to an I/V protocol once every minute, consisting of 10 mV steps depolarising steps from -90 to +40 mV (duration 250 ms) from a holding potential of -60 mV. The amplitude of currents measured 5 ms from the start of voltage step +40 mV were plotted once per minute. If SR changed >5 MOhms, the data was omitted. **a.** 1 mM TEA perfusion at 30 secs (shaded area). **Right:** Representative traces at 0 minutes (blue), 3 mins (red) and 6 minutes (green). Each trace has a corresponding data point in a matching colour. **b.** No TEA is added (n =2, CBA/Ca, P13, one animal)

**Kv3 channels mediate ~half the total outward K<sup>+</sup> current in the LSO and MNTB**

Next, I wanted to establish the contribution of Kv3 mediated current to total outward K<sup>+</sup> current in the LSO and MNTB in CBA/Ca mice (P14-P16). Here, I/Vs were recorded under voltage clamp from MNTB and LSO principal neurons (-90mV to +40 mV, 10 mV steps) (fig 4.13). Currents recorded under control conditions (no TEA) are shown in black, whilst currents recorded 3 or 4 mins following TEA application are shown in red (mean  $\pm$  SEM). To the left are mean traces at voltage step +40 mV for the control condition (black), after TEA addition (red) and the difference between the two (subtraction, green), which represents the Kv3 mediated current. (Please note, I have included data collected from paired TEA experiments, and control I/Vs where no TEA was applied). There was a clear reduction in amplitude of outward K<sup>+</sup> current following TEA addition; with a 41% reduction in currents measured at voltage step +40 mV in the LSO ( $20 \pm 1$  nA, Mean  $\pm$  SEM, TEA =  $11.8 \pm 12.55$  nA) and a 56% decrease in the MNTB ( $20.5 \pm 0.9$  nA, TEA =  $9.1 \pm 9.4$  nA). This indicates that Kv3 currents mediate roughly half of outward voltage-gated K<sup>+</sup> current in both cell types.

Figure 4.13 Kv3 channels contribute ~half outward  $K^+$  current in the LSO and MNTB

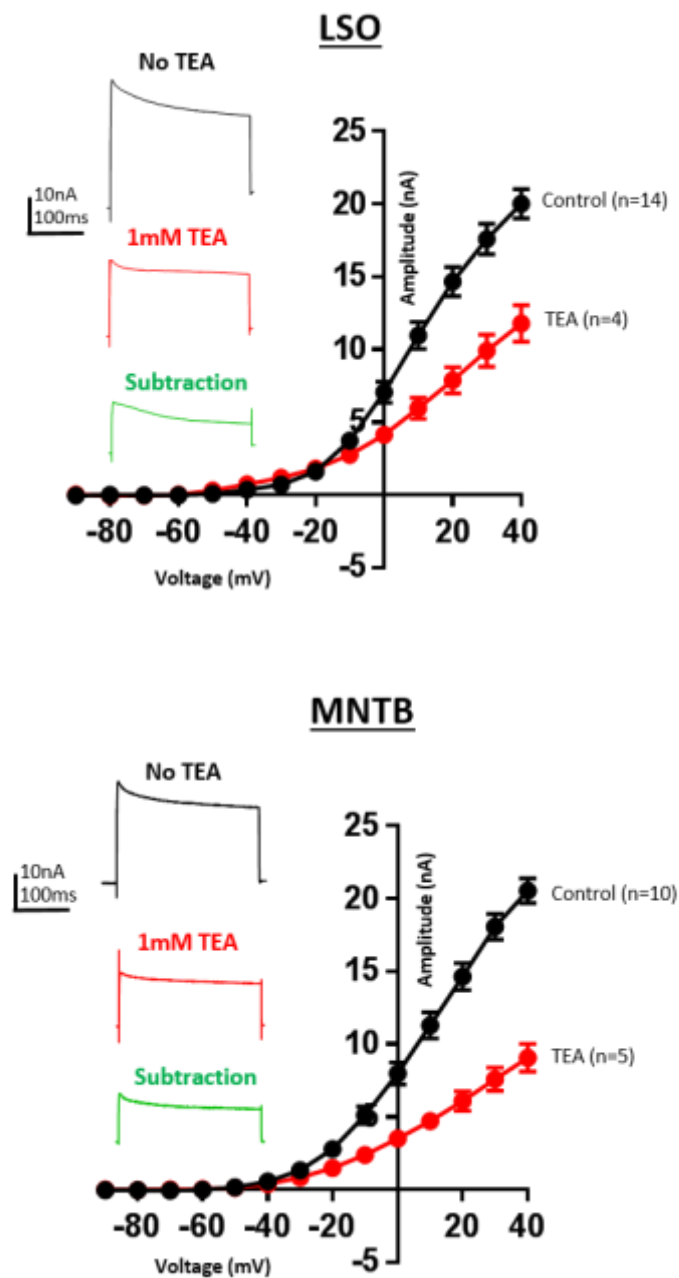


**Fig 4.13. Kv3 channels contribute ~ half outward  $K^+$  current in the LSO and MNTB.** I/Vs (-90 mV to +40 mV, 10 mV steps of 250 ms duration) were measured with addition of 1 mM TEA (red) or without TEA (black) in either LSO (top) or MNTB principal neurons (bottom) from CBA/Ca mice (P14-P16) (mean  $\pm$  SEM). Holding potential = -60mV. Left: Example raw traces at +40 mV voltage step. Top: without TEA (control, black). Middle: with addition of 1mM TEA (red). Bottom: Kv3 mediated current (no TEA – 1mM TEA = subtraction, green).

In the MNTB, Kv3 currents are mediated by Kv3.1 and Kv3.3, in contrast, for the LSO  
 Kv3.3 mediates the majority of Kv3 currents

So far, I have shown that both LSO and MNTB principal neurons have Kv3 mediated currents, however the subunit composition of Kv3 channels remains unclear. Immunohistochemistry revealed Kv3.1 and Kv3.3 protein is abundant in the SOC, but this does not confirm these subunits form functional channels. To assess the contribution of Kv3.1 and Kv3.3 to outward K<sup>+</sup> currents in the LSO and MNTB, KO mice were used which lack either Kv3.1 or Kv3.3. Here, we can assume the dominant Kv3 subunit in the SOC of Kv3.1 KO mice is Kv3.3, and visa versa.

To establish the contribution of either Kv3.1 or Kv3.3, I have recorded I/Vs with and without TEA in the LSO and MNTB from KO mice and compared them with recordings from CBA/Ca mice. Fig 4.14 shows mean I/Vs recorded from the LSO (left) and MNTB (right) of Kv3.1 KO mice (top) and Kv3.3 KO mice (bottom). In the LSO we see a small reduction in the overall amplitude (no TEA) in Kv3.1 KO compared to CBA/Ca mice (blue dashed line) (amplitude at voltage step +40 mV =  $17.1 \pm 1.3$  nA, (mean  $\pm$  SEM), n = 14, and  $20 \pm 1$  nA, n=14, respectively). Similarly, in the MNTB, there is a small reduction in the amplitude in Kv3.1 KO mice, compared to recordings taken from CBA/Ca (amplitude at HP +40 mV =  $18 \pm 1.2$  nA, n=16 and  $20.5 \pm 0.8$  nA, n=10). TEA blocks around half the outward K<sup>+</sup> current in both the LSO and MNTB of Kv3.1 KO mice, similar to the effect of TEA in CBA/Ca mice. I/Vs recorded from MNTB neurons in Kv3.3 KO mice show no reduction in the overall amplitude of currents compared to CBA/Ca (amplitude at HP +40 mV =  $20.3 \pm 2.1$  nA (mean  $\pm$  SEM), n = 14 and  $20.5 \pm 0.8$  nA, n = 10, respectively). In contrast LSO neurons show drastically reduced currents compared to CBA/Ca (amplitude at HP +40 mV =  $7.5 \pm 1.2$  nA, n = 13 and  $20 \pm 1$  nA, n = 14, respectively).

In summary, in the absence of Kv3.1 both the LSO and MNTB show compensation by utilizing Kv3.3 to rescue outward K<sup>+</sup> current to near-normal levels. In contrast, LSO currents are greatly depressed in Kv3.3 KO mice, whilst MNTB currents are normal. Overall, this suggests the MNTB is able to use either Kv3.1 or Kv3.3 to form functional channels in the absence of the other, however the LSO cannot rescue current in the

absence of Kv3.3. This demonstrates Kv3.3 is vital for normal intrinsic excitability in the LSO.

Figure 4.14 In the MNTB, Kv3 current is mediated by both Kv3.1 and Kv3.3; in the LSO, Kv3.3 mediates the majority of Kv3 current

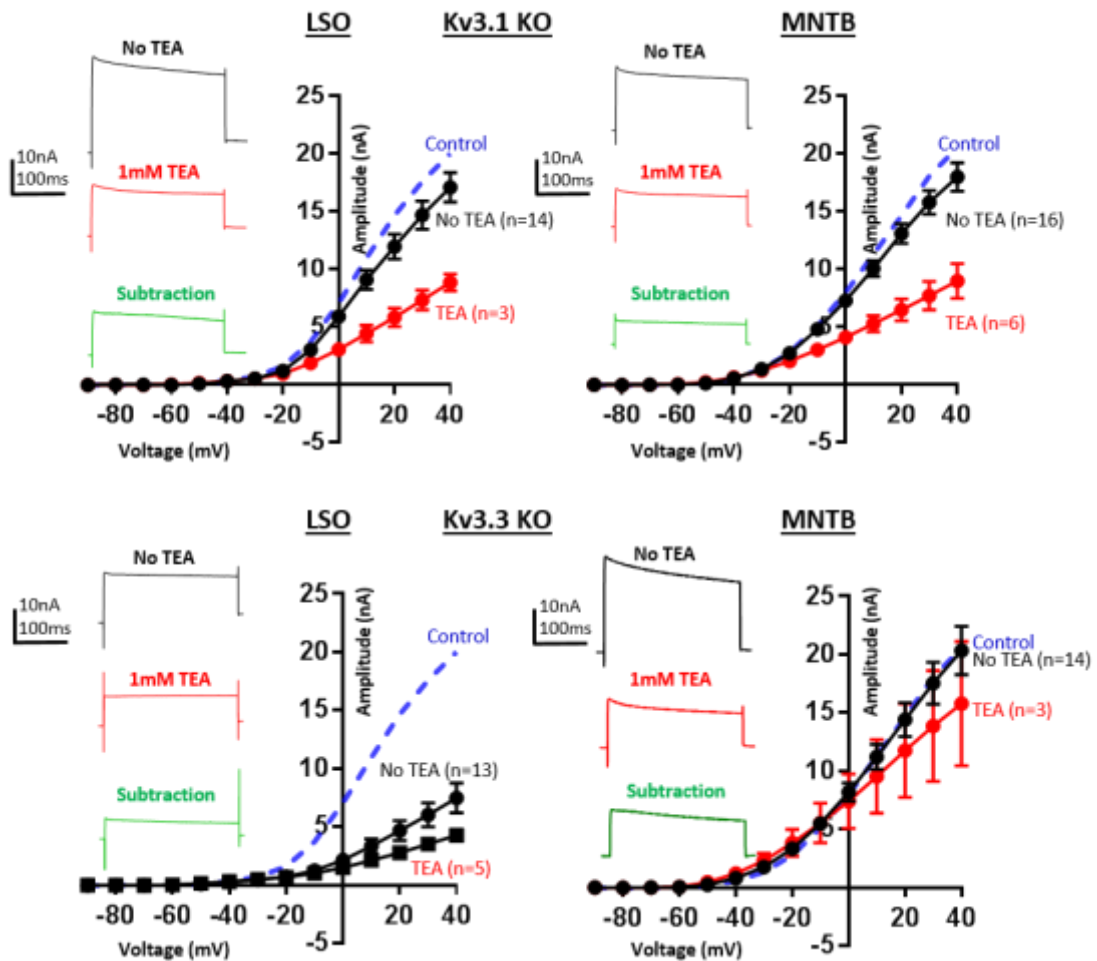


**Fig 4.14. In the MNTB, Kv3 current is mediated by both Kv3.1 and Kv3.3; in the LSO, Kv3.3 mediates the majority of Kv3 current. Top:** Kv3.1 KO: I/Vs (10 mV voltage steps of 250 ms duration from -90 mV to +40 mV) were measured with addition of 1 mM TEA (red) or without TEA (black) in either LSO (top left) or MNTB neurons (top right) from Kv3.1 KO mice (P14-P16) (Mean  $\pm$  SEM). Control (CBA/Ca) I/V (without addition of TEA) represented by blue dashed line (same data as shown in fig. 4.13). Holding potential = -60 mV. **Bottom:** Kv3.3 KO: I/Vs taken from Kv3.3 KO mice. Raw traces at +40 mV voltage step are shown on the left of each I/V: Top: without TEA (no TEA, black). Middle: with addition of 1mM TEA (red). Bottom: Kv3 mediated current (No TEA - 1mM TEA = subtraction, green).

### Kv3.3 accelerates AP firing in the LSO

Next, I compared APs between CBA/Ca, Kv3.1 KO and Kv3.3 KO mice in both the LSO and MNTB. Kv3 mediated current contributes to fast AP firing (Rudy and McBain, 2001) and thus measurement of the half width gives insight into the amount of Kv3 mediated current (i.e. increased half width = less Kv3 current). Neurons were subjected to 200 ms current injection steps ranging from -0.25 to 0.9 nA (0.05 nA steps). Half width was then measured from the first elicited AP, to eliminate the influence of Na<sup>+</sup> channel inactivation caused by preceding APs.

Fig 4.15 (a) shows the half width of APs recorded from the LSO in CBA/Ca, Kv3.1 KO and Kv3.3 KO mice (left to right), with representative AP traces above. APs recorded from Kv3.1 KO mice showed no change in half width compared to CBA/Ca ( $0.33 \pm 0.03$  ms, mean  $\pm$  SEM, n = 11, and  $0.3 \pm 0.02$  ms, n = 9 respectively), p = 0.859. However, APs recorded from Kv3.3 KO mice were dramatically slowed, with a mean half width of  $0.67 \pm 0.05$  ms, n = 7, approximately double that of APs in CBA/Ca and Kv3.1 KOs. In the MNTB, APs from both Kv3.1 and Kv3.3 KO mice showed a significant increase in half width compared to CBA/Ca mice, but not as dramatic as the Kv3.3 KO LSO. Specifically, MNTB AP half widths were: CBA/Ca =  $0.29 \pm 0.02$  ms, n = 14, Kv3.1 KO =  $0.42 \pm 0.03$  ms, n = 11, p = 0.0029 and Kv3.3 KO =  $0.48 \pm 0.02$  ms, n = 11, p < 0.0001.

In summary, both Kv3.1 and Kv3.3 contribute to AP repolarisation in the MNTB, which is able to partially compensate for the lack of either subunit. In the LSO, when only Kv3.3 is available (Kv3.1 KO), AP half width is unaffected. However when only Kv3.1 is available (Kv3.3 KO) APs are dramatically slowed. This demonstrates that Kv3.3 is essential for fast AP firing in the LSO, and Kv3.1 by itself cannot rescue fast AP firing. I therefore believe that Kv3.3 may be the exclusive Kv3 subunit in LSO neurons.

Figure 4.15 Kv3.1 has no impact on AP half width in the LSO

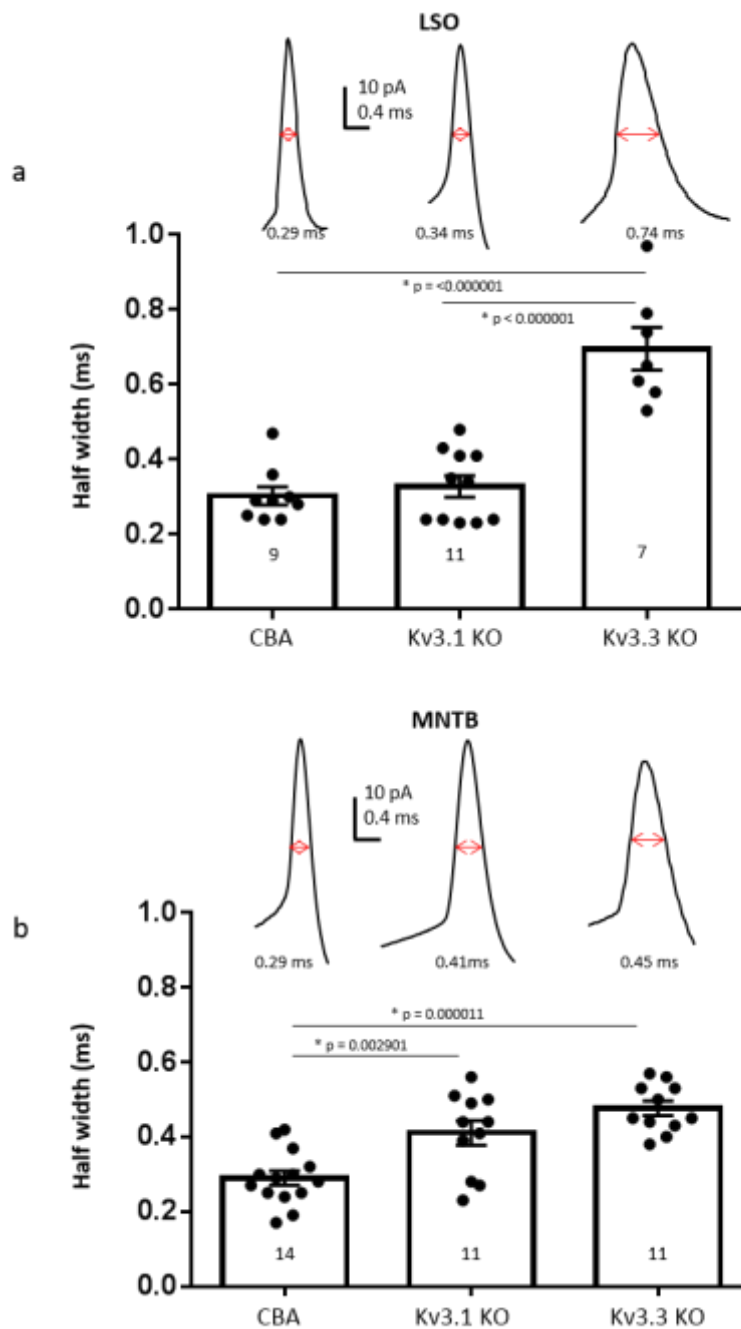


**Fig 4.15. Kv3.1 has no impact on AP half width in the LSO.** **a:** Half width of the first elicited AP from the LSO of CBA/Ca, Kv3.1 KO and Kv3.3 KO mice, P14-P16 (200 ms depolarising current injection steps from -0.25 to 0.9 nA) (mean  $\pm$  SEM). Holding potential = -60 mV. Closed circles = individual data points. Above: Representative example of raw AP traces corresponding to the mouse genotype below. Statistical significance were determined by one-way ANOVA, with Tukey post hoc testing. **b.** Half width of APs recorded from the MNTB. All subsequent figures showing APs were recorded using the same current step protocol, from a HP of -60 mV, with a holding current that did not exceed  $\pm$  450 pA.

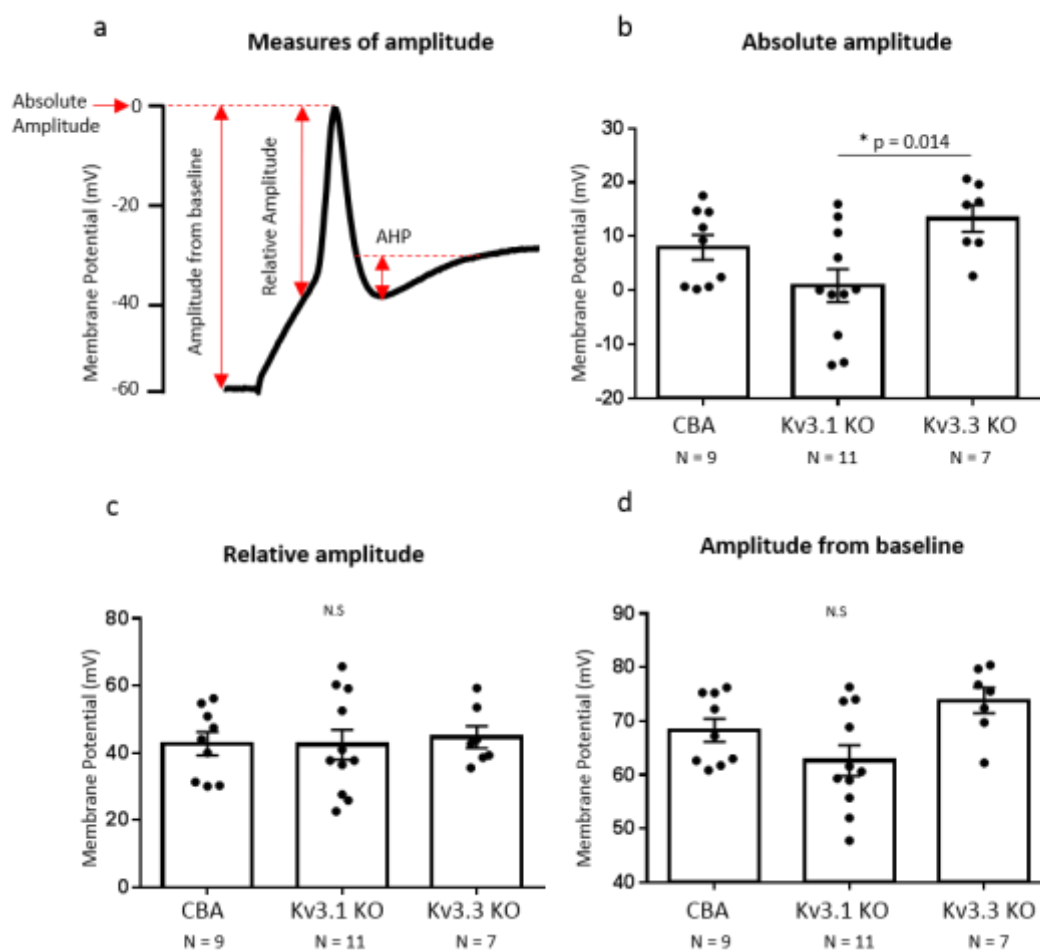
### AP characteristics from Kv3.1 and Kv3.3 deficient mice

As well as differences in half width, other AP characteristics were also compared between CBA/Ca, Kv3.1 KO and Kv3.3 KO mice. Firstly, three separate measurements of amplitude were taken from the first evoked AP of each cell: absolute amplitude, relative amplitude and the amplitude from baseline (fig 4.16, a). Absolute amplitude was defined as the membrane potential at which the AP peaks, whilst relative amplitude was the difference between the membrane potential at which the AP was initiated and the absolute amplitude. Amplitude from the baseline was defined as the difference between the absolute amplitude and the membrane potential before the current injection step, where the membrane potential of the neuron was held at -60 mV.

Fig 4.16 (b) shows the 'absolute amplitude' of APs measured from the LSO of Kv3.1 KO mice was significantly lower compared to Kv3.3 KO mice ( $0.87 \pm 3.05$  mV, (mean  $\pm$  SEM),  $n = 11$  and  $13.29 \pm 2.5$  mV  $n = 7$ , respectively)  $p = 0.014$ . This is due to lower AP threshold initiation (more negative) in the LSO in Kv3.1 KO mice (fig 4.17) (CBA =  $-34.55 \pm 1.96$  mV (mean SEM),  $n = 9$ , Kv3.1 KO =  $-41.58 \pm 1.56$  mV,  $n = 11$ , Kv3.3 KO =  $-31.48 \pm 2.51$  mV,  $n = 7$ ). Other measurements of amplitude do not show any difference between genotypes, so it seems APs are in fact the same size in Kv3.1 KO mice, but are initiated at more negative potentials.

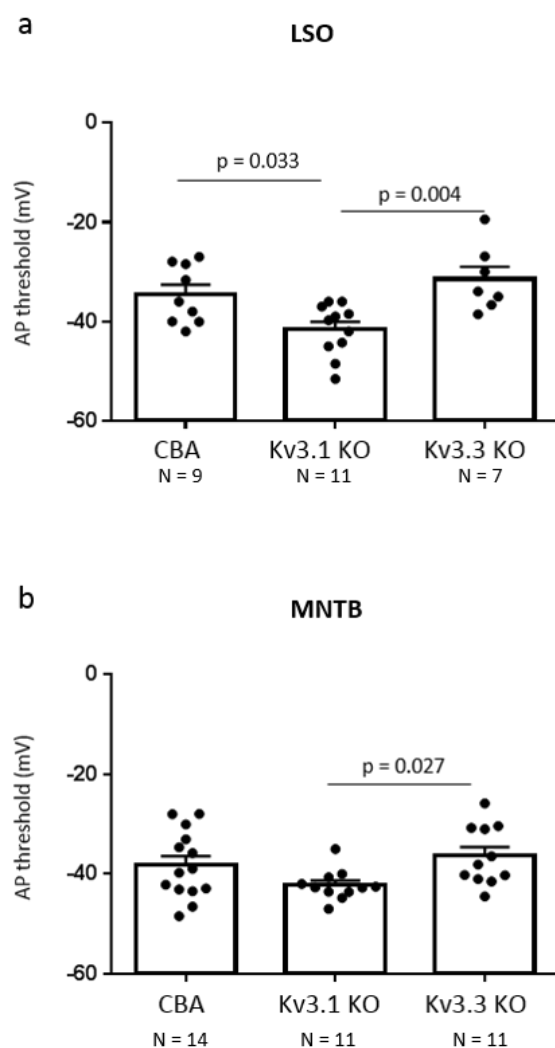
In contrast APs recorded from the MNTB do not show any differences in amplitude (fig 4.18), despite Kv3.1 KO mice having a significantly lower AP threshold than Kv3.3 KO mice ( $-42.22 \pm 0.92$  mV, (mean  $\pm$  SEM),  $n = 11$  &  $-36.34 \pm 1.79$  mV,  $n = 11$ , respectively)  $p = 0.027$  (fig 4.17, b). Finally, AHP amplitude in the MNTB is not significantly affected by a lack of either Kv3.1 or Kv3.3 (fig 4.19). In contrast, in LSO principal neurons, AHP is significantly reduced in Kv3.3 KO mice. This again supports the theory that the MNTB is able to utilize both Kv3.1 and Kv3.3, however the LSO is unable to compensate for the lack of Kv3.3, resulting in less outward  $K^+$  current, and consequently smaller AHP.

Figure 4.16 LSO: AP amplitude in CBA/Ca, Kv3.1 KO and Kv3.3 KO mice



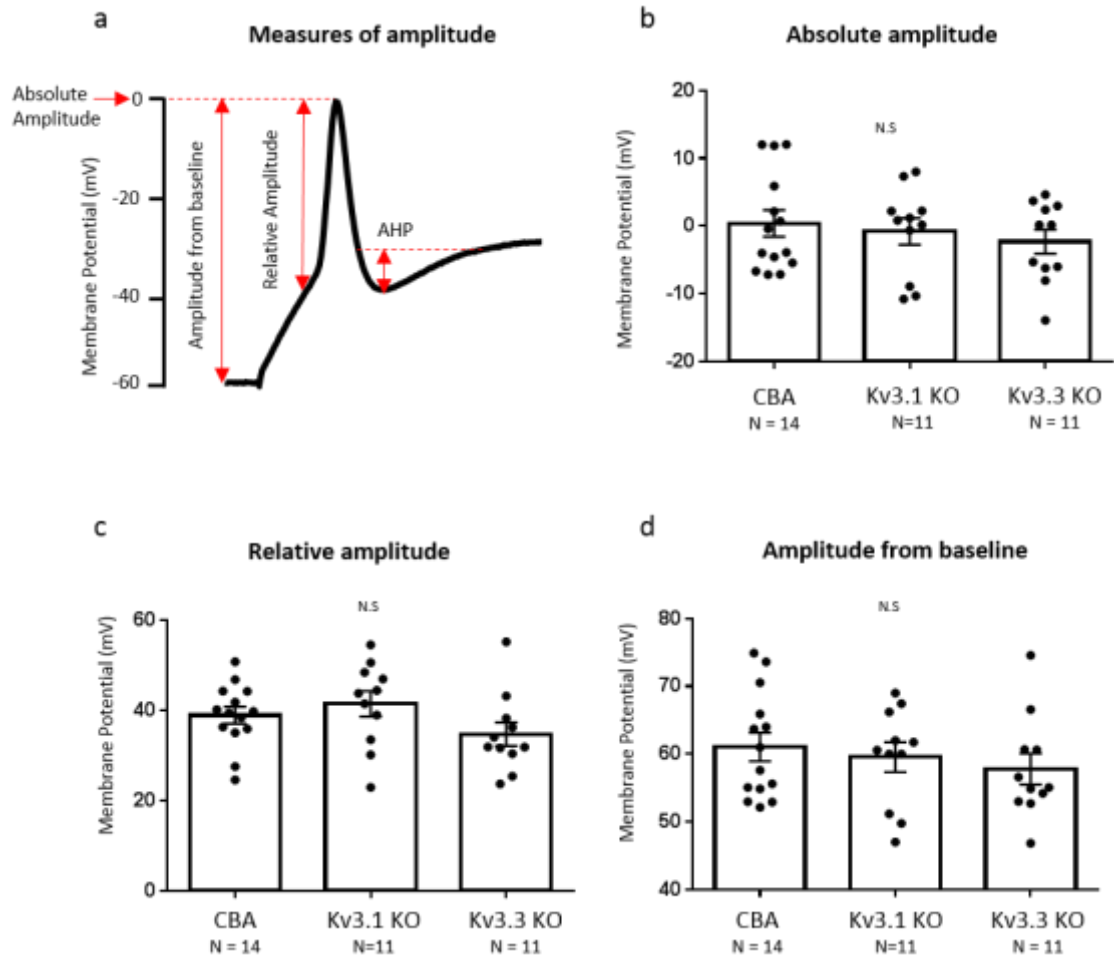
**Fig 4.16. LSO: AP amplitude in CBA/Ca, Kv3.1 KO and Kv3.3 KO mice.** The amplitude of the first AP elicited in LSO principal neurons from CBA/Ca, Kv3.1 KO and Kv3.3 KO mice were analysed in a variety of ways. **a.** Diagram of an action potential showing the different measures of amplitude. **b.** Absolute amplitude: CBA/Ca =  $7.96 \pm 2.32$  mV (mean  $\pm$  SEM), Kv3.1 KO =  $0.87 \pm 3.05$  mV, Kv3.3 KO =  $13.29 \pm 2.5$  mV. **c.** Relative amplitude: CBA/Ca =  $42.79 \pm 3.48$  mV, Kv3.1 KO =  $42.45 \pm 4.48$  mV, Kv3.3 KO =  $44.72 \pm 4.48$  mV. **d.** Amplitude from baseline: CBA/Ca =  $68.31 \pm 2.1$  mV, Kv3.1 KO =  $62.66 \pm 2.85$  mV, Kv3.3 KO =  $73.86 \pm 2.4$  mV. Filled circles indicate individual data points (b-d). Significance was determined using one-way ANOVA, with Tukey post-hoc testing.

Figure 4.17 Action potential threshold in the MNTB and LSO



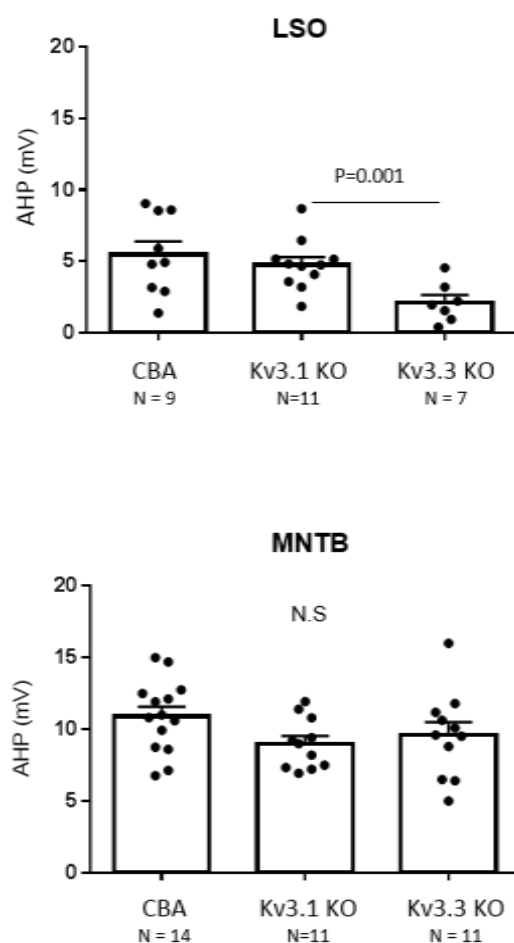
**Fig 4.17. Action potential threshold in the MNTB and LSO. a. LSO:** AP thresholds were compared between CBA/Ca ( $n = 9$ ), Kv3.1 KO ( $n = 11$ ) and Kv3.3 KO mice ( $n = 7$ ) (age = P14-P16). AP threshold was significantly lower in Kv3.1 KO mice compared to both CBA/Ca mice ( $p = 0.033$ ) and Kv3.3 KO mice ( $p = 0.004$ ). AP thresholds: CBA/Ca =  $-35.55 \pm 1.96$  mV (mean  $\pm$  SEM), Kv3.1 KO =  $-41.58 \pm 1.56$  mV, Kv3.3 KO =  $-31.48 \pm 2.5$  mV. **b. MNTB:** AP threshold was significantly lower in Kv3.1 KO mice compared to Kv3.3 KO mice ( $p = 0.027$ ). AP thresholds: CBA =  $-38.18 \pm 1.79$  mV,  $n = 14$ , Kv3.1 KO =  $-42.22 \pm 0.92$  mV,  $n = 11$ , Kv3.3 KO =  $-36.34 \pm 1.79$  mV,  $n = 11$ . Significance was determined using one-way ANOVA, with Tukey (LSO) and Game-Howell (MNTB) post-hoc testing.

Figure 4.18 MNTB: AP amplitude is unaltered in Kv3.1 and Kv3.3 KO mice



**Fig 4.18. MNTB AP amplitude remains the same in Kv3.1 and Kv3.3 KO mice.** The amplitude of the first AP elicited in LSO principal neurons from CBA/Ca, Kv3.1 KO and Kv3.3 KO mice were analysed in a variety of ways. **a.** Diagram of an action potential showing the different measures of amplitude. **b.** Absolute amplitude: CBA/Ca =  $0.39 \pm 1.96$  mV (mean  $\pm$  SEM), Kv3.1 KO =  $-0.77 \pm 1.96$  mV, Kv3.3 KO =  $-2.3 \pm 1.79$  mV. **c.** Relative amplitude: CBA/Ca =  $38.9 \pm 1.87$  mV, Kv3.1 KO =  $41.39 \pm 2.84$  mV, Kv3.3 KO =  $34.67 \pm 2.62$  mV. **d.** Amplitude from baseline: CBA/Ca =  $61.07 \pm 2.1$  mV, Kv3.1 KO =  $59.54 \pm 2.2$  mV, Kv3.3 KO =  $57.81 \pm 2.29$  mV. Filled circles indicate individual data points (b-d).

Figure 4.19 AHP is reduced in the LSO of Kv3.3 KO mice

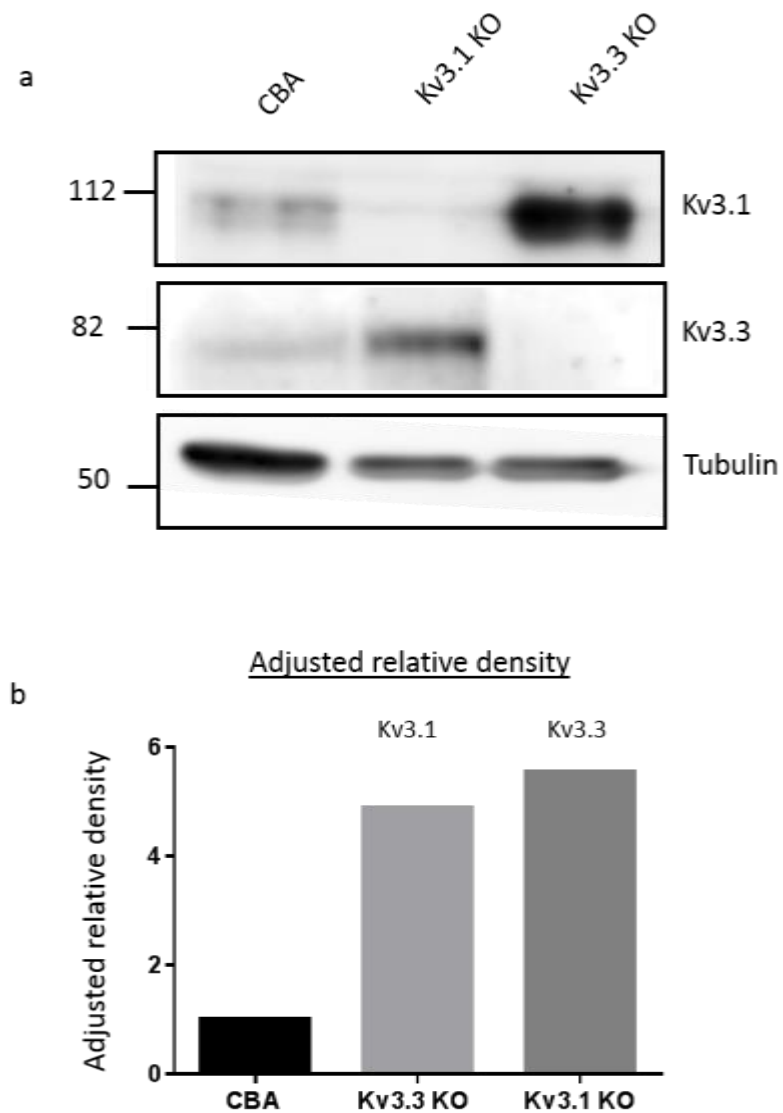


**Fig 4.19. AHP is reduced in the LSO of Kv3.3 KO mice.** AHP was measured from the first evoked AP recorded in the LSO and MNTB of either CBA/Ca, Kv3.1 KO or Kv3.3 KO mice (P14-P16). **LSO:** CBA/Ca =  $5.48 \pm 0.92$  mV (mean  $\pm$  SEM), n = 9. Kv3.1 KO =  $4.77 \pm 0.53$  mV, n = 11, Kv3.3 KO =  $2.12 \pm 0.53$  mV, n = 7. Significance was determined using one-way ANOVA, with Games Howell post-hoc testing. **MNTB:** CBA/Ca =  $10.9 \pm 0.67$ , n = 14, Kv3.1 KO =  $9 \pm 0.53$  mV, n = 11, Kv3.3 KO =  $9.6 \pm 0.91$  mV, n = 11. Closed circles = individual data points. Significance was determined using one-way ANOVA, with Tukey post-hoc testing.

### Kv3.1 and Kv3.3 protein is upregulated in knockout mice

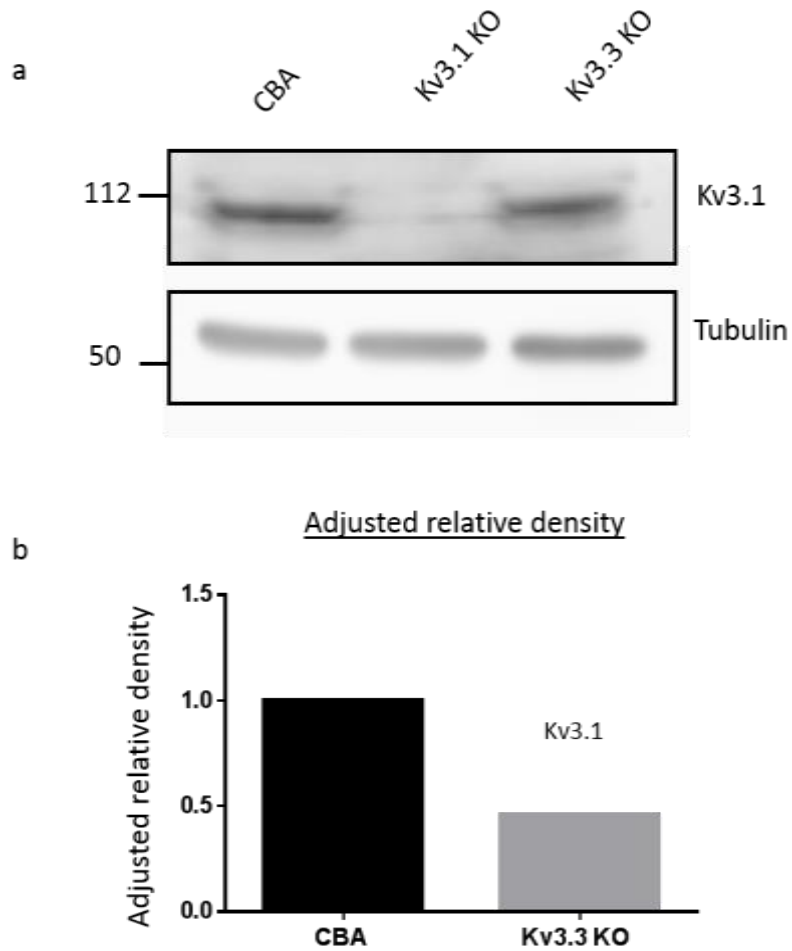
Upregulation of Kv3.1 mRNA has previously been observed in laser microdissected LSO tissue in Kv3.3 KO compared to WT using qRT PCR (data not shown). Whether this upregulation is translated into protein was unknown. To address this, a preliminary western blot was performed using dissected brainstem tissue containing the LSO from CBA/Ca, Kv3.1 KO and Kv3.3 KO mice (see chapter 2, section 2.8 for method). Here there is more Kv3.1 subunit protein in the Kv3.3 KO mouse compared to CBA/Ca control, as evidenced by the darker band (Fig 4.20). Similarly, there is more Kv3.3 protein in Kv3.1 KO LSO tissue compared to CBA/Ca, despite qRT PCR showing little upregulation. In contrast, the opposite result was observed in whole cerebellum samples, Kv3.1 was reduced in Kv3.3 KO mice (fig 4.21) (see discussion). Details of how the relative adjusted density was calculated can be found in the appendix (section 8.3).

Figure 4.20 LSO: Kv3.1 and Kv3.3 are upregulated in KO mice



**Fig 4.20. LSO: Kv3.1 and Kv3.3 are upregulated in KO mice.** **a.** Western blots were performed using lateral auditory brainstem tissue (containing the LSO) from CBA/Ca, Kv3.1 KO and Kv3.3 KO mice (P14-P16). Blots were probed with antibodies targeting either Kv3.1 (top row) and Kv3.3 (middle row). A tubulin control is shown below. **b.** The density of each band relative to CBA (1) was adjusted according to the tubulin control.

Figure 4.21 Cerebellum: Kv3.1 is down-regulated in Kv3.3 KO mice



**Fig 4.21. Cerebellum: Kv3.1 is down-regulated in Kv3.3 KO mice.** Western blots were performed using cerebellar tissue from CBA/Ca and Kv3.3 KO mice (P14-P16). Blots were probed with antibodies targeting Kv3.1 (top) or tubulin (bottom). **b.** The density of each band relative to CBA (1) was adjusted according to the tubulin control.

## 4.1 DISCUSSION

In this chapter, I have examined the intrinsic excitability of LSO and MNTB principal neurons. In particular, I have focused on Kv3 channels, which are a key determinate of excitability in the ascending auditory pathway. Currently the subunit composition of Kv3 channels (Kv3.1, Kv3.2, Kv3.3 & Kv3.4) in the LSO and MNTB is unconfirmed. To address this, qRT PCR was used to measure levels of Kv3 subunit in the SOC, and Kv3.1b and Kv3.3 were found to dominate. Furthermore, immunohistochemistry showed both Kv3.1 and Kv3.3 mRNA in the SOC were translated into protein. Next, I have examined if this protein forms functional Kv3 channels by comparing I/Vs from the MNTB and LSO of control (CBA/Ca), Kv3.1 KO, and Kv3.3 KO mice, and then blocked the Kv3 mediated current with TEA. This allowed me to assess the contribution of each subunit to the total voltage-gated K<sup>+</sup> conductance and Kv3 conductance. Finally, I have compared AP half widths between CBA/Ca, Kv3.1 KO and Kv3.3 KO mice to determine the contribution of Kv3.1 and Kv3.3 to AP repolarisation.

The main findings were:

- Kv3.1b and Kv3.3 mRNA dominate in the SOC, whilst levels of Kv3.2 and Kv3.4 mRNA are negligible.
- Kv3.1 and Kv3.3 subunit protein are present in all nuclei of the SOC.
- MNTB neurons contain both Kv3.1 and Kv3.3 in the cell membranes.
- LSO neurons contain Kv3.3 in the cell membrane, whilst Kv3.1 is in the neuropil only.
- MNTB neurons can use either Kv3.1 or Kv3.3 to rescue outward K<sup>+</sup> current and partially restore fast AP firing in Kv3.1 and K3.3 KO mice.
- LSO K<sup>+</sup> conductance is dramatically reduced in Kv3.3 KO mice, but remains unchanged in Kv3.1 KO mice.
- In the LSO, Kv3.3 subunits are essential, and Kv3.1 alone (Kv3.3 KO) cannot rescue fast AP repolarisation.

- Preliminary western blots show Kv3.1 protein is downregulated in the cerebellum compared to CBA/Ca. In contrast, Kv3.1 protein is upregulated in the LSO of Kv3.3 KO mice compared to CBA/Ca mice. Similarly, Kv3.3 protein is upregulated in the LSO of Kv3.1 KO mice.

#### Both Kv3.1 and Kv3.3 are utilized by the MNTB

I have shown both Kv3.1b and Kv3.3 mRNA are expressed at high levels in the SOC, with the latter dominating in each nuclei (fig 4.1). This mRNA is translated into protein, where both Kv3.1 and Kv3.3 are present across the SOC (fig 4.3). Furthermore, it is likely they form heteromeric channels as Kv3.1 and Kv3.3 transcripts are often co-expressed (Weiser et al., 1994b). Despite this, the majority of previous research has overlooked Kv3.3 in the auditory pathway, and has instead focussed on the function of Kv3.1, particularly in the MNTB (Brown and Kaczmarek, 2011). Consistent with my findings, others have found Kv3.1 is expressed in the MNTB. *In situ* hybridisation has shown the Kv3.1 gene (KCNC1) is present in both MNTB neurons and the presynaptic calyx of held (Wang et al., 1998). Similarly, a developmental switch from Kv3.1a to Kv3.1b mRNA at hearing onset has been observed in rats (Perney et al., 1992, Liu and Kaczmarek, 1998), and Kv3.1b protein has been identified by immunohistochemistry (Tong et al., 2013). Similar studies have observed a tonotopic gradient of Kv3.1 protein in the MNTB, with high density of staining in the medial regions which encode high frequencies and lower level staining in the more lateral regions, which encode low frequency sounds (von Hehn et al., 2004). I did not observe a similar gradient, due to differences in cell numbers at the medial and lateral regions of the MNTB, which made the staining difficult to quantify.

Previously Kv3.1 KO mice have been used measure the contribution of Kv3.1 to outward K<sup>+</sup> conductance. Macica et al (2003) found HVA currents in the MNTB (under voltage clamp) were reduced by ~90% in Kv3.1 KO mice compared to WT, to only 1-2 nA amplitude at voltage step +60 mV. This is in stark contrast to my findings, which showed MNTB neurons from Kv3.1 KO mice retain most of their total outward K<sup>+</sup> conductance of ~18nA (at +40 mV), compared to ~20 nA in CBA/Ca mice. Furthermore, around half the outward K<sup>+</sup> current in my experiments was blocked by the addition of

1mM TEA, demonstrating there is still a large Kv3 mediated component in the MNTB of Kv3.1 KO mice (Fig 4.14). Based on the low levels of both Kv3.2 and Kv3.4 mRNA in the SOC and high levels of Kv3.3 mRNA and protein (Fig 4.1 & 4.3), the remaining Kv3 current in a Kv3.1 KO mouse is most likely Kv3.3 mediated. Thus, I believe previous studies have overestimated the contribution of Kv3.1 to Kv3 mediated current in the MNTB, and largely ignored the contribution of Kv3.3.

Computer modelling predicted Kv3.1 is required for high frequency AP firing in the MNTB, but at a cost to accuracy of timing (Wang et al., 1998, Song et al., 2005). This was later confirmed by the inability of MNTB neurons from Kv3.1 null mice to faithfully follow a frequency stimuli > 200 Hz (*in vitro*) (Macica et al., 2003). These errors are thought to arise due to an increase in the relative refractory period (Brown and Kaczmarek, 2011).

Similarly, I have found Kv3.1 null mice have significantly longer MNTB AP half widths compared to CBA/Ca mice (Fig 4.15) which could explain AP failures at high frequency firing. However, Kv3.3 KO mice showed a similar increase in AP half width, thus it appears Kv3.1 and Kv3.3 contribute equally to Kv3 current in the MNTB. Thus, I believe if MNTB neurons from Kv3.3 KO mice were required to follow high frequency stimuli, they too would sustain AP failures.

In summary, both Kv3.1b and Kv3.3 mRNA and protein are found in the MNTB. Whilst other studies have focused exclusively on Kv3.1 in the MNTB, I have found Kv3.3 contributes equally to fast AP repolarisation. Here, the MNTB was able to partially compensate for the lack of either Kv3.1 or Kv3.3, suggesting the MNTB normally utilizes both to mediate Kv3 current.

### **Kv3.1 as a target for drug therapy**

More recently, novel compounds have been developed to act on Kv3.1 as its target. Application of these drugs to both CHO cells expressing Kv3.1 and native MNTB neurons *in vitro* shifted the voltage activation towards negative potentials, and increased open probability in single channel recordings (Brown et al., 2016). This ability to manipulate the properties of Kv3.1, and thus the excitability of the cell could provide therapeutic

benefit in treating hearing disorders such as tinnitus, by boosting existing Kv3.1 current. My work has shown that Kv3.3 contributes equally to Kv3 current in the MNTB. Furthermore, Kv3.1 does not appear to be present in LSO cell membranes, which is instead dominated by Kv3.3, and thus the compounds would likely have no effect. My work highlights the importance of Kv3.3 in central auditory processing, which could provide an alternative target for controlling excitability.

#### Kv3.3 is vital for fast AP firing in the LSO

Whilst many studies have concentrated on Kv3.1 in the MNTB, this is the first comprehensive study of Kv3 subunits in the LSO. Here we found Kv3.3 mRNA dominates in the LSO, with low amounts of Kv3.1b mRNA, and negligible amounts of Kv3.2 and Kv3.4 mRNA. Similarly, other studies have examined Kv3 subunit mRNA and concluded Kv3.3 dominates, (Grigg et al., 2000, Li et al., 2001) and Kv3.1 mRNA levels are either absent or low respectively. We have also observed that Kv3.3 mRNA is translated to protein in the SOC through immunohistochemistry (fig 4.3). Whilst Kv3.3 is clearly in the LSO soma and neuropil, Kv3.1 does not appear to be present in the soma, and is instead relegated to the neuropil (Fig 4.5).

Loss of Kv3.1 in the LSO has little effect on the voltage activated currents or AP half width (fig 4.14 & 4.15). In contrast, loss of Kv3.3 results in dramatically reduced outward K<sup>+</sup> currents (fig 4.14), reduced AHP (fig 4.19) and APs with half widths of ~double those of CBA/Ca mice (fig 4.15). Thus, Kv3.3 is vital for fast AP firing in the LSO, and may be the exclusive subunit. Similarly, both *in vitro* and *in vivo* recordings from mature Purkinje neurons show no change in AP half width duration in Kv3.1 KO mice, yet in Kv3.3 KO mice, AP half-width is doubled (Hurlock et al., 2008, McMahon et al., 2004, Zagha et al., 2008). This is consistent with immunohistochemical staining of adult Purkinje cells, which showed Kv3.3 subunit expression, but not Kv3.1 (McMahon et al., 2004). Furthermore, the electrophysiological changes could be restored by selectively re-introducing Kv3.3 channels into Kv3.3 KO Purkinje cells (Hurlock et al., 2008).

What are the consequences of substantially broadened APs in the LSO in Kv3.3 KOs?  
The LSO projects to both the inferior colliculus and lateral lemniscus. Longer duration

APs at the synaptic terminals would lead to voltage-gated  $\text{Ca}^{2+}$  channels remaining open for longer, and could lead to  $\text{Ca}^{2+}$  mediated cytotoxicity (Kass and Orrenius, 1999). Additionally, there may be increased transmitter release, leading to excitotoxicity in the postsynaptic neuron. Slow APs in the LSO may also affect auditory processing by disrupting sound localisation, which requires fast, high fidelity APs to detect subtle volume and timing differences between each ear to accurately encode ILD in the LSO (Tollin, 2003). However, auditory processing could equally be impaired by neurodegeneration of the nerves by  $\text{Ca}^{2+}$  influx and/or excitotoxicity.

#### SCA13 impairs sound localisation

An opportunity to study the effect of Kv3.3 absence in the auditory pathway of humans has arisen by examining people afflicted with the rare genetic disease spinocerebellar ataxia type 13 (SCA13). This disorder is caused by mutation to the Kv3.3 subunit, and is characterised by a loss of motor control due to cerebellar degeneration.

The main symptom of SCA13 in all cases is ataxia, thus previously little attention was given to the affect the disease has on hearing. To gain insight into the function of Kv3.3 in the auditory pathway, Middlebrooks et al (2013) assessed the effects of SCA13 on hearing thresholds, and the ability to detect both ITDs and ILDs, which are processed in the MSO and LSO respectively. Here, they examined the extended family of the Filipino kindred, who have the mutation R420H. This mutation affects the voltage sensor in the S4 domain of the Kv3.3 subunit, and results in dramatically reduced current and fewer Kv3.3 channels at the cell membrane (Gallego-Irardi et al., 2014). Middlebrooks found that whilst hearing thresholds were normal in affected listeners, both ILD (first extracted in LSO) and ITD processing (MSO) were compromised when compared to unaffected family members, or non-familial age matched controls, suggesting Kv3.3 is vital for processing sound localisation cues in the LSO and MSO. This supports my findings, where LSO principal neurons from Kv3.3 KO mice showed massively reduced outward  $\text{K}^+$  conductance, and substantially broadened AP half width. This could undermine the fast, temporal precision required for accurate ILD coding, and may be the cause of impaired ILD processing in SCA13.

In summary, Kv3.3 may be the exclusive subunit in the LSO, with Kv3.1 and Kv3.3 in the neuropil. Kv3.3 is vital for fast AP firing in the LSO, and cannot be rescued by Kv3.1 alone (Kv3.3 KO mouse). A unique insight into the function of Kv3.3 in humans has arisen by studying patients with the rare genetic disorder SCA13, in which the deleterious effect of Kv3.3 in the auditory pathway can be studied. People afflicted with SCA13 had normal hearing thresholds, but showed impaired sound localisation (both ILDs and ITDS). This could be due to broadened APs in the LSO due to lack of Kv3.3 current, as observed in Kv3.3 KO mice.

Kv3.1 is down-regulated in the cerebellum of Kv3.1 KO mice, but upregulated in the LSO. Preliminary western blots have shown Kv3.1 protein is down-regulated in the cerebellum of Kv3.3 KO mice (fig 4.21). In contrast, the LSO shows increased Kv3.1 levels in Kv3.3 KO mice and *visa versa* (fig 4.20). Here, the whole cerebellum was used for protein extraction, whilst LSO tissue was instead dissected from a brainstem slice (Chapter 2, fig 2.10). This was difficult as the dissections were so small (~1 mm diameter) 3 LSO had to be pooled together to ensure enough protein for detection. Thus, although every effort was made to ensure consistency between dissections, upregulation of Kv3.1 and Kv3.3 in the LSO of KO mice could be a result of irregular tissue sample sizes. Laser microdissection would be required to confirm the upregulation of Kv3.1 and Kv3.3 in the LSO of KO mice, by accurate, consistent extraction of LSO tissue. Unfortunately, I did not have access to this equipment.

Assuming Kv3.1 is increased in Kv3.3 KO, this does not rescue outward  $K^+$  conductance (fig 4.14) or fast AP repolarisation (fig 4.15). Again, this implies Kv3.1 is not expressed in the LSO soma, or maybe requires Kv3.3 to traffic to the membrane. Whilst Kv3.3 protein upregulation was predicted by substantial upregulation of mRNA, Kv3.1 mRNA levels were similar in Kv3.3 WT compared to KO (data not shown). This highlights that mRNA levels do not always accurately predict protein expression.

In contrast to the LSO, Kv3.1 protein expression in the cerebellum was reduced in Kv3.3 KO mice. This is interesting, as it appears that rather than rescuing Kv3 current in the absence of Kv3.3 in the cerebellum, Kv3 channels may be down-regulated instead, or cells of the cerebellum are utilizing other Kv3 subunits (Kv3.4 or Kv3.2) that were not tested for. Indeed, both Kv3.2 and Kv3.4 are expressed in the cerebellum (Joho and Hurlock, 2009).

In summary, these preliminary results show the LSO and cerebellum respond very differently to Kv3.3 deletion, showing upregulation and downregulation of Kv3.1 protein respectively. Interestingly, people with R420H mutation of SCA13 showed no correlation between ILD scores and severity of symptoms, suggesting the disease progresses differently in the LSO compared to the cerebellum.

### Summary

In this chapter I have shown both Kv3.1 and Kv3.3 mRNA and protein dominate in the SOC. The MNTB is able to use both Kv3.1 and Kv3.3 in the absence of the other to partially restore fast AP firing, suggesting it normally utilizes both. In contrast, the Kv3.3 KO LSO shows dramatically reduced outward K<sup>+</sup> conductance and slowed APs with half widths ~ double that of CBA/Ca mice. Thus, Kv3.3 is vital for fast AP firing in the LSO, and Kv3.1 alone cannot rescue Kv3 current, despite preliminary western blots showing upregulated levels of Kv3.1 in Kv3.3 KO LSO. Meanwhile, fast AP firing was maintained in Kv3.1 KO mice. Therefore, I believe Kv3.3 is the exclusive subunit in the LSO. This is supported by immunohistochemistry, which showed Kv3.3 in both the soma and neuropil of the LSO, with Kv3.1 in the neuropil only. Here, slowed APs caused by Kv3.3 absence could undermine ILD processing, and may be the underlying cause of ILD deficits observed in SCA13.

## 5 THE EFFECT OF ACOUSTIC OVER-EXPOSURE ON INTRINSIC AND SYNAPTIC EXCITABILITY IN THE AUDITORY BRAINSTEM

---

Previously, I have compared whole cell patch clamp recordings from neurons of the LSO and MNTB *in vitro*, using brain slices taken from control CBA/Ca mice with no prior AOE. Here I have shown that LSO principal neurons can be divided into two distinct groups based on their AP firing properties: single-spiking (where  $\leq 3$  APs are fired), or a multi-spiking phenotype (5 - 120 spikes fired) (see fig 3.3). This is in contrast to MNTB principal neurons which predominantly maintain a single-spiking phenotype in response to increasing current injection steps, due to the action of Kv1 mediated currents (Brew and Forsythe, 1995a). I have also examined the synaptic excitability of LSO principal neurons, where evoked EPSCs (both AMPAR and NMDAR mediated) showed developmental acceleration of decay kinetics, and reaching maturity by P17 ( $\sim 1$  ms and  $\sim 3$  ms respectively).

Whilst there is extensive research on the effects of AOE in the periphery, relatively little is known about the effect of AOE further up the ascending auditory pathway. Here, I assess whether AOE alters the excitability of principal neurons of the LSO and MNTB. Whilst many studies have focused on the acute effects of AOE, this chapter provides a snapshot of excitability in the SOC one week post acoustic insult. To induce acoustic trauma, CBA/Ca mice (P17:P20) were anaesthetised and exposed to 110 dB SPL broadband noise (5-50 kHz) for two hours. One week later, the mice were culled for brain slice preparation and patch clamping.

Throughout this chapter, I will compare whole cell patch clamp recordings from AOE treated mice and age matched controls (both P23:P27). In the first half of the chapter, I will concentrate on assessing the effect of AOE on principal neurons of the MNTB. Firstly, I examine AOE mediated changes to the intrinsic excitability of MNTB neurons, by comparing AP firing patterns in response to increasing current injection. Secondly, I assess the properties of the APs themselves, by comparing the first evoked AP from control and AOE treated mice. Finally, I examine current/voltage relationships

recorded from MNTB neurons under voltage clamp, to establish if AOE changes voltage activated currents.

In the second half of the chapter, I concentrate on the excitability of LSO principal neurons, and how AOE may change this. Firstly, I assess any changes to intrinsic excitability, by comparing AP firing patterns and properties of LSO principal neurons from control and AOE treated mice. Next, I investigate AOE mediated changes to synaptic conductance in the LSO, by comparing the kinetics of both AMPAR mediated EPSCs and NMDAR EPSCs (with and without AOE).

### 5.1 MNTB: THE EFFECT OF AOE ON INTRINSIC EXCITABILITY

**MNTB: AOE converts neurons from a single-spiking to multi-spiking phenotype**

I have examined the effect of AOE in the MNTB by comparing APs recorded from control mice to those treated with AOE one week earlier (both aged P23: P27). Mice were culled and brainstem slices prepared as described in chapter 2 (section 2.2). MNTB neurons were then visually identified and subjected to whole cell patch clamp, in current clamp mode. Current injection ranging from -0.25 nA to 0.9 nA (0.05 nA steps) were applied to MNTB neurons from a holding potential of -60 mV.

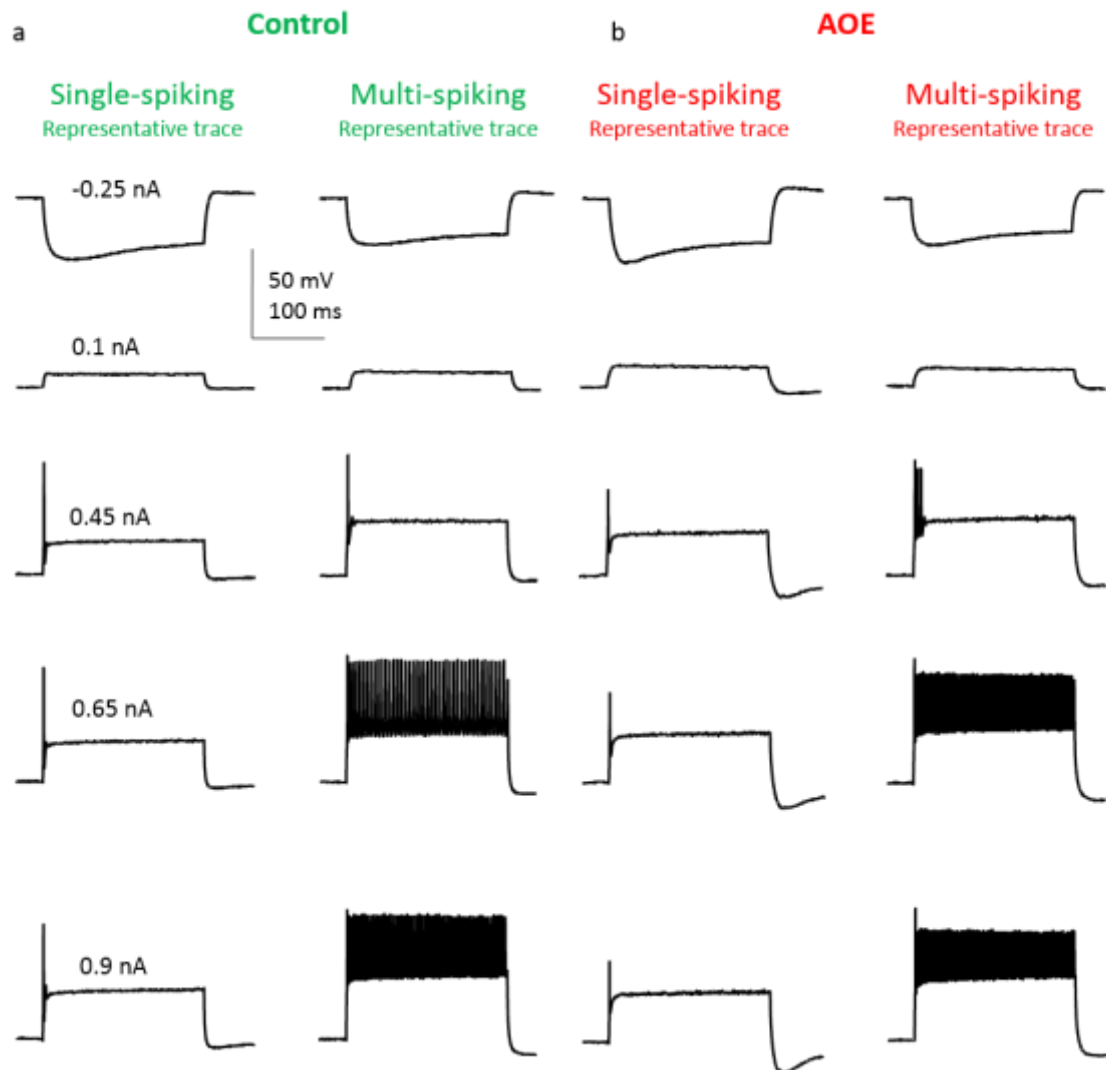
Following AOE, MNTB AP firing patterns underwent a drastic change, switching from a predominantly single-spiking firing pattern to a multi-spiking pattern. Figure 5.1 shows example raw current clamp data from MNTB neurons, comparing the voltage response from control mice (green, left) and AOE treated mice (red, right) to increasing current injection steps (top to bottom, values indicated far left). APs from 4 representative MNTB neurons are shown in total (left to right), with examples of single-spiking and multi-spiking neurons from both control (left) and AOE treated mice (right). Of the 22 MNTB neurons tested in the control mice, 19 were single-spiking (maintained  $\leq 3$  APs in response to increased current injection), whilst only 3 were found to be multi-spiking (fired  $>5 -120$  APs in response to increased current injection). Conversely, following AOE, a dramatic switch occurred where the majority of the neurons now showed a multi-spiking phenotype. Here 21 of the cells following AOE were found to

be multi-spiking, whilst only 6 cells maintained a single-spiking firing pattern. The number of single-spiking vs multi-spiking MNTB neurons from control and AOE treated mice is summarised in fig 5.2 (a).

It is sometimes the case that MNTB neurons may fire an additional AP in response to very high levels of depolarising current injection, thus it was important to distinguish these cells from multi-spiking neurons. Single-spiking was defined as firing 1 AP at 100 pA of current injection beyond threshold, and  $\leq 3$  APs in response to the highest current injection (0.9 nA), whilst multi-spiking neurons were defined as firing  $>5 - 120$  APs. Figure 5.2 (b) shows the number of APs fired by 5 example multi-spiking MNTB neurons (red) and 5 example single-spiking neurons (green) in response to increasing current injection steps. Most multi-spiking cells responded with a single AP upon sufficient current injection to reach AP threshold. However, with increasing current injection, multi-spiking neurons responded with multiple APs, often with only a 0.05 nA increase in current injection, and rapidly reached high AP firing rates of up to  $\sim 500$  Hz ( $\sim 100$  APs in 200 ms current step). In contrast, 4 out of 5 example single-spiking neurons responded with a single AP, which was maintained with increasing current injection, whilst the remaining single-spiking neuron fired 2 APs at the higher levels of current injection (fig 5.2, c).

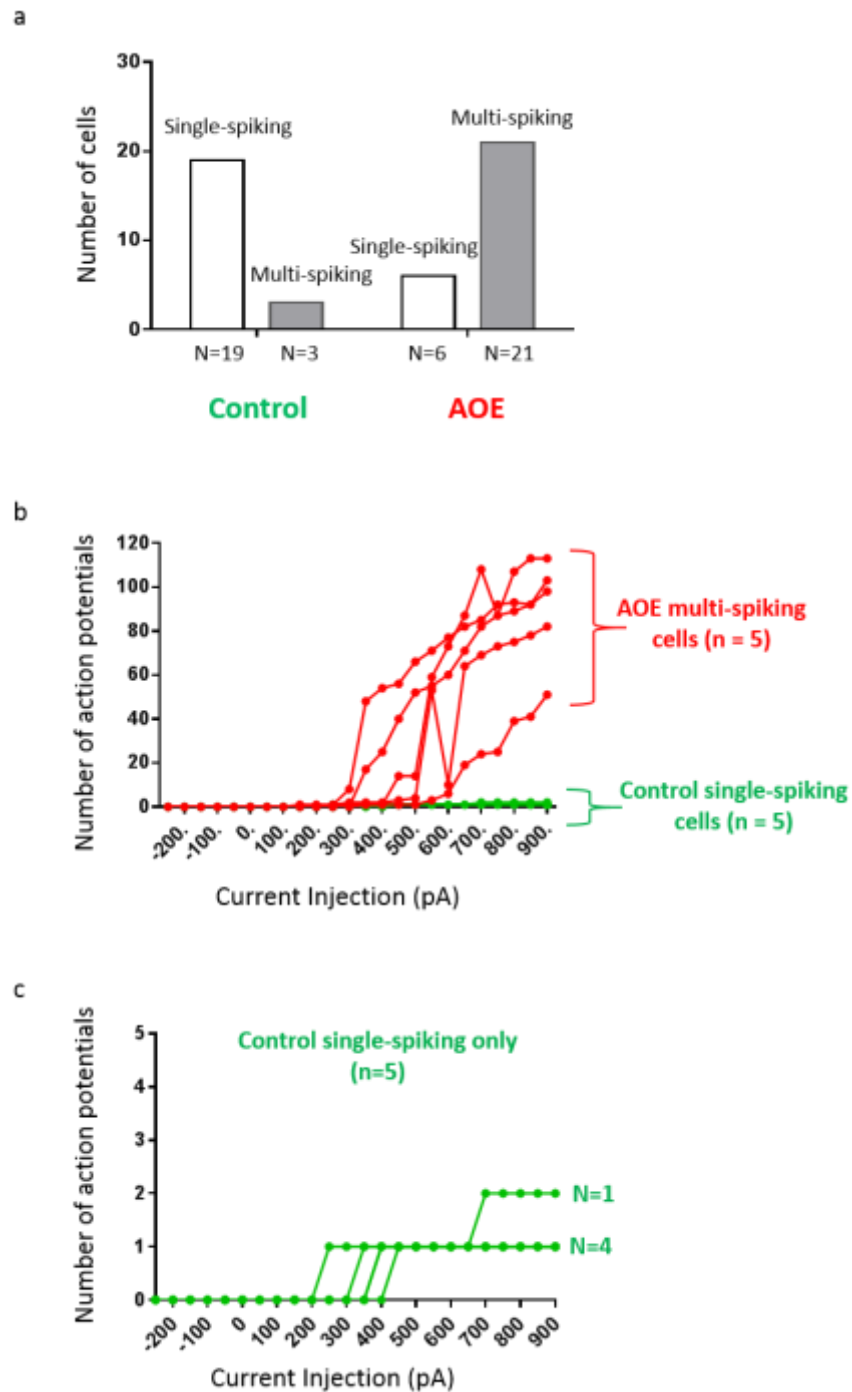
In summary, following AOE MNTB neurons undergo a dramatic transformation from a predominantly single-spiking phenotype to a multi-spiking phenotype. Multi-spiking MNTB neurons fire up to  $\sim 100$  APs in response to a single depolarising current injection step of 0.9 nA (200 ms), whilst single-spiking neurons fire  $\leq 3$  APs.

Figure 5.1 MNTB: AOE converts neurons from a single-spiking to a multi-spiking phenotype



**Fig 5.1. MNTB: AOE converts neurons from a single-spiking to a multi-spiking phenotype.** Select raw current clamp traces from MNTB neurons, comparing the voltage response from control mice (green, left) and AOE treated mice (red, right) to increasing current injection steps (-0.25 to 0.9 nA, 0.05 nA steps) (top to bottom, values indicated far left). APs from 4 representative MNTB neurons are shown in total (left to right), with examples of single-spiking and multi-spiking neurons from both control (left) and AOE treated mice (right). Single-spiking was defined as firing 1AP at 100 pA of current injection beyond threshold, and  $\leq 3$  APs in response to the highest current injection (0.9 nA). All subsequent figures showing APs elicited from the MNTB were recorded using the same current step protocol, from a HP of -60 mV, with a holding current which did not exceed  $\pm 300$  pA.

Figure 5.2 MNTB: Multi-spiking neurons show high spiking rates with increased current injection



**Fig 5.2. MNTB: Multi-spiking neurons show high spiking rates with increased current injection.**

APs were recorded from the MNTB from either control mice (green), or mice subjected to AOE (red) **a**. Bar chart depicting the number of MNTB cells showing either single-spiking or multi-spiking firing pattern in control (green) and AOE (red) mice. **b**. Number of APs in response to increasing current injection for representative examples of single-spiking control cells (green) and multi-spiking AOE cells (red). **c**. AP count of the same control single-spiking neurons as part **b**, with a reduced Y axis amplitude for increased clarity.

### MNTB: AP Half width is accelerated following AOE

Next, I wanted to establish if AOE changes the properties of the APs themselves, by analysing the first evoked AP from MNTB neurons in response to depolarising current injections. The reason for analysing the first AP, was to eliminate the influence of Na<sup>+</sup> channel inactivation caused by preceding APs. I began by comparing the half width (HW) of MNTB APs from control and AOE treated mice, which ultimately dictates upper limits of firing rates.

Following AOE, 2 MNTB neurons exhibited spontaneous firing in the absence of current injection, and as a result the voltage clamp was insufficient to maintain a holding potential of -60 mV before and after current injection steps. Fig 5.3 (a) shows the HW measurements of MNTB APs from both control and AOE treated mice, with single-spiking neurons represented by closed circles, and multi-spiking neurons represented by open triangles. The spontaneous firing neurons both had markedly different AP half widths of 1.35 ms and 1.56 ms (highlighted by red circle) compared to the mean (0.39 ms). With these two neurons included there was no significant difference between control ( $0.43 \pm 0.03$  ms (Mean  $\pm$  SEM,  $n = 22$ ) and MNTB neurons following AOE ( $0.39 \pm 0.06$  ms,  $n = 27$ ),  $p = 0.58$  (as measured via unpaired t-test) (fig 5.3, a).

I decided to remove the spontaneous firing neurons from the dataset because: 1) these neurons obviously had markedly lower AP thresholds and 2) APs may be affected by Na<sup>+</sup> channel inactivation from previous APs. As a result, these 2 neurons were also excluded from any further analysis. Upon removal of the spontaneous firing neurons, the amended AOE HW mean ( $0.31 \pm 0.01$  ms,  $n = 25$ ) was significantly shorter than control ( $p = 0.0002$ ) (fig 5.3, b).

In summary, AOE accelerates half width of APs in the MNTB and has even resulted in causing spontaneous activity in a very small percentage of MNTB neurons.

Figure 5.3 MNTB: AP half width accelerates following AOE

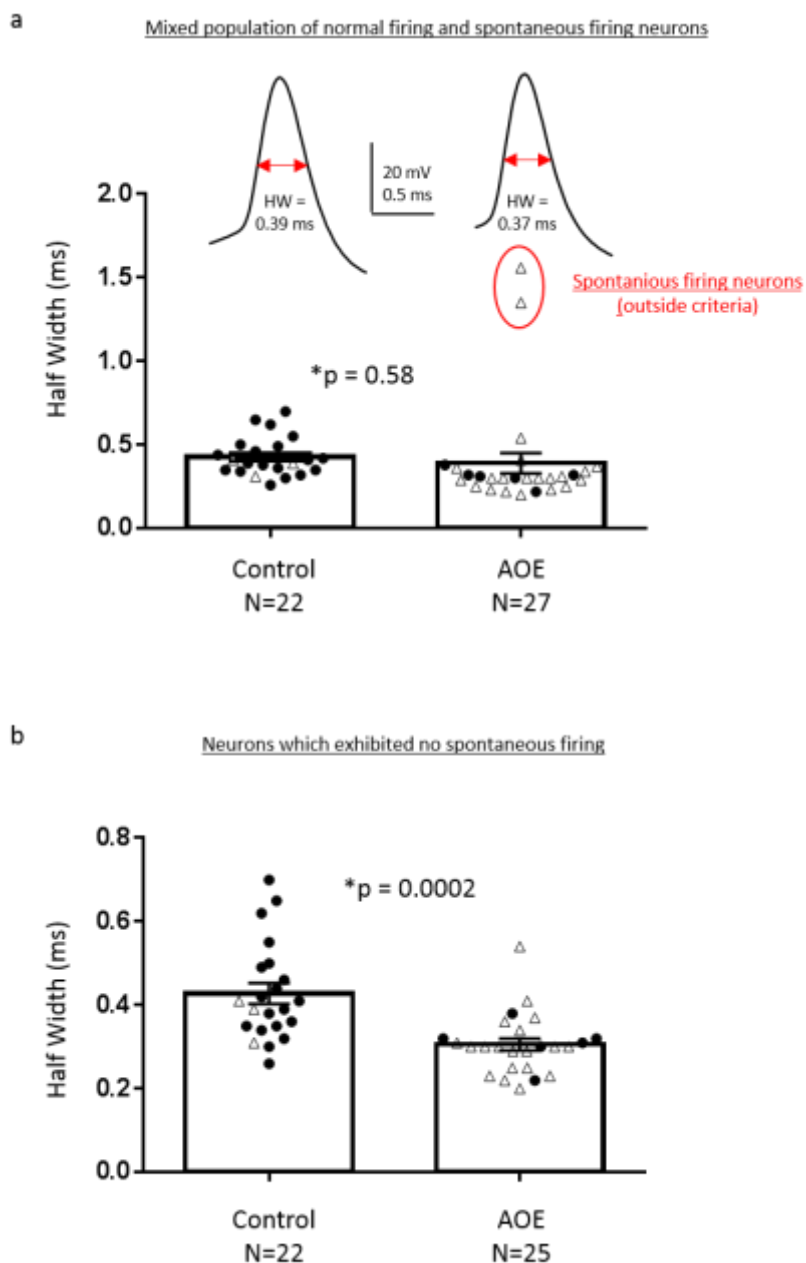


**Fig 5.3. MNTB: AP half width accelerates following AOE** **a.** Below: Bar chart showing half width of the first elicited AP from the MNTB of control and AOE mice. Control =  $0.43 \pm 0.03$  ms (Mean  $\pm$  SEM),  $n = 22$ , AOE =  $0.39 \pm 0.06$  ms,  $n = 27$ , with no significant difference found ( $p = 0.5816$ ) as measured by an unpaired t-test with Welch's correction. Filled circles represent single-spiking neurons, open triangles indicate multi-spiking neurons. Red circle highlights two neurons that showed spontaneous firing in the absence of current injection. Above: representative APs from a control neuron (left) and AOE neuron (right). **b.** Same data set showing mean half-width of control and AOE MNTB neurons, but with two outliers highlighted by red circle in part **a** removed (AOE only). Amended AOE mean =  $0.31 \pm 0.01$  ms,  $n = 25$ . A significant difference was found between control and AOE following removal of the spontaneous firing cells ( $p = 0.0002$ ).

### MNTB: $I_H$ current is unaffected by AOE

Following this, I wanted to assess if there were any changes to  $I_H$  current following AOE.  $I_H$  current is a slowly activating inward current, which is only activated by hyperpolarisation (Hille, 2001). In current clamp,  $I_H$  current can be activated by negative current injection step (in this instance  $-0.25$  nA), which hyperpolarizes the neuron. Here, the slowly activating inward current results in a membrane potential that is more positive at the end of the hyperpolarising current step than at the beginning of the current step, resulting in a hyperpolarising sag. Thus, by measuring the difference between the membrane potential at the beginning and the end of the hyperpolarising current step ( $-0.25$  nA), I can compare the difference in  $I_H$  activity between MNTB neurons from control and AOE treated mice. I found no significant difference in the hyperpolarising sag between control cells ( $8.74 \pm 1.61$  mV (mean  $\pm$  SEM),  $n = 22$ ) and following AOE, ( $11.26 \pm 1.33$  mV,  $n = 25$ ),  $p = 0.232$  (as measured via an unpaired t-test) (fig 5.4).

In summary, AOE does not alter  $I_H$  current in MNTB neurons.

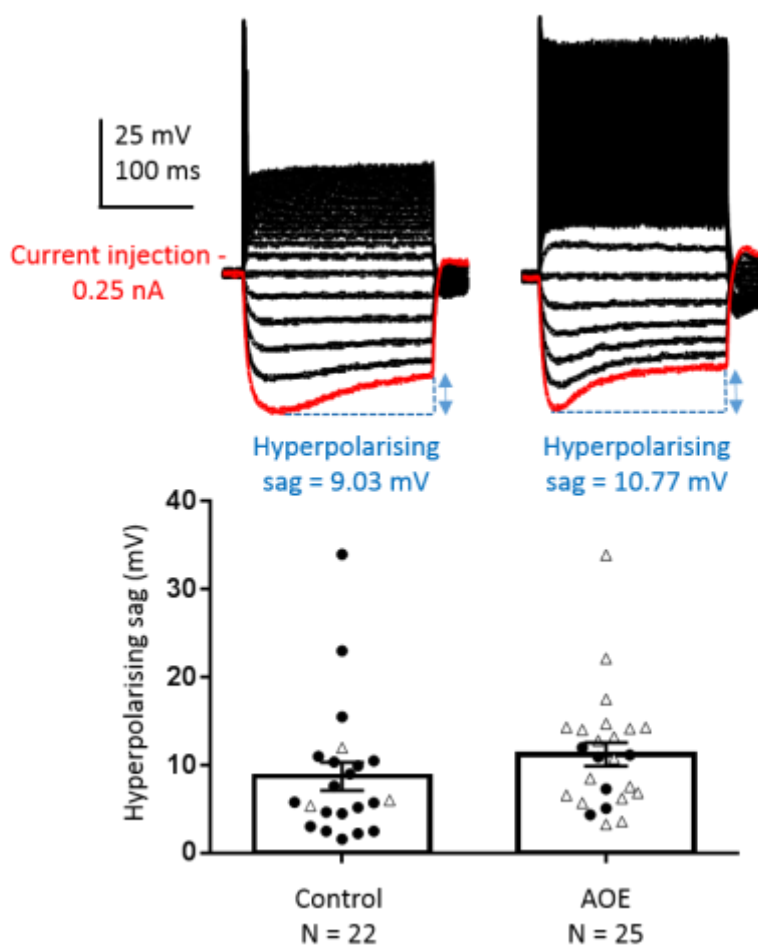
### MNTB: Amplitude of APs are unaltered by AOE

To assess whether AOE affected AP amplitude in the MNTB, three separate measurements of amplitude were taken from the first evoked AP of each cell: absolute amplitude, relative amplitude and the amplitude from baseline (fig 5.5, a). Absolute amplitude was defined as the membrane potential at which the AP peaks, whilst relative amplitude was the difference between the membrane potential where the AP was initiated and the absolute amplitude. Amplitude from the baseline was defined as the difference between the absolute amplitude and the membrane potential before the current injection step, where the membrane potential of the neuron was held at  $-60$  mV.

For each measure of amplitude, there was no change in the AOE group compared to control. Specifically, absolute amplitude values for control and AOE conditions were:  $1.94 \pm 1.6$  mV (Mean  $\pm$  SEM),  $n = 22$ , and  $-2.74 \pm 1.81$  mV,  $n = 25$ ,  $p = 0.7466$  (as measured by unpaired t-test) (fig 5.5, b). Relative amplitude: control =  $33.77 \pm 1.92$

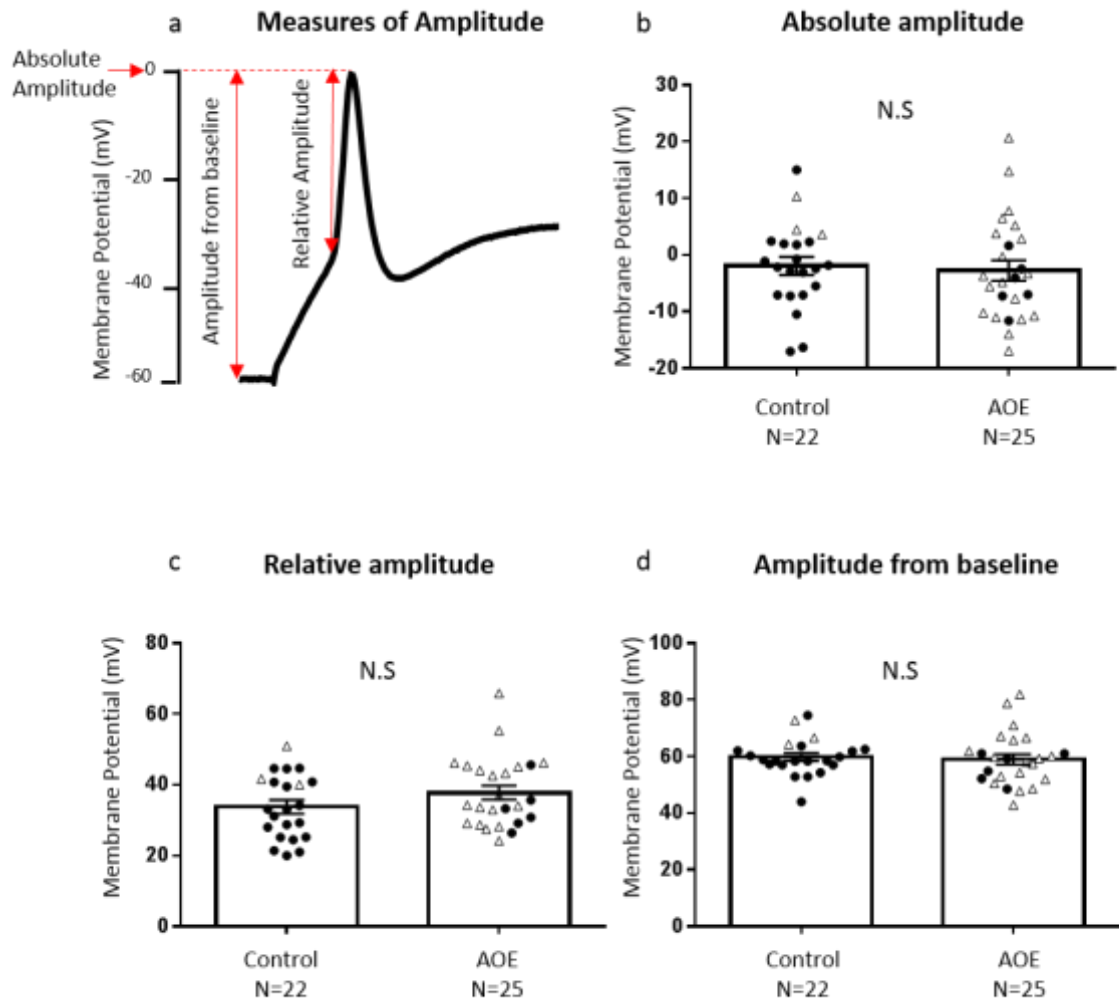
mV,  $n = 22$  and AOE =  $37.8 \pm 1.99$  mV,  $n = 25$   $p = 0.1549$  (fig 5.5, c). Amplitude from baseline: control =  $59.84 \pm 1.39$  mV,  $n = 22$  & AOE =  $58.96 \pm 1.87$  mV  $n = 25$ ,  $p = 0.7143$  (fig 5.5, d).

Figure 5.4 MNTB: Hyperpolarising sag is not affected by AOE.



**Fig 5.4. MNTB: Hyperpolarising sag is not affected by AOE.** Above: Example current clamp recordings from control and AOE mice. The amplitude of the hyperpolarising sag in response to  $-0.25$  nA current injection (red) was given as the difference between the membrane voltage (mV) at its most negative point during the current injection and the least negative point (as indicated by the blue dashed lines). Below: Mean amplitude of hyperpolarising sag for both control and AOE mice ( $8.74 \pm 1.61$  mV (mean  $\pm$  SEM),  $n = 22$ ,  $11.26 \pm 1.33$  mV,  $n = 25$ ) respectively. Filled circles represent single-spiking neurons, open triangles indicate multi-spiking neurons. There is no significant difference in hyperpolarising sag amplitude between control and AOE groups ( $p = 0.232$ ).

Figure 5.5 MNTB: AP amplitude is not affected by AOE



**Fig 5.5. MNTB: AP amplitude is not affected by AOE.** APs were recorded from the MNTB of both control and AOE mice in response. The first AP elicited in response to depolarising current injection was then analysed. **a.** Diagram of an action potential showing the different measures of amplitude. **b.** Absolute amplitude: Control =  $-1.94 \pm 1.6$  mV (Mean  $\pm$  SEM),  $n = 22$ , AOE =  $-2.74 \pm 1.81$  mV,  $n = 25$ ,  $p = 0.7466$  (unpaired t-test). **c.** Relative amplitude: Control =  $33.77 \pm 1.92$  mV, AOE =  $37.8 \pm 1.99$  mV,  $p = 0.1549$ . **d.** Amplitude from baseline: Control =  $59.84 \pm 1.39$  mV, AOE =  $58.96 \pm 1.87$  mV,  $p = 0.7143$ . Filled circles indicate single spiking neurons, open triangles represent multi-spiking neurons.

**MNTB: AP threshold was lowered following AOE, however RMP and AHP remain unaffected**

Next, I analysed other properties of the first elicited AP from the MNTB, as well as the RMP to establish if AOE changes the excitability of MNTB neurons. Here, the AP threshold (membrane potential at which AP is initiated) was found to be significantly lower in the AOE group compared to the control ( $-40.45 \pm 0.89$  mV, (mean  $\pm$  SEM),  $n = 25$  and  $-35.12 \pm 1.32$  mV,  $n = 22$ ) respectively,  $p = 0.0013$  (as measured via unpaired t-test) (fig 5.6, a). In turn, the amount of current injection needed to evoke an AP was lower in the AOE group ( $283 \pm 22$  pA (mean  $\pm$  SEM),  $n = 25$ ) compared to control cells ( $384 \pm 24$  pA,  $n = 22$ ),  $p = 0.0036$  (unpaired t-test) (data not shown). In contrast AOE did not alter the RMP (control =  $-50.37 \pm 1.39$  mV,  $n = 22$  and AOE =  $-50.35 \pm 1.27$  mV,  $n = 25$ ,  $p = 0.9683$  (fig 5.6, b). AHP was also unaffected by AOE (control =  $10.15 \pm 0.85$  mV,  $n = 22$ , AOE =  $12.09 \pm 1.06$  mV,  $n = 25$ ),  $p = 0.1569$  (unpaired t-test) (fig 5.6 c).

In conclusion, AOE lowers the threshold of AP initiation in the MNTB, but has no effect on RMP or AHP. Lower thresholds would increase the likelihood of an AP firing in response to a given excitatory input, and therefore may be a compensatory adjustment for decreased excitatory input from the periphery following acoustic trauma.

**MNTB: Assessing low voltage activated currents**

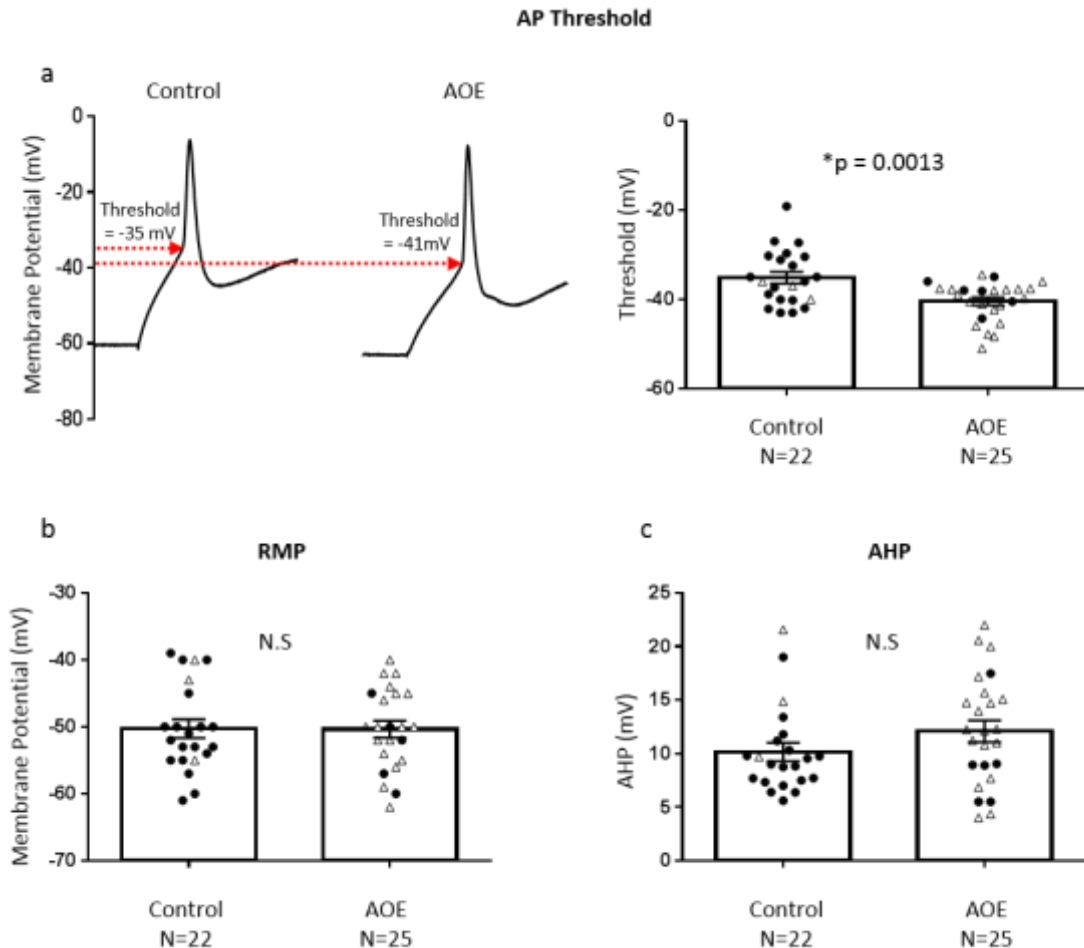
MNTB neurons usually fire a single AP in response to depolarisation due to the presence of Kv1 channels (Brew and Forsythe, 1995a) Kv1 channels have fast kinetics, and are described as 'low voltage activated' (LVA) channels, opening after only modest depolarisation, close to threshold. The presence of high levels of Kv1 mediated  $K^+$  current limits AP firing, so that only one AP, rather than a train of APs occur in response to a single depolarising input, thus reducing temporal summation (Oertel, 1983).

One hypothesis for the conversion from a single-spiking to multi-spiking phenotype in MNTB neurons following AOE, is that acoustic insult disrupts normal Kv1 function. Here, I examined currents produced under voltage clamp at  $-40$  mV HP, from an I/V

protocol, which consisted of 10 mV, steps from -90mV to +40 mV. At -40 mV, only LVA channels (including Kv1, Kv4 and Kv7) are open (Johnston et al., 2010). MNTB neurons are known to have high levels of Kv1, and thus one would expect to find lower current amplitudes at low voltages following AOE if the hypothesis was correct. Unfortunately, the I/Vs collected were of poor quality due to high series resistances (see discussion). Following AOE, there was a decrease in amplitude of currents measured at -40 mV ( $294 \pm 28$  pA,  $n = 7$ ), compared to control MNTB neurons ( $353 \pm 34$  pA (mean  $\pm$  SEM),  $n = 8$ ) however this difference was not significant ( $p = 0.2$ , as measured via an unpaired t-test) (fig 5.7).

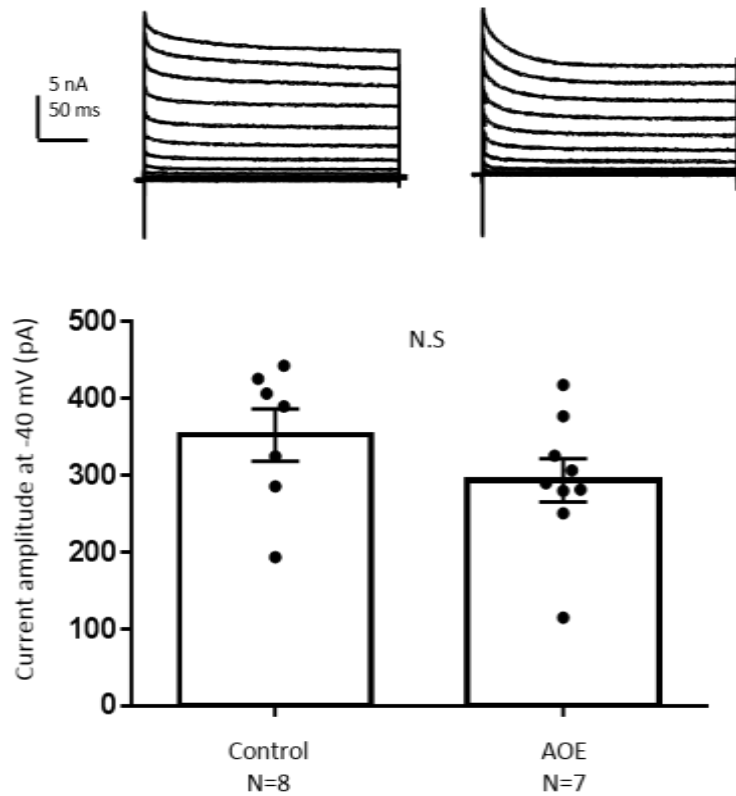
In summary, the aim here was to establish whether a decrease in LVA currents occurred in the MNTB following AOE, which would explain the dramatic switch of MNTB neurons from a single-spiking to multi-spiking phenotype. Whilst there was a decrease in the mean amplitude of LVA currents recorded in the AOE condition, this was not significant. Overall, data was of poor quality, with very high SR, and further experiments would be needed to establish whether an AOE mediated decrease in LVA currents occurs in the MNTB. The hyper-excitability of MNTB neurons following AOE could form the basis of a new project, to find a mechanism for the switch from single to multi-spiking AP firing pattern.

Figure 5.6 AP threshold is lowered following AOE, however RMP and AHP remain unaffected



**Fig 5.6. MNTB: AP threshold is lowered following AOE, however RMP and AHP remain unaffected.** **a.** AP threshold is lowered following AOE. Left: example APs recorded from both control and AOE mice. Red dashed line indicates membrane threshold of the first AP initiation. Right: Bar chart showing AP threshold from both control and AOE mice ( $-35.12 \pm 1.32$  mV (mean  $\pm$  SEM),  $n = 22$ ,  $-40.45 \pm 0.89$  mV,  $n = 25$  respectively). Control threshold is significantly higher ( $p = 0.0013$ , measured via unpaired t-test). **b.** RMP of MNTB neurons does not alter between control mice ( $-50.27 \pm 1.39$  mV,  $n = 22$ ) and AOE mice ( $-50.35 \pm 1.27$  mV,  $n = 25$ )  $p = 0.9683$ . **c.** AHP does not alter between control ( $10.15 \pm 0.85$  mV,  $n = 22$ ) and AOE mice ( $12.09 \pm 1.06$  mV,  $n = 25$ ),  $p = 0.1569$ . Filled circles indicate single-spiking neurons, open triangles represent multi-spiking neurons.

Figure 5.7 MNTB: Measuring low voltage threshold currents following AOE



**Fig 5.7. MNTB: Measuring low voltage threshold currents following AOE.** **Above:** Currents recorded from representative MNTB neurons of both control mice (left) and AOE mice (right) in response to 250 ms, 10 mV depolarising steps from -90 mV to +40 mV, from a HP of -60 mV. **Below:** Amplitude of currents recorded at the voltage step of - 40 mV for both control ( $353 \pm 33.9$  pA (mean  $\pm$  SEM),  $n = 8$ ), and AOE mice ( $294 \pm 28.32$  pA,  $n = 7$ ),  $p = 0.2$ , as measured by an unpaired t-test. Filled circles indicate individual data points.

## 5.2 LSO: THE EFFECT OF AOE ON INTRINSIC EXCITABILITY

In this section, I repeat the same analysis as performed in the MNTB, but instead focus on the effects of AOE on the intrinsic excitability of LSO principal neurons.

Unexpectedly, AOE had no effect on nearly all parameters measured.

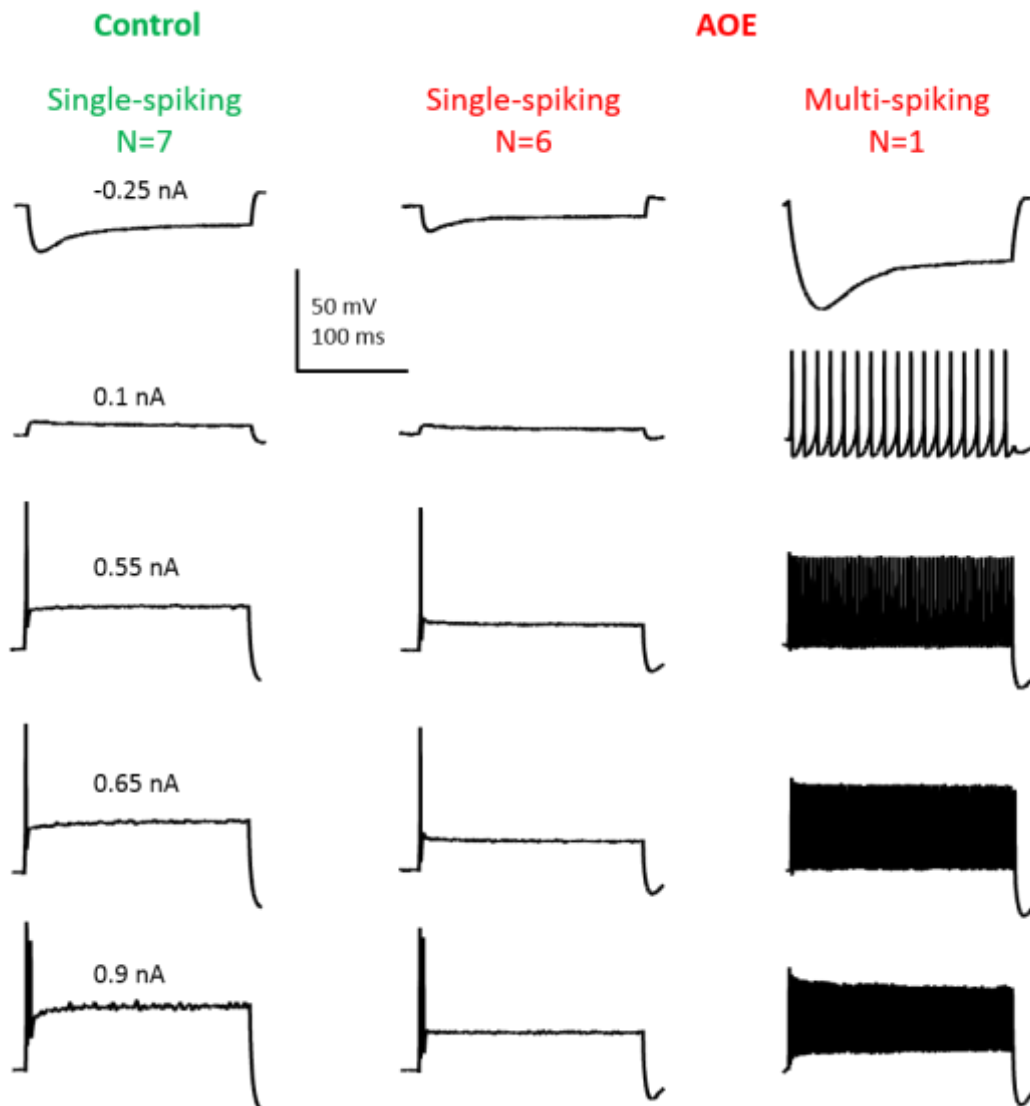
### LSO: AOE does not alter the AP firing pattern

I examined the effect of AOE on the AP firing phenotype of LSO principal neurons. This is less definitive than in the MNTB, as rather than possessing one principal cell type that primarily fires single APs (as the MNTB does), the LSO contains both single and multi-spiking principal neurons. However, by chance, all LSO principal neurons recorded in the control group were single-spiking ( $n=7$ ) and all but one cell in the AOE group were also single-spiking ( $n=6$ ) (fig 5.8). I therefore conclude AOE does not alter the AP firing pattern of LSO principal neurons.

### LSO: $I_H$ current is unaffected by AOE

Secondly, I wanted to identify whether AOE had any effect on  $I_H$  current in the LSO by examining the hyperpolarising sag in response to the most negative current injection of  $-0.25$  nA. No significant difference was detected between control ( $6.5 \pm 1.2$  mV, (mean  $\pm$  SEM),  $n = 7$ ) and AOE mice ( $8.3 \pm 2.7$  mV,  $n = 6$ ),  $p = 0.5748$  (unpaired t-test) (fig 5.9). One neuron in the AOE dataset (highlighted by red circle) possessed a much larger  $I_H$  current than the rest of the neurons tested. This neuron was the only multi-spiking LSO neuron observed (raw traces can be seen in fig 5.8, far right), and showed spontaneous AP firing in the absence of current injection. Spontaneous firing was also observed in 2 MNTB neurons following AOE, and were excluded from the dataset for reasons discussed earlier. Removal of the spontaneous firing neuron from the dataset did not alter the overall conclusion: AOE does not affect  $I_H$ . (The amended amplitude of the hyperpolarising sag in AOE mice was  $5.6 \pm 0.7$  mV,  $n = 6$ ,  $p = 0.5355$ ). The spontaneous firing neuron was then removed from all subsequent analysis.

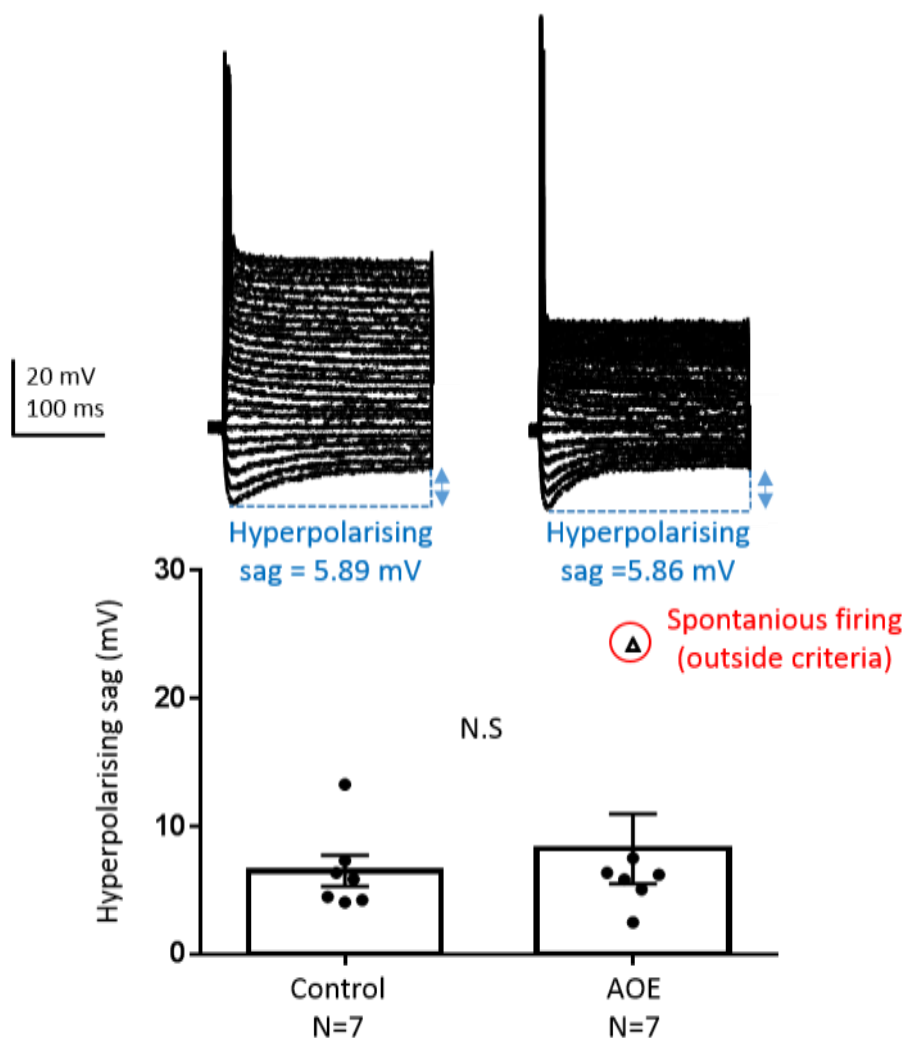
Figure 5.8 LSO: Single-spiking neurons do not convert to a multi-spiking phenotype following AOE



**Fig 5.8. LSO: Single-spiking neurons do not convert to a multi-spiking phenotype following AOE.**

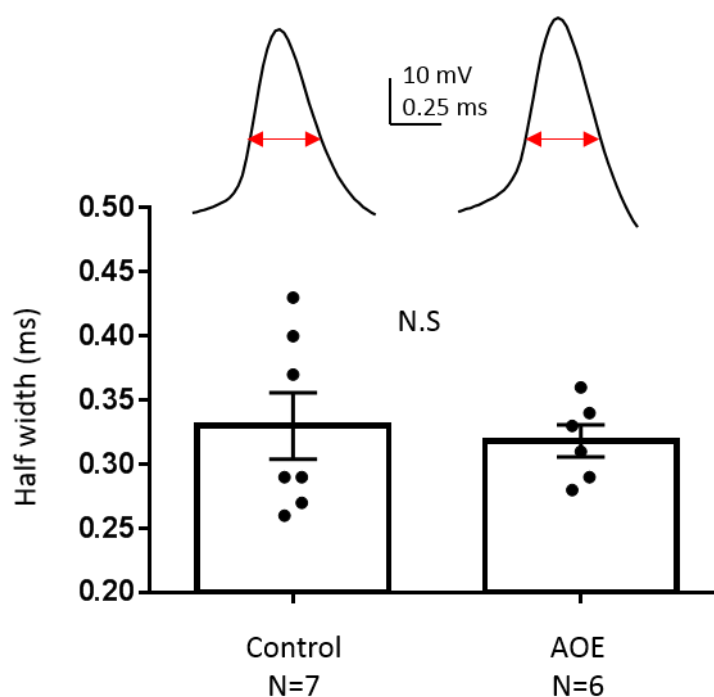
Select raw current clamp traces from LSO neurons, comparing the voltage response from control mice (green) and AOE mice (red) following 200 ms depolarising current injections from -0.25 to 0.9 nA, (shown top to bottom) from a HP of -60 mV. All LSO neurons tested from the control group were single-spiking ( $n = 7$ ). Following AOE 6 neurons were single-spiking, and 1 neuron was multi-spiking. All subsequent figures showing APs elicited from the LSO were recorded using the same current step protocol, from a HP of -60 mV, with a holding current which did not exceed  $\pm 600$  pA.

Figure 5.9 LSO: AOE does not affect hyperpolarising sag in the LSO



**Fig 5.9. LSO: AOE does not affect hyperpolarising sag in the LSO.** **Above:** Example current clamp recordings from LSO principal neurons from both control (left) and AOE mice (right). The amplitude of the hyperpolarising sag in response to  $-0.25$  nA current injection was given as the difference between the membrane voltage (mV) at its most negative point during the current injection and the least negative point (as indicated by the blue dashed lines). **Below:** Bar chart showing the amplitude of the hyperpolarising sag for both control ( $6.54 \pm 1.21$  mV, (mean  $\pm$  SEM),  $n = 7$ ) and AOE mice ( $8.26 \pm 2.72$  mV,  $n = 6$ ). No significant difference was observed  $p = 0.5748$  (as measured by an unpaired t-test). Red circle highlights a multi-spiking cell that showed spontaneous firing in the absence of current injection. With outlier removed, amended AOE =  $5.6 \pm 0.7$  mV,  $n = 6$ ,  $p = 0.5355$ . Filled circles represent single-spiking neurons, open triangles indicate multi-spiking neurons.

Figure 5.10 LSO: AP half width is not altered by AOE



**Fig 5.10. LSO: AP half width is not altered by AOE. Below:** Bar chart showing the half width of the first elicited AP from LSO principal neurons in control and AOE mice. Control =  $0.33 \pm 0.03$  ms (mean  $\pm$  SEM),  $n = 7$ , AOE =  $0.32 \pm 0.01$  ms,  $n = 6$ ,  $p = 0.7086$  (measured using an unpaired t-test). **Above:** Representative APs from a control neuron (left) and AOE neuron (right). Filled circles represent individual data points from single-spiking neurons.

#### LSO: AOE does not affect AP half width or amplitude

Following this, I compared the HW of the first elicited AP in response to depolarising current injections in LSO principal neurons. Fig 5.10 shows the mean half width of APs recorded from both control and AOE LSO neurons ( $0.33 \pm 0.03$  ms (mean  $\pm$  SEM),  $n = 7$  and  $0.32 \pm 0.01$  ms,  $n = 6$ ) respectively, with representative raw AP traces shown above for each condition. There was no significant difference in half width between APs recorded from control and AOE mice ( $p = 0.7086$ , as measured by unpaired t-test). This is in contrast to the MNTB, which showed an acceleration in half width following AOE. Next, the amplitude of the first evoked APs (LSO) were compared between control and AOE treated mice. Three measurements of amplitude were used as shown in fig 5.11 (a). For each measure of amplitude there was no change in the AOE group compared to control. Specifically, values of absolute amplitude in control and AOE cells were 9.93

$\pm 4.0$  mV (mean  $\pm$  SEM),  $n = 7$  and  $8.61 \pm 3.56$ ,  $n = 6$  respectively,  $p = 0.8814$  (unpaired t-test) (fig 5.11, b). Relative amplitude: control =  $45.91 \pm 3.56$  mV, AOE =  $49.97 \pm 4.05$  mV,  $p = 0.9337$  (fig 5.11, c). Amplitude from baseline: control =  $72.8 \pm 3.6$  mV, AOE =  $69.2 \pm 3.5$ ,  $p = 0.5051$  (fig 5.11, d).

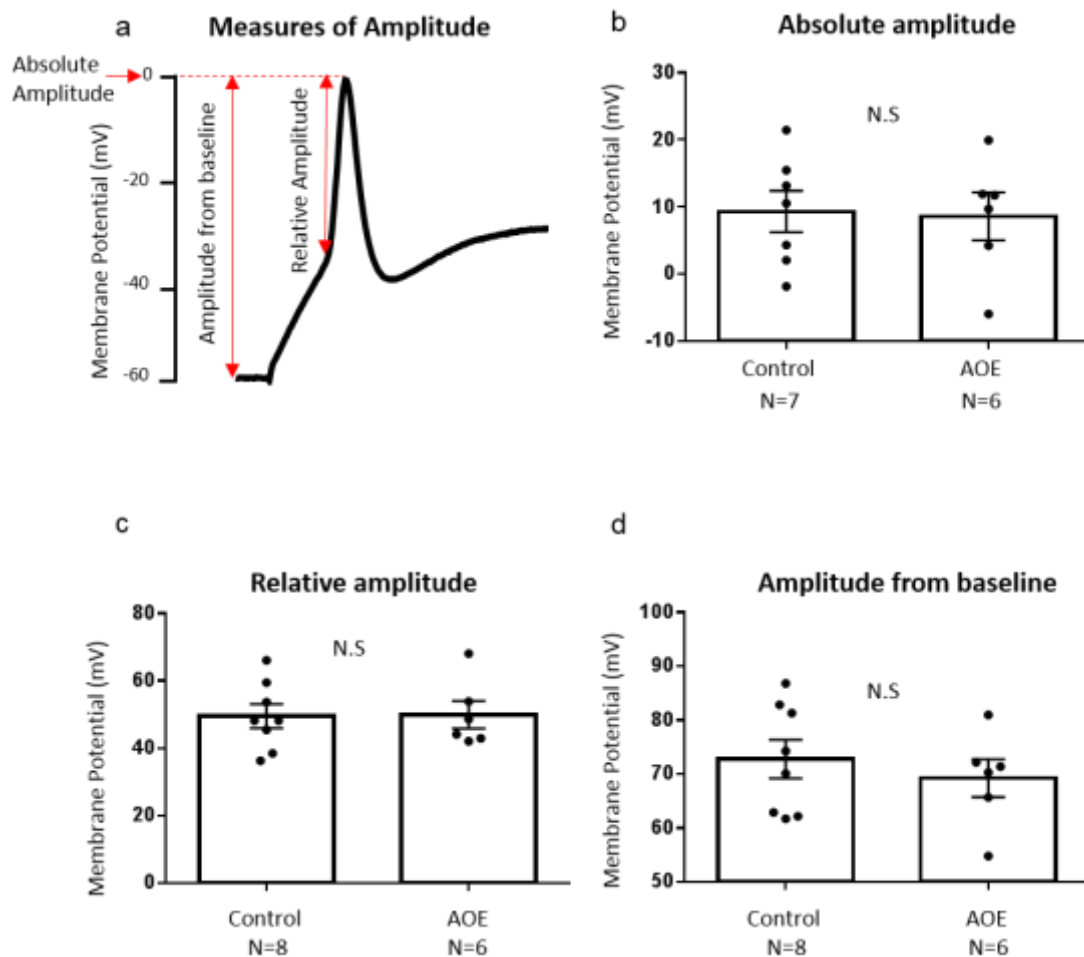
In conclusion, AOE does not alter the amplitude or HW of APs evoked from LSO principal neurons.

Next, I examined other characteristics of LSO principal neurons and their first evoked AP, to ascertain whether AOE alters any other properties. In contrast to the MNTB, LSO AP threshold was unaltered between control and AOE neurons ( $-38.73 \pm 2.3$  mV (mean  $\pm$  SEM),  $n=7$  &  $-41.32 \pm 2.35$  mV,  $n = 6$ , respectively),  $p = 0.4503$  (as measured via paired t-test) (fig 5.12, a). The amount of current injection needed to trigger an AP in the LSO was also unchanged between control and AOE neurons ( $581 \pm 69$  pA and  $525 \pm 40$  pA) respectively,  $p = 0.5314$  (unpaired t-test) (data not shown).

In contrast to the MNTB, RMP was significantly lower in LSO principal neurons from AOE treated mice (control =  $-44.43 \pm 2.19$  mV,  $n = 7$ , AOE =  $-53.17 \pm 1.94$  mV,  $p = 0.0135$ ) (fig 5.12, c). Finally, AHP from LSO principal neurons was unaltered following AOE (control =  $6.01 \pm 1.9$  mV,  $n = 7$ , AOE =  $6.79 \pm 1.3$  mV,  $n = 6$ ,  $p = 0.7246$ ) (fig 5.12 b).

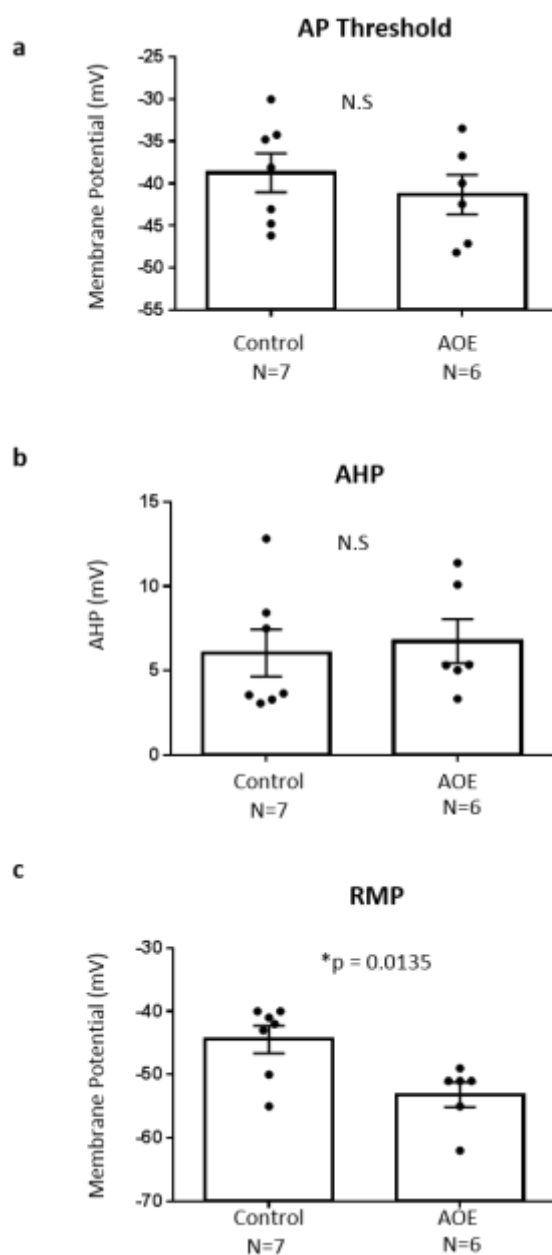
In summary, AOE does little to alter the intrinsic excitability of LSO principal neurons, with the exception of lowering the RMP. This is in stark contrast to the MNTB, where AOE caused dramatic changes to AP firing patterns, AHP, half width & initiation thresholds.

Figure 5.11 LSO: There is no change in AP amplitude following AOE



**Fig 5.11. LSO: There is no change in AP amplitude following AOE.** The amplitude of the first AP elicited in LSO principal neurons in response to depolarising current injection was analysed in a variety of ways. **a.** Diagram of an action potential showing the different measurements of amplitude. **b.** Absolute amplitude: Control =  $9.93 \pm 4$  mV (mean  $\pm$  SEM),  $n = 7$ , AOE =  $8.61 \pm 3.56$  mV,  $n = 6$ ,  $p = 0.8814$ , as measured by an unpaired t-test. **c.** Relative amplitude: Control =  $45.91 \pm 3.56$  mV, AOE =  $49.97 \pm 4.05$  mV,  $p = 0.9337$ . **d.** Amplitude from baseline: Control =  $72.77 \pm 3.57$  mV, AOE =  $69.24 \pm 3.53$ ,  $p = 0.5051$ . Filled circles represent individual data points from single-spiking neurons.

Figure 5.12 LSO: RMP is reduced following AOE



**Fig 5.12. LSO: RMP is reduced following AOE.** APs were recorded from LSO principal neurons in both control and AOE mice. **a.** AOE does not alter AP threshold: Control =  $-38.73 \pm 2.3$  mV (mean  $\pm$  SEM), n=7, AOE =  $-41.32 \pm 2.35$  mV, n = 6, p = 0.4503 (as measured by unpaired t-test). **b.** AOE does not alter AHP: Control =  $6.05 \pm 1.4$  mV, AOE =  $6.74 \pm 1.3$  mV, p = 0.7246. **c.** AOE reduces RMP: Control =  $-44.43 \pm 2.19$  mV, AOE =  $-53.17 \pm 1.94$  mV, p = 0.0135. Filled circles represent individual data points from single-spiking neurons.

### 5.3 LSO: THE EFFECT OF AOE ON SYNAPTIC EXCITABILITY

Having studied the effect of AOE on the LSO and MNTB, next I wanted to examine any changes in the synaptic excitability of LSO principal neurons. I have chosen to focus solely on the LSO and not the MNTB for a number of reasons. Firstly, the MNTB receives only one large presynaptic input (the calyx of Held) which can be easily damaged in the slicing process. Damage to the CN input can render an MNTB neuron incapable of producing postsynaptic currents, and thus the chance of successful recordings is much lower in the MNTB compared to the LSO. Secondly, previous work in the lab has focused on AMPAR mediated EPSCs in LSO principal neurons. Here I have replicated these experiments, and have expanded the findings by recording NMDAR EPSCs from LSO principal neurons, using the same AOE protocol to allow direct comparison.

#### AMPA EPSCs slow following AOE

Firstly, I examined the effect of AOE on AMPAR mediated EPSCs evoked from LSO principal neurons. EPSCs were recorded using a bipolar stimulating electrode placed over the fibers between the ipsilateral CN and the LSO (see chapter 2, fig 2.6), using stimulation pulses of 20  $\mu$ s duration at a frequency of 0.25 Hz, amplitude (0.1 - 99V), supplied by a constant voltage stimulator. AMPAR EPSCs were pharmacologically isolated by perfusing the brain slice with aCSF containing 1  $\mu$ M strychnine, 10  $\mu$ M bicuculline, and 20  $\mu$ M d-AP5, to block glycineRs, GABARs and NMDARs respectively. Following AOE, AMPAR mediated EPSC mean decay tau was significantly slower compared to age matched controls.

Figure 5.13 (a) shows representative example traces of AMPAR mediated EPSCs from HP -70 mV from an LSO neuron from a control mouse (above, green) and from a mouse which had been subjected to AOE (below, blue). Here, the decay tau is slower following AOE (2.5 ms), compared to the control condition (1.09 ms). The decay tau and rise time values of AMPAR EPSCs are summarised in Fig 5.13 b. LSO AMPAR EPSCs decay tau is significantly slower in the AOE treated mice (control =  $0.97 \pm 0.09$  ms, (mean  $\pm$  SEM), n = 4 and AOE =  $1.8 \pm 0.28$  ms, n = 4), p = 0.0387 (as determined via an unpaired t-test). Rise-time was defined as the time it takes the EPSC to reach peak

amplitude from its baseline membrane potential following stimulation. In contrast to the decay tau, LSO AMPAR EPSC rise-time was unaltered by AOE (control =  $0.88 \pm 0.22$  ms,  $n = 4$  and AOE =  $0.97 \pm 0.18$  ms,  $n = 4$ ),  $p = 0.7405$  (fig 5.13, b).

The slowing of LSO AMPAR EPSC decay tau following AOE may be due to changes in AMPAR subunit expression (see discussion). Indeed, qRT PCR performed on isolated LSO sections showed two key changes in mRNA expression after AOE (fig 5.13, c). Firstly there was an increase in GluA1 mRNA ( $p = 0.022$ ), and secondly GluA4 subunit expression decreased ( $p = 0.019$ ). Significance was determined via one way ANOVA in both instances. Data from figure 5.13 (c) was collected and analysed by Dr Haresh Selvaskand.

LSO AMPAR EPSCs from control and AOE treated mice were previously recorded in the lab by Dr Nadia Pilati, using the same AOE protocol as used in my experiments (110 dB SPL broadband stimulus for 2 hours). She also observed an AOE mediated slowing of LSO AMPAR EPSC decay kinetics, however overall AMPAR EPSCs had faster decay kinetics than shown in my experiments. Fig 5.14 shows AMPAR EPSC data collected from control and AOE animals by Dr Nadia Pilati in part a, and for comparison, AMPAR EPSC data collected by myself in part b (this is the same data as shown in Fig 5.13 a and b). Decay tau of LSO AMPAR EPSCs recorded by Dr Nadia Pilati were  $0.69 \pm 0.05$  ms, (mean  $\pm$  SEM),  $n = 11$  in control LSO principal neurons (green), and  $1.23 \pm 0.05$  ms in AOE condition, (blue),  $n = 13$ ,  $P < 0.001$  (fig 5.14, a). Overall LSO AMPAR EPSCs recorded by myself were slower compared to those recorded by Dr Pilati (see discussion).

In summary, AOE slows AMPAR mediated EPSCs in the LSO. This change has previously been observed in the lab, however overall decay kinetics were slower than previously observed, for reasons that will be discussed later.

Figure 5.13 LSO: AOE slows AMPAR EPSC decay time constant

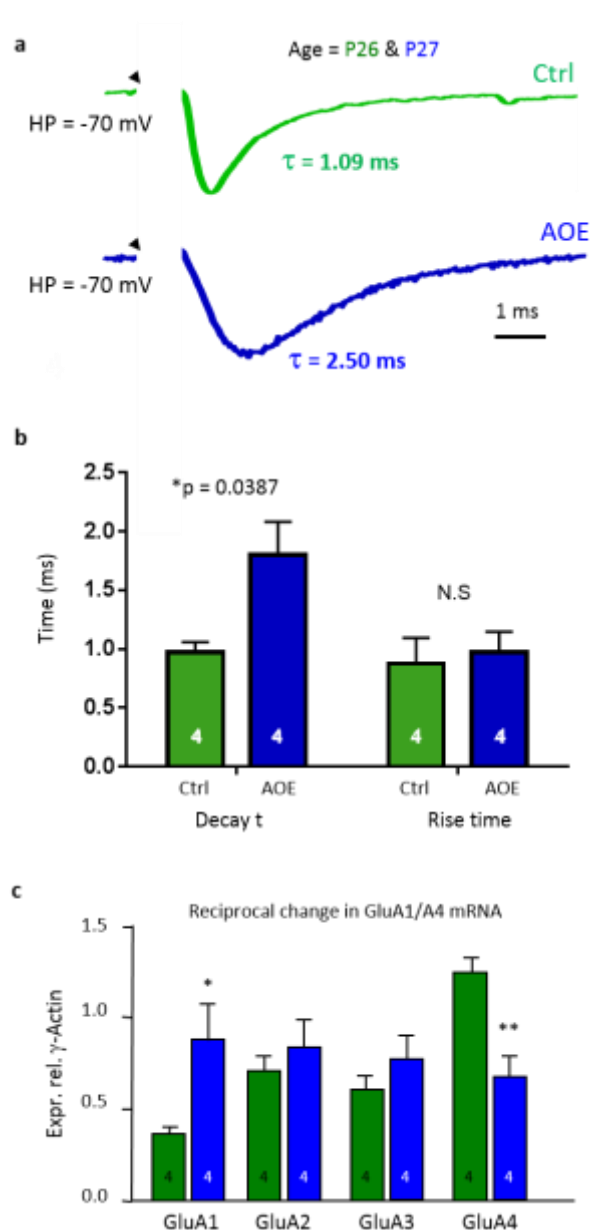
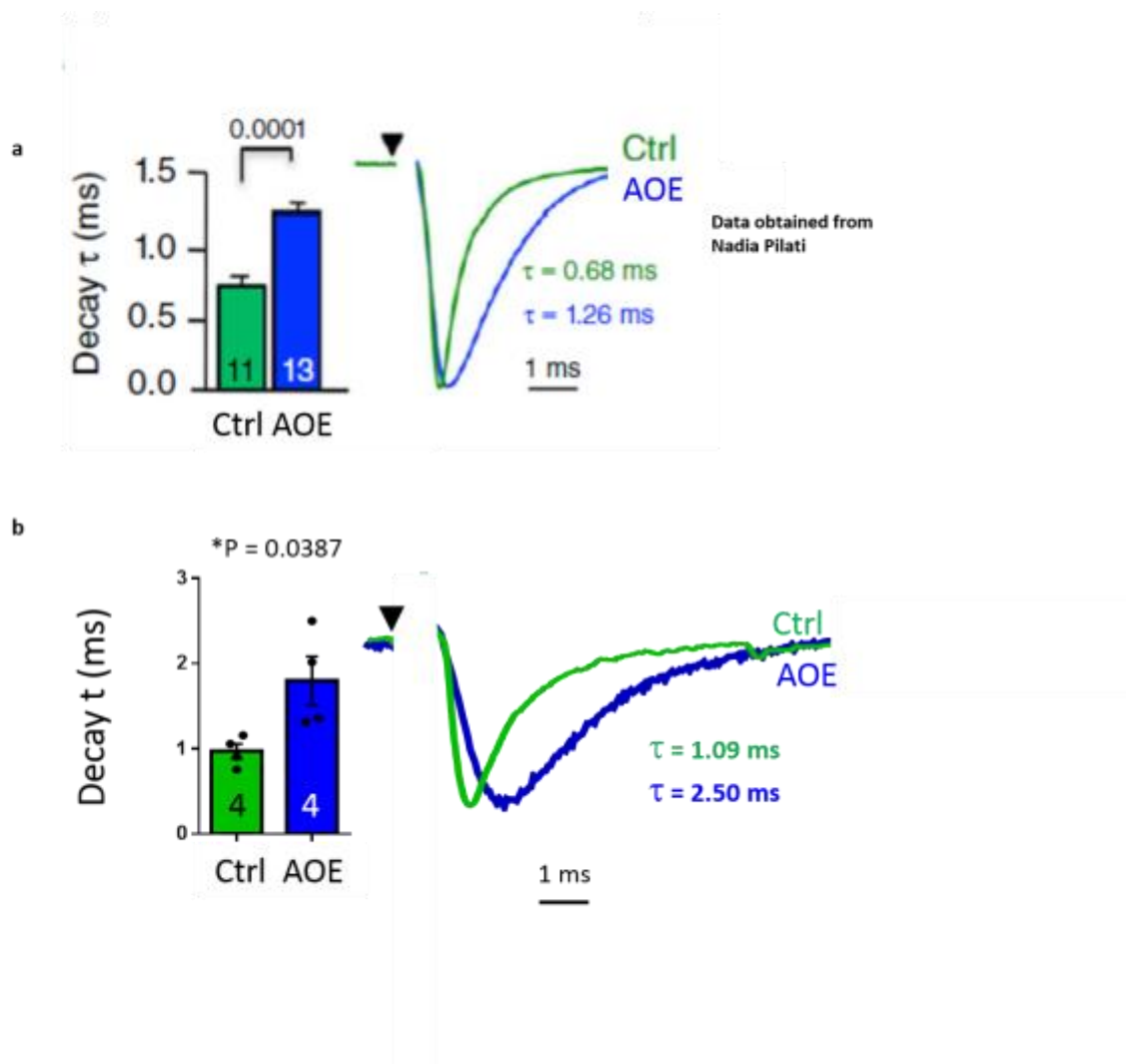


Figure 5.14 LSO: Comparison of my AMPAR EPSC data set to published results



**Fig 5.14. LSO: Comparison of my AMPAR EPSC data set to published results. a.** Data collected by Dr Nadia Pilati (previous member of the lab) shows a slowing in AMPAR EPSCs following AOE. Left: bar chart showing mean AMPAR EPSC decay tau from LSO principal neurons, recorded in the presence of 10  $\mu$ M bicuculline, 0.5  $\mu$ M strychnine and 20  $\mu$ M d-AP5 (control =  $0.699 \pm 0.05$  ms, (mean  $\pm$  SEM), n = 11 (green); AOE =  $1.23 \pm 0.05$  ms, n = 13 (blue). Right: Example EPSCs from control and AOE mice (HP = -70 mV). **b.** My own data-set, as shown in fig 5.13 (b). A similar increase in decay kinetics is observed following AOE, however overall decay tau is longer (control =  $0.97 \pm 0.09$  ms, (mean  $\pm$  SEM), n = 4 and AOE =  $1.8 \pm 0.28$  ms, n = 4). Age range of mice tested in part a is older (P29-P36) compared to my own data set in part b (P23-P27).

AOE accelerates rise-time of NMDAR EPSCs in the LSO, but does not alter decay tau

Finally, I examined the effects of AOE on NMDAR mediated EPSCs in LSO principal neurons. NMDAR EPSCs were pharmacologically isolated by perfusing the slices with aCSF containing 10  $\mu$ M bicuculline, 1  $\mu$ M strychnine and 10  $\mu$ M NBQX to block GABARs, glycineRs and AMPARs respectively. Fig 5.15 (a) shows an I/V of EPSCs from a representative LSO neuron taken from a control mouse (P23). A classic non-linear I/V relationship was observed consistent with NMDAR EPSCs. Current amplitude is lower at negative HPs compared to positive HPs, due to external  $Mg^{2+}$  block of the NMDARs at negative potentials (Nowak et al., 1984, ChesnoyMarchais and Barthe, 1996). To the left are average raw traces from HPs of -70 mV and +40 mV, again illustrating non-linearity of the response, where the amplitude is much greater at +40 mV than -70 mV.

In chapter 3 it was shown that NMDAR EPSCs with mature decay kinetics (<20 ms) displayed a rapid, irreversible run-down in amplitude when held at +40 mV, taking only  $43.4 \pm 1.8$  secs (mean  $\pm$  SEM),  $n = 5$ , to reach half the initial amplitude (fig.3.12 & 3.13). This run-down in amplitude has the potential to skew current voltage relationships, as NMDAR EPSC currents collected soon after stepping to +40 mV may be larger in amplitude compared to those collected a few minutes later. Thus, it was vital a clear criteria was established, to show the EPSCs recorded were indeed non-linear in accordance with  $Mg^{2+}$  block, and not simply as a result of amplitude run-down over time. To achieve this, EPSCs were recorded at a HP of -70 mV, after which the HP was immediately increased to +40 mV. The amplitude of the EPSC recorded at HP of +40 mV could be used to calculate amplitude at -70 mV, assuming a linear I/V. If the actual amplitude of the EPSC recorded at HP -70 mV was smaller than the calculated amplitude, this showed non-linearity. As the EPSCs recorded at HP of -70mV were recorded immediately before the EPSCs at HP of +40 mV, we can assume the 'run-down' effect seen previously has no influence on the EPSC amplitudes.

Previously, I have shown immature NMDAR EPSCs decay with a double exponential comprising a  $\tau_{fast}$  of  $44.8 \pm 5.4$  ms and a  $\tau_{slow}$  of  $115 \pm 17.1$  ms ( $n = 8$ ), where  $\tau_{slow}$  contributed 34% of the total amplitude. Upon maturation,  $\tau_{fast}$  accelerated to  $\sim 3$  ms, whilst the  $\tau_{slow}$  component was significantly reduced to limits of detectability,

contributing only 8.7% to the total amplitude. Following AOE,  $\tau_{\text{slow}}$  could no longer be detected, meaning EPSC decay tau could only be reliably fit using a single exponential.

The decay tau and rise-times of NMDAR EPSCs from control and AOE mice are summarised in fig 5.15 (c). Decay tau was unaltered following AOE, with both control and AOE treated mice showing similarly fast kinetics ( $2.6 \pm 0.4$  ms, (mean  $\pm$  SEM)  $n = 6$ , and  $2.2 \pm 0.3$  ms,  $n = 11$ ) respectively,  $p = 0.351$  (as measured via unpaired t-test). In contrast, rise-time was significantly faster compared to control neurons (control =  $0.99 \pm 0.06$  ms  $n = 6$ , AOE =  $0.60 \pm 0.07$  ms,  $n = 8$ ),  $p = 0.002$  (unpaired t-test). The acceleration in rise-time following AOE was accompanied by an increase in GluN1b mRNA ( $p = 0.001$ ), while GluN1a and the GluN2 subunits were unchanged (fig 5.15, d). The inset in fig 5.15 (d) shows the developmental maturation of expression of GluN2 subunits in the LSO, where GluNC dominates  $>P15$ , which may contribute to the developmental acceleration observed previously (chapter 3, section 3.2).

In summary, AOE has no effect on the decay kinetics of NMDAR EPSCs in LSO principal neurons, however rise-time of NMDAR EPSCs is faster following AOE, accompanied by an increase in GluN1b mRNA.

Figure 5.15 LSO: NMDAR EPSC rise-time is accelerated following AOE, yet decay kinetics are unaffected.

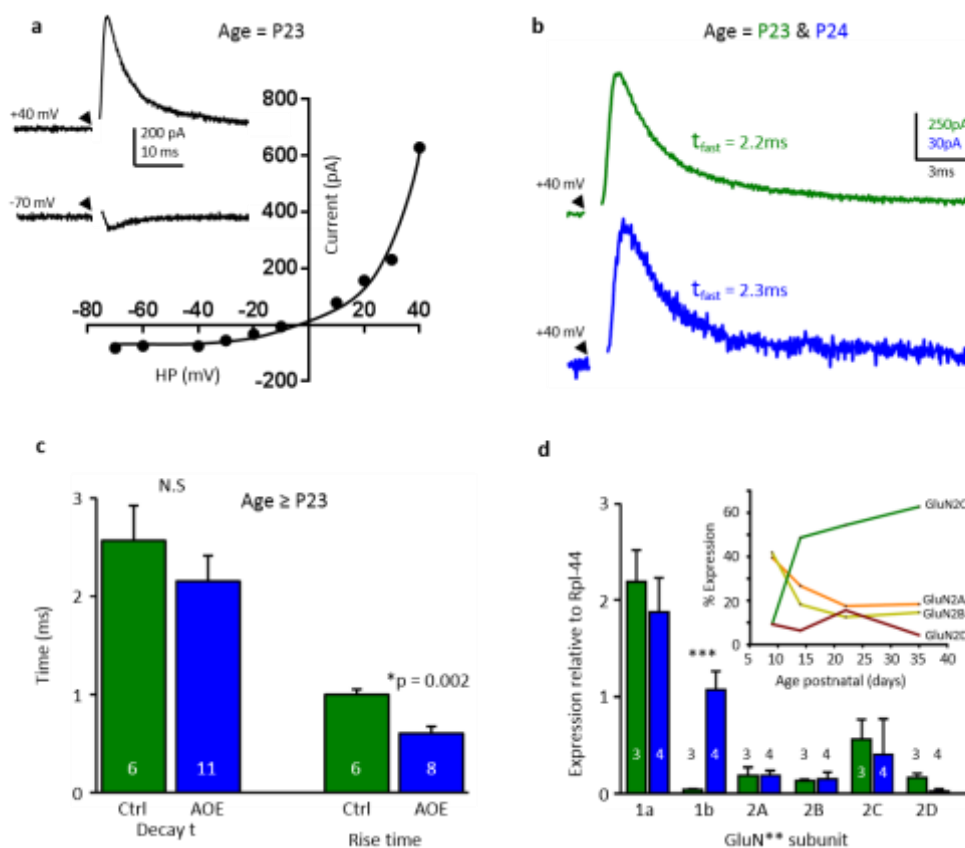


**Fig 5.15. LSO: NMDAR EPSC rise-time is accelerated following AOE, yet decay kinetics are unaffected.** AOE in mature mice increased GluN1b mRNA and decreased the NMDAR-EPSC rise time, but had no impact on decay time-course. **a.** NMDAR EPSC I/V curve from a mature mouse aged P23, recorded in the presence of 10 $\mu$ m bicuculline, 1 $\mu$ m strychnine and 10 $\mu$ m NBQX. Inset: Average traces from HP +40 mV and -70 mV. **b.** Normalized NMDAR EPSCs from control (green) and AOE (blue) exposed mice (>P23) show similar decay time-course at +40 mV HP. **c.** Bar chart showing NMDAR EPSC decay tau and rise-time for control and AOE mice. There is no change in decay tau (control =  $\tau_{fast}$  of  $2.6 \pm 0.4$  ms, (mean  $\pm$  SEM) n = 6 and AOE =  $\tau_{fast}$  of  $2.2 \pm 0.3$  ms, n = 11, p = 0.351 however rise-time is significantly faster following AOE (control =  $0.99 \pm 0.06$  ms, n = 6, AOE =  $0.60 \pm 0.07$  ms (n = 8), p = 0.002). Statistical comparison was via unpaired t-tests. **d.** Relative expression of GluN1 and GluN2 subunit mRNA in the LSO from control and following AOE. GluN1b mRNA at P35 was significantly increased following AOE (p=0.001, via unpaired t-test). Inset: Developmental profile of GluN2 subunit mRNA expression shows GluN2C mRNA levels increase and dominate over maturation. Statistical comparison was performed using one-way ANOVA (\*\*\* p < 0.0001). **Declaration:** 7 cells from the AOE group in part c were recorded and analysed by Dr Naida Pilati, and merged with my existing data set. All data in part d was collected, analysed and presented by Dr Haresh Selvaskandan.

## 5.4 DISCUSSION

In this chapter I have assessed whether AOE changes the intrinsic and synaptic excitability of neurons in the SOC. Following AOE, the intrinsic excitability of MNTB neurons was significantly altered, yet surprisingly the LSO remained largely unaffected. In contrast, the LSO underwent significant changes in synaptic excitability, yet no one has shown any evidence of long term synaptic plasticity in the MNTB. The main findings are summarised below:

### **AOE mediated changes:**

#### **MNTB**

- Neurons show hyper-excitability (switch from single-spiking to multi-spiking AP firing pattern).
- AP half-width accelerates from 0.43 ms (mean) in control mice to 0.39 ms following AOE.
- AP threshold is more negative (-35 mV (mean) in control mice & -40 mV following AOE).

#### **LSO**

- RMP is more negative, (-44 mV (mean) in control mice & -53 mV following AOE).
- AMPAR mediated EPSC decay tau slows from 0.97 ms (mean) in control mice to 1.8 ms following AOE.
- NMDAR EPSCs show accelerated rise-time from 1 ms (mean) in control mice to 0.6 ms following AOE.

What are the possible causes for the AOE mediated changes listed above? I will first focus on intrinsic and synaptic changes in the MNTB, and then discuss the AOE mediated changes to LSO principal neurons.

#### **MNTB: Neurons show hyper-excitability following AOE**

In current clamp mode, MNTB neurons typically fire with a single AP at the beginning of a depolarising current step, and maintain this single-spiking AP firing pattern with increased current injection. The origin of the single-spiking AP is due to the action of

LVA Kv1 channels, which open in response to minor depolarisation (close to RMP), ensuring only 1 AP is fired in response to a single depolarising input, thus reducing temporal summation (Clark et al., 2009, Dodson et al., 2002). Without Kv1 mediated current, neurons remain more depolarised following the initial AP, increasing the likelihood of triggering another AP. Kv1 channels are highly expressed in the MNTB, and are composed of Kv1.1 and Kv1.2 subunits (Brew and Forsythe, 1995b, Dodson et al., 2002). Blocking Kv1 channels with DTX-I (a Kv1 antagonist) in MNTB neurons results in a multi-spiking AP firing pattern in response to a single depolarising EPSP, and a more negative AP threshold (Dodson et al., 2002, Brew and Forsythe, 1995a).

Following AOE, a dramatic switch occurred in the MNTB from a predominantly single-spiking to multi-spiking phenotype. APs reached up to ~100 APs in response to the highest levels of current injection (fig 5.2), similar to the hyper-excitability observed following DTX-I application. I therefore believe AOE-mediated disruption of Kv1 mediated current is responsible for the hyper-excitability and increased AP threshold of MNTB neurons. In support of this hypothesis, AOE also caused a negative shift in AP threshold (control =  $-35.12 \pm 1.32$  mV (mean  $\pm$  SEM), n = 22, AOE =  $-40.45 \pm 0.89$  mV, n = 25), consistent with decreased Kv1 current (Dodson et al., 2002).

#### Assessing LVA currents in the MNTB

Reduced Kv1 current following AOE should manifest as reduced current at -40 mV HP compared to control (fig 5.7). Whilst the mean amplitude at -40 mV in the AOE treated mice was lower than control, this difference was not significant, most likely due to the quality of the data and subsequent variability. Low quality I/V data was due to high SRs. At the time of recording, the priority of the experiments was to collect current clamp data from MNTB neurons. Secondary to this I/Vs were recorded, often 6 to 7 minutes following whole cell configuration. During this time, SR climbed up to mean values of 23.5 MOhm (control) and 20.4 MOhm (AOE), both outside my normal criteria for acceptance (15 MOhm). This was reflected by low amplitudes at +40 mV HP, which is normally ~15-20 nA, but was as low as 3 nA in this data set, due to high series resistances.

Clearly further experiments with higher quality data and lower comparable series resistances between the control and AOE MNTB neurons are needed to uncover whether AOE affects LVA currents. Unfortunately, due to time constraints I was unable to undertake further testing. If time had allowed, I would have compared the amplitude of LVA currents in the MNTB with and without the presence of DTX I (Kv1 antagonist) in control and AOE treated mice. Here, if Kv1 mediated currents were disrupted following AOE, DTX I should have less effect on the already depressed Kv1 currents in the AOE condition.

#### Possible mechanisms of diminished Kv1 activity

Whilst it is likely AOE mediated disruption of Kv1 mediated currents causes hyper-excitability in the MNTB, the mechanism remains unclear. There exists two possibilities 1) Kv1 channels remain at the membrane, but are modulated (such as by phosphorylation) resulting in depressed current & 2) The number of Kv1 channels at the membrane is reduced. Is there any evidence for either of these hypotheses?

##### 1) Modulation of Kv1 channels

Youssofian and Walmsley (2007) showed excitability of MNTB neurons was increased following application of brain derived neurotrophin factor (BDNF). Here, brain slices from CBA mice (P12-14) were incubated with BDNF 2 hours prior to patch clamping, resulting in around half the MNTB neurons firing >4 APs in response to 0.2 nA current injection (200 ms). In contrast, only 13% of control neurons fired > 4 APs (2 out of 15 neurons). Similarly, in my study 14% of MNTB neurons in the control condition also fired > 5 APs (3 out of 22 neurons), re-emphasising that incidents of multi-spiking MNTB neurons under control conditions are low.

Youssofian et al (2007) found that overall outward  $K^+$  currents were reduced in MNTB neurons treated with BDNF, particularly LVA currents. Reduced LVA currents, and concomitant hyper-excitability of MNTB neurons could be due to phosphorylation of Kv1 channels, via BDNF activation of tropomyosin receptor kinase B (TrKB). Indeed, TrKB receptors have previously been reported to phosphorylate other Kv channels. For example, Kir3 current is suppressed by TrKB mediated tyrosine phosphorylation

(Rogalski et al., 2000). Furthermore, BDNF activation of TrKB in Kv1.3 subunits from cultured mouse olfactory bulb neurons suppresses outward  $K^+$  current, by phosphorylation of multiple tyrosine residues in the N and C terminals (Colley et al., 2004).

Kv1.1 and Kv1.2 (both expressed in MNTB) are subject to current depression by tyrosine phosphorylation. Imbrici et al (2000) showed Kv1.1 currents were irreversibly decreased in an oocyte system by phosphorylation of tyrosine residues. Similarly, tyrosine phosphorylation of Kv1.2 channel has been shown to depress current, via muscarinic stimulation (Huang et al., 1993). Tyrosine phosphorylation of Kv1.2 can also disrupt the interaction of Kv1.2 with the cytoskeletal protein cortactin, thus reducing total Kv1.2 current in a heterologous expression system (Hattan et al., 2002).

In summary, there is evidence that Kv1 channel subunits are subject to phosphorylation of tyrosine residues, resulting in suppressed currents. MNTB neurons have shown hyper-excitability in response to increased BDNF levels, a neurotrophin which is known to activate TrKB (a tyrosine kinase). Thus, one hypothesis for the AOE induced hyper-excitability of MNTB neurons is: AOE increases BDNF levels in MNTB neurons, which in turn activates TrKB mediated suppression of Kv1 currents. Indeed, acoustic trauma has been shown to increase levels of BDNF in the cochlea and auditory cortex of rats (Yang et al., 2016). This hypothesis could be tested in future investigations.

#### Modulation by phosphoinositides

Alternate means of modulation of Kv1 channel is through  $PIP_2$ . Depletion of  $PIP_2$  reduces Kv1 mediated current in heterologous systems, and causes a negative shift in the activation curve (Rodriguez-Menchaca et al., 2012, Kruse and Hille, 2013). Smith et al (2015) investigated Kv1 channels in cultured SGNs (mouse), and found they were composed of Kv1.1 and Kv1.2 (same as MNTB). Depletion of  $PIP_2$  in SGNs caused a reduction in LVA currents and hyper-excitability (Smith et al., 2015). It is therefore possible that the hyper-excitability observed in MNTB neurons following AOE is due to a depletion in  $PIP_2$ .

## 2) A reduction in Kv1 channels

Reduced Kv1 mediated current could also result from a reduction of Kv1 channels in the membrane. Tong et al (2010) found Kv1 mRNA expression in MNTB neurons is dependent on the levels of depolarisation experienced by the neuron. Organotypic cultures of MNTB neurons maintained in a high K<sup>+</sup> medium (therefore experience high levels depolarisation) had significantly higher Kv1.1 mRNA levels compared to MNTB neurons maintained in a low K<sup>+</sup> medium (low levels of depolarisation). Whole cell patch clamping of the neurons revealed the 'high K<sup>+</sup> cultures' maintained a single-spiking AP firing pattern up to 0.6 nA current injection, in contrast to 'low K<sup>+</sup> cultures' which reverted to a multi-spiking AP firing pattern, and had reduced K<sup>+</sup> currents, indicative of low levels of Kv1 channels (Tong et al., 2010).

In summary, levels of Kv1 mRNA in the MNTB are dependent of the amount of depolarisation MNTB neurons experience. Following acoustic trauma, the peripheral drive to the MNTB is likely to be diminished. Thus, a second hypothesis for the hyper-excitability observed following AOE is: AOE mediated damage reduces the synaptic drive to MNTB neurons, leading to reduced expression of Kv1 channels, and therefore reduced Kv1 current.

### Central hyper-excitability following AOE

There have been many reports of hyper-excitability of neurons in the auditory pathway within just a few hours of acoustic insult (Norena and Eggermont, 2003). This has been reported in the DCN, IC and auditory cortex, however this is the first study to report hyper-excitability in the MNTB following AOE (Norena and Eggermont, 2003, Salvi et al., 2000). In the DCN (hamster), hyper-excitability did not occur immediately, but instead developed 2- 5 days post AOE (4 hours, 125 dB SPL), where the magnitude of activity continued to increase in the following 6 months (Kaltenbach et al., 2000). Hyper-excitability in the DCN has previously been ascribed to reduced GABAergic inhibition (Middleton et al., 2011). Partial recovery from hyper-excitability in the IC has been achieved through cochlear or DCN ablation, suggesting it is altered peripheral

input that drives central changes in excitability (Manzoor et al., 2012, Mulders and Robertson, 2009).

Here, I have provided a snap shot of excitability in the MNTB 1 week post acoustic insult. It is currently unknown how MNTB hyper-excitability develops over time, or how this would change if a different AOE protocol was used (e.g. less volume), which could form the basis of future investigations.

#### **MNTB: AP half width accelerates following AOE**

Following AOE, AP half width was accelerated from 0.43 (mean) in control mice to 0.31 ms in AOE treated mice, however the mechanism remains unclear. Steinhert et al (2010) showed activity dependent AP acceleration in the MNTB, through a nitric oxide (NO) mediated signalling pathway. Here, synaptic stimulation raised NO levels, which triggered increased Kv2 activity at the membrane (>3 fold) and reduction in Kv3. Overall, Kv levels were increased, resulting in rapid repolarisation. Whilst this study focused on the acute effects of synaptic stimulation my experiments focused on the long term consequences of sustained stimulation, where mice were tested 1 week following AOE. Indeed, the acceleration of APs observed by Steinhert et al disappeared after only 1 hour post stimulation. Clearly further work is required to reconcile the short term and long term effects of synaptic stimulation in the MNTB.

#### **Synaptic plasticity in the MNTB: LTP cannot be induced**

The MNTB experiences drastic changes to intrinsic excitability following AOE, however the effect of AOE on synaptic excitability remains unknown. I have not examined the synaptic excitability of MNTB neurons due to the following reasons: 1) The primary objective of my thesis was to examine the effect of AOE on the LSO, with the MNTB as a secondary experiment. 2) EPSC recordings from MNTB neurons are difficult to obtain, as the singular synaptic input can easily be damaged during the slicing process. Despite this, insight into the possible effects of AOE on the MNTB can be gathered by examining previous studies focusing on short term and long term synaptic plasticity in the calyx/MNTB synapse. Here, high frequency stimulation was applied to the calycal projection to the MNTB in an attempt to induce short term depression/potential (STD/STP) or long term depression/potential (LTD/LTP) (Friauf et al., 2015). This

high frequency stimulation mirrors the high frequency input to the MNTB experienced during AOE. Whilst STD has been described at length both *in vitro* and *in vivo* (Friauf et al., 2015), no-one has yet found evidence of LTP, although a direct citation of this negative result is difficult to obtain. This contrasts with the MNTB/LSO synapse, where both LTP and LTD of IPSCs has been described (Kotak and Sanes, 2000, Kotak and Sanes, 2014).

As yet, no one has tested the effects of AOE on the synaptic excitability in the MNTB. Based on the inability to induce LTP in MNTB neurons, and rapid recovery from STD, where full recovery is achieved in seconds (Friauf et al., 2015), it is unlikely that synaptic excitability of MNTB neurons is altered following an acoustic insult. However, if a change was observed following AOE, this would be an exciting result, as it would mark the first long term change in synaptic excitability observed in the MNTB.

#### Intrinsic excitability of the LSO: Resting membrane potential is more negative following AOE

So far I have discussed the effects of AOE on the intrinsic and synaptic excitability of the MNTB. Following AOE, MNTB neurons showed hyper-excitability, decreased AP half width and lower AP thresholds, consistent with a reduction in Kv1 mediated currents. In contrast, the intrinsic excitability of the LSO remained largely unaltered. The only significant finding was that following AOE, RMP of LSO neurons was more negative ( $53.2 \pm 1.9$  mV,  $n = 6$ ) compared to age matched controls ( $-44.4 \pm 2.2$  mV,  $n = 7$ ) (fig 5.12, c). RMP is generally set by non-voltage activated channels Kir channels and K2P channels. Kir is an inwardly rectifying channel, and dominates the leak current at negative potentials. In addition, the voltage-gated channels HCN (mediate  $I_H$  current) and Kv1 channels are both activated around resting potential, and may contribute to RMP (Johnston et al., 2010). A change in activity of any of these channels would affect RMP.

Both  $I_H$  and Kv1 channel activity was unchanged following AOE, the latter evidenced by LSO principal neurons retaining their single-spiking AP firing phenotype.

I therefore believe the negative shift in the RMP in the LSO following AOE is due to the depression of Kir and/or K2P. A mechanism or reason for this change remains unclear. Perhaps it is a neuroprotective adjustment, in response to the barrage of synaptic input received during AOE. LSO principal neurons would then require higher levels of depolarisation to reach AP threshold (which was unaltered by AOE) (fig 5.12, a).

Synaptic excitability of the LSO:

AMPA mediated EPSC decay tau is slowed following AOE

Whilst the intrinsic excitability of LSO principal was largely unaltered by AOE, there were significant changes in synaptic excitability. AMPAR mediated EPSCs were slowed from  $\sim 1$  ms to nearly 2 ms following AOE, whilst rise-time remained unchanged (fig 5.13 b). Under control conditions, fast AMPAR EPSCs are associated with high levels of GluA4-containing AMPARs (Mosbacher et al., 1994). GluA4 containing AMPARs are broadly expressed in the auditory system, including the SOC (Rubio and Wenthold, 1999), and are predominantly of the flop splice variant (Schmid et al., 2001). The importance of GluA4 subunits in the SOC was demonstrated by Yang et al (2011) who found synaptic responses from the MNTB were slower in GluA4 KO mice compared to wild-type mice. GluA4 is also highly expressed in the LSO (Schwartz and Eager, 1999), and I believe a reduction in GluA4 following AOE was responsible for the slowed AMPAR mediated EPSCs. In support of this hypothesis, GluA4 mRNA levels in the LSO were significantly lower following AOE, and GluA1 mRNA significantly raised (work by Dr Haresh Selvaskandan) (fig 5.13, c).

Changes in AMPAR subunit composition have previously been observed following repetitive synaptic stimulation, sensory deprivation, and during epileptic seizures (Goel et al., 2011, Liu and Cull-Candy, 2000, Grooms et al., 2000). AOE mediated slowing of AMPAR EPSCs could be a recovery mechanism to compensate for reduced input from the damaged periphery. Here, longer lasting EPSCs boost the excitatory charge transfer and increase the likelihood of AP firing in LSO principal neurons.

Previously in the lab, Dr Nadia Pilati showed AOE induced slowing of AMPAR EPSC decay tau following AOE, using the same AOE protocol. Furthermore, she found

glycinergic IPSC kinetics were unchanged following AOE. Mis-matched EPSC and IPSC kinetics would result in a shift in the ILD function and less precise ILD detection performance (Park et al., 1996b, Tollin, 2003). Thus, it appears AOE induced slowing of AMPAR EPSC decay kinetics may help preserve binaural hearing, but at the expense of accurate ILD processing.

Whilst both Dr Pilati and myself both observed slowed AMPAR EPSC decay kinetics, overall the EPSCs in my data set were slower (fig 5.14). This may be because the animals used in my data set were younger (P23:P27) compared to the animals used by Dr Pilati (P29:P36). However, developmental acceleration of AMPAR EPSC decay kinetics has been shown to reach maturity by P17 by both Dr Pilati and myself (see chapter 3, fig 3.10 a & b). I therefore believe the slower AMPAR EPSCs observed in my data is due to high series resistance. Low n numbers in my dataset may also account for the differences in decay tau.

In conclusion, following AOE, AMPAR mediated EPSC decay kinetics were slowed. This was accompanied by a decrease in GluA4 mRNA and an increase in GluA1 mRNA. I believe AOE mediated slowing of AMPAR EPSCs is a compensatory mechanism in response to reduced input from the damaged periphery, in an attempt to boost excitation and preserve binaural hearing at low firing rates, albeit at the expense of accurate ILD processing.

#### LSO: NMDAR EPSCs rise-time is accelerated following AOE

In contrast to AMPAR EPSCs, there was no observed changes to NMDAR EPSC decay tau following AOE, which remained fast at ~2-3 ms (fig 5.15, b,c), (fast NMDAR EPSCs are discussed in chapter 3, section 3.3). In contrast, rise-time accelerated from 0.99 ms (mean) in control mice to 0.6 ms in AOE treated mice (5.15, d). This was accompanied by a change in NMDAR subunit mRNA expression, where GluN1b was significantly increased following AOE. It is possible this increase in GluN1b is responsible for the acceleration in rise-time observed following AOE, which will be a topic for further study.

## Summary

AOE causes different changes in the LSO versus the MNTB. In the MNTB AOE changes the intrinsic excitability, where multiple APs are fired in response to depolarising currents, AP half width was accelerated and AP thresholds lowered. However, there is no evidence of long term synaptic changes in the MNTB. In the LSO, there is little change in intrinsic excitability, but a dramatic change in AMPAR EPSC decay tau, which was significantly slowed by AOE, accompanied by an increase in GluA1 and a decrease in GluA4 mRNA. This could serve as a mechanism to rescue ascending auditory signals, yet could undermine the precision of ILD processing. Thus, whilst there are many similarities in the electrophysiological properties of the LSO and MNTB (e.g.  $I_H$  current, Kv1 current, Kv3 current etc.), they are modulated very differently by AOE.

## 6 THE EFFECT OF AOE ON EVOKED AUDITORY BRAINSTEM RESPONSES (ABRs)

---

In the previous chapter (5), I examined the effect of damaging levels of noise on the excitability of individual neurons (*in vitro*) from the SOC of mice. Auditory brainstem responses (ABRs) were measured before culling in the same mice, to establish the extent of hearing loss following AOE. ABRs can provide a broad overview of the activity of the ascending auditory pathway. They consist of synchronous auditory evoked potentials recorded in response to brief sound stimuli, recorded via sub-dermal electrodes in the scalp. ABRs can be evoked by two types of sound stimuli: clicks and tone-pips. Click stimuli are a broadband stimulus, and therefore excite a large area of the BM, and thus produce large ABRs. In contrast, tone-pip stimuli only excite a small area of the cochlea, corresponding to the frequency of the tone-pip, and thus produce smaller ABRs. Tone-pip evoked ABRs therefore provide insight into how AOE affects different hearing frequencies, and by extension, different areas of the cochlea.

The ABR consists of waves (see chapter 2, fig 2.7) which reflect the neural activity of successive nuclei in the ascending auditory pathway. ABR waves in the mouse (I-IV) are thought to correspond with the activity of the I) auditory nerve, II) cochlear nucleus, III) SOC and IV) lateral lemniscus/inferior colliculus (Melcher et al., 1996).

Throughout this chapter I shall compare different properties of ABRs recorded from mice subjected to AOE 1 week previously and age matched controls. Firstly, I will compare the ABR thresholds (both click evoked and tone-pip evoked), to assess the extent of hearing loss following AOE. Secondly, I shall compare the amplitude of ABR waves in control and AOE treated mice, where each wave provides a measure of excitability in sequential nuclei of the auditory brainstem. Thirdly, I compare the amplitude of tone-pip evoked ABRs, to ascertain whether any differences in amplitude are frequency specific. Finally, I will examine the effects of AOE on conduction velocity in the auditory brainstem, by comparing the latency of each ABR wave (both click and tone-pip evoked).

## 6.1 AOE SIGNIFICANTLY RAISES ABR THRESHOLDS

The aim here was to study the impact of AOE on hearing. The experimental design was to deafen mice using damaging levels of sound, and then assess the impact of AOE on hearing using ABRs. Firstly, P17 – P20 CBA/Ca mice were anaesthetised, and ABRs were recorded in response to tone-pip stimuli (1 ms rise and fall time, 5 ms duration) and click stimuli (10 ms duration), presented in 5 dB SPL steps, from 0 to 85 dB SPL. Immediately following the ABR, mice were subject to AOE, using a broadband sound (5 -50 kHz) at a volume of 110 dB SPL for two hours. One week later, ABRs were measured again in the same mice (now aged P23-P27). Age-matched control animals received identical treatment without the AOE (sham exposure).

Figure 6.1 shows click evoked ABRs plotted as mean traces, in response to increasing sound intensity levels (values indicated on the far left), with the SEM indicated by the lighter shading. ABR traces from control mice are plotted in green (left), and traces from AOE treated mice are shown in red (right). ABR wave number (I:IV) is indicated above the ABR trace at 85 dB SPL for both control and AOE treated mice. Hearing threshold was defined as the lowest volume of sound stimulus required to produce a recognizable ABR wave. Mice treated with AOE showed substantially elevated ABR thresholds at ~ 65 dB SPL, whilst control mice have thresholds of ~ 35 dB SPL (actual thresholds for click ABR are summarised in figure 6.2).

In conclusion, I have shown that the AOE protocol used in my experiments consistently resulted in substantial hearing loss, raising click ABR thresholds by ~ 30 dB SPL. Furthermore, ABRs recorded from both control and AOE treated mice were highly reproducible, as evidenced by the small SEM.

**ABR thresholds are raised at all frequencies tested, except 6 kHz**

So far, I have shown that click evoked ABRs are elevated following exposure to damaging level of sound. Clicks are a broadband stimulus, and thus stimulate a large area of the cochlea, in turn producing large, robust ABR waves. Using click ABR alone, it is not possible to establish which specific frequency regions of the cochlea are

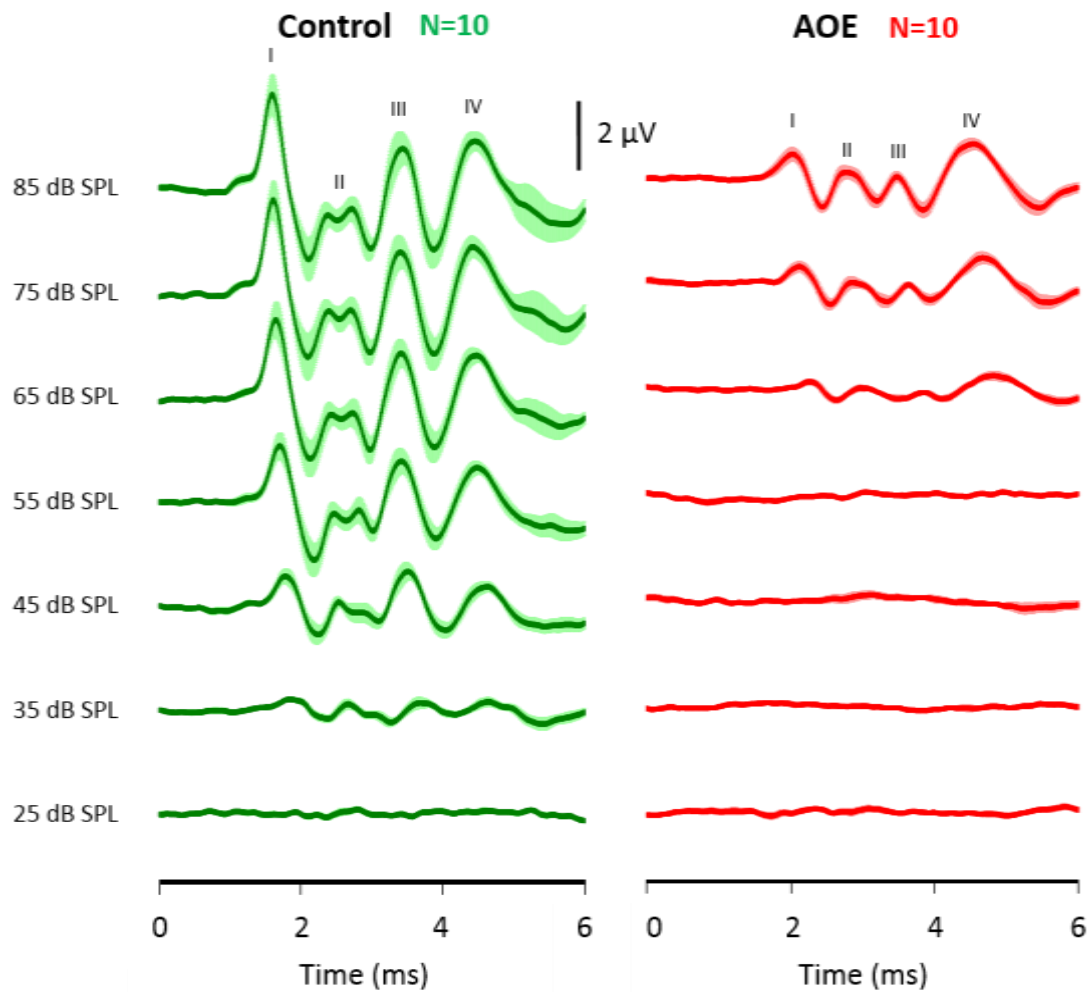
damaged by AOE. To address this, frequency specific tone-pip evoked ABRs were recorded immediately after click ABRs. Tone-pip ABRs primarily stimulate areas of the cochlea that correspond to the frequency of the tone-pip.

To establish which hearing frequencies, and by extension, which areas of the cochlea were damaged by AOE, I have compared ABR thresholds from control and AOE treated mice in response to tone-pips of 6, 12, 18, 24 and 30 kHz. Fig 6.2 (a) shows the mean ABR thresholds ( $\pm$  SEM) from both control (green) and AOE treated mice (red) (ages P23:P27) in response to individual tone-pip frequencies and click stimuli. AOE caused a significant increase in ABR thresholds at all frequencies tested (including click stimuli) with the exception of 6 kHz, which remained unchanged ( $p < 0.05$ ). Specifically, thresholds for control mice were: **6 kHz** =  $46 \pm 3$  dB SPL (mean  $\pm$  SEM),  $n = 5$ , **12 kHz** =  $30 \pm 1$  dB SPL,  $n = 10$ , **18 kHz** =  $32 \pm 2$  dB SPL,  $n = 10$ , **24 kHz** =  $33 \pm 2$  dB SPL,  $n = 10$ , **30 kHz** =  $37 \pm 2$  dB SPL,  $n = 9$  and **click** =  $35 \pm 2$  dB SPL,  $n = 10$ . AOE treated mice had thresholds of: **6 kHz** =  $46 \pm 2$  dB SPL,  $n = 9$ , **12 kHz** =  $62 \pm 4$  dB SPL,  $n = 10$ , **18 kHz** =  $76 \pm 1$  dB SPL,  $n = 10$ , **24 kHz** =  $76 \pm 1$  dB SPL,  $n = 9$ , **30 kHz** =  $76 \pm 1$  dB SPL,  $n = 9$  and **click** =  $67 \pm 2$  dB SPL,  $n = 10$ .

Following this, I wanted to examine the effect of AOE in the same mice, by comparing ABR thresholds taken immediately before AOE at age (P17:P20) and again one week later (P23:P27) (fig 6.2 b). Threshold at 6 kHz prior to noise exposure (age P17-P20) was higher than thresholds measured 1 week post noise exposure (P23:P27) at  $65 \pm 0$  dB SPL,  $n=3$ , and  $46 \pm 2$  dB SPL,  $n = 9$ , respectively (see discussion). ABR thresholds of all other frequencies tested prior to AOE (P17:P20) were comparable to thresholds observed in older control mice (P23: P27) in part a. Specifically, thresholds prior to AOE (P17:P20) were: **12 kHz** =  $29 \pm 1$  dB SPL,  $n = 9$ , **18 kHz** =  $33 \pm 3$  dB SPL,  $n = 9$ , **24 kHz** =  $31 \pm 2$  dB SPL,  $n = 9$ , **30 kHz** =  $33 \pm 1$  dB SPL,  $n = 8$  and **click** =  $36 \pm 2$  dB SPL,  $n = 10$ . Following AOE, ABR thresholds were significantly elevated for all frequencies  $>6$  kHz (including click evoked ABR thresholds), furthermore, because the ABRs were performed in the same animals, variability of hearing thresholds (as shown by SEM bars) were even smaller.

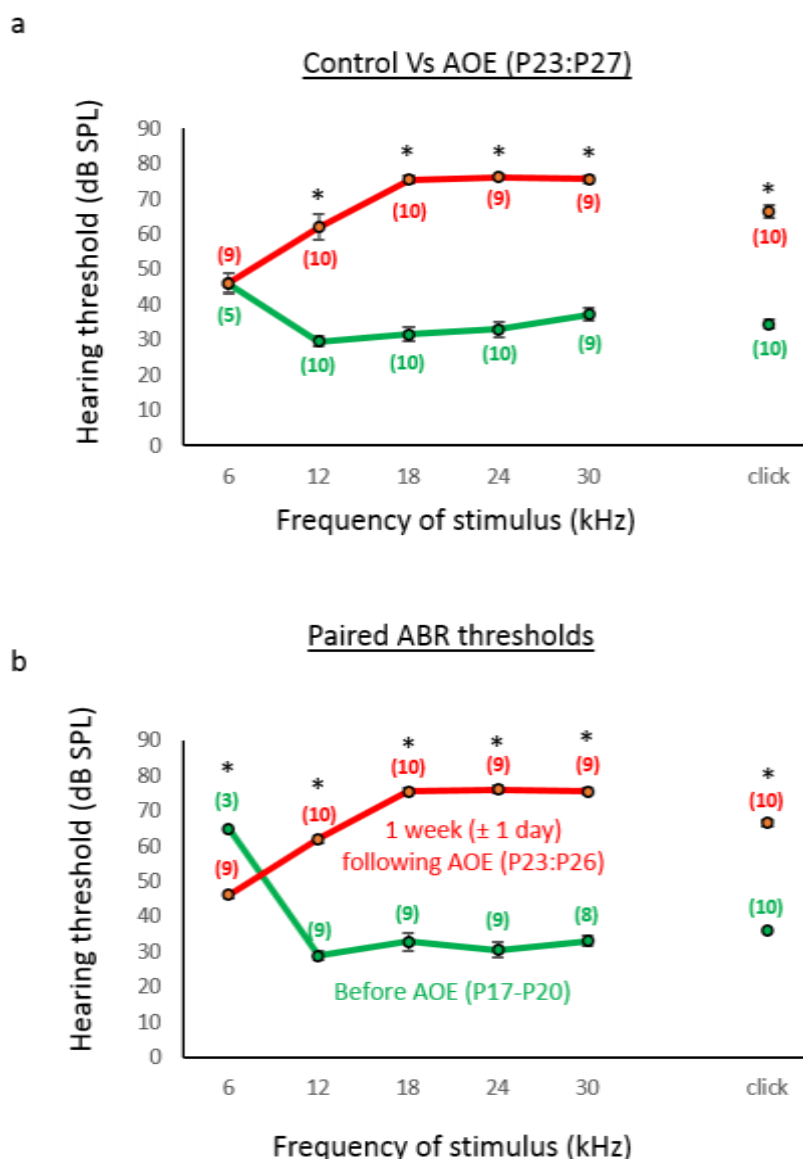
In summary, I have demonstrated AOE elevates hearing thresholds at all frequencies > 6 kHz. This is evident when comparing hearing thresholds from age matched controls (P23:P27) (fig 6.2, a) or when comparing the thresholds from the same mice prior to exposure (P17:P23) (fig 6.2, b).

Figure 6.1 Click ABR threshold is significantly higher following AOE



**Fig 6.1. Click ABR threshold is significantly higher following AOE.** Click evoked ABR responses are shown from control CBA/Ca mice (green, left) and mice previously subjected to AOE 1 week earlier, (red, right) (ages P23:P27). ABRs are plotted in response to increasing click amplitude level (bottom to top, 25 dB to 85 dB SPL, with alternate traces removed for clarity), (Mean  $\pm$  SEM). Responses were evoked by click stimuli of 10  $\mu$ s duration, at a repetition rate of 42.6/s (512 repetitions in total), presented in 5 dB SPL steps from 0 dB SPL to 85 dB SPL.

Figure 6.2 Following AOE, ABR thresholds were raised across frequencies  $\geq 12$  kHz



**Fig 6.2. Following AOE, ABR thresholds were raised across frequencies  $\geq 12$  kHz.** **a.** A plot of ABR thresholds vs the frequency of the tone-pip stimuli (6, 12, 18, 24, 30 kHz, (Mean  $\pm$  SEM), from control CBA/Ca mice and mice exposed 1 week earlier, ages P23:P27). Hearing thresholds for click stimuli are also summarised from fig 1. **b.** A plot showing paired ABR thresholds vs frequency of stimuli, from mice immediately prior to AOE (P17:P20, green) and from the same mice 1 week post AOE (P23:P26, red). The AOE dataset (red) is the same as that shown in part a. Significance in part a (\* $p < 0.05$ ) was determined via multiple t-tests (not assuming equal variance), using Sidak Holm corrections for multiple comparisons. Significance in part b was determined via paired t test with Sidak Holm correction (adjusted p value = 0.0085134). N numbers = number of mice, and are shown in brackets above or below each data point for the remainder of the chapter.

## 6.2 EFFECT OF AOE ON ABR WAVE AMPLITUDE

### Amplitude of wave I is reduced following AOE

Next, I wanted to assess the effect of AOE on the excitability of the auditory brainstem. Amplitude of successive ABR waves is an indicator of excitability in sequential nuclei of the auditory brainstem. Here, I compared the amplitude of ABRs waves from mice treated with AOE one week earlier, and age matched controls (both aged P23:P27). Figure 6.3 (a) shows mean click evoked ABR traces ( $\pm$  SEM) in response to 85 dB SPL stimulus from both control mice (green) and those treated with AOE (red). Amplitude of each wave was defined as the difference between the amplitude at the peak of the wave and the amplitude at the following trough, which is depicted for wave I by dashed arrows. Each ABR wave (I:IV) is labelled above.

To compare the amplitude of wave I between control and AOE treated mice in response increasing click intensity, I have chosen to plot the data two different ways. Firstly, I have plotted the 'absolute amplitude' (fig 6.3, b). Here the amplitudes of wave I were plotted in response to increasing stimulus intensity in 5 dB SPL steps, from control ABR threshold to 85 dB SPL. Amplitude of ABRs from control mice are plotted in green, whilst AOE treated mice are shown in red. Secondly, I have presented the 'relative amplitude' (fig 6.3, d), where amplitudes were plotted in response to increasing stimulus intensity (5dB steps) from ABR threshold (normalized to 0dB SPL). To represent the relative ABR traces, mean ABR traces +10 dB SPL relative to threshold are shown in fig 6.3 c. Both ways of plotting the data have advantages and limitations (see discussion).

Absolute amplitude of wave I (auditory nerve activity) of click evoked ABRs was significantly reduced in AOE treated mice at each stimulus intensity tested ( $p < 0.05$ ) (fig 6.3, b). However, whilst the mean of the relative amplitude of wave I from the AOE group was lower at  $\geq 10$  dB SPL, this effect was not significant (fig 6.3, d) (see discussion).

Figure 6.3 Wave I: Amplitude is reduced following AOE

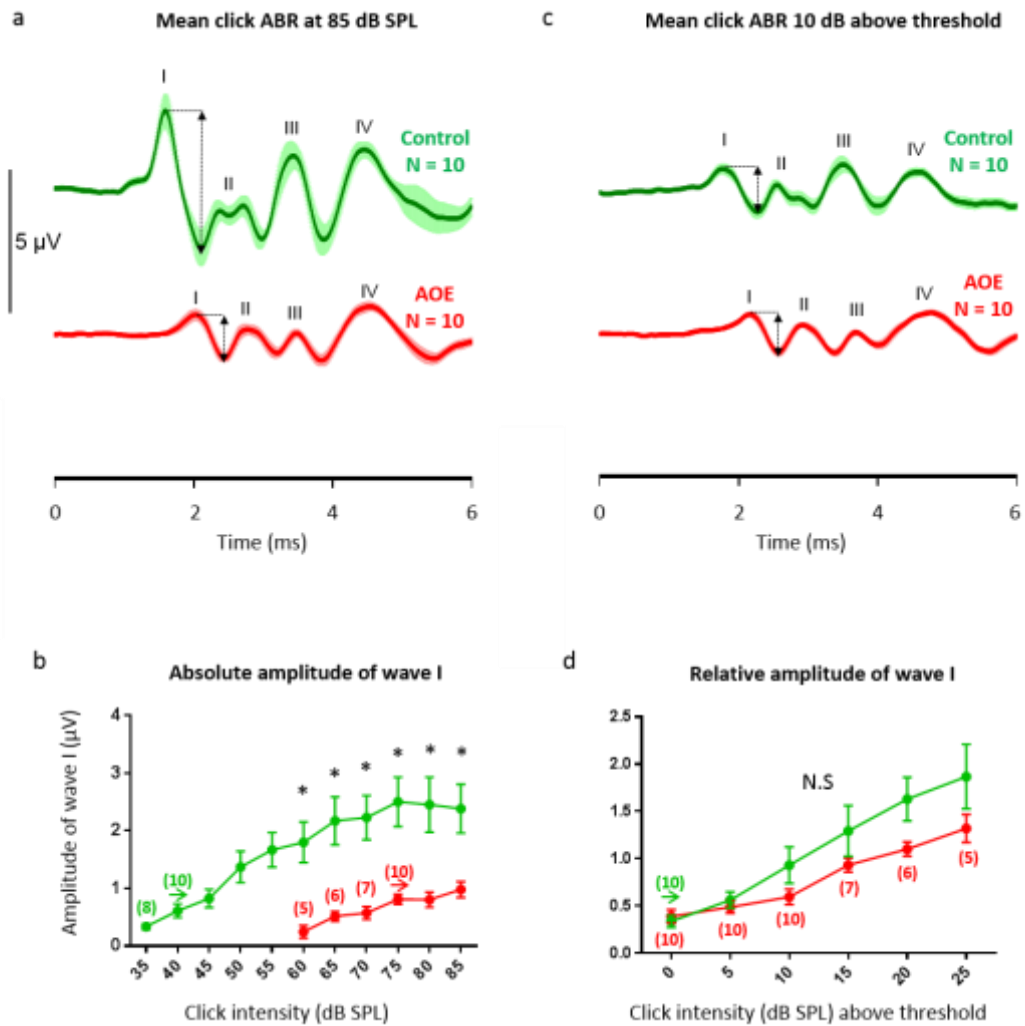


**Fig 6.3. Wave I: Amplitude is reduced following AOE.** **a.** ABR traces are shown in response to click stimuli intensity of 85 dB SPL in both control mice (green) and mice subjected to AOE (red) (Mean  $\pm$  SEM). Amplitude of wave I is indicated by the vertical dashed arrow. **b.** Plot showing the ‘absolute amplitude’ of wave I vs click stimulus intensity for both control and AOE groups. Wave I amplitude is plotted in response to increasing click intensity steps (5 dB SPL) starting from the lowest threshold recorded (35 dB SPL in control mice) up to 85 dB SPL, (Mean  $\pm$  SEM). N numbers are indicated in brackets above each data point. **c.** ABR traces are shown in response to click stimuli 10 dB SPL above threshold. **d.** Plot showing the relative amplitude of wave I from click evoked ABRs vs click intensity, in both control and AOE treated mice. The amplitude of wave I is plotted in response to increasing stimulus intensity (5dB steps) from ABR threshold (normalised to 0 dB SPL). Significance (\* $p < 0.05$ ) was determined using multiple t-tests (not assuming equal variance), using Sidak Holm corrections for multiple comparisons.

In summary, AOE causes a reduction in the amplitude of wave I, which reflects depressed excitability of the auditory nerve (AN). Next I wanted to establish whether the diminished excitatory input from the AN had an effect on the successive nuclei (and thus ABR waves) in the auditory pathway. Throughout the rest of the chapter, each successive wave will be analysed in a similar manner to wave I (fig 6.3), by plotting both the relative and absolute amplitude of the waves in response to increased stimulus intensity. Wave II was excluded, due to the wave splitting into two peaks in control recordings.

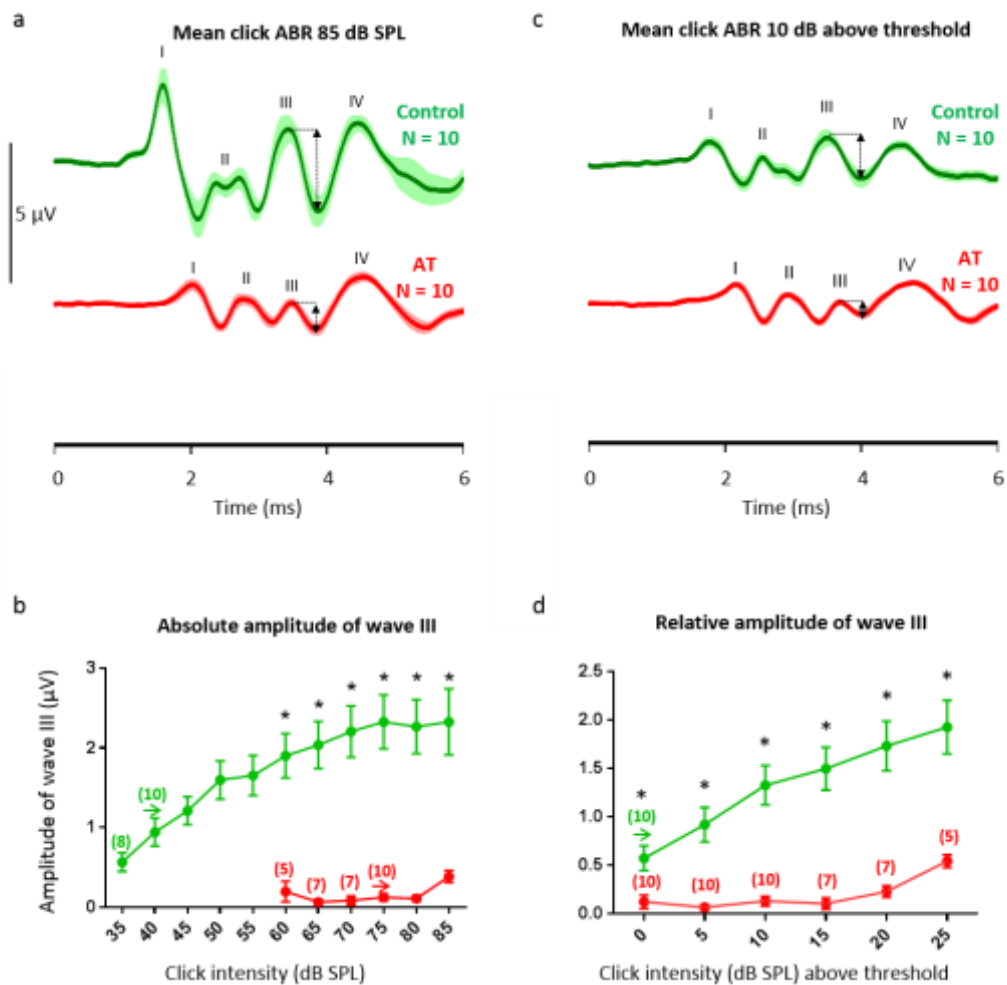
#### Wave IV shows compensatory increase in amplitude following AOE

Next I wanted to observe whether the diminished excitatory input from the AN had an effect on the successive nuclei (and thus ABR waves) in the auditory pathway.

Following AOE, absolute amplitude of wave III was drastically reduced at each click intensity tested, to an even greater extent than wave I (fig 6.4, b). Furthermore, the relative amplitude of wave III was also significantly reduced (fig 6.4, d). Remarkably, despite the diminished excitatory input from wave III in AOE treated mice, relative amplitude of wave IV (SOC) recovered to almost identical levels as control (fig 6.5, d). Absolute amplitude of wave IV was reduced at each click intensity tested in the AOE group, but to a much lesser extent than wave III (fig 6.5, c).

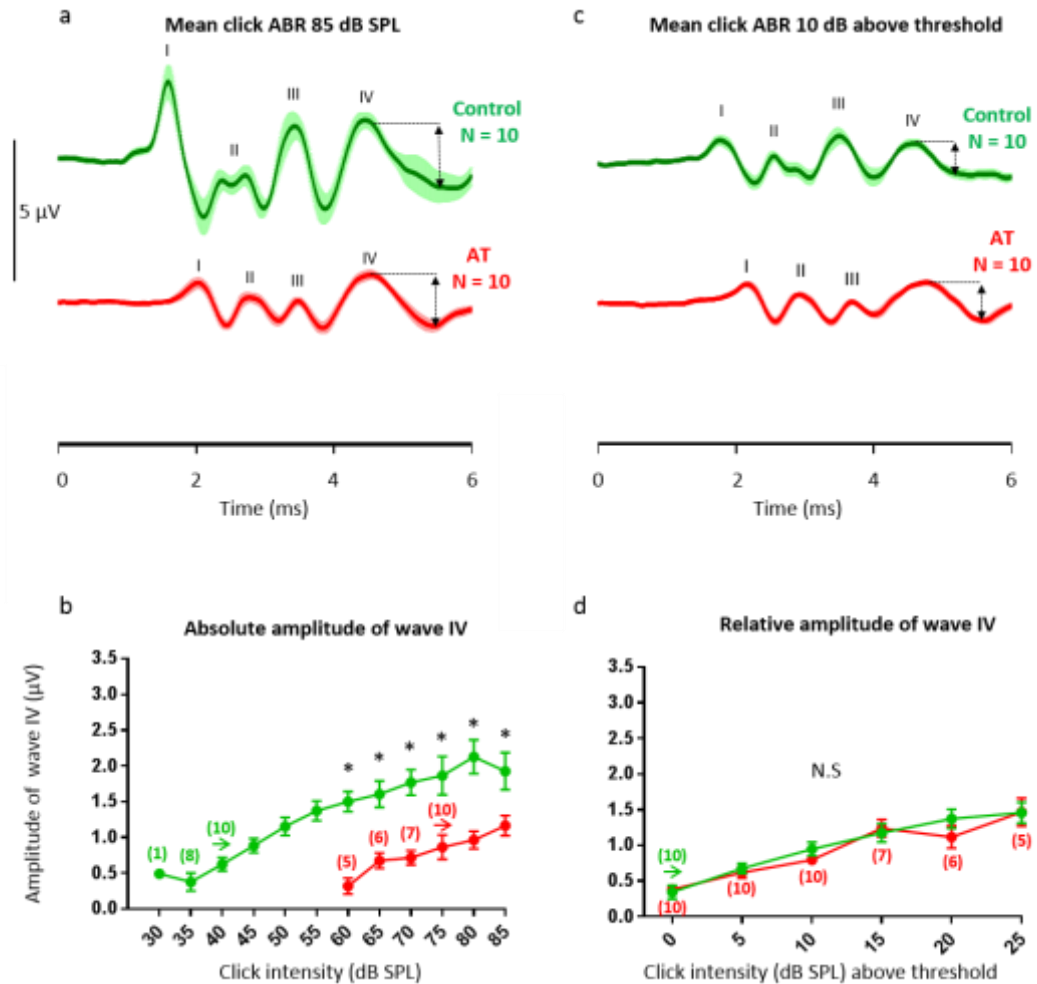
To quantify the relationship of the amplitude of wave III to wave IV in both control and AOE treated mice, the ratios of wave III/wave IV were calculated. Fig 6.6 (a) shows the ratio of wave III/wave IV amplitude at click stimulus level 85 dB SPL (control =  $1.28 \pm 0.22 \mu\text{V}$  (mean  $\pm$  SEM),  $n = 10$  and AOE =  $0.29 \pm 0.08 \mu\text{V}$ ,  $n = 10$ ,  $P = 0.0068$ ). This shows that in control mice, wave III has a larger amplitude than wave IV, in contrast to the AOE group, which have a much smaller wave III compared to wave IV. A similar pattern was observed at relative stimulus intensity +10 dB SPL (control =  $1.45 \pm 0.18 \mu\text{V}$ ,  $n = 10$  and AOE =  $0.16 \pm 0.06 \mu\text{V}$ ,  $n = 10$ ,  $P = 0.0027$ ) (fig 6.6, b). Thus it appears the lemniscus/inferior colliculus provides a compensatory excitatory boost, in response to diminished input from lower levels of the ascending auditory pathway.

Figure 6.4 Wave III: Amplitude is reduced following AOE



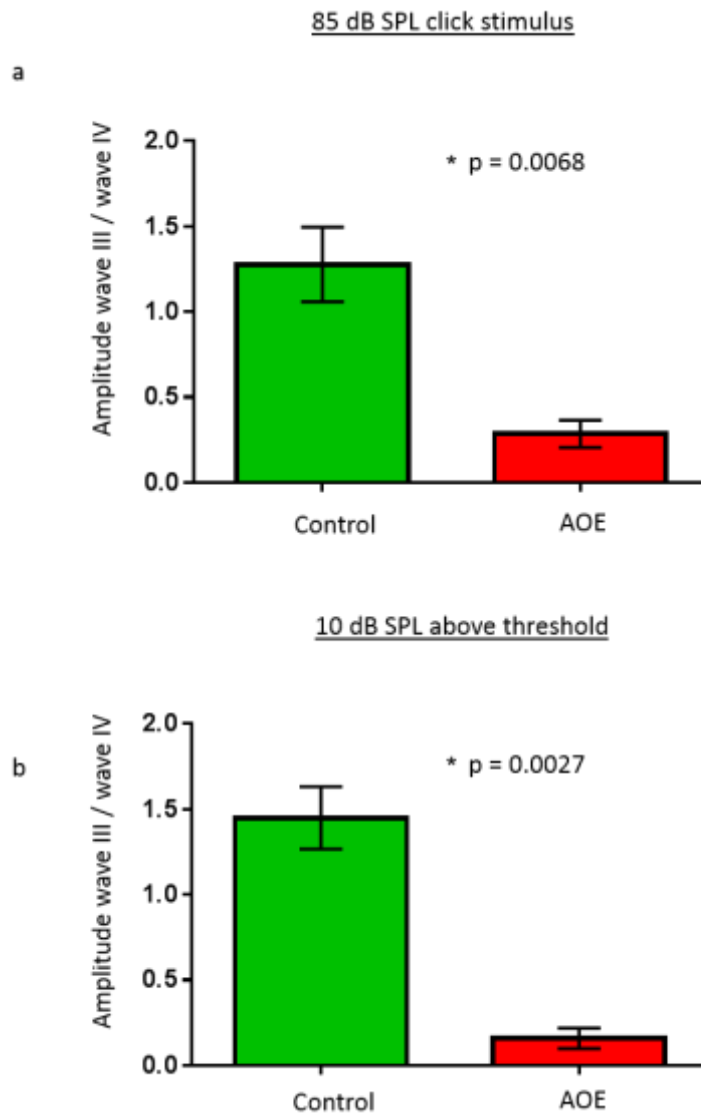
**Fig 6.4. Wave III: Amplitude is reduced following AOE.** **a.** ABR traces are shown in response to click stimuli intensity of 85 dB SPL in both control mice (green) and mice subjected to AOE (red) (Mean  $\pm$  SEM). Amplitude of wave III is indicated by the vertical dashed arrow. **b.** Plot showing the ‘absolute amplitude’ of wave III vs click stimulus intensity for both control and AOE groups. **c.** Click evoked ABR traces 10 dB SPL above threshold. **d.** Plot showing the relative amplitude of wave III from click evoked ABRs vs click intensity, in both control and AOE treated mice. Significance (\* $p < 0.05$ ) was determined using multiple t-tests (not assuming equal variance), using Sidak Holm corrections for multiple comparisons.

Figure 6.5 Wave IV: Following AOE, amplitude recovers to control values (as measured from threshold)



**Fig 6.5. Wave IV: Following AOE, amplitude recovers to control values (as measured from threshold).** ABR traces are shown in response to 85 dB SPL in both control mice (green) and mice subjected to AOE (red) (Mean  $\pm$  SEM). **b.** Plot showing the absolute amplitude of wave IV vs click stimulus intensity for both control and AOE groups. **c.** ABR traces recorded in response to click stimuli 10 dB SPL above threshold. **d.** Plot showing the relative amplitude of wave IV from click evoked ABRs vs click intensity, in both control and AOE treated mice. Significance (\*p < 0.05) was determined using multiple t-tests (not assuming equal variance), using Sidak Holm corrections for multiple comparisons.

Figure 6.6 Following AOE, wave IV amplitude is greater than wave III



**Fig 6.6. Following AOE, wave IV amplitude is greater than wave III.** **a.** Bar chart comparing the ratio of wave III amplitude / wave IV amplitude from the click evoked ABRs (85 dB SPL) of both control mice (green) and AOE treated mice (red). Mean  $\pm$  SEM. **b.** Wave III amplitude / wave IV amplitude, from click evoked ABR 10 dB SPL above threshold. There is a significant shift in the ratio following AOE in both **a** and **b**, whereby the amplitude of wave IV is larger than wave III. Significance (\* $p < 0.05$ ) in each instance was determined by an unpaired t-test.

### Tone-pip evoked ABRs show a reduction of ABR wave amplitude at higher frequencies following AOE

So far I have shown that AOE diminishes click ABR waves I and III amplitude, but shows compensatory recovery at wave IV. However, click ABR does not show which frequency regions were affected by AOE. Tone-pip evoked ABRs reflect a frequency specific tonotopic pathway through the brainstem.

Here I will compare tone-pip ABR wave amplitudes from control and AOE treated mice, to establish whether any AOE mediated changes occur, and if so, determine which frequency regions are affected. Figure 6.7 shows ABR traces from control (green) and AOE treated mice (red) in response to the different frequency tone-pips (12, 18, 24 and 30 kHz, top to bottom) (mean  $\pm$  SEM). On the left, ABRs are shown in response to tone-pip intensity 85 dB SPL, whilst on the right ABRs are shown in response to 10 dB SPL intensity above threshold. At 85 dB SPL, there was little difference in the amplitude of ABR waves at 12 kHz between control and AOE treated mice, however at higher frequencies there was a visible decrease in the amplitude of particular waves in mice subjected to AOE. In contrast, at 10 dB SPL relative to threshold, the AOE treated mice have larger ABR wave amplitudes at all frequencies tested.

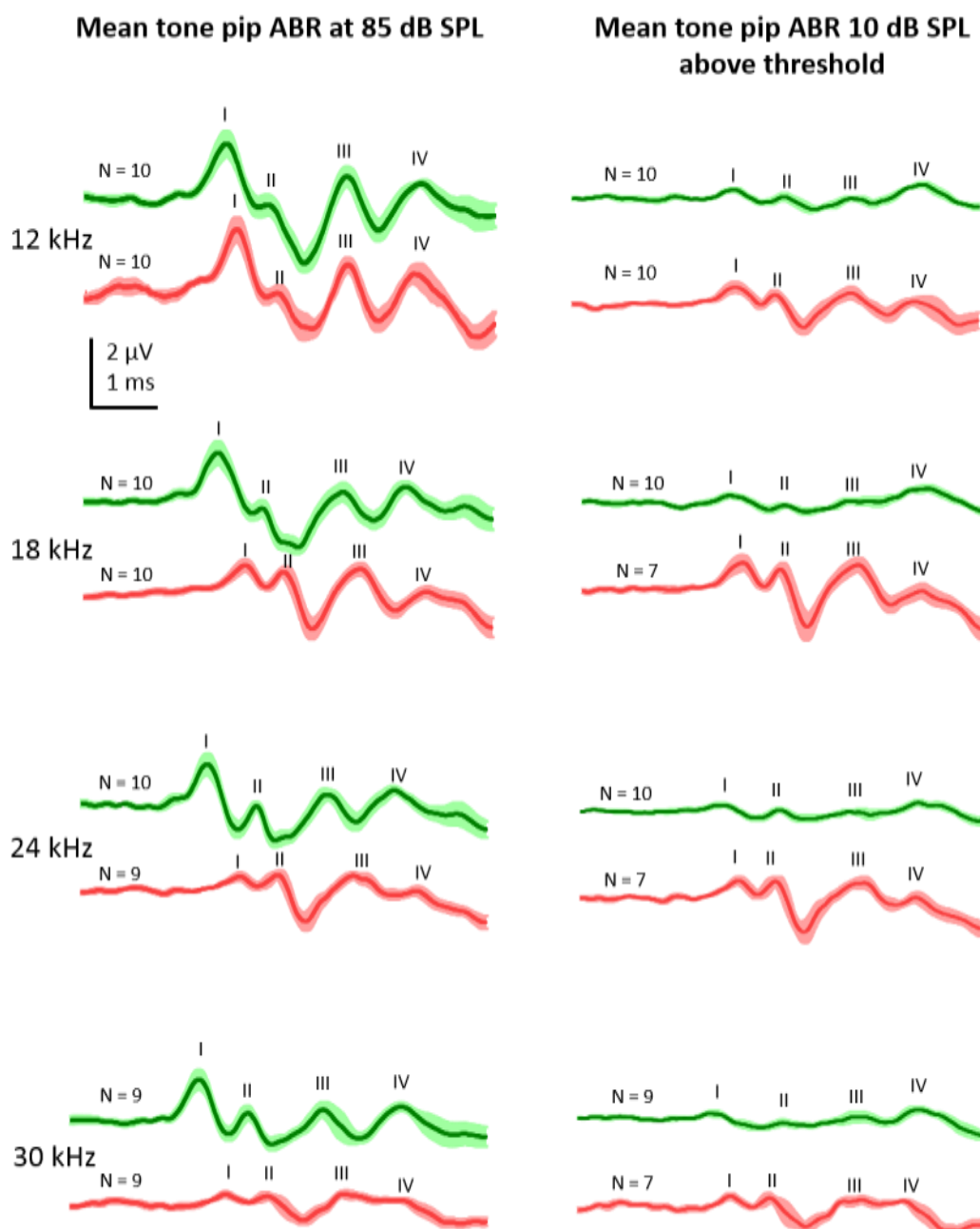
To understand why AOE causes an increase in ABR wave amplitude at + 10 dB SPL relative to threshold, it was necessary to examine ABRs at each stimulus intensity. Here, I plotted ABRs evoked by 12 kHz tone-pips (fig 6.8) in response to increasing stimulus intensity from 25 dB to 85 dB SPL (values indicated on the far left) for both control (green left) and AOE treated mice (red, right) (mean  $\pm$  SEM). Amplitude of the ABR waves in the control group increased with small increments from threshold ( $\sim$ 25 dB SPL) in response to +10 dB SPL stimulus intensity steps. In contrast, whilst the AOE treated mice initially had small ABR waves at threshold ( $\sim$ 65 dB SPL), there was a rapid growth of amplitude with increasing stimulus intensity, so that at 85 dB SPL, wave amplitudes appear equal to the control group. I have therefore decided to omit the relative amplitude analysis of tone-pip evoked ABRs, as ABR waves evoked from AOE treated mice show steep amplitude growth with increased stimulus intensity, and thus

a reduced dynamic range. This could falsely show that AOE increases ABR wave amplitude when compared to control.

So far, only tone-pip evoked ABR traces at two stimulus intensities (85 dB SPL and +10 dB relative to threshold) have been shown. Next, I quantified differences in ABR wave amplitude caused by AOE in response to different sound intensities. Figure 6.9 shows the absolute amplitude of wave I from control (green) and AOE treated mice (red) in response to increasing stimulus intensity for each frequency tested (12, 18, 24 and 30 kHz). In some instances, particular ABR waves could not clearly be identified. In such cases, rather than exclude the data from analysis, amplitude was instead measured from the calculated mean latency (particular to the wave and tone-pip frequency) to prevent bias against waves with very small amplitudes. AOE caused significant reductions in the amplitude of wave I in response to 18 kHz, 24 kHz and 30 kHz stimuli at each stimulus intensity where N numbers  $\geq 3$ , but had no effect on the wave amplitude at 12 kHz ( $P < 0.05$ ). Wave III and IV amplitudes were low in both control and AOE treated mice ( $\sim 0.5 \mu\text{V}$  at 85 dB SPL) at each frequency tested (fig 6.10 & 6.11). Nonetheless, there was a reduction in the absolute amplitude of wave III and IV in the AOE treated mice at both 24 kHz and 30 kHz ( $P < 0.05$ ).

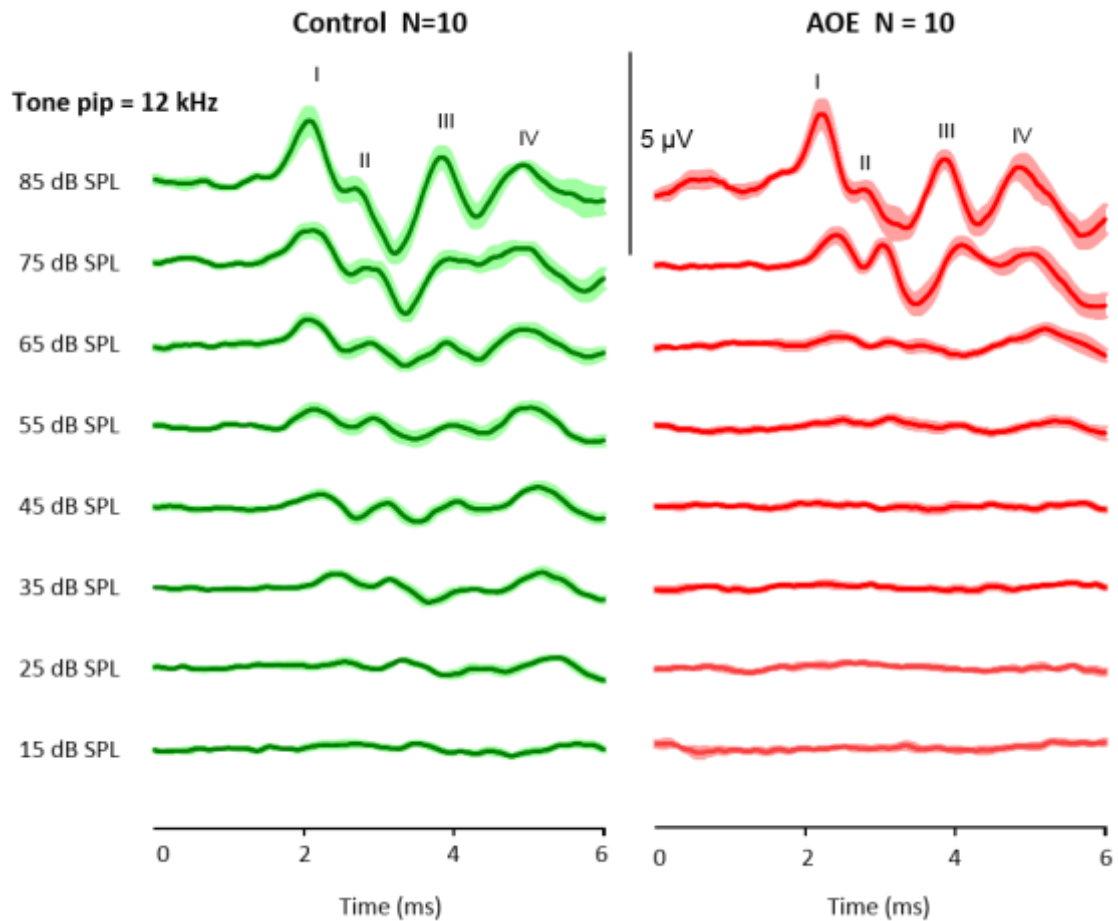
In summary, in agreement with click ABR data, AOE caused a reduction in the absolute amplitude of wave I (and thus excitability of the AN). Specifically, AOE reduced amplitudes of higher frequency regions (18, 24 and 30 kHz). In contrast to click ABR, no excitatory boost in amplitude of wave IV (activity of the lateral lemniscus/inferior colliculus) was observed in AOE treated mice. Instead, wave IV showed a similar reduction at 24 kHz and 30 kHz as wave III (AOE) (see discussion).

Figure 6.7 Mean tone-pip (frequency specific) ABRs in control and AOE treated mice



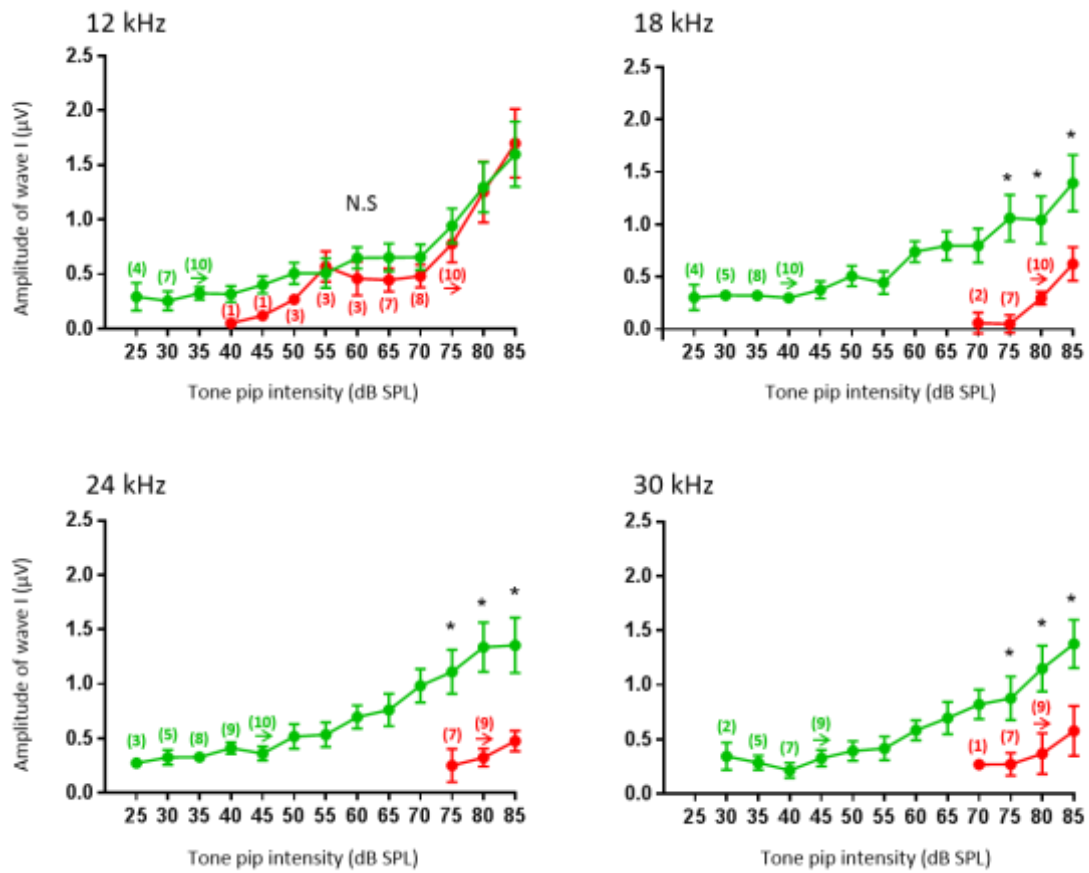
**Fig 6.7. Mean tone-pip (frequency specific) ABRs in control and AOE treated mice.** ABRs are shown in response to frequency specific tone-pip stimuli (12, 18, 24 and 30 kHz, top to bottom) from both control mice (green), and those subjected to AOE (red). Mean  $\pm$  SEM. The peaks of waves I, II, III and IV are labelled above each ABR trace. **Left:** ABRs at 85 dB SPL tone-pip intensity. **Right:** ABRs 10 dB above threshold.

Figure 6.8 Tone-pip evoked ABRs show a reduced dynamic range following AOE



**Fig 6.8. Tone-pip evoked ABRs show a reduced dynamic range following AOE.** ABR responses evoked by 12 kHz tone-pip stimuli are shown from both control mice (green, left) and mice previously treated with AOE (red, right). ABRs are plotted in response to increasing tone-pip amplitude (bottom to top, 15 dB SPL to 85 dB SPL, with alternate traces removed for clarity). Mean  $\pm$  SEM.

Figure 6.9 Wave I: Absolute amplitude is reduced following AOE at mid to high frequency ranges



**Fig 6.9. Wave I: Absolute amplitude is reduced following AOE at mid to high frequency ranges.**

ABRs were recorded from both control mice and those subjected to AOE, in response to frequency specific tone-pip stimuli (12, 18, 24 and 30 kHz). For each tone-pip frequency, a plot of the absolute amplitude of wave I vs increasing stimulus intensity (5 dB SPL steps) is shown, comparing control mice (green) and mice treated with AOE (red). Mean  $\pm$  SEM. Significance (\* $p < 0.05$ ) was determined using multiple t-tests (not assuming equal variance), with Sidak Holm corrections for multiple comparisons.

Figure 6.10 Wave III: Absolute amplitude is low and variable in both control and AOE treated mice

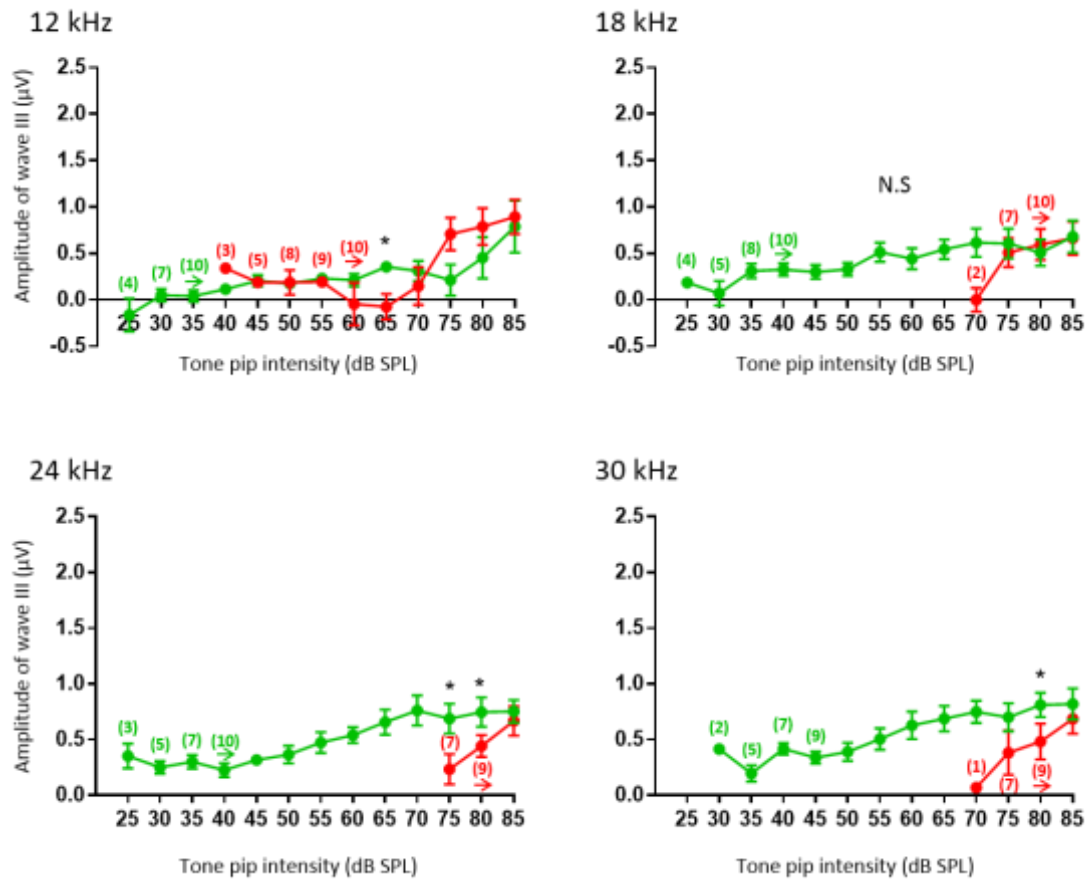


**Fig 6.10. Wave III: Absolute amplitude is low and variable in both control and AOE treated mice.**

ABRs were recorded from both control mice and those subjected to AOE, in response to frequency specific tone-pip stimuli (12, 18, 24 and 30 kHz). For each tone-pip frequency, a plot of the absolute amplitude of wave III vs increasing stimulus intensity (5 dB SPL steps) is shown, comparing control mice (green) and mice treated with AOE (red). Mean  $\pm$  SEM. Significance (\* $p < 0.05$ ) was determined using multiple t-tests (not assuming equal variance), with Sidak Holm corrections for multiple comparisons.

Figure 6.11 Wave IV: Absolute amplitude is reduced following AOE at higher frequencies only

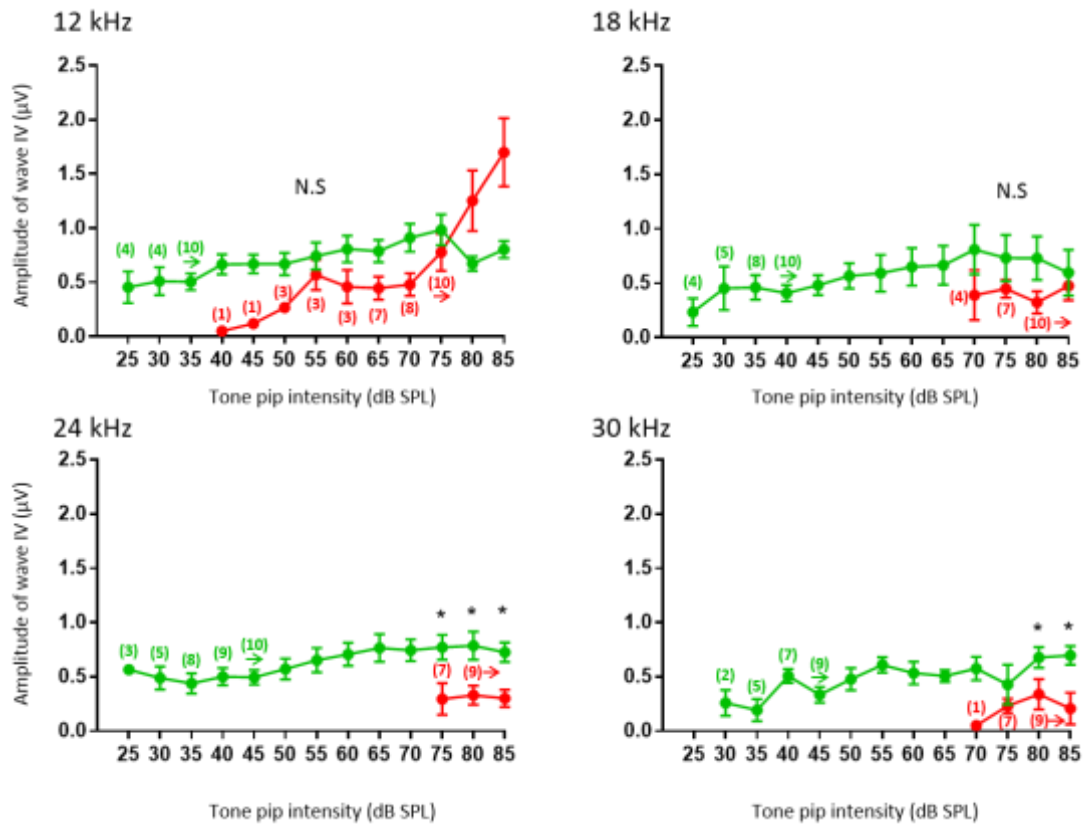


**Fig 6.11. Wave IV: Absolute amplitude is reduced following AOE at higher frequencies only.** ABRs were recorded from both control mice and those subjected to AOE, in response to frequency specific tone-pip stimuli (12, 18, 24 and 30 kHz). For each tone-pip frequency, a plot of the absolute amplitude of wave IV vs increasing stimulus intensity (5 dB SPL steps) is shown, comparing control mice (green) and mice treated with AOE (red). Mean  $\pm$  SEM. Significance (\* $p < 0.05$ ) was determined using multiple t-tests (not assuming equal variance), with Sidak Holm corrections for multiple comparisons.

### 6.3 EFFECT OF AOE ON ABR WAVE LATENCY

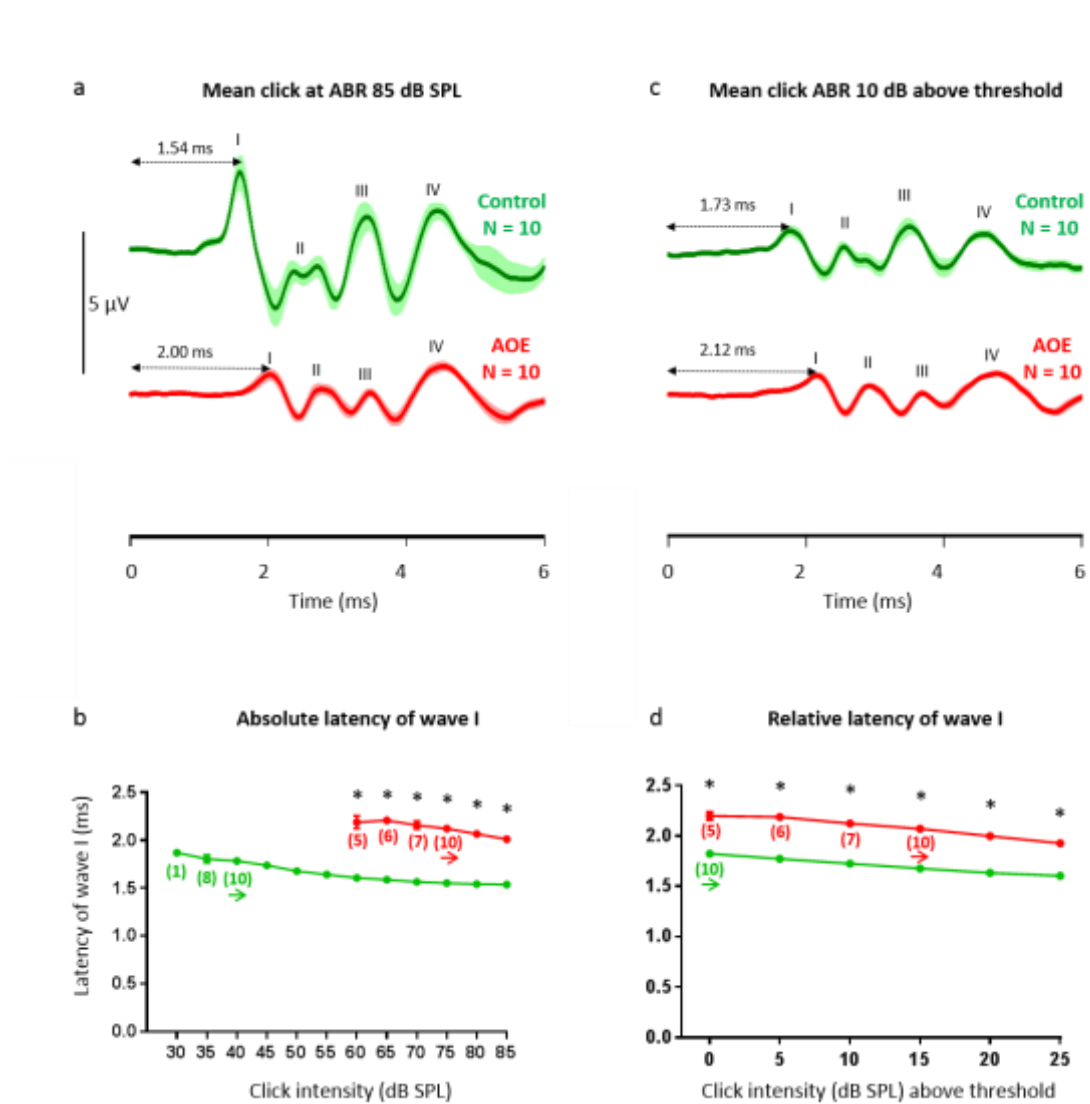
#### AOE slows latency of ABR waves

Next, I examined the latency of each ABR wave (I, III and IV), to determine whether conduction velocity in the auditory brainstem is altered following AOE. This section follows a similar format to the amplitude analysis, where both the 'absolute' and 'relative' latency are presented. Again, wave II has not been analysed due to the waveform splitting to create two distinct peaks.

Latency was defined as the time from stimulus delivery (0 ms) to the peak of a wave in question, depicted here for wave I (fig 6.12 a & c), wave III (fig 6.13 a & c) and wave IV (fig 6.14 a & c). Fig 6.12 shows that both the absolute and relative latency of wave I from click evoked ABRs were significantly prolonged in the AOE treated mice, at each stimulus intensity tested ( $*p < 0.0001$ ), indicative of slowed propagation in the auditory nerve. Wave III was delayed to a lesser extent (fig 6.13), and even more so by wave IV (fig 6.14). Fig 6.15 shows a summary of the latency for all three waves (I, III and IV), to allow direct comparison of both the absolute and relative latency. The most drastic effect of AOE is the on wave I, which was delayed to a greater extent compared to successive waves.

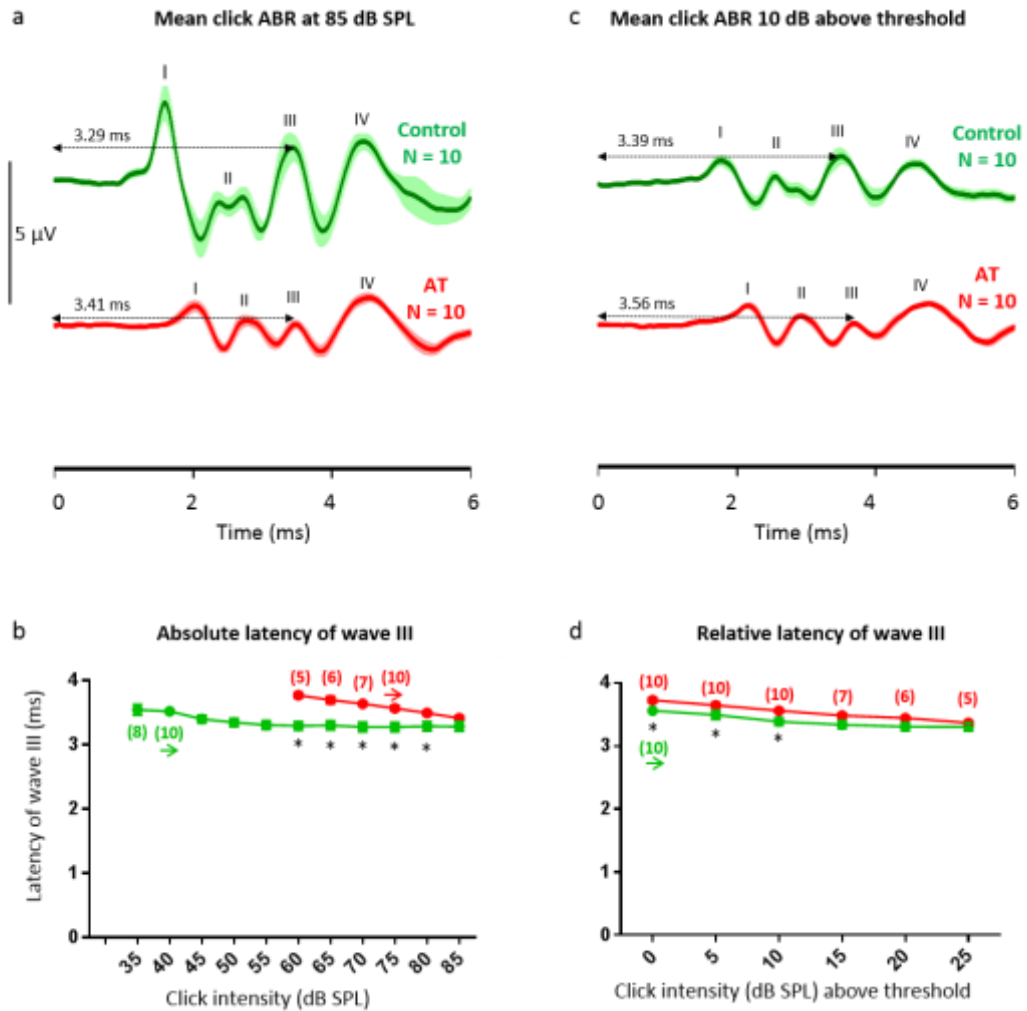
In conclusion, AOE slows conduction in the auditory nerve (wave I), however there is compensatory acceleration by successive nuclei, so that by wave IV, relative latency is indistinguishable from control mice.

Figure 6.12 Wave I: Latency is prolonged following AOE



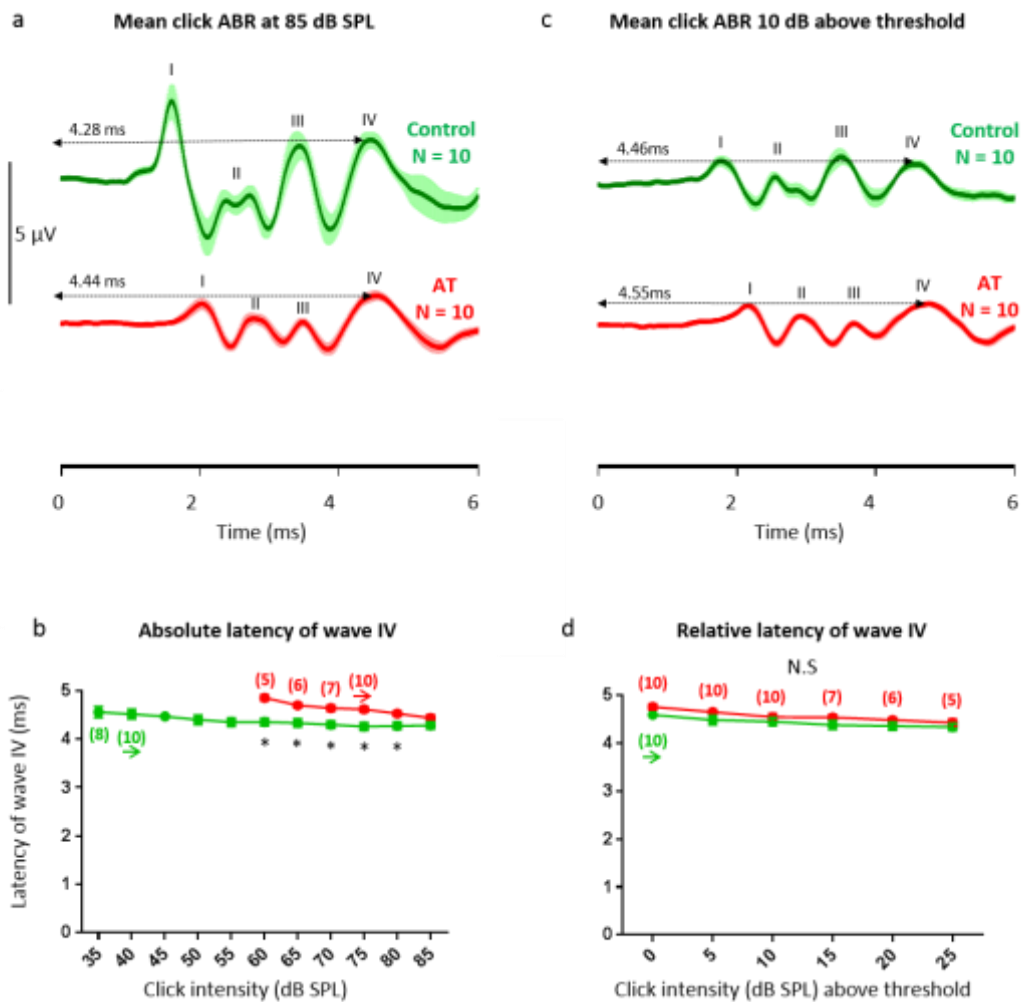
**Fig 6.12. Wave I: Latency is prolonged following AOE.** **a.** ABR traces are shown in response to click stimuli intensity of 85 dB SPL in both control mice (green) and mice subjected to AOE (red) (Mean  $\pm$  SEM). Latency of wave I is indicated by the horizontal dashed arrow. **b.** Plot showing the absolute latency of wave I vs click stimulus intensity for both control and AOE groups. **c.** ABR traces are shown in response to click stimuli 10 dB SPL above threshold. **d.** Plot showing the relative latency of wave I from click evoked ABRs vs click intensity, in both control and AOE treated mice. Significance ( $*p < 0.0001$ ) in each instance was determined via two-way ANOVA with pairwise comparisons.

Figure 6.13 Wave III: Latency is prolonged to a lesser extent than wave I following AOE



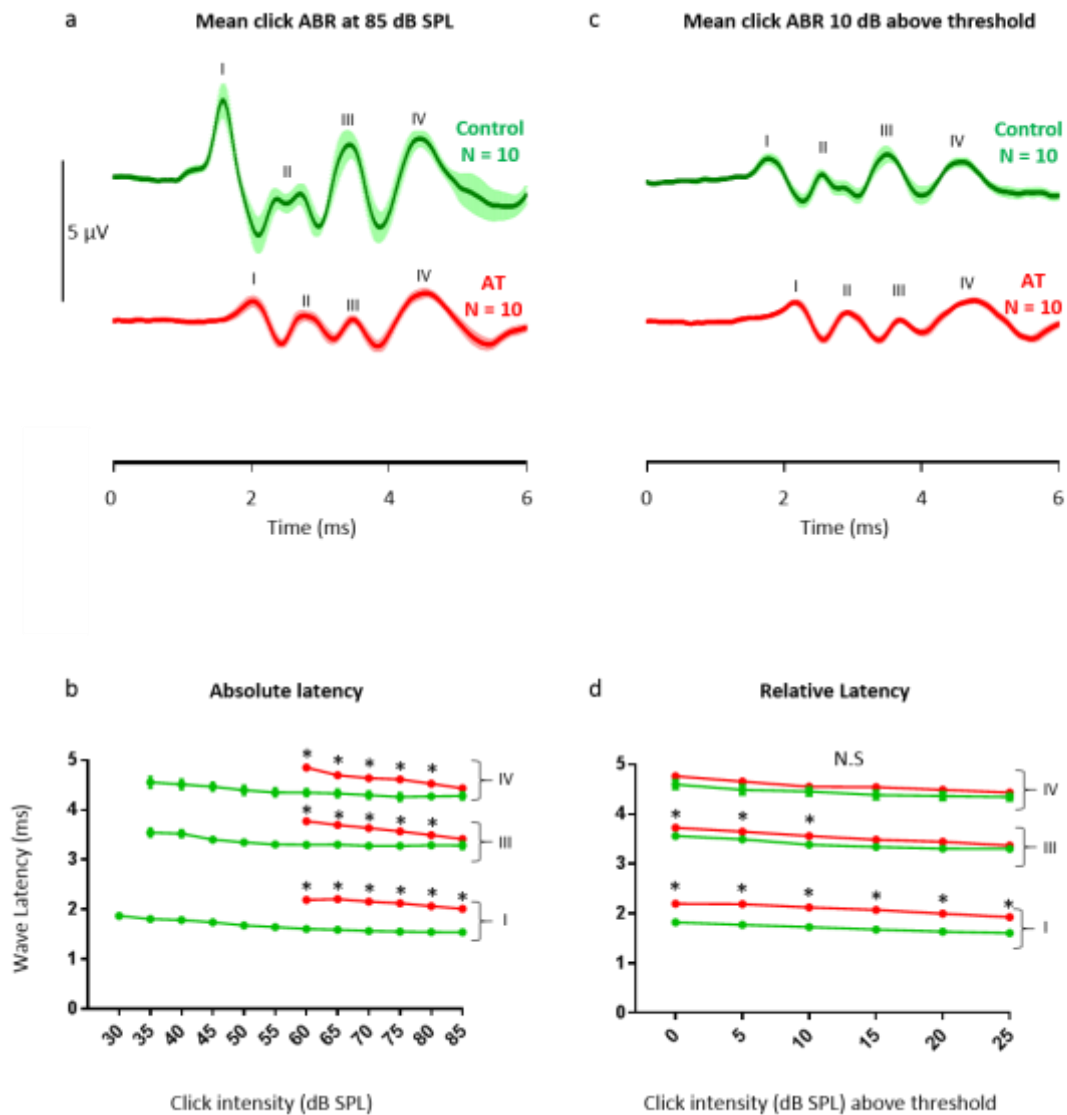
**Fig 6.13. Wave III: Latency is prolonged to a lesser extent than wave I following AOE** **a.** ABR traces are shown in response to click stimuli intensity of 85 dB SPL in both control mice (green) and mice subjected to AOE (red) (Mean  $\pm$  SEM). Latency of wave III is indicated by the horizontal dashed arrow. **b.** Plot showing the absolute latency of wave III vs click stimulus intensity for both control and AOE groups. **c.** ABR traces are shown in response to click stimuli 10 dB SPL above threshold. **d.** Plot showing the relative latency of wave III from click evoked ABRs vs click intensity, in both control and AOE treated mice. Significance (\* $p < 0.05$ ) in each instance was determined via two-way ANOVA with pairwise comparisons.

Figure 6.14 Wave IV: Relative latency is unchanged by AOE



**Fig 6.14. Wave IV: Relative latency is unchanged by AOE.** **a.** ABR traces are shown in response to click stimuli intensity of 85 dB SPL in both control mice (green) and mice subjected to AOE (red) (Mean  $\pm$  SEM). Latency of wave IV is indicated by the horizontal dashed arrow. **b.** Plot showing the absolute latency of wave IV vs click stimulus intensity for both control and AOE groups. **c.** ABR traces are shown in response to click stimuli 10 dB SPL above threshold. **d.** Plot showing the relative latency of wave IV from click evoked ABRs vs click intensity, in both control and AOE treated mice. Significance ( $*p < 0.05$ ) in each instance was determined via two-way ANOVA with pairwise comparisons.

Figure 6.15 Wave I is delayed to a greater extent than subsequent waves



**Fig 6.15. Click ABR latency summary: Wave I is delayed to a greater extent than subsequent waves.** **a.** ABR traces are shown in response to click stimuli intensity of 85 dB SPL in both control mice (green) and mice subjected to AOE (red) (Mean  $\pm$  SEM). **b.** Plot showing the absolute latency of waves I, III and IV versus click stimulus intensity for both control and AOE groups. **c.** ABR traces are shown in response to click stimuli 10 dB SPL above threshold. **d.** Plot showing the relative latency of wave I, III and IV from click evoked ABRs versus click intensity, in both control and AOE treated mice. Significance (\* $p < 0.05$ ) in each instance was determined via two-way ANOVA with pairwise comparisons.

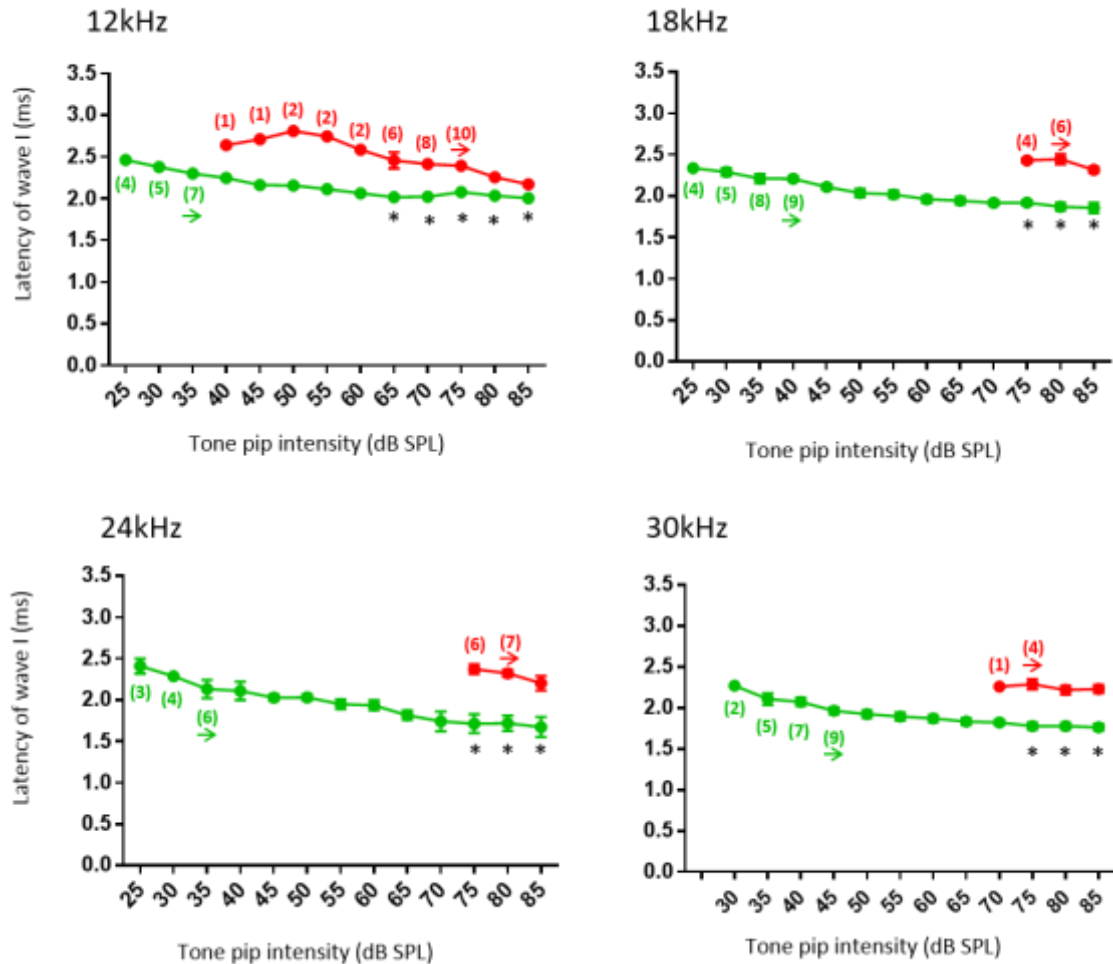
### AOE delays ABR waves in high frequency regions

Next, I wanted to establish which frequency regions of the ascending auditory pathway were affected, by comparing the tone-pip ABR wave latencies from control and AOE treated mice. Click ABRs showed wave I latency was most severely delayed following AOE, and wave IV the least. I have therefore decided to examine the latencies of wave I and IV of tone-pip evoked ABRs to establish if a similar trend (as observed in click ABR) is observed.

In this section, both the absolute and relative latencies are presented for each frequency tone-pip (12, 18, 24, 30 kHz) in response to increasing stimulus intensity. Fig 6.16 shows absolute latency of wave I is prolonged in AOE treated mice for all frequencies, at each stimulus intensity tested (for n numbers  $\geq 3$ ), whilst the relative latency of wave I in AOE mice is only prolonged at 30 kHz (fig 6.17) ( $p < 0.05$ ). In contrast, absolute latency of wave IV is only increased in the AOE group at 30 kHz (fig 6.18), whilst relative latency is unaffected by AOE (fig 6.19).

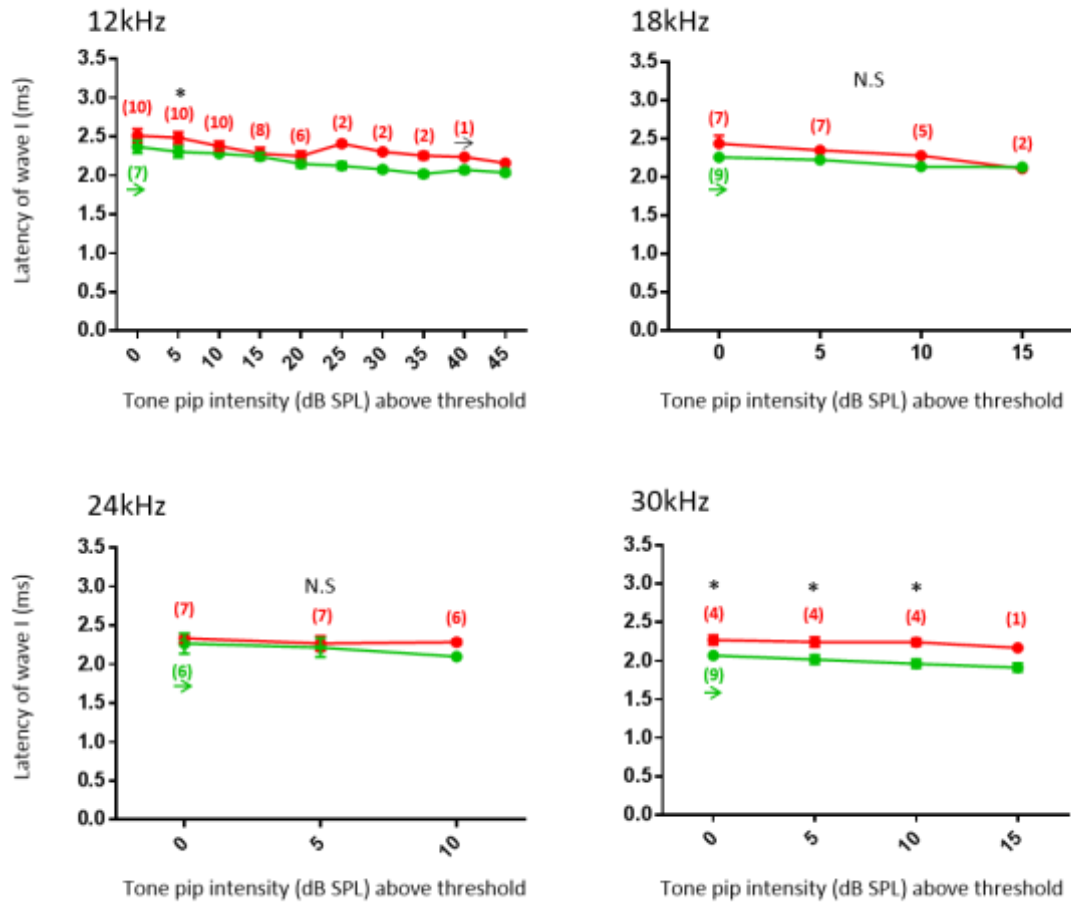
In summary, wave I from tone-pip evoked ABRs were delayed to a greater extent than wave IV, and concurs with click ABR latencies. Furthermore, AOE had most effect at high frequency regions (30 kHz), where both the relative and absolute amplitude of wave I were delayed.

Figure 6.16 Wave I: Absolute latency is prolonged following AOE at all frequencies tested (12:30 kHz)



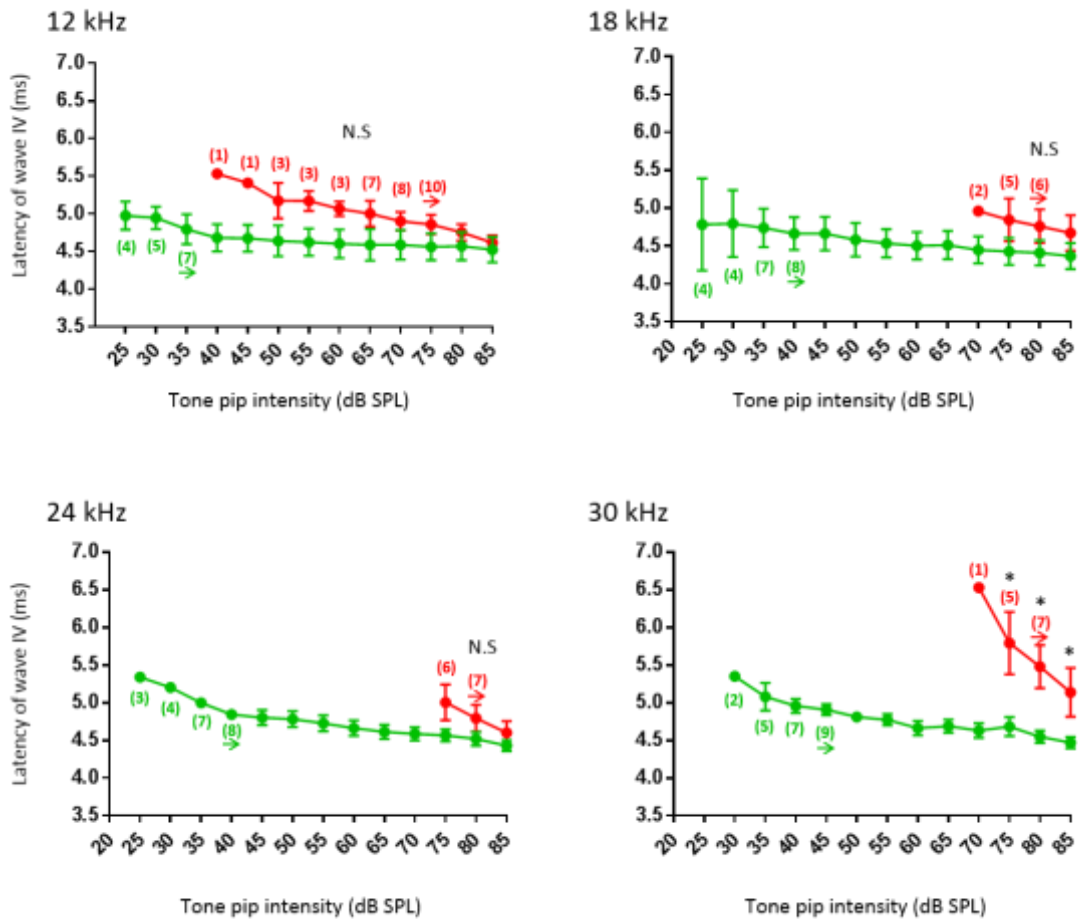
**Fig 6.16. Wave I: Absolute latency is prolonged following AOE at all frequencies tested (12:30 kHz).** ABRs were recorded from both control mice and those previously subjected to AOE, in response to frequency specific tone-pip stimuli (12, 18, 24 and 30 kHz). The absolute mean latency of wave I is plotted in response to increasing stimulus intensity for both control (green) and AOE treated mice (red). Significance (\* $p > 0.05$ ) was determined using 2-way ANOVA with pairwise comparisons in datasets found to have equal variance (18 kHz, 24 kHz and 30 kHz). For datasets with unequal variance (12 kHz), significance was determined using multiple t-tests (not assuming equal variance), with Sidak Holm corrections for multiple comparisons

Figure 6.17 Wave I: Relative latency is prolonged at high frequencies (30 kHz)



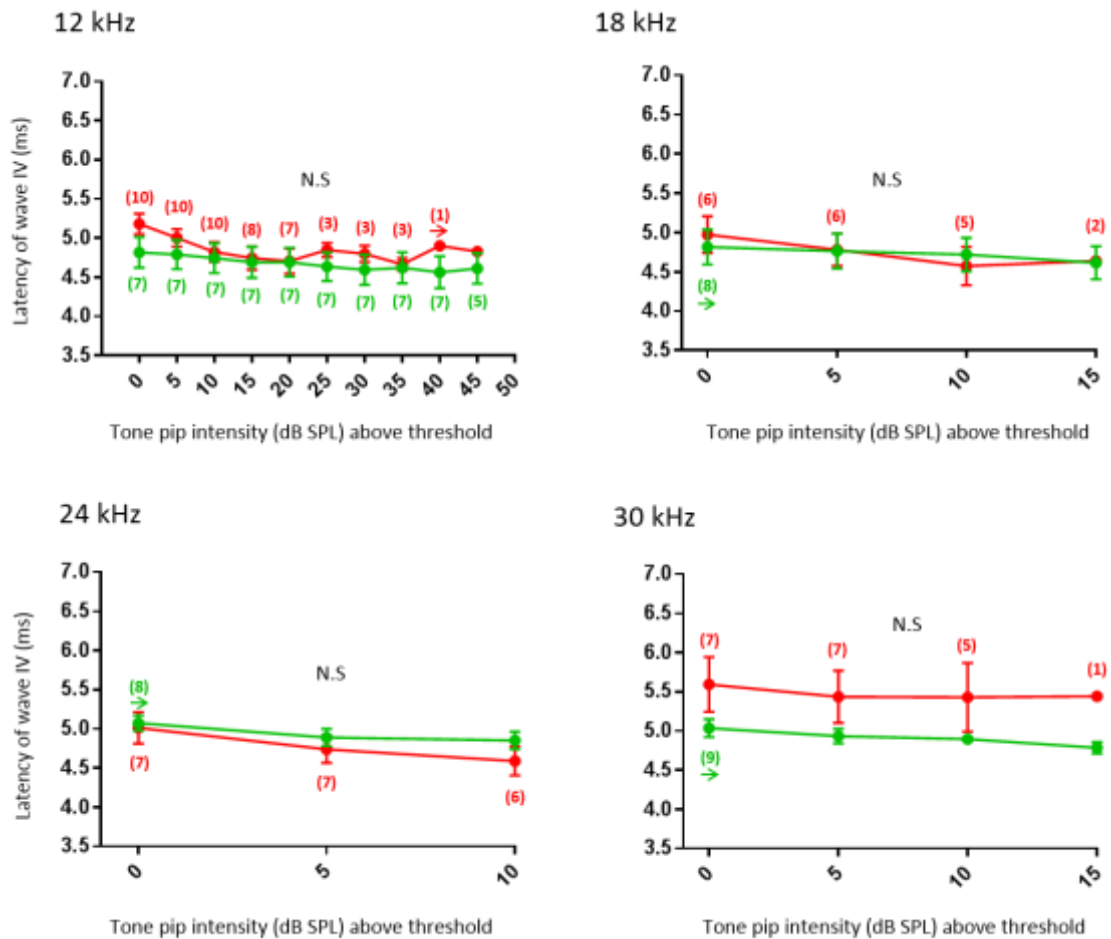
**Fig 6.17. Wave I: Relative latency is prolonged at high frequencies (30 kHz).** ABRs were recorded from both control mice and those subjected to AOE, in response to frequency specific tone-pip stimuli (12, 18, 24 and 30 kHz). For each tone-pip frequency, a plot of the relative latency of wave I vs stimulus intensity is shown, comparing control mice (green) and mice treated with AOE (red). Mean  $\pm$  SEM. Significance (\* $p < 0.05$ ) was determined via two-way ANOVA, using pairwise comparisons.

Figure 6.18 Wave IV: Absolute latency is prolonged only at high frequencies (30 kHz)



**Fig 6.18. Wave IV: Absolute latency is prolonged only at high frequencies (30 kHz).** ABRs were recorded from both control mice and those subjected to AOE, in response to frequency specific tone-pip stimuli (12, 18, 24 and 30 kHz). For each tone-pip frequency, a plot of the absolute latency of wave IV vs stimulus intensity is shown, comparing control mice (green) and mice treated with AOE (red). Mean  $\pm$  SEM. Significance (\* $p < 0.05$ ) was determined via 2-way ANOVA with pairwise comparisons for datasets which showed equal variance (12, 18 and 24 kHz). Multiple t-tests (not assuming equal variance), with Sidak Holm corrections for multiple comparisons were used to determine significance in datasets with unequal variance (30kHz).

Figure 6.19 Wave IV: Relative latency is unaffected by AOE



**Fig1.19. Wave IV: Relative latency is unaffected by AOE.** ABRs were recorded from both control mice and those subjected to AOE, in response to frequency specific tone-pip stimuli (12, 18, 24 and 30 kHz). For each tone-pip frequency, a plot of the relative latency of wave IV vs stimulus intensity is shown, comparing control mice (green) and mice treated with AOE (red). Mean  $\pm$  SEM. Significance ( $*p < 0.05$ ) was determined via 2-way ANOVA with pairwise comparisons for datasets which showed equal variance (12, 18 and 24 kHz). Multiple t-tests (not assuming equal variance), with Sidak Holm corrections for multiple comparisons were used to determine significance in datasets with unequal variance (30kHz).

## 6.4 DISCUSSION

Previously, I investigated the effect of AOE on the synaptic and intrinsic excitability of individual neurons in the SOC. To compliment this data, this chapter examines the overall hearing of the mice by measuring evoked ABRs, which allows a broader look at the effects of AOE on the ascending auditory pathway. I investigated how AOE affects ABR thresholds, wave amplitude and latencies. The main findings are summarised below:

- AOE caused significant elevations in ABR thresholds in CBA/Ca mice
- Wave I showed a reduction in amplitude in AOE treated mice
- Wave IV showed a compensatory boost in amplitude following AOE, despite reduced wave III input
- Wave I latency was significantly prolonged following AOE
- Compensatory acceleration of latency from wave I to wave IV occurred in AOE treated mice

**Hearing thresholds are significantly elevated following AOE**

In control CBA/Ca mice click ABR and frequency specific ABR thresholds ( $\geq 12$  kHz) were similar to those previously reported at  $\sim 30 - 35$  dB SPL (Grimsley and Sivaramakrishnan, 2014, Zheng et al., 1999). Following AOE, thresholds were significantly raised by  $\sim 30$  dB SPL for click evoked ABRs and between  $30 - 45$  dB SPL for tone-pip evoked ABRs  $\geq 12$  kHz (fig 6.2, a). Elevation of ABR thresholds following AOE have been observed in many other studies, however the extent of hearing loss was dependent on many factors including: age of the mice at time of exposure (Kujawa and Liberman, 2006), noise type (e.g. broadband, single frequency), mouse strain (Myint et al., 2016) and duration of exposure and recovery time (Fernandez et al., 2015). For example, Kujawa and Liberman (2009) examined the effect of AOE on CBA/CaJ mice, and also found ABR thresholds were elevated following noise trauma, however the extent of elevation was not as severe as observed in my experiments, most likely due to the differences in AOE regimes. Whilst duration of AOE was the same (2 hours), the noise stimuli used in my experiments was a louder broadband stimulus (110 dB SPL, 5

– 50 kHz), and so contained more energy than the lower power, octave band stimulus used by Kujawa and Liberman (100 dB SPL, 8-16 kHz).

Overall, despite differences in the two AOE procedures, both showed significant elevations in threshold at mid-high frequency range, but no change at 6 kHz, consistent with similar AOE studies (Wang et al., 2002, Kujawa and Liberman, 2006). This is unsurprising, as broadband stimuli causes most damage in the high frequency (basal) end of the cochlea (Gravendeel and Plomp, 1959, Ylikoski and Ylikoski, 1994). Intense octave band exposure stimuli cause most damage to test frequencies half an octave higher, known as the half-octave shift (Robles and Ruggero, 2001). Indeed, Kujawa and Liberman (2009) found the largest threshold shift at test frequencies >20 kHz in response to octave band exposure stimuli of 8-16 kHz. This was accompanied by synaptic ribbon loss in noise exposed ears throughout the basal half of the cochlea, even when thresholds had recovered to normal values.

Interestingly, CBA/Ca mice tested immediately prior to AOE at (P17-P20) showed higher ABR thresholds at 6 kHz compared to 1 week post-AOE when retested (P23:P27) (fig 6.2, b). I have already shown that AOE has no effect on ABR thresholds at 6 kHz compared to age-matched control mice (fig 6.3, a). I believe the improvement in ABR threshold at 6 kHz is a developmental change, rather than an effect of noise exposure. In my study, it must be noted that only 3 of the 10 mice tested prior to AOE had sufficiently clear data to establish a threshold at 6 kHz, in contrast to one week post AOE, where 9 mice had clear ABR waves at 6 kHz. Whether the differences in threshold at 6 kHz before and after AOE are due to the low n numbers pre-AOE (P17-P20) (n=3), or due to a developmental change remains unclear.

In summary the AOE protocol produced a large elevation in threshold one week post acoustic insult, and primarily affected mid-high frequencies, in accordance with similar studies examining AOE in mice (Kujawa and Liberman, 2006, Kujawa and Liberman, 2009, Wang et al., 2002).

### Absolute vs relative measurements of ABR amplitude

I compared the amplitude and latency of ABR waves from mice receiving AOE and age matched sham controls. Amplitude can provide an insight into the levels of excitation in different areas of the ascending auditory brainstem, whilst latency provides information about the speed of propagation. I presented the data in two different ways to allow the reader a more complete overview, since both have different advantages and disadvantages. First, I presented the 'absolute' measures of amplitude and latency, which were plotted against increasing stimulus intensity (25 to 85 dB SPL, 5 dB steps). Here, the amplitude/latency of ABR waves from control and AOE treated mice were compared to the same stimulus intensities. The disadvantage of presenting data in this manner was that at threshold, ABR wave amplitudes are inevitably very small, and ABR latencies are often more prolonged. Consequently this presents a problem when comparing ABR waves from mice with markedly different hearing thresholds (i.e. with and without AOE). Here, stimulus levels close to threshold in AOE treated mice (~70 dB SPL) produced small ABR amplitudes with more prolonged latencies; however the same stimulus level in normal hearing mice would be ~ 40 dB SPL beyond threshold, and thus produce large ABR waves, with faster latencies.

To address this problem, I also plotted the 'relative' values, where ABR wave amplitudes & latencies from control and AOE treated mice were normalized to threshold (0 dB SPL), and then plotted against increasing stimulus intensity. One issue with plotting the 'relative' data is that dB SPL is a logarithmic scale, so that a 5 dB SPL stimulus increase from a high threshold in AOE treated mice (e.g. 75 to 80 dB SPL) represents a greater energy increase than from a lower threshold (e.g. 35 to 40 dB SPL).

Another problem specific to the 'relative amplitude' only, was that tone-pip evoked ABR waves from AOE treated mice showed rapid amplitude growth with increased stimulus intensity compared to normal hearing mice, so that at +10 dB SPL relative to threshold, AOE treated mice had larger ABR waveforms (fig 6.7 & 6.8). This is likely due to damage/disruption of normal OHC motility. The ability of the auditory system to respond to a large range of sound intensities is due to the action of OHCs. In a healthy

cochlea, the BM is much more sensitive to low level stimuli, due to OHC motility providing gain. The OHCs also cause a highly compressive, non-linear input-output (I-O) response of the BM (Oxenham and Bacon, 2003). Disruption to OHCs by either acoustic overstimulation or intravenous injection of ototoxic substances leads to elevated thresholds, and a linear I-O BM function (Ruggero et al., 1997). A similar pattern is observed here, where thresholds are elevated in AOE treated mice, and the I-O growth of ABR wave amplitude is more linear compared to control. I therefore postulate that OHC function is disrupted following AOE, and this is responsible for the elevated thresholds and decreased dynamic range observed. OHC viability could be assessed by DPOAEs (a measure of OHC function) and/or sectioning the cochlea and counting the hair cells, however only physical damage to the OHCs would be apparent in the latter test. This phenomenon was not apparent in click evoked ABRs for reasons unknown. I postulate that some frequency regions along the cochlea (which were not tested by tone-pip ABR), retained some OHC function following AOE. The activity of these remaining, functional OHCs then contributed to click ABRs that showed non-linear growth in response to increasing stimulus intensity.

In conclusion, I have decided to plot both the absolute and relative measures of amplitude and latency to show a complete view of the results. Both ways of interpreting the data can be used together to assess whether any changes observed are real. For example, a change in both absolute and relative amplitude of a wave provides stronger evidence that the change observed is a real effect, compared to a change in absolute amplitude alone.

#### **AOE causes a reduction in wave I amplitude**

Following AOE, absolute amplitude of wave I (auditory nerve activity) from click evoked ABR, was significantly reduced at each stimulus intensity tested (fig 6.3, b). Whilst the mean relative amplitude of wave I from AOE treated mice was lower at each click intensity  $\geq 10$  dB SPL, this was not significant (fig 6.3, d). This may be because some AOE treated mice had very high thresholds of  $\geq 75$  dB SPL, and so only three or fewer traces (at 75, 80 and 85 dB SPL click intensity) could be included. When plotting

relative amplitude, this means n numbers are reduced at click intensities  $\geq 15$  dB SPL above threshold, where only AOE treated mice with lower ABR thresholds remain. Along with large variability of amplitude, reduced n numbers may have contributed to the lack of significant difference following AOE.

Li et al (2015) also observed a decrease in relative amplitude of wave I, one week following AOE. Furthermore, Hickox & Liberman (2014) found wave I reduction correlated with the intensity of noise delivered, with a greater reduction in mice exposed to 100 dB SPL compared to 96 dB SPL. A reduction in wave I has also been linked to tinnitus, with human studies showing wave I is reduced in patients suffering with tinnitus, despite having normal thresholds (Schaette and McAlpine, 2011, Gu et al., 2012a). This may be due to what is termed 'hidden hearing loss', where high threshold, auditory neuronal fibers are preferentially damaged by AOE, despite hearing levels returning to normal (Kujawa and Liberman, 2009). Tinnitus often arises following damage to the cochlea via AOE, so it is unsurprising that wave I is reduced in patients with tinnitus. However a reduction in wave I amplitude does not necessarily lead to development of tinnitus. Indeed, wave I amplitude was decreased in both mice with tinnitus and without tinnitus (as measured via behavioural testing) following AOE, with no significant difference in amplitude observed between the two (Li et al., 2015).

Reduction in wave I was only observed at mid to high frequencies (18-30 kHz) (fig 6.9) suggesting it is the mid- basal areas of the cochlea which is damaged, whilst lower frequency amplitude (12 kHz) remained unchanged. Indeed, ABR thresholds were not elevated to the same extent at 12 kHz compared to 18, 24 and 30 kHz (fig 6.2), suggesting less damage at these areas. Similarly, Kujawa and Liberman (2009) found initial ABR thresholds shifts were not as severe at 12 kHz compared to 32 kHz, and in turn, wave I amplitude was not depressed to the same degree at 12 kHz than 32 kHz.

In summary, AOE caused a reduction in wave I of click evoked ABRs, which reflects reduced activity of the auditory nerve. This has previously been observed in both animals and humans (Schaette and McAlpine, 2011, Gu et al., 2012a). Furthermore, AOE reduced the amplitude of mid to high frequency tone-pip ABRs (18-30 kHz). Again,

this shows AOE causes the most damage at mid to high frequency areas of the cochlea, as evidenced by higher ABR thresholds and reduced wave I amplitude at these frequencies.

Following AOE ABR wave amplitude is centrally compensated

AOE caused a reduction in wave I amplitude of click evoked ABR which is even more pronounced by wave III, where a substantial decline of both absolute and relative amplitude of wave III was observed (fig 6.4), followed by increased gain at wave IV, so that relative amplitude returned to normal levels (fig 6.5, d). Thus, it appears the central auditory nuclei provide a compensatory excitatory boost, in response to diminished input from lower levels of the ascending auditory pathway. A similar study in rats compared wave I and wave IV following AOE, and found that the relative amplitude of wave I was diminished, while wave IV amplitude was restored to normal amplitude relative to threshold (Mohrle et al., 2016). Furthermore, central compensation has also been observed in humans following cochlear damage (Gu et al., 2012b).

Compensatory boost of click ABR wave IV was not observed in tone-pip evoked ABRs (fig 10 & 11). Overall, amplitudes of wave III and wave IV from tone-pip ABRs were very low in both control and AOE treated mice, and showed large variability. This may be because tone-pip stimuli only activate a very narrow portion of the cochlea, and consequently ABR waves are small and more susceptible to masking by myogenic noise. In contrast, click evoked ABRs are large and robust, as the broadband stimulus activates a large portion of the cochlea. On this basis, I believe that central compensation does occur at wave IV, but is not seen in tone-pip ABRs, due to the small size and variability of the waves.

In summary, I have shown that following AOE, the brain centrally compensates for reduced input from the cochlea. This is reflected by an increase in wave IV compared to wave III, so that the relative amplitude of wave IV was indistinguishable from mice with no previous acoustic trauma (control).

### Latency of wave I is delayed following AOE

Following AOE, both the relative and absolute latency of wave I (click ABR) were prolonged (fig 6.12). Tone-pip evoked ABRs showed this largely affected higher frequency regions of the cochlea (fig 6.17). Wave I is linked to the activity of the auditory nerve, which contains mainly myelinated type I spiral ganglion neurons which terminate with neurons of the CN, allowing fast, precise transmission of signals from the cochlea (Toesca, 1996). In rodents, increased latency of wave I has been linked with mutations affecting myelin (Jyothi et al., 2010, Starr et al., 2003). AOE has also been shown to reduce myelin in the auditory nerves innervating IHCs from the basal region of the cochlea of rats by ~50%, 3-4 days post AOE (Pilati et al., 2012). To examine the relationship between myelination and ABR wave I, Tagoe et al (2014) performed AOE on P15-P19 rats, using a single tone frequency stimuli (14.8 kHz) at 110 dB SPL for 3 hours, on 3 consecutive days (9 hours total exposure). ABR testing on day 4 revealed increased ABR thresholds at  $\geq 16$  kHz, and in turn, increased latency of wave I at  $\geq 16$  kHz test frequencies compared to ABRs measured day 0 (pre-exposure). This indicates a slowing of AP propagation along the auditory nerve, possibly due to a demyelination of the auditory nerve (AN). Indeed, electron microscopy of transverse sections of the AN revealed myelin thickness was decreased following AOE. Furthermore, AOE caused elongations of the Nodes of Ranvier, which could contribute to slowed conduction velocity (Hartline and Colman, 2007).

Whilst a delay in wave I shown here may be due to abnormal myelin in the auditory nerve, it may also be due to peripheral damage sustained following AOE, or a combination of both. To establish whether the AOE protocol used in my experiments caused myelin reduction of the AN, similar electron microscopy of transverse sections of the AN could be used. Furthermore, the mice used in my experiments were relatively young at the time of AOE (P17:P20) and may still have been in the process of myelin formation at the time of AOE insult. Indeed myelin formation in rats starts at P10 with the maximal rate of myelin accumulation occurring at P20 (Downes and Mullins, 2014). Thus, it is difficult to determine whether AOE interrupted myelin development, or directly disrupted the myelin itself. To untangle this, older animals

could be used to examine whether AOE has the same effect on ABR latencies and myelin morphology.

#### Central compensation of ABR latency

Following a significant delay of wave I (absolute and relative), subsequent waves were delayed to a lesser extent, so that by wave IV, there was no difference in relative latency between control and AOE treated mice (fig 15). Here, the time between wave I and wave IV is reduced in AOE treated mice, to compensate for the large increase in wave I latency. I believe this to be a novel result, as I cannot find similar findings in the literature, this may be because it was simply not examined or it may be specific the particular AOE protocol and recovery time before ABR. Possible origins of central compensation are discussed in the final summary.

#### Summary

ABRs provide an overview of the hearing of the animal *in vivo*, and allow insight into the excitability and propagation speeds of the ascending auditory brainstem. Following AOE, ABR thresholds were elevated, and a decrease in wave I amplitude and latency was observed. This was followed by central compensation, so that by wave IV both the relative amplitude and latency were indistinguishable from control mice.

## 7 FINAL SUMMARY

---

The aim of this thesis was to examine normal intrinsic and synaptic excitability of LSO principal neurons, and assess how this changes following AOE. In addition, I have measured AOE mediated changes to intrinsic excitability in the neighbouring MNTB, which provides an inhibitory input to the LSO, essential for ILD processing (Pollak, 1988, Park et al., 1996, Park et al., 2004). The main technique I have used is whole cell patch clamp (in mouse brainstem slices), where I have recorded synaptic excitability (EPSCs and IPSCs), and intrinsic excitability (APs and I/Vs, using current clamp and voltage clamp respectively).

A major determinant of normal intrinsic excitability in the SOC are Kv3 channels, whose fast kinetics facilitate rapid AP firing throughout the ascending auditory pathway, vital for accurate processing of sound information (Wang et al., 1998, Macica et al., 2003, Song et al., 2005, Brown and Kaczmarek, 2011). I have determined which Kv3 subunits dominate in the LSO and MNTB using qRT PCR and immunohistochemistry. I have then compared I/Vs and APs recorded *in vitro* from control CBA/Ca, Kv3.1 KO and Kv3.3 KO mice. Finally I have measured ABRs from CBA/Ca mice *in vivo* before and after AOE, to assess levels of hearing. ABRs also provide a broad overview of excitability and conduction velocity of successive nuclei in ascending auditory brainstem.

The main findings were:

### **Synaptic excitability in the LSO**

- AMPAR mediated EPSCs and glycinergic IPSCs decay kinetics accelerate and converge during development to have sub-millisecond decay kinetics by P14 and P17 respectively.
- Following AOE, AMPAR EPSC decays are slowed from <1 ms to ~2 ms, potentially undermining ILD processing.
- NMDAR EPSCs have a dual decay component ( $\tau_{fast}$  and  $\tau_{slow}$ )

- NMDAR  $\tau_{\text{fast}}$  showed developmental acceleration from  $\sim 45$  ms to  $\sim 2$ -3 ms by P14. This is faster than any other NMDAR EPSC decay tau reported in the literature. Meanwhile  $\tau_{\text{slow}}$  contribution to total amplitude was significantly reduced by P17.
- NMDAR EPSCs show rapid irreversible depression of amplitude at positive holding potentials.
- NMDAR EPSC decay tau does not alter following AOE, whilst rise-time is accelerated from 1 ms to 0.6ms.

### **Intrinsic excitability in the LSO & MNTB**

#### **Kv3 in the MNTB and SOC**

- Kv3.1b and Kv3.3 mRNA and protein dominate in the SOC, whilst levels of Kv3.2 and Kv3.4 levels are negligible.
- The MNTB utilizes both Kv3.1 and Kv3.3 to partially rescue outward  $K^+$  current and fast AP firing in the absence of either subunit.
- In the LSO of Kv3.3 KO mice, APs are dramatically slowed, whilst APs in Kv3.1 KOs are indistinguishable from control.
- Thus Kv3.1 alone cannot rescue fast AP firing in the LSO, despite a western blot showing Kv3.1 upregulation in Kv3.3 KO mice
- Kv3.3 may be the exclusive subunit in the LSO, with both Kv3.3 and Kv3.1 in the neuropil.

#### **Following AOE**

- Intrinsic excitability of LSO principal neurons remained largely unaffected by AOE.
- In contrast, MNTB neurons became hyperexcitable, had lower AP thresholds and accelerated AP half widths.

### **The effect of AOE on the ascending auditory pathway (ABRs)**

- Wave I was delayed and amplitude reduced in AOE treated mice.
- Central compensation occurred so that by wave IV, relative latency and amplitudes were indistinguishable from control mice.

I have demonstrated that both AMPAR EPSCs and NMDAR EPSCs exhibit developmental acceleration of decay kinetics, which stabilize by P14 (chapter 3, fig 3.10 & 3.11). Mature NMDAR EPSCs show such rapid decay kinetics (2-3 ms) they may have been previously been mistaken for GluA1 containing AMPAR EPSCs. NMDAR EPSCs also showed a rapid run-down in amplitude at positive holding potentials, during whole cell patch recording, so that after only ~ 50 secs of recording, amplitude was halved (chapter 3, fig. 3.13 & 3.13). NMDAR EPSC run-down is reported to be caused by increased  $Ca^{2+}$  levels in the cell (Tong et al., 1995, Wild et al., 2014), however increased  $Ca^{2+}$  buffering did not prevent run-down, and results were varied and inconclusive.

AOE did not affect NMDAR decay kinetics, however the NMDAR EPSC rise-time accelerated from 1 ms to 0.6 ms. AOE also caused an increase in GluN1B mRNA, which may be responsible for the change in rise-time kinetics. In contrast, AOE caused AMPAR EPSC decay tau to increase from ~1 ms to ~2 ms, concomitant with a switch from GluA4 mRNA to GluA1 mRNA (chapter 5, fig. 5.13), however IPSCs remained unchanged (Pilati et al., 2016). Mismatched kinetics of bilateral inputs to the LSO could potentially undermine ILD processing (Pilati et al., 2016, Park et al., 1996b, Tollin, 2003). Sound localisation problems have previously been reported in human listeners with NIHL (Moore, 2016). My results suggest slower AMPAR EPSC decay contributes to impaired sound localisation experienced by listeners with NIHL.

AOE mediated slowing of AMPAR EPSCs may be a mechanism to preserve binaural hearing. Here, longer EPSC decay tau in the LSO increases the probability of the membrane potential reaching AP threshold. In support of this, click ABR recordings showed a compensatory boost of wave IV in AOE treated mice to overcome reduced

wave I and wave III input (chapter 6, fig 6.5 and 6.6). Increased amplitude of an ABR wave indicates increased excitability of the neural generator. Origin of wave IV is currently debated as either the SOC (as defined by the Jackson laboratory ([http://phenome.jax.org/db/q?rtn=projects/docstatic&doc=Jaxpheno8/Jaxpheno8\\_Procedure#Procedure\\_ABR](http://phenome.jax.org/db/q?rtn=projects/docstatic&doc=Jaxpheno8/Jaxpheno8_Procedure#Procedure_ABR)), or lateral lemniscus/inferior colliculus (Melcher et al., 1996). My results suggest the former is correct, as longer EPSCs should result in increased excitability in the LSO (located in the SOC), and thus produce a larger ABR wave amplitude, as observed in wave IV. Similarly, whilst MNTB neurons usually exhibit a single-spiking phenotype due to the action of Kv1 channels, following AOE they were hyperexcitable, firing multiple APs in response to a single depolarising current step, which may also contribute to increased amplitude of wave IV.

My results also showed ABR wave I was delayed in AOE treated mice, followed by compensatory acceleration of subsequent waves, so that by wave IV relative latency was indistinguishable from control (no AOE) (chapter 6, fig 6.15). The delay in wave I is most likely a result of demyelination of the auditory nerve (Tagoe et al., 2014). The subsequent acceleration of the signal could be achieved by a decrease in AP half width. Indeed, MNTB neurons showed faster AP half widths following AOE, which would help accelerate signal propagation through the ascending auditory pathway (see chapter 5, fig. 5.3).

Here, I have demonstrated that AOE alters LSO and MNTB neurons differently. We see dramatic alterations to intrinsic excitability of MNTB neurons (hyperexcitability, lower AP threshold, decreased AP half width), yet the intrinsic excitability of LSO neurons remain largely unaltered. In contrast, there is no evidence of long term synaptic plasticity in the MNTB, however LSO neurons undergo significant slowing of AMPAR EPSC decay tau.

A key determinant of normal intrinsic excitability in the ascending auditory pathway are Kv3 channels, which mediate rapid AP firing (Wang et al., 1998, Brown and Kaczmarek, 2011, Macica et al., 2003, Rudy and McBain, 2001). Until now, no one has performed a comprehensive study of Kv3 subunits in the LSO. I have demonstrated

that Kv3.1 and Kv3.3 mRNA and protein dominate in the SOC, and form functional channels, as measured by whole cell patch clamp. Here we see Kv3 currents mediate ~50% out total outward  $K^+$  conductance in both the LSO and MNTB (chapter 4, fig. 4.13). The MNTB is able to utilize both Kv3.1 and Kv3.3, as demonstrated by rescued outward  $K^+$  conductance and partial recovery of fast AP firing in Kv3.1 KO and Kv3.3 KO mice (chapter 4, fig.4.14). In contrast, the LSO of Kv3.3 KO mice show AP half width ~double that of control or Kv3.1 KO mice, and massively reduced outward  $K^+$  conductance (chapter 4, fig. 4.14 & 15). Thus, Kv3.3 is vital for fast AP firing in the LSO, and may explain why people with SCA13 (Kv3.3 mutation) have sound localisation problems (Middlebrooks et al., 2013).

The majority of previous research has emphasised the importance of Kv3.1 in the SOC, in particular the MNTB. This has led to the development of novel compounds to act on Kv3.1 as its target, to control the excitability of neurons in the auditory pathway (Brown et al., 2016). My study has demonstrated that Kv3.3 is as important as Kv3.1 for mediating fast AP firing in the MNTB. Furthermore, in the LSO, it is likely Kv3.3 is the exclusive subunit. This is supported by immunohistochemistry, which revealed Kv3.1 does not appear in LSO cell membranes, and is instead relegated to the neuropil. This study has highlighted the vital role of Kv3.3 in the ascending auditory pathway, thus offering an alternative target for modulation by drug therapy.

## 7.1 FUTURE WORK

### **Is AOE induced hyperexcitability of MNTB neurons caused by decreased Kv1 current?**

MNTB neurons usually fire a single AP in response to a single EPSP, due to the action of Kv1 mediated current (Brew and Forsythe, 1995b, Dodson et al., 2002). I believe AOE disrupts Kv1 current, so that multiple APs are fired in response to depolarising current steps. This could be tested by adding DTX I (a Kv1 inhibitor) to the brainstem slice, and then assessing the amplitude MNTB currents under voltage clamp at HP -40 mV (where Kv1 are half activated, but Kv3 channels are closed) (Brew et al., 2003a, Rudy et al., 1999). If Kv1 mediated current is lower in the MNTB of AOE treated mice, we should

observe low current amplitudes at HP -40 mV, with little change following DTX I addition.

Potential mechanisms of reduced Kv1 activity include reduced PIP<sub>2</sub> (Smith et al., 2015), and increased BDNF via activation of TrKB (Youssoufian and Walmsley, 2007, Colley et al., 2004). The contribution (if any) of these mechanisms to hyperexcitability in the MNTB could be explored by adding TrKB inhibitor or palmitoylated peptide (to sequester PIP<sub>2</sub>) to acute brain slices taken from control and AOE treated mice.

#### *In vivo* sound localisation experiments

Kv1 current is crucial for temporal precision in the MNTB, which in turn is required for accurate sound localisation (Grothe, 1994; Joris and Yin, 1998). Indeed, deletion of Kv1.1 resulted in decreased temporal precision in the MNTB, and poor sound localisation (Karcz et al., 2011). Similarly, we have shown AMPAR EPSC decay tau in the LSO are also slowed following AOE (chapter 5, fig 5.13), which computer modelling predicts will undermine sound localisation (Pilati et al., 2016). To date, *in vivo* sound localisation following AOE has not been tested in mice. This can be performed using behavioural testing in awake mice using a 'speaker swap' procedure (Allen and Ison, 2012a). However, if ILD performance was compromised, it would be difficult to untangle whether this is due to hyper-excitability of the MNTB (due to decreased Kv1) or extended AMPAR EPSC decay tau, or some other unknown disruption.

Similarly, we have shown that Kv3.3 dominates the LSO, where Kv3.3 KO mice show much longer half widths. Humans with SCA13 (Kv3.3 mutation) are poor at ILD discrimination, which could be a result of slowed APs in the LSO (observed here in Kv3.3 KO mice). Again, behavioural ILD testing in awake Kv3.3 KO mice would elucidate whether increase half width of APs in the LSO result in impaired ILD processing. This work would need to be collaborative, as I did not have access to equipment to perform these experiments.

### SCA13 mutation causes cerebellar degeneration

It is not simply reduced Kv3.3 current which causes SCA13 symptoms, as evidenced by Kv3.3 KO mice, which do not present with ataxia, and only display mild balance problems when challenged (Ho et al., 1997, Joho et al., 2006, Hurlock et al., 2009). Thus, further work is needed to reconcile why SCA13 causes neurodegeneration, whilst simply removing Kv3.3 does not (Hurlock et al., 2009). Development of a SCA13 mutant mouse could provide insight into the function of Kv3.3, by finding the cause of SCA13 mediated neurodegeneration, and what separates it from other closely linked Kv3.1 mutations, which have no degenerative effects (Muona et al., 2015). SCA13 can be caused by several different mutations, which result in different prognosis (e.g. early onset or late onset) (Zhang and Kaczmarek, 2015). Middlebrooks (2013) tested human listeners with the mutation R42OH (late onset), whom he found had poor ILD processing. Development of a mouse with the same mutation could uncover the reasons for poor ILD processing, and elucidate whether it is neurodegeneration in the auditory pathway (as observed in the cerebellum), or increased AP half widths in the LSO that are responsible for poor sound localisation.

### Effect of different levels of AOE, assessed over time

I have investigated the effect of AOE 1 week post exposure in the LSO and MNTB. It is well established that intensity noise and length of exposure correlate with the amount of damage to the cochlea (Kujawa and Liberman, 2006, Fernandez et al., 2015, Hickox and Liberman, 2014). The AOE protocol used here resulted in raised ABR thresholds 1 week later (chapter 6, fig. 6.2) and only partial recovery 3 months later (Pilati et al., 2016). Here, we could observe how changes in synaptic and intrinsic excitability change over time, starting immediately after acoustic insult. Unfortunately, the age of the mouse would limit the ability to patch beyond ~ 2 months, due to decreased visibility of the neurons.

The AOE protocol appeared to disrupt the OHCs, as evidenced by the steep growth curve and reduced dynamic range of ABR waves (chapter 6, fig. 6.7 & 6.8). There are many studies now assessing the effects of moderate AOE, which do not damage hair cells, but cause degeneration of innervating SGNs (Wang et al., 2002, Kujawa and

Lieberman, 2009). Here, we could assess the impact of moderate AOE on excitability in the LSO and MNTB.

In conclusion, the auditory system shows remarkable plasticity and change following AOE. I have demonstrated both synaptic and intrinsic changes in response to AOE in the LSO and MNTB respectively. ABR measurements confirmed central compensation of excitability and conduction velocity along the ascending auditory pathway. I have also shown that the LSO undergoes massive developmental changes in the kinetics of both AMPAR EPSCs and NMDAR EPSCs, and established that Kv3.3 is vital for normal K<sup>+</sup> conductance in the LSO, which has previously been overlooked.

## 8 APPENDIX

---

### 8.1 BASIC THEORETICAL PRINCIPALS OF WHOLE CELL PATCH CLAMP

#### **The phospholipid bilayer enables the establishment of concentration gradients**

All mammalian cells are enveloped by a phospholipid bilayer that acts as a barrier, separating the inside of the cell from the extracellular space. The phospholipids composing the membrane are arranged so that the hydrophilic heads face outwards and the hydrophobic fatty acid tails face inwards (fig 8.1), forming a barrier through which charged particles cannot pass. Various proteins are embedded in the bilayer, such as ion channels, which enable ions to pass from one side to the other. Thus, the membrane allows osmotic control over the environment, and the establishment of concentration gradients. The most striking of these is the difference in  $\text{Na}^+$  and  $\text{K}^+$  concentration across the membrane.  $\text{Na}^+$  is low inside animal cells (5-20 mM) but has high extracellular levels (130-160 mM). Conversely, intracellular  $\text{K}^+$  levels are high (130-160 mM) and extracellular levels low (4-8 mM) (Molleman, 2003). These differences are maintained by specialized proteins, such as the  $\text{Na}^+/\text{K}^+$  pump, which uses the breakdown of ATP to ADP to pump 3  $\text{Na}^+$  ions out of the cell and pump 2  $\text{K}^+$  ions into the cell. This sets a concentration gradient that is the basis of many physiological processes, including action potentials.

Figure 8.1 The phospholipid membrane acts as a capacitor

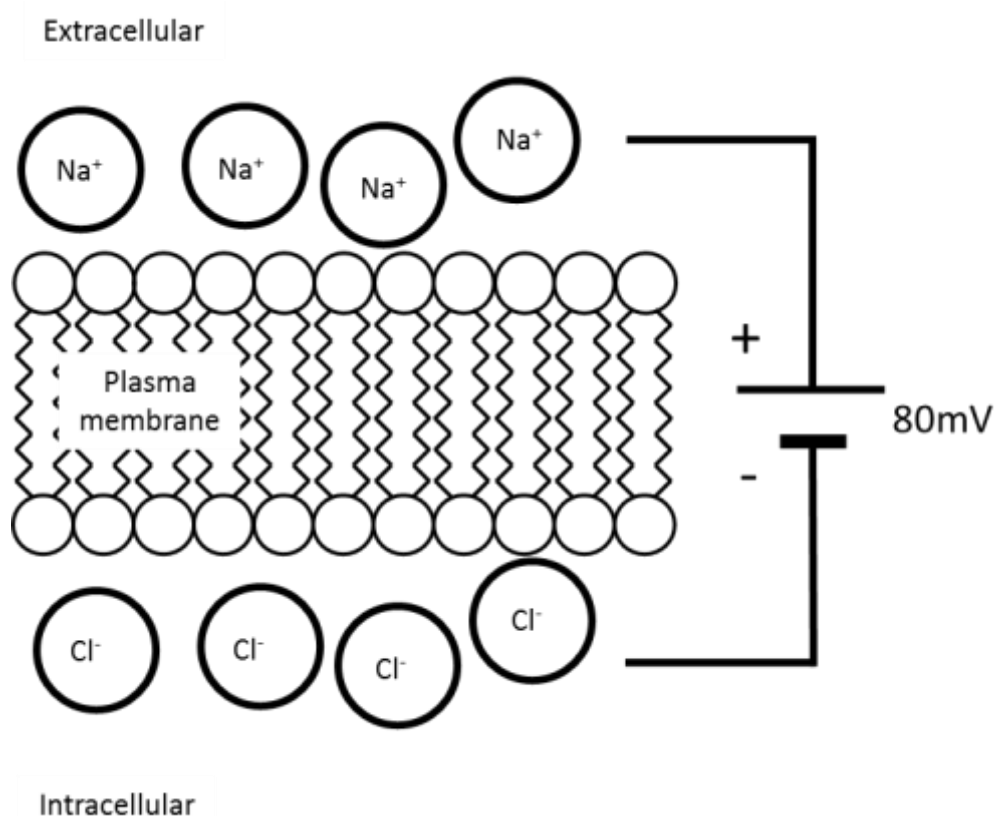


**Fig 8.1. The phospholipid membrane acts as a capacitor.** Positive ions (shown here as  $\text{Na}^+$ ) on the extracellular side are attracted to the negatively charged intracellular side, and so gather at the cell membrane. At the same time, negatively charged ions ( $\text{Cl}^-$ ) are attracted to the positively charged extracellular space. Figure is adapted from Molleman (2003).

When a concentration gradient is established, an equilibrium potential for a particular ion can be calculated. There are two driving forces on any charged ion: electrical and chemical. When these forces are balanced, there is no net flow of ions across a semi-permeable membrane from one side to the other; the membrane potential at which this occurs is known as the equilibrium potential. This is distinct from the reversal potential, which refers to membrane potential at which there is no net flow of the sum of all ions (which may not be the same as the equilibrium potential for any of the individual ions). The Nernst equation seen below gives the equilibrium potential for a particular ion when intracellular and extracellular concentrations are known.

$$E_{\text{ion}} = \frac{RT}{zF} \ln \frac{[\text{ion}]_o}{[\text{ion}]_i}$$

Here,  $E_{\text{ion}}$  is the equilibrium potential for the ion under consideration,  $R$  is the universal gas constant,  $T$  is the temperature in Kelvin,  $z$  is the oxidation state of the ion in question,  $F$  is Faradays constant ( $9.65 \times 10^4 \text{ Cmol}^{-1}$ ),  $[\text{ion}]_o$  is the ion concentration outside the cell, and  $[\text{ion}]_i$  is the concentration inside the cell. For  $\text{K}^+$ , this equates to around  $-90\text{mV}$ , and for  $\text{Na}^+$  around  $+50\text{mV}$  (Hille, 2001). However, the Nernst equation assumes a single-ion system, thus the equilibrium and reversal potential are the same. However, animal cells are in fact multi-ion systems. To address this, the Goldman-Hodgkin-Katz equation includes a number of ions to which the cell has significant permeability ( $\text{Na}^+$ ,  $\text{K}^+$ ,  $\text{Cl}^-$ ) to give the reversal potential.

$$V_m = \frac{RT}{F} \ln \left( \frac{p_{\text{K}}[\text{K}^+]_o + p_{\text{Na}}[\text{Na}^+]_o + p_{\text{Cl}}[\text{Cl}^-]_i}{p_{\text{K}}[\text{K}^+]_i + p_{\text{Na}}[\text{Na}^+]_i + p_{\text{Cl}}[\text{Cl}^-]_o} \right)$$

Here,  $V_m$  is the reversal potential,  $p_{\text{K}}$  is the permeability to  $\text{K}^+$ ,  $p_{\text{Na}}$  is the permeability to  $\text{Na}^+$  and  $p_{\text{Cl}}$  is the permeability to  $\text{Cl}^-$ . This equation takes into account the permeability of the cell to different ions; the more permeable a cell is to a particular ion, the more the equilibrium potential of that particular ion will dominate. At rest a cell is more permeable to  $\text{K}^+$  than  $\text{Na}^+$ , thus the RMP is much closer to the equilibrium potential for  $\text{K}^+$  ( $E_{\text{K}}$ ) ( $-90\text{mV}$ ), than for  $\text{Na}^+$  ( $E_{\text{Na}}$ ) ( $+50\text{mV}$ ) at around  $-65 \text{ mV}$  (Purves D, 2002). When an action potential is fired in a nerve cell, voltage-gated  $\text{Na}^+$  channels open, making the cell far more permeable to  $\text{Na}^+$ , thus increasing the membrane potential nearer to  $E_{\text{Na}}$  ( $+50\text{mV}$ ), at around  $+30\text{mV}$ .

### Series resistance and capacitance

The phospholipid bilayer in a cell forms a capacitor, which can store charge. This occurs because there is a potential difference across the cell membrane, as the intracellular side is more negative than the extracellular side. This creates an electromagnetic field,

where intracellular anions are attracted to the positively charged outside and accumulate near the membrane. At the same time, extracellular cations are attracted to the negatively charged intracellular space, again collecting near the membrane (fig 8.1). The amount of charge that can accumulate is proportional to the membrane surface area. Thus, by measuring capacitance, this can provide an estimate of the membrane surface area. The consequence of capacitance is that any changes to the membrane potential must first overcome the stored charge. In whole cell voltage clamp this will slow any stepwise changes to the membrane potential.

Figure 8.2 Whole cell configuration can be represented by a simple RC circuit

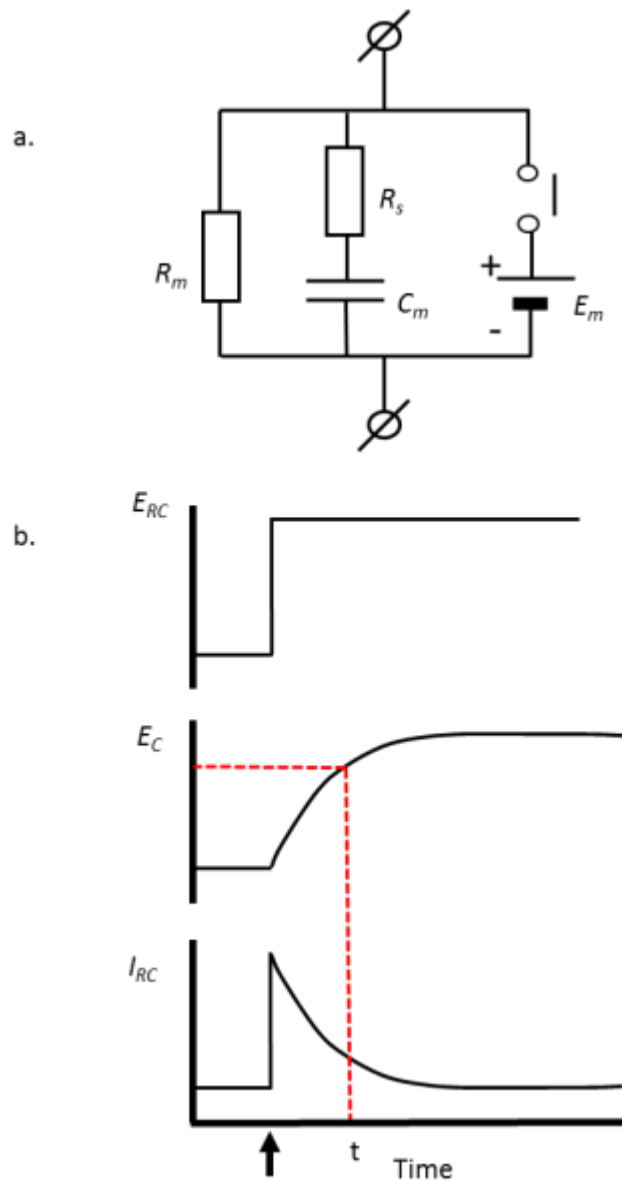


**Fig 8.2. Whole cell configuration can be represented by a simple RC circuit.** **a.** The membrane acts as a capacitor ( $C_m$ ), and is in series with the access resistance and pipette resistance, which together form the series resistance ( $R_s$ ), with the membrane resistance ( $R_m$ ) in parallel. When the switch is closed this changes the potential across the whole circuit. **b.** The effect of voltage change across the RC circuit. Closing the switch (black arrow) causes an instantaneous change in potential across the whole circuit ( $E_{RC}$ ), top graph. However, voltage only changes gradually and exponentially over the capacitor ( $E_C$ ), middle graph. The current across the circuit ( $I_{RC}$ ) initially surges, before decaying exponentially. The time constant ( $t$ ) is denoted as 63% of the exponential curve. Figure is adapted from Molleman (2003).

As well as the capacitance charges of the membrane ( $C_m$ ), the amplifier must also overcome the series resistance present in the circuit. Series resistance is the sum of access resistance ( $R_m$ ) and pipette resistance ( $R_p$ ). Current ( $I$ ) through a resistor is proportional to the voltage difference ( $E$ ) and inversely proportional to the resistance.

$$I = E/R$$

Thus high resistance results in low current, so the voltage command must be scaled to compensate for the voltage drop caused by series resistance.

### **RC circuit**

Because a cell has resistances, capacitance, and a voltage drop across the membrane, this can be represented as a simple RC circuit (see fig 8.2 a). Here the series resistance and capacitor are in series, with the membrane resistance in parallel. The speed of charging and discharging the capacitor (plasma membrane) depends upon the size of the resistances. If the switch is closed in figure 8.2 (mimicking a current applied in voltage clamp) the voltage over the whole circuit is changed instantaneously (fig 8.2, b, upper graph), however voltage over the capacitor builds up exponentially (fig 8.2 b, middle graph), whilst the current initially surges, then declines exponentially (fig 8.2 b, lower graph). Both the resistance and capacitance are linearly proportional to the time constant ( $\tau$ ) (63% of exponential curve).

$$\tau = RC$$

Where  $\tau$  is Tau, R is resistance and C is capacitance. The capacitance transients can be clearly identified when a cell is in whole cell patch configuration, as large capacitive transients appear in response to the 5mV test pulse.

The equivalent circuit of whole cell configuration can be seen in figure 8.3. Here, the patch of membrane underneath the patch pipette has been disrupted, allowing electrical access inside the cell. The circuit consists of the pipette resistance ( $R_{pipette}$ ), the access resistance ( $R_{access}$ ) in series. Parallel to the circuit is the membrane resistance ( $R_{membrane}$ ), and the leak resistance ( $R_{leak}$ ), the latter of which should be as high as possible to prevent short circuiting.

Figure 8.3 Equivalent circuit for whole cell patch configuration

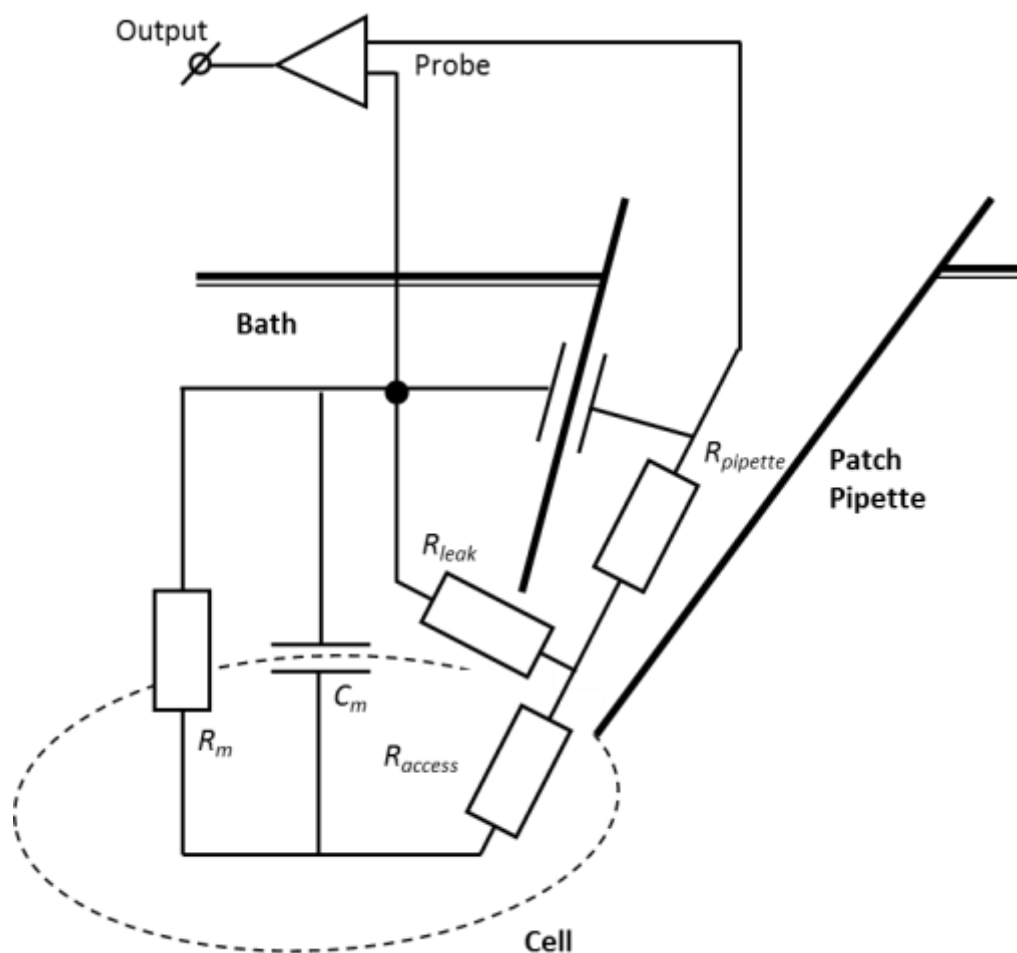


**Fig 8.3. Equivalent circuit for whole cell patch configuration.** Here the cell membrane directly beneath the patch pipette has been disrupted so that the pipette electrode has direct electrical contact with the cytoplasm. This allows recording of all ionic currents travelling through the cell membrane. The circuit consists of resistances ( $R_{pipette}$ ,  $R_{access}$ ) in series with capacitance of the membrane ( $C_m$ ). Parallel to the circuit is  $R_m$  (membrane resistance), and  $R_{leak}$  (leak resistance) the latter of which must be as high as possible to prevent short circuiting. Figure is adapted from Molleman (2003).

## 8.2 CALIBRATION OF NOISE EXPOSURE EQUIPMENT

Prior to sound delivery, the system was calibrated to measure the power spectrum of the output signal, and was adjusted accordingly to ensure an output of 105-110 dB SPL across (5-50) kHz. The power spectrum gives a measure how much volume is being generated at each particular frequency in a broadband signal.

Briefly, the calibration procedure first requires an acoustic calibrator to generate a specified signal (of known volume level and frequency), which is connected to a signal analyser. If the signal analyser displays the correct level and frequency of the acoustic calibrator input, this shows the signal analyser is correctly calibrated. The signal analyser itself may then be used to analyse the broadband output from the speaker used for AOE, within the sound attenuated booth, by generating a power spectrum of the broadband output signal. The volume of the output signal can be corrected accordingly to match the desired broadband intensity (see fig 8.4).

For a more detailed overview, to start the process of calibration the following protocol was used:

- 1.** Connect the acoustic calibrator (Brüel & Kjær Sound Calibrator, type 4231) to the microphone (free field microphone ½ inch cartridge (Brüel & Kjær, type 4191) in conjunction with a microphone preamplifier (Brüel & Kjær, type 2669-C).
- 2.** Attach the output from the microphone to the microphone power supply (Brüel & Kjær Battery Driven Power Supply, type 2804).
- 3.** Connect the output from the microphone power supply to the signal analyser (Agilent HP3566A Dynamic Signal Analyser), via input 1.
- 4.** Activate the the acoustic calibrator (type 4231) to generate a tone of 94dB SPL at 1 kHz. The signal analyser gives an output in dB Volts root mean squared (dB Vrms), which must be converted to dB SPL to ascertain whether this matches the 94 dB SPL input from the acoustic calibrator.

A general conversion of dB Vrms to dB SPL is not possible, because different microphones will convert the same sound pressure wave into different electrical output. Thus the conversion must be specific to the exact type of microphone used. The Brüel & Kjær, type 4191 has been carefully calibrated by the manufacturers to produce a signal of 38 mV peak to peak, when applying 1 kHz tone at 94 dB SPL (the equivalent of 1 pascal of air pressure). Here we can convert Vpp (volts peak to peak) to Vrms (volts root mean squared) using the following equation:

$$V_{rms} = 0.707 \times V_{max}$$

To find Vmax, we must divide Vpp by 2

$$V_{max} = V_{pp}$$

$$/2 = 38/2 = 19$$

$$\text{Thus } V_{rms} = 0.707 \times 19 = 13.4 \text{ mV rms}$$

This must then be converted to a dB scale to give dB Vrms as shown below:

$$\begin{aligned} \text{dB scale} &= 20 * \log_{10} \frac{V_1}{V_2} \\ &= 20 * \log_{10} \frac{0.0134}{1} \\ &= -37 \text{ dB Vrms} \end{aligned}$$

Thus, if the signal analyser gives an output of -37 dB Vrms in response to 1 kHz input at 94 dB SPL from the acoustic calibrator, this confirms the signal analyser is correctly calibrated. We can use this known input and output (94 dB SPL = -37 dB Vrms) to convert the scale from dB SPL to dB Vrms.

If we know -37 dB Vrms is the output at 94dB SPL, then the output at 0dB Vrms is  $94+37 = 131$  dB SPL. Therefore, if we want to find 110 dB SPL (our desired measurement of the broadband output) we must subtract 21 dB from 0 dB Vrms (131 dB SPL) to give -21 dB Vrms, which is equal to 110 dB SPL.

Figure 8.4 Analysing the output of the acoustic over-exposure (AOE) set-up

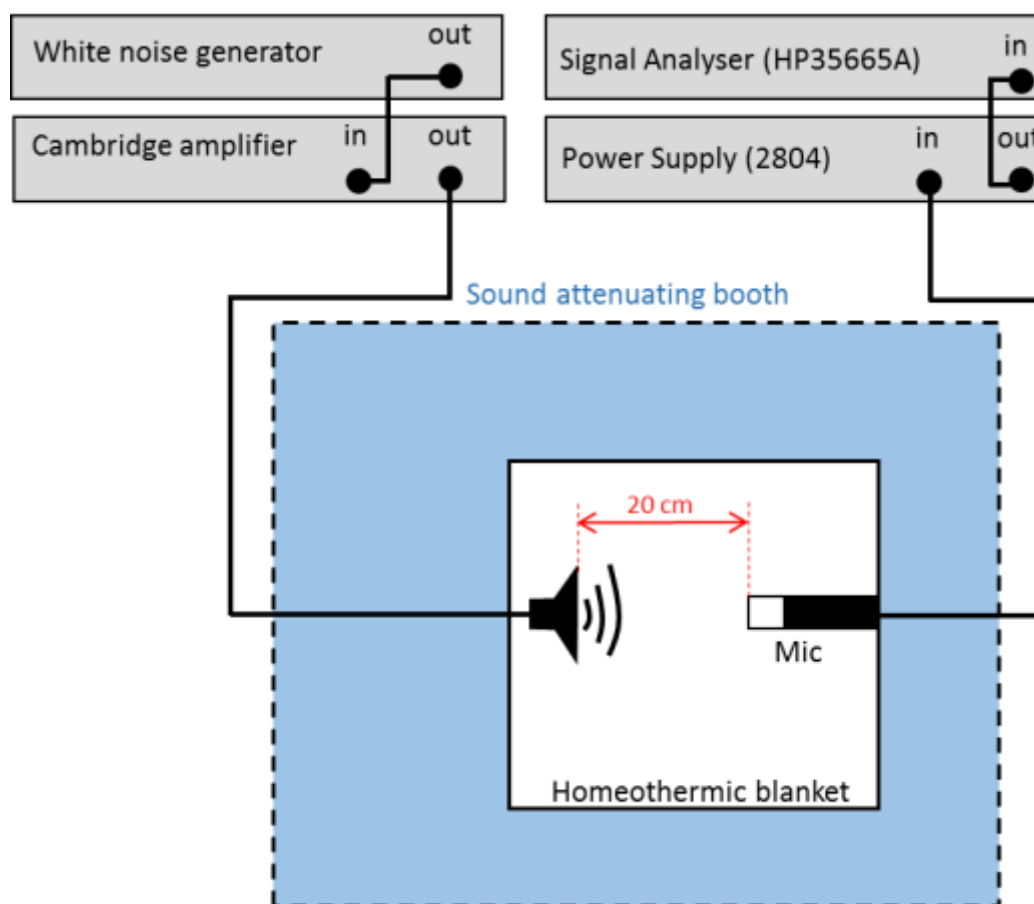


**Fig 8.4. Analysing the output of the acoustic over-exposure (AOE) set-up.** The white noise generator (custom-built, Dr M Mulharen), is connected to the amplifier (Cambridge Audio Topaz AM1 integrated amplifier), which in turn inputs to the speaker (Piezo horn), which is housed within the sound attenuated booth. The free field microphone (B&K, model 4191) and pre-amplifier (B&K, model 2669-C) were placed at a distance of 20cm, at 0° to the speaker. The microphone inputs to the signal generator (Agilent HP3566A Dynamic Signal Analyser) which enables an average power spectrum of the broadband (white noise) output from the speaker to be generated.

Next, it was necessary to test the actual output of the signal from the 'acoustic-overexposure' set up as shown in figure 8.4. The set-up consists of a custom-made white noise generator (Dr M. Mulheran, University of Leicester) whose signal is then amplified by a Cambridge Audio Topaz AM1 integrated amplifier before output through a Piezo Horn Tweeter sound transducer (speaker). The speaker is located within a sound attenuated booth and is directed towards the centre of the homoeothermic blanket on which the anaesthetised mouse sits during the ABR procedure.

To analyse the output from the AOE setup the following protocol was used:

- Remove the microphone (cartridge type 4191+preamplifier 2669-C) from the acoustic calibrator and place in the sound attenuated booth, 20cm from the speaker, at 0°.
- Set the signal analyser (Agilent HP3566A) to 'bandpass' function,
- Set the bandpass markers at 5 kHz and 50 kHz.
- Generate an average power spectrum (100 sweeps) for the signal falling between these two frequencies. In this example, the average output is -23.19 dB rms, which is the equivalent of 107.8 dB SPL (fig 8.5).

Figure 8.5 Average power spectrum of broadband noise generator



**Fig 8.5. Average power spectrum of broadband noise generator.** A signal analyser (Agilent HP3566A Dynamic Signal Analyser) was used to calculate the average power spectrum (100 sweeps) of the noise generated by the ‘acoustic overexposure set-up’ at a calibrated distance from the speaker (20 cm) within a sound attenuated booth. Bandpass markers were set between 5 and 50 kHz, with the mean power of signal falling between the bandpass markers measured at -23.191 dB Vrms (equal to 107.8 dB SPL)

### 8.3 WESTERN BLOT IMAGE ANALYSIS

Image J software can be used to compare the density of bands on a western blot using the following protocol:

- Open the image of the western blot in Image J and convert to greyscale (8-bit)
- Draw a rectangular section around each lane (fig 8.6, a)
- Draw a profile plot for each lane. The profile plot represents the relative density (RD) of the contents of the rectangle. Each peak corresponds to the dark bands found in the western blot image, with the first peak within the profile plot (left to right) corresponding to the first band in the highlighted western blot lane (top to bottom). High amplitude peaks represent darker bands, whereas wider peaks are the result of bands that cover a larger area on the gel (fig 8.6).
- Identify the band of interest by its molecular weight.
- Using the 'straight line' selection tool draw a line across the base of each peak to enclose it. This allows the area of the enclosed peak to be measured. Note: only select the peak that corresponds to the band of interest in each lane (e.g. Kv3.1 in CBA and Kv3.3 KO).
- Next, using the 'wand' tool, highlight each peak of interest on the profile plot. For each peak highlighted a results window will appear showing the size of the area of the enclosed peak, and next to this, the area of the peak expressed as a percentage of the total size of all the highlighted peaks.
- Using this data, calculate the RD of each peak. Nominate a lane (e.g. CBA, Kv3.1 KO or Kv3.3 KO) to become the standard, to which other bands will be compared to.

$$\text{Relative density} = \text{Percent value of sample} / \text{Percent value of standard}$$

This gives the density of the different bands analyzed relative to nominated standard. The purpose of the using tubulin as a loading control is to check for any difference in protein levels between samples in each lane of the western blot. Tubulin is consistently expressed regardless of the genotype of the mice the tissue was extracted

from. Thus, any differences in the RD of tubulin bands is due to unequal loading of protein. Unequal protein levels can be corrected for by adjusting the RD from each band (e.g. CBA, Kv3.1 Ab) according to the relative density of the tubulin band produced from the same sample.

- First, calculate the relative density of each tubulin band (in this case CBA, Kv3.1 KO and Kv3.3 KO).
- For each band of interest, divide the RD by the corresponding RD of tubulin to give the adjusted density. For example, the RD of Kv3.1 band in a Kv3.3 KO should be divided by the RD of tubulin from a Kv3.3 KO. The adjusted density can then be used to compare bands of interest from different samples.

Figure 8.6 Analysing the density of western blot bands

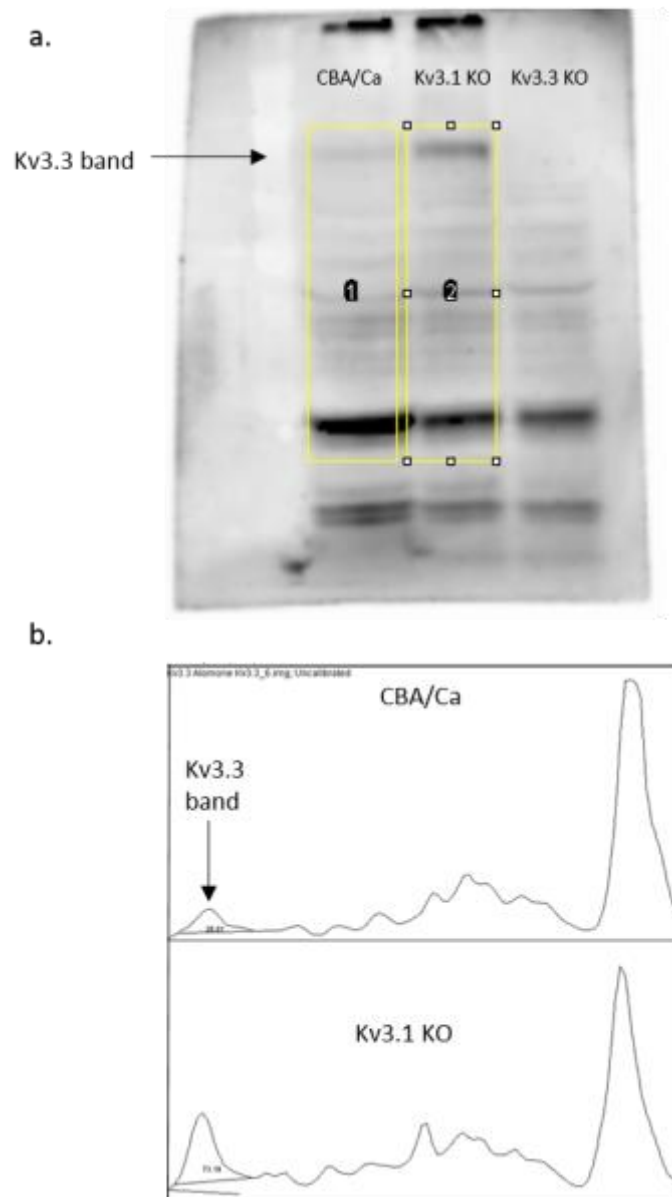


**Fig 8.6 Analysing the density of western blot bands.** **a.** A western blot image using Kv3.3 Ab, with brainstem tissue extracted from CBA (lane 1, left to right), Kv3.1 KO (lane 2) and Kv3.3 KO mice (lane 3). The image has been converted to 8-bit greyscale using ImageJ and a rectangle drawn over each lane (yellow). The band corresponding to Kv3.3 is indicated by arrow. **b.** Profile plots of each lane (as highlighted by yellow rectangle in part a). Each peak represents the density of a band. The first peak (left to right) corresponds to Kv3.3.



- ADAM, T. J., FINLAYSON, P. G. & SCHWARZ, D. W. F. 2001. Membrane properties of principal neurons of the lateral superior olive. *Journal of Neurophysiology*, 86, 922-934.
- ADAM, T. J., SCHWARZ, D. W. & FINLAYSON, P. G. 1999a. Firing properties of chopper and delay neurons in the lateral superior olive of the rat. *Exp Brain Res*, 124, 489-502.
- ADAM, T. J., SCHWARZ, D. W. F. & FINLAYSON, P. G. 1999b. Firing properties of chopper and delay neurons in the lateral superior olive of the rat. *Experimental Brain Research*, 124, 489-502.
- ADLER, E. M., AUGUSTINE, G. J., DUFFY, S. N. & CHARLTON, M. P. 1991. Alien Intracellular Calcium Chelators Attenuate Neurotransmitter Release at the Squid Giant Synapse. *Journal of Neuroscience*, 11, 1496-1507.
- ALAMILLA, J. & GILLESPIE, D. C. 2011. Glutamatergic Inputs and Glutamate-Releasing Immature Inhibitory Inputs Activate a Shared Postsynaptic Receptor Population in Lateral Superior Olive. *Neuroscience*, 196, 285-296.
- ALBRECHT, D. G. & HAMILTON, D. B. 1982. Striate cortex of monkey and cat: contrast response function. *J Neurophysiol*, 48, 217-37.
- ALLEN, P. D. & ISON, J. R. 2012a. Kcna1 gene deletion lowers the behavioral sensitivity of mice to small changes in sound location and increases asynchronous brainstem auditory evoked potentials but does not affect hearing thresholds. *J Neurosci*, 32, 2538-43.
- ALLEN, P. D. & ISON, J. R. 2012b. Kcna1 Gene Deletion Lowers the Behavioral Sensitivity of Mice to Small Changes in Sound Location and Increases Asynchronous Brainstem Auditory Evoked Potentials But Does Not Affect Hearing Thresholds. *Journal of Neuroscience*, 32, 2538-2543.
- AZEREDO, W. J., KLIMENT, M. L., MORLEY, B. J., RELKIN, E., SLEPECKY, N. B., STERNS, A., WARR, W. B., WEEKLY, J. M. & WOODS, C. I. 1999. Olivocochlear neurons in the chinchilla: a retrograde fluorescent labelling study. *Hear Res*, 134, 57-70.
- BANKS, M. I. & SMITH, P. H. 1992. Intracellular recordings from neurobiotin-labeled cells in brain slices of the rat medial nucleus of the trapezoid body. *J Neurosci*, 12, 2819-37.
- BARNES-DAVIES, M., BARKER, M. C., OSMANI, F. & FORSYTHE, I. D. 2004. Kv1 currents mediate a gradient of principal neuron excitability across the tonotopic axis in the rat lateral superior olive. *Eur J Neurosci*, 19, 325-33.
- BARTH, A. L. & MALENKA, R. C. 2001. NMDAR EPSC kinetics do not regulate the critical period for LTP at thalamocortical synapses. *Nature Neuroscience*, 4, 235-236.
- BECKER, C. M., HOCH, W. & BETZ, H. 1988. Glycine receptor heterogeneity in rat spinal cord during postnatal development. *EMBO J*, 7, 3717-26.
- BÉKÉSY, G. V. 1944. über die mechanische Frequenzanalyse in der Schnecke verschiedener. *Akust Zeits*, 9.
- BELLINGHAM, M. C., LIM, R. & WALMSLEY, B. 1998. Developmental changes in EPSC quantal size and quantal content at a central glutamatergic synapse in rat. *Journal of Physiology-London*, 511, 861-869.
- BERGLUND, A. M. & RYUGO, D. K. 1987. Hair cell innervation by spiral ganglion neurons in the mouse. *J Comp Neurol*, 255, 560-70.
- BORGES, K. & DINGLEDINE, R. 1998. AMPA receptors: molecular and functional diversity. *Prog Brain Res*, 116, 153-70.
- BORST, J. G. & SAKMANN, B. 1996. Calcium influx and transmitter release in a fast CNS synapse. *Nature*, 383, 431-4.
- BOUDREAU, J. C. & TSUCHITANI, C. 1968. Binaural interaction in the cat superior olive S segment. *J Neurophysiol*, 31, 442-54.
- BOUDREAU, J. C. & TSUCHITANI, C. 1970. Cat superior olive S-segment cell discharge to tonal stimulation. *Contrib Sens Physiol*, 4, 143-213.
- BRAND, A., BEHREND, O., MARQUARDT, T., MCALPINE, D. & GROTHE, B. 2002. Precise inhibition is essential for microsecond interaural time difference coding. *Nature*, 417, 543-7.

- BRANDT, A., STRIESSNIG, J. & MOSER, T. 2003. CaV1.3 channels are essential for development and presynaptic activity of cochlear inner hair cells. *J Neurosci*, 23, 10832-40.
- BRENMANN, C. J., GROTE, J. J. & RUTTEN, W. L. 1987. Acoustic transfer characteristics in human middle ears studied by a SQUID magnetometer method. *J Acoust Soc Am*, 82, 1646-54.
- BREW, H. M. & FORSYTHE, I. D. 1995a. Two voltage-dependent K<sup>+</sup> conductances with complementary functions in postsynaptic integration at a central auditory synapse. *J Neurosci*, 15, 8011-22.
- BREW, H. M. & FORSYTHE, I. D. 1995b. Two voltage-dependent K<sup>+</sup> conductances with complementary functions in postsynaptic integration at a central auditory synapse. *Journal of Neuroscience*, 15, 8011-8022.
- BREW, H. M., HALLOWS, J. L. & TEMPEL, B. L. 2003a. Hyperexcitability and reduced low threshold potassium currents in auditory neurons of mice lacking the channel subunit Kv1.1. *J Physiol*, 548, 1-20.
- BREW, H. M., HALLOWS, J. L. & TEMPEL, B. L. 2003b. Hyperexcitability and reduced low threshold potassium currents in auditory neurons of mice lacking the channel subunit Kv1.1. *Journal of Physiology-London*, 548, 1-20.
- BROWN, M. C. & NUTTALL, A. L. 1984. Efferent Control of Cochlear Inner Hair Cell Responses in the Guinea-Pig. *Journal of Physiology-London*, 354, 625-646.
- BROWN, M. R., EL-HASSAR, L., ZHANG, Y., ALVARO, G., LARGE, C. H. & KACZMAREK, L. K. 2016. Physiological modulators of Kv3.1 channels adjust firing patterns of auditory brain stem neurons. *J Neurophysiol*, 116, 106-21.
- BROWN, M. R. & KACZMAREK, L. K. 2011. Potassium channel modulation and auditory processing. *Hear Res*, 279, 32-42.
- BRUGHERA, A., DUNAI, L. & HARTMANN, W. M. 2013. Human interaural time difference thresholds for sine tones: the high-frequency limit. *J Acoust Soc Am*, 133, 2839-55.
- BULANKINA, A. V. & MOSER, T. 2012. Neural circuit development in the mammalian cochlea. *Physiology (Bethesda)*, 27, 100-12.
- CAICEDO, A. & EYBALIN, M. 1999. Glutamate receptor phenotypes in the auditory brainstem and mid-brain of the developing rat. *Eur J Neurosci*, 11, 51-74.
- CAICEDO, A., KUNDEL, M., PUJOL, R. & FRIAUF, E. 1998. Glutamate-induced Co<sup>2+</sup> uptake in rat auditory brainstem neurons reveals developmental changes in Ca<sup>2+</sup> permeability of glutamate receptors. *Eur J Neurosci*, 10, 941-54.
- CANT, N. B. & CASSEDAY, J. H. 1986. Projections from the anteroventral cochlear nucleus to the lateral and medial superior olivary nuclei. *J Comp Neurol*, 247, 457-76.
- CARR, C. E. & KONISHI, M. 1990. A circuit for detection of interaural time differences in the brain stem of the barn owl. *J Neurosci*, 10, 3227-46.
- CASE, D. T. & GILLESPIE, D. C. 2011. Pre- and postsynaptic properties of glutamatergic transmission in the immature inhibitory MNTB-LSO pathway. *J Neurophysiol*, 106, 2570-9.
- CASE, D. T., ZHAO, X. W. & GILLESPIE, D. C. 2011. Functional Refinement in the Projection from Ventral Cochlear Nucleus to Lateral Superior Olive Precedes Hearing Onset in Rat. *Plos One*, 6.
- CHEN, L., XU, R., SUN, F. J., XUE, Y., HAO, X. M., LIU, H. X., WANG, H., CHEN, X. Y., LIU, Z. R., DENG, W. S., HAN, X. H., XIE, J. X. & YUNG, W. H. 2015. Hyperpolarization-activated cyclic nucleotide-gated (HCN) channels regulate firing of globus pallidus neurons in vivo. *Mol Cell Neurosci*, 68, 46-55.
- CHEN, Z., KUJAWA, S. G. & SEWELL, W. F. 2007. Auditory sensitivity regulation via rapid changes in expression of surface AMPA receptors. *Nat Neurosci*, 10, 1238-40.
- CHESNOYMARCHAIS, D. & BARTHE, J. Y. 1996. Voltage-dependent block of NMDA responses by 5-HT agonists in ventral spinal cord neurones. *British Journal of Pharmacology*, 117, 133-141.

- CHITTKA, L. & BROCKMANN, A. 2005. Perception space--the final frontier. *PLoS Biol*, 3, e137.
- CHOW, A., ERISIR, A., FARB, C., NADAL, M. S., OZAITA, A., LAU, D., WELKER, E. & RUDY, B. 1999. K(+) channel expression distinguishes subpopulations of parvalbumin- and somatostatin-containing neocortical interneurons. *J Neurosci*, 19, 9332-45.
- CLARK, B. D., GOLDBERG, E. M. & RUDY, B. 2009. Electrogenic tuning of the axon initial segment. *Neuroscientist*, 15, 651-68.
- COLLEY, B., TUCKER, K. & FADOOL, D. A. 2004. Comparison of modulation of Kv1.3 channel by two receptor tyrosine kinases in olfactory bulb neurons of rodents. *Receptors Channels*, 10, 25-36.
- CUMMINGS, K. A. & POPESCU, G. K. 2015. Glycine-dependent activation of NMDA receptors. *Journal of General Physiology*, 145, 513-527.
- DANNHOF, B. J. & BRUNS, V. 1993. The innervation of the organ of Corti in the rat. *Hear Res*, 66, 8-22.
- DARROW, K. N., MAISON, S. F. & LIBERMAN, M. C. 2007. Selective removal of lateral olivocochlear efferents increases vulnerability to acute acoustic injury. *J Neurophysiol*, 97, 1775-85.
- DARROW, K. N., SIMONS, E. J., DODDS, L. & LIBERMAN, M. C. 2006. Dopaminergic innervation of the mouse inner ear: evidence for a separate cytochemical group of cochlear efferent fibers. *J Comp Neurol*, 498, 403-14.
- DINGLELINE, R., BORGES, K., BOWIE, D. & TRAYNELIS, S. F. 1999. The glutamate receptor ion channels. *Pharmacol Rev*, 51, 7-61.
- DOAN, D. E., COHEN, Y. E. & SAUNDERS, J. C. 1994. Middle-ear development. IV. Umbo motion in neonatal mice. *J Comp Physiol A*, 174, 103-10.
- DODSON, P. D., BARKER, M. C. & FORSYTHE, I. D. 2002. Two heteromeric Kv1 potassium channels differentially regulate action potential firing. *Journal of Neuroscience*, 22, 6953-6961.
- DONDZILLO, A., SATZLER, K., HORSTMANN, H., ALTROCK, W. D., GUNDELFINGER, E. D. & KUNER, T. 2010. Targeted three-dimensional immunohistochemistry reveals localization of presynaptic proteins Bassoon and Piccolo in the rat calyx of Held before and after the onset of hearing. *J Comp Neurol*, 518, 1008-29.
- DOWNES, N. & MULLINS, P. 2014. The development of myelin in the brain of the juvenile rat. *Toxicol Pathol*, 42, 913-22.
- DOYLE, D. A., MORAIS CABRAL, J., PFUETZNER, R. A., KUO, A., GULBIS, J. M., COHEN, S. L., CHAIT, B. T. & MACKINNON, R. 1998. The structure of the potassium channel: molecular basis of K<sup>+</sup> conduction and selectivity. *Science*, 280, 69-77.
- DUNCAN, J. S. & FRITZSCH, B. 2012. Transforming the vestibular system one molecule at a time: the molecular and developmental basis of vertebrate auditory evolution. *Adv Exp Med Biol*, 739, 173-86.
- DURLACH, N. I., THOMPSON, C. L. & COLBURN, H. S. 1981. Binaural interaction of impaired listeners. A review of past research. *Audiology*, 20, 181-211.
- EHRlich, I., LOHRKE, S. & FRIAUf, E. 1999. Shift from depolarizing to hyperpolarizing glycine action in rat auditory neurones is due to age-dependent Cl<sup>-</sup> regulation. *J Physiol*, 520 Pt 1, 121-37.
- ELGOYHEN, A. B., JOHNSON, D. S., BOULTER, J., VETTER, D. E. & HEINEMANN, S. 1994. Alpha 9: an acetylcholine receptor with novel pharmacological properties expressed in rat cochlear hair cells. *Cell*, 79, 705-15.
- ELGOYHEN, A. B., VETTER, D. E., KATZ, E., ROTHLIN, C. V., HEINEMANN, S. F. & BOULTER, J. 2001. alpha 10: A determinant of nicotinic cholinergic receptor function in mammalian vestibular and cochlear mechanosensory hair cells. *Proceedings of the National Academy of Sciences of the United States of America*, 98, 3501-3506.
- ENYEDI, P. & CZIRJAK, G. 2010. Molecular background of leak K<sup>+</sup> currents: two-pore domain potassium channels. *Physiol Rev*, 90, 559-605.

- ERISIR, A., LAU, D., RUDY, B. & LEONARD, C. S. 1999. Function of specific K<sup>+</sup> channels in sustained high-frequency firing of fast-spiking neocortical interneurons. *Journal of Neurophysiology*, 82, 2476-2489.
- ESPINOSA, F., MCMAHON, A., CHAN, E., WANG, S., HO, C. S., HEINTZ, N. & JOHO, R. H. 2001. Alcohol hypersensitivity, increased locomotion, and spontaneous myoclonus in mice lacking the potassium channels Kv3.1 and Kv3.3. *J Neurosci*, 21, 6657-65.
- EYBALIN, M. 1993. Neurotransmitters and Neuromodulators of the Mammalian Cochlea. *Physiological Reviews*, 73, 309-373.
- FERNANDEZ, K. A., JEFFERS, P. W., LALL, K., LIBERMAN, M. C. & KUJAWA, S. G. 2015. Aging after noise exposure: acceleration of cochlear synaptopathy in "recovered" ears. *J Neurosci*, 35, 7509-20.
- FETTIPLACE, R. 2009. Defining features of the hair cell mechano-electrical transducer channel. *Pflügers Archiv-European Journal of Physiology*, 458, 1115-1123.
- FORD, M. C., GROTHE, B. & KLUG, A. 2009. Fenestration of the Calyx of Held Occurs Sequentially Along the Tonotopic Axis, Is Influenced by Afferent Activity, and Facilitates Glutamate Clearance. *Journal of Comparative Neurology*, 514, 92-106.
- FORSYTHE, I. D. & BARNES-DAVIES, M. 1993. The binaural auditory pathway: excitatory amino acid receptors mediate dual timecourse excitatory postsynaptic currents in the rat medial nucleus of the trapezoid body. *Proc Biol Sci*, 251, 151-7.
- FORSYTHE, I. D. & WESTBROOK, G. L. 1988. Slow excitatory postsynaptic currents mediated by N-methyl-D-aspartate receptors on cultured mouse central neurones. *J Physiol*, 396, 515-33.
- FRIAUF, E., FISCHER, A. U. & FUHR, M. F. 2015. Synaptic plasticity in the auditory system: a review. *Cell and Tissue Research*, 361, 177-213.
- FROUD, K. E., WONG, A. C., CEDERHOLM, J. M., KLUGMANN, M., SANDOW, S. L., JULIEN, J. P., RYAN, A. F. & HOUSLEY, G. D. 2015. Type II spiral ganglion afferent neurons drive medial olivocochlear reflex suppression of the cochlear amplifier. *Nat Commun*, 6, 7115.
- FUJINO, K., KOYANO, K. & OHMORI, H. 1997. Lateral and medial olivocochlear neurons have distinct electrophysiological properties in the rat brain slice. *Journal of Neurophysiology*, 77, 2788-2804.
- FURMAN, A. C., KUJAWA, S. G. & LIBERMAN, M. C. 2013. Noise-induced cochlear neuropathy is selective for fibers with low spontaneous rates. *Journal of Neurophysiology*, 110, 577-586.
- FUTAI, K., OKADA, M., MATSUYAMA, K. & TAKAHASHI, T. 2001. High-fidelity transmission acquired via a developmental decrease in NMDA receptor expression at an auditory synapse. *Journal of Neuroscience*, 21, 3342-3349.
- GALAMBOS, R., SCHWARTZKOPFF, J. & RUPERT, A. 1959. Microelectrode study of superior olivary nuclei. *Am J Physiol*, 197, 527-36.
- GALLEGO-IRADI, C., BICKFORD, J. S., KHARE, S., HALL, A., NICK, J. A., SALMASINIA, D., WAWROWSKY, K., BANNYKH, S., HUYNH, D. P., RINCON-LIMAS, D. E., PULST, S. M., NICK, H. S., FERNANDEZ-FUNEZ, P. & WATERS, M. F. 2014. KCNC3(R420H), a K(+) channel mutation causative in spinocerebellar ataxia 13 displays aberrant intracellular trafficking. *Neurobiol Dis*, 71, 270-9.
- GEIGER, J. R., MELCHER, T., KOH, D. S., SAKMANN, B., SEEBURG, P. H., JONAS, P. & MONYER, H. 1995. Relative abundance of subunit mRNAs determines gating and Ca<sup>2+</sup> permeability of AMPA receptors in principal neurons and interneurons in rat CNS. *Neuron*, 15, 193-204.
- GILLESPIE, D. C., KIM, G. & KANDLER, K. 2005. Inhibitory synapses in the developing auditory system are glutamatergic. *Nature Neuroscience*, 8, 332-338.
- GITTELMAN, J. X. & TEMPEL, B. L. 2006. Kv1.1-containing channels are critical for temporal precision during spike initiation. *Journal of Neurophysiology*, 96, 1203-1214.

- GLENDENNING, K. K., BAKER, B. N., HUTSON, K. A. & MASTERTON, R. B. 1992. Acoustic chiasm V: inhibition and excitation in the ipsilateral and contralateral projections of LSO. *J Comp Neurol*, 319, 100-22.
- GLENDENNING, K. K., HUTSON, K. A., NUDO, R. J. & MASTERTON, R. B. 1985. Acoustic chiasm II: Anatomical basis of binaurality in lateral superior olive of cat. *J Comp Neurol*, 232, 261-85.
- GLOWATZKI, E. & FUCHS, P. A. 2002. Transmitter release at the hair cell ribbon synapse. *Nature Neuroscience*, 5, 147-154.
- GOEL, A., XU, L. D. W., SNYDER, K. P., SONG, L. H., GOENAGA-VAZQUEZ, Y., MEGILL, A., TAKAMIYA, K., HUGANIR, R. L. & LEE, H. K. 2011. Phosphorylation of AMPA Receptors Is Required for Sensory Deprivation-Induced Homeostatic Synaptic Plasticity. *Plos One*, 6.
- GRAVENDEEL, D. W. & PLOMP, R. 1959. The relation between permanent and temporary noise dips. *AMA Arch Otolaryngol*, 69, 714-9.
- GRIGG, J. J., BREW, H. M. & TEMPEL, B. L. 2000. Differential expression of voltage-gated potassium channel genes in auditory nuclei of the mouse brainstem. *Hear Res*, 140, 77-90.
- GRIMSLEY, C. A. & SIVARAMAKRISHNAN, S. 2014. Postnatal developmental changes in the medial nucleus of the trapezoid body in a mouse model of auditory pathology. *Neurosci Lett*, 559, 152-7.
- GROFF, J. A. & LIBERMAN, M. C. 2003. Modulation of cochlear afferent response by the lateral olivocochlear system: activation via electrical stimulation of the inferior colliculus. *J Neurophysiol*, 90, 3178-200.
- GROOMS, S. Y., OPITZ, T., BENNETT, M. V. L. & ZUKIN, R. S. 2000. Status epilepticus decreases glutamate receptor 2 mRNA and protein expression in hippocampal pyramidal cells before neuronal death. *Proceedings of the National Academy of Sciences of the United States of America*, 97, 3631-3636.
- GROTHER, B., PECKA, M. & MCALPINE, D. 2010. Mechanisms of sound localization in mammals. *Physiol Rev*, 90, 983-1012.
- GU, J. W., HERRMANN, B. S., LEVINE, R. A. & MELCHER, J. R. 2012a. Brainstem Auditory Evoked Potentials Suggest a Role for the Ventral Cochlear Nucleus in Tinnitus. *Jaro-Journal of the Association for Research in Otolaryngology*, 13, 819-833.
- GU, J. W., HERRMANN, B. S., LEVINE, R. A. & MELCHER, J. R. 2012b. Brainstem auditory evoked potentials suggest a role for the ventral cochlear nucleus in tinnitus. *J Assoc Res Otolaryngol*, 13, 819-33.
- GUINAN, J. J., JR. 2006. Olivocochlear efferents: anatomy, physiology, function, and the measurement of efferent effects in humans. *Ear Hear*, 27, 589-607.
- HAFTER, E. R., DYE, R. H., NUETZEL, J. M. & ARONOW, H. 1977. Difference thresholds for interaural intensity. *J Acoust Soc Am*, 61, 829-34.
- HARDINGHAM, G. E. & BADING, H. 2010. Synaptic versus extrasynaptic NMDA receptor signalling: implications for neurodegenerative disorders. *Nat Rev Neurosci*, 11, 682-96.
- HARTLINE, D. K. & COLMAN, D. R. 2007. Rapid conduction and the evolution of giant axons and myelinated fibers. *Curr Biol*, 17, R29-35.
- HATTAN, D., NESTI, E., CACHERO, T. G. & MORIELLI, A. D. 2002. Tyrosine phosphorylation of Kv1.2 modulates its interaction with the actin-binding protein cortactin. *J Biol Chem*, 277, 38596-606.
- HELD, H. 1893. Die centrale Gehorleitung. *Anat. Physiol. Anat. Abt.* , 201-248.
- HELMHOLTZ, V. 1877. *On the sensations of tone* New York, Dover Publications.
- HENDERSON, D., BIELEFELD, E. C., HARRIS, K. C. & HU, B. H. 2006. The role of oxidative stress in noise-induced hearing loss. *Ear and Hearing*, 27, 1-19.

- HENRY, K. R. & CHOLE, R. A. 1980. Genotypic differences in behavioral, physiological and anatomical expressions of age-related hearing loss in the laboratory mouse. *Audiology*, 19, 369-83.
- HIBINO, H., INANOBE, A., FURUTANI, K., MURAKAMI, S., FINDLAY, I. & KURACHI, Y. 2010. Inwardly rectifying potassium channels: their structure, function, and physiological roles. *Physiol Rev*, 90, 291-366.
- HICKOX, A. E. & LIBERMAN, M. C. 2014. Is noise-induced cochlear neuropathy key to the generation of hyperacusis or tinnitus? *Journal of Neurophysiology*, 111, 552-564.
- HILLE, B. 2001. *Ionic Channels of Excitable Membranes*, Sinauer Associates.
- HIND, S. E., HAINES-BAZRAFSHAN, R., BENTON, C. L., BRASSINGTON, W., TOWLE, B. & MOORE, D. R. 2011. Prevalence of clinical referrals having hearing thresholds within normal limits. *Int J Audiol*, 50, 708-16.
- HIRAI, H., KIRSCH, J., LAUBE, B., BETZ, H. & KUHSE, J. 1996. The glycine binding site of the N-methyl-D-aspartate receptor subunit NR1: Identification of novel determinants of co-agonist potentiation in the extracellular M3-M4 loop region. *Proceedings of the National Academy of Sciences of the United States of America*, 93, 6031-6036.
- HIRTZ, J. J., BRAUN, N., GRIESEMER, D., HANNES, C., JANZ, K., LOHRKE, S., MULLER, B. & FRIAUF, E. 2012. Synaptic Refinement of an Inhibitory Topographic Map in the Auditory Brainstem Requires Functional Ca(V)1.3 Calcium Channels. *Journal of Neuroscience*, 32, 14602-14616.
- HO, C. S., GRANGE, R. W. & JOHO, R. H. 1997. Pleiotropic effects of a disrupted K<sup>+</sup> channel gene: reduced body weight, impaired motor skill and muscle contraction, but no seizures. *Proc Natl Acad Sci U S A*, 94, 1533-8.
- HOFFPAUIR, B. K., KOLSON, D. R., MATHERS, P. H. & SPIROU, G. A. 2010. Maturation of synaptic partners: functional phenotype and synaptic organization tuned in synchrony. *J Physiol*, 588, 4365-85.
- HOLLMANN, M. & HEINEMANN, S. 1994. Cloned glutamate receptors. *Annu Rev Neurosci*, 17, 31-108.
- HOLLMANN, M., MARON, C. & HEINEMANN, S. 1994. N-glycosylation site tagging suggests a three transmembrane domain topology for the glutamate receptor GluR1. *Neuron*, 13, 1331-43.
- HUANG, X. Y., MORIELLI, A. D. & PERALTA, E. G. 1993. Tyrosine kinase-dependent suppression of a potassium channel by the G protein-coupled m1 muscarinic acetylcholine receptor. *Cell*, 75, 1145-56.
- HUANGFU, M. & SAUNDERS, J. C. 1983. Auditory development in the mouse: structural maturation of the middle ear. *J Morphol*, 176, 249-59.
- HURLEY, P. A., CROOK, J. M. & SHEPHERD, R. K. 2007. Schwann cells revert to non-myelinating phenotypes in the deafened rat cochlea. *Eur J Neurosci*, 26, 1813-21.
- HURLOCK, E. C., BOSE, M., PIERCE, G. & JOHO, R. H. 2009. Rescue of motor coordination by Purkinje cell-targeted restoration of Kv3.3 channels in Kcnc3-null mice requires Kcnc1. *J Neurosci*, 29, 15735-44.
- HURLOCK, E. C., MCMAHON, A. & JOHO, R. H. 2008. Purkinje-cell-restricted restoration of Kv3.3 function restores complex spikes and rescues motor coordination in Kcnc3 mutants. *J Neurosci*, 28, 4640-8.
- INGHAM, N. J., PEARSON, S. & STEEL, K. P. 2011. Using the Auditory Brainstem Response (ABR) to Determine Sensitivity of Hearing in Mutant Mice. *Curr Protoc Mouse Biol*, 1, 279-87.
- IRVINE, D. R. F. & GAGO, G. 1990. Binaural Interaction in High-Frequency Neurons in Inferior Colliculus of the Cat - Effects of Variations in Sound Pressure Level on Sensitivity to Interaural Intensity Differences. *Journal of Neurophysiology*, 63, 570-591.
- ISACOFF, E. Y., JAN, Y. N. & JAN, L. Y. 1990. Evidence for the formation of heteromultimeric potassium channels in *Xenopus* oocytes. *Nature*, 345, 530-4.

- ISOM, L. L., DE JONGH, K. S. & CATTERALL, W. A. 1994. Auxiliary subunits of voltage-gated ion channels. *Neuron*, 12, 1183-94.
- J. ZWISLOCKI, R. S. F. 1956. Just noticeable differences in dichotic phase. *J Acoust Soc Am*, 28, 860 - 864.
- JALABI, W., KOPP-SCHEINPFLUG, C., ALLEN, P. D., SCHIAVON, E., DIGIACOMO, R. R., FORSYTHE, I. D. & MARICICH, S. M. 2013. Sound localization ability and glycinergic innervation of the superior olivary complex persist after genetic deletion of the medial nucleus of the trapezoid body. *J Neurosci*, 33, 15044-9.
- JAMES BYRON SNOW, P. A. W., JOHN JACOB BALLENGER 2009. *Ballenger's Otorhinolaryngology: Head and Neck Surgery*, PMPH-USA.
- JEFFRESS, L. A. 1948. A place theory of sound localization. *J Comp Physiol Psychol*, 41, 35-9.
- JIANG, D., MCALPINE, D. & PALMER, A. R. 1997. Detectability index measures of binaural masking level difference across populations of inferior colliculus neurons. *J Neurosci*, 17, 9331-9.
- JOHNSTON, J., FORSYTHE, I. D. & KOPP-SCHEINPFLUG, C. 2010. Going native: voltage-gated potassium channels controlling neuronal excitability. *J Physiol*, 588, 3187-200.
- JOHNSTON, J., POSTLETHWAITE, M. & FORSYTHE, I. D. 2009. The impact of synaptic conductance on action potential waveform: evoking realistic action potentials with a simulated synaptic conductance. *J Neurosci Methods*, 183, 158-64.
- JOHO, R. H. & HURLOCK, E. C. 2009. The Role of Kv3-type Potassium Channels in Cerebellar Physiology and Behavior. *Cerebellum*, 8, 323-333.
- JOHO, R. H., STREET, C., MATSUSHITA, S. & KNOPFEL, T. 2006. Behavioral motor dysfunction in Kv3-type potassium channel-deficient mice. *Genes Brain Behav*, 5, 472-82.
- JONAS, P., BISCHOFBERGER, J. & SANDKUHLER, J. 1998. Corelease of two fast neurotransmitters at a central synapse. *Science*, 281, 419-424.
- JORIS, P. & YIN, T. C. 2007. A matter of time: internal delays in binaural processing. *Trends Neurosci*, 30, 70-8.
- JOSHI, I., SHOKRALLA, S., TITIS, P. & WANG, L. Y. 2004. The role of AMPA receptor gating in the development of high-fidelity neurotransmission at the calyx of held synapse. *Journal of Neuroscience*, 24, 183-196.
- JOSHI, I. & WANG, L. Y. 2002. Developmental profiles of glutamate receptors and synaptic transmission at a single synapse in the mouse auditory brainstem. *Journal of Physiology-London*, 540, 861-873.
- JYOTHI, V., LI, M., KILPATRICK, L. A., SMYTHE, N., LARUE, A. C., ZHOU, D., SCHULTE, B. A., SCHMIEDT, R. A. & LANG, H. 2010. Unmyelinated auditory type I spiral ganglion neurons in congenic Ly5.1 mice. *J Comp Neurol*, 518, 3254-71.
- KAKAZU, Y. 2000. [Regulation of intracellular chloride by cotransporters in developing lateral superior olive neurons]. *Fukuoka Igaku Zasshi*, 91, 217-22.
- KAKAZU, Y., AKAIKE, N., KOMIYAMA, S. & NABEKURA, J. 1999. Regulation of intracellular chloride by cotransporters in developing lateral superior olive neurons. *J Neurosci*, 19, 2843-51.
- KALTENBACH, J. A., ZHANG, J. & AFMAN, C. E. 2000. Plasticity of spontaneous neural activity in the dorsal cochlear nucleus after intense sound exposure. *Hear Res*, 147, 282-92.
- KANDLER, K., CLAUSE, A. & NOH, J. 2009a. Tonotopic reorganization of developing auditory brainstem circuits. *Nat Neurosci*, 12, 711-7.
- KANDLER, K., CLAUSE, A. & NOH, J. 2009b. Tonotopic reorganization of developing auditory brainstem circuits. *Nature Neuroscience*, 12, 711-717.
- KANDLER, K. & FRIAUF, E. 1993. Pre- and postnatal development of efferent connections of the cochlear nucleus in the rat. *J Comp Neurol*, 328, 161-84.
- KANDLER, K. & FRIAUF, E. 1995. Development of glycinergic and glutamatergic synaptic transmission in the auditory brainstem of perinatal rats. *J Neurosci*, 15, 6890-904.

- KANDLER, K., KULLMANN, P. H., ENE, F. A. & KIM, G. 2002. Excitatory action of an immature glycinergic/GABAergic sound localization pathway. *Physiol Behav*, 77, 583-7.
- KARCZ, A., ALLEN, P. D., WALTON, J., ISON, J. R. & KOPP-SCHEINPFLUG, C. 2015. Auditory deficits of Kcna1 deletion are similar to those of a monaural hearing impairment. *Hear Res*, 321, 45-51.
- KARCZ, A., HENNIG, M. H., ROBBINS, C. A., TEMPEL, B. L., RUBSAMEN, R. & KOPP-SCHEINPFLUG, C. 2011. Low-voltage activated Kv1.1 subunits are crucial for the processing of sound source location in the lateral superior olive in mice. *J Physiol*, 589, 1143-57.
- KASS, G. E. & ORRENIUS, S. 1999. Calcium signaling and cytotoxicity. *Environ Health Perspect*, 107 Suppl 1, 25-35.
- KATAOKA, Y. & OHMORI, H. 1994. Activation of glutamate receptors in response to membrane depolarization of hair cells isolated from chick cochlea. *J Physiol*, 477 ( Pt 3), 403-14.
- KAVANAGH, G. L. & KELLY, J. B. 1992. Midline and lateral field sound localization in the ferret (*Mustela putorius*): contribution of the superior olivary complex. *J Neurophysiol*, 67, 1643-58.
- KERCHNER, G. A. & NICOLL, R. A. 2009. Silent synapses and the emergence of a postsynaptic mechanism for LTP (vol 9, pg 813, 2008). *Nature Reviews Neuroscience*, 10.
- KIL, J., KAGEYAMA, G. H., SEMPLE, M. N. & KITZES, L. M. 1995. Development of ventral cochlear nucleus projections to the superior olivary complex in gerbil. *J Comp Neurol*, 353, 317-40.
- KLECKNER, N. W. & DINGLEDINE, R. 1988. Requirement for Glycine in Activation of Nmda-Receptors Expressed in Xenopus Oocytes. *Science*, 241, 835-837.
- KNIPPER, M., KOPSCHALL, I., ROHBOCK, K., KOPKE, A. K., BONK, I., ZIMMERMANN, U. & ZENNER, H. 1997. Transient expression of NMDA receptors during rearrangement of AMPA-receptor-expressing fibers in the developing inner ear. *Cell Tissue Res*, 287, 23-41.
- KOPP-SCHEINPFLUG, C., FUCHS, K., LIPPE, W. R., TEMPEL, B. L. & RUBSAMEN, R. 2003. Decreased temporal precision of auditory signaling in Kcna1-null mice: An electrophysiological study in vivo. *Journal of Neuroscience*, 23, 9199-9207.
- KOPP-SCHEINPFLUG, C., TOLNAI, S., MALMIERCA, M. S. & RUBSAMEN, R. 2008. The medial nucleus of the trapezoid body: comparative physiology. *Neuroscience*, 154, 160-70.
- KOPP-SCHEINPFLUG, C., TOZER, A. J., ROBINSON, S. W., TEMPEL, B. L., HENNIG, M. H. & FORSYTHE, I. D. 2011. The sound of silence: ionic mechanisms encoding sound termination. *Neuron*, 71, 911-25.
- KOPPL, C. & CARR, C. E. 2008. Maps of interaural time difference in the chicken's brainstem nucleus laminaris. *Biol Cybern*, 98, 541-59.
- KOTAK, V. C., KORADA, S., SCHWARTZ, I. R. & SANES, D. H. 1998. A developmental shift from GABAergic to glycinergic transmission in the central auditory system. *J Neurosci*, 18, 4646-55.
- KOTAK, V. C. & SANES, D. H. 2000. Long-lasting inhibitory synaptic depression is age- and calcium-dependent. *Journal of Neuroscience*, 20, 5820-5826.
- KOTAK, V. C. & SANES, D. H. 2014. Developmental expression of inhibitory synaptic long-term potentiation in the lateral superior olive. *Frontiers in Neural Circuits*, 8.
- KROS, C. J., RUPPERSBERG, J. P. & RUSCH, A. 1998. Expression of a potassium current in inner hair cells during development of hearing in mice. *Nature*, 394, 281-4.
- KRUSE, M. & HILLE, B. 2013. The phosphoinositide sensitivity of the K-V channel family. *Channels*, 7, 530-536.
- KUJAWA, S. G. & LIBERMAN, M. C. 2006. Acceleration of age-related hearing loss by early noise exposure: evidence of a misspent youth. *J Neurosci*, 26, 2115-23.
- KUJAWA, S. G. & LIBERMAN, M. C. 2009. Adding insult to injury: cochlear nerve degeneration after "temporary" noise-induced hearing loss. *J Neurosci*, 29, 14077-85.

- KULLMANN, P. H., ENE, F. A. & KANDLER, K. 2002. Glycinergic and GABAergic calcium responses in the developing lateral superior olive. *Eur J Neurosci*, 15, 1093-104.
- KUWABARA, N., DICAPRIO, R. A. & ZOOK, J. M. 1991. Afferents to the Medial Nucleus of the Trapezoid Body and Their Collateral Projections. *Journal of Comparative Neurology*, 314, 684-706.
- KUWABARA, N. & ZOOK, J. M. 1992. Projections to the medial superior olive from the medial and lateral nuclei of the trapezoid body in rodents and bats. *J Comp Neurol*, 324, 522-38.
- KUYPER, P. 1972. The cocktail party effect. *Audiology*, 11, 277-82.
- LAUTER, J. L., HERSCOVITCH, P., FORMBY, C. & RAICHLE, M. E. 1985. Tonotopic organization in human auditory cortex revealed by positron emission tomography. *Hear Res*, 20, 199-205.
- LAVEZZARI, G., MCCALLUM, J., DEWEY, C. M. & ROCHE, K. W. 2004. Subunit-specific regulation of NMDA receptor endocytosis. *Journal of Neuroscience*, 24, 6383-6391.
- LAWRENCE, J. J. & TRUSSELL, L. O. 2000. Long-term specification of AMPA receptor properties after synapse formation. *Journal of Neuroscience*, 20, 4864-4870.
- LEE, H., BACH, E., NOH, J., DELPIRE, E. & KANDLER, K. 2016. Hyperpolarization-independent maturation and refinement of GABA/glycinergic connections in the auditory brain stem. *J Neurophysiol*, 115, 1170-82.
- LEIJON, S. & MAGNUSSON, A. K. 2014. Physiological Characterization of Vestibular Efferent Brainstem Neurons Using a Transgenic Mouse Model. *Plos One*, 9.
- LEMASURIER, M. & GILLESPIE, P. G. 2005. Hair-cell mechanotransduction and cochlear amplification. *Neuron*, 48, 403-15.
- LEWIS TILNEY, J. S. 1983. Actin filaments, stereocilia, and hair cells of the bird cochlea. I. Length, number, width, and distribution of stereocilia of each hair cell are related to the position of the hair cell on the cochlea. *J Cell Biol*, 96, 807-21.
- LI, S., KALAPPA, B. I. & TZOUNOPOULOS, T. 2015. Noise-induced plasticity of KCNQ2/3 and HCN channels underlies vulnerability and resilience to tinnitus. *Elife*, 4.
- LI, W., KACZMAREK, L. K. & PERNEY, T. M. 2001. Localization of two high-threshold potassium channel subunits in the rat central auditory system. *J Comp Neurol*, 437, 196-218.
- LIBERMAN, L. D., SUZUKI, J. & LIBERMAN, M. C. 2015. Dynamics of cochlear synaptopathy after acoustic overexposure. *J Assoc Res Otolaryngol*, 16, 205-19.
- LIBERMAN, M. C., DODDS, L. W. & PIERCE, S. 1990. Afferent and efferent innervation of the cat cochlea: quantitative analysis with light and electron microscopy. *J Comp Neurol*, 301, 443-60.
- LIM, R., ALVAREZ, F. J. & WALMSLEY, B. 2000. GABA mediates presynaptic inhibition at glycinergic synapses in a rat auditory brainstem nucleus. *Journal of Physiology-London*, 525, 447-459.
- LISMAN, J., YASUDA, R. & RAGHAVACHARI, S. 2012. Mechanisms of CaMKII action in long-term potentiation. *Nature Reviews Neuroscience*, 13, 169-182.
- LIU, S. Q. J. & CULL-CANDY, S. G. 2000. Synaptic activity at calcium-permeable AMPA receptors induces a switch in receptor subtype. *Nature*, 405, 454-458.
- LODGE, D. 2009. The history of the pharmacology and cloning of ionotropic glutamate receptors and the development of idiosyncratic nomenclature. *Neuropharmacology*, 56, 6-21.
- LU, T., RUBIO, M. E. & TRUSSELL, L. O. 2008. Glycinergic transmission shaped by the corelease of GABA in a mammalian auditory synapse. *Neuron*, 57, 524-35.
- LYNCH, G., LARSON, J., KELSO, S., BARRIONUEVO, G. & SCHOTTLER, F. 1983. Intracellular injections of EGTA block induction of hippocampal long-term potentiation. *Nature*, 305, 719-21.
- LYNCH, J. W. 2009. Native glycine receptor subtypes and their physiological roles. *Neuropharmacology*, 56, 303-309.

- MACICA, C. M., VON HEHN, C. A. A., WANG, L. Y., HO, C. S., YOKOYAMA, S., JOHO, R. H. & KACZMAREK, L. K. 2003. Modulation of the Kv3.1b potassium channel isoform adjusts the fidelity of the firing pattern of auditory neurons. *Journal of Neuroscience*, 23, 1133-1141.
- MAISON, S. F. & LIBERMAN, M. C. 2000. Predicting vulnerability to acoustic injury with a noninvasive assay of olivocochlear reflex strength. *J Neurosci*, 20, 4701-7.
- MAISON, S. F., USUBUCHI, H. & LIBERMAN, M. C. 2013. Efferent feedback minimizes cochlear neuropathy from moderate noise exposure. *J Neurosci*, 33, 5542-52.
- MALENKA, R. C., KAUER, J. A., ZUCKER, R. S. & NICOLL, R. A. 1988. Postsynaptic calcium is sufficient for potentiation of hippocampal synaptic transmission. *Science*, 242, 81-4.
- MALOSIO, M. L., MARQUEZE-POUEY, B., KUHSE, J. & BETZ, H. 1991. Widespread expression of glycine receptor subunit mRNAs in the adult and developing rat brain. *EMBO J*, 10, 2401-9.
- MANLEY GA, POPPER AN & RR, F. 2004. *Evolution of the vertebrate auditory system*, Springer, New York.
- MANZOOR, N. F., LICARI, F. G., KLAPCHAR, M., ELKIN, R. L., GAO, Y., CHEN, G. & KALTENBACH, J. A. 2012. Noise-induced hyperactivity in the inferior colliculus: its relationship with hyperactivity in the dorsal cochlear nucleus. *J Neurophysiol*, 108, 976-88.
- MARCOTTI, W., JOHNSON, S. L., RUSCH, A. & KROS, C. J. 2003. Sodium and calcium currents shape action potentials in immature mouse inner hair cells. *J Physiol*, 552, 743-61.
- MASTERTON, B., JANE, J. A. & DIAMOND, I. T. 1967. Role of brainstem auditory structures in sound localization. I. Trapezoid body, superior olive, and lateral lemniscus. *J Neurophysiol*, 30, 341-59.
- MATEI, V., PAULEY, S., KAING, S., ROWITCH, D., BEISEL, K. W., MORRIS, K., FENG, F., JONES, K., LEE, J. & FRITZSCH, B. 2005. Smaller inner ear sensory epithelia in Neurog 1 null mice are related to earlier hair cell cycle exit. *Dev Dyn*, 234, 633-50.
- MCINTOSH, P., MORENO, H., ROBERTSON, B. & RUDY, B. 1998. Isoform-specific modulation of rat Kv3 potassium channel splice variants. *Journal of Physiology-London*, 511P, 147p-147p.
- MCCMAHON, A., FOWLER, S. C., PERNEY, T. M., AKEMANN, W., KNOPFEL, T. & JOHO, R. H. 2004. Allele-dependent changes of olivocerebellar circuit properties in the absence of the voltage-gated potassium channels Kv3.1 and Kv3.3. *Eur J Neurosci*, 19, 3317-27.
- MELCHER, J. R., GUINAN, J. J., JR., KNUDSON, I. M. & KIANG, N. Y. 1996. Generators of the brainstem auditory evoked potential in cat. II. Correlating lesion sites with waveform changes. *Hear Res*, 93, 28-51.
- MICHEYL, C., SCHRATER, P. R. & OXENHAM, A. J. 2013. Auditory Frequency and Intensity Discrimination Explained Using a Cortical Population Rate Code. *Plos Computational Biology*, 9.
- MIDDLEBROOKS, J. C. & GREEN, D. M. 1991. Sound localization by human listeners. *Annu Rev Psychol*, 42, 135-59.
- MIDDLEBROOKS, J. C., MAKOUS, J. C. & GREEN, D. M. 1989. Directional Sensitivity of Sound-Pressure Levels in the Human Ear Canal. *Journal of the Acoustical Society of America*, 86, 89-108.
- MIDDLEBROOKS, J. C., NICK, H. S., SUBRAMONY, S. H., ADVINCULA, J., ROSALES, R. L., LEE, L. V., ASHIZAWA, T. & WATERS, M. F. 2013. Mutation in the kv3.3 voltage-gated potassium channel causing spinocerebellar ataxia 13 disrupts sound-localization mechanisms. *PLoS One*, 8, e76749.
- MIDDLETON, J. W., KIRITANI, T., PEDERSEN, C., TURNER, J. G., SHEPHERD, G. M. G. & TZOUNOPOULOS, T. 2011. Mice with behavioral evidence of tinnitus exhibit dorsal cochlear nucleus hyperactivity because of decreased GABAergic inhibition. *Proceedings of the National Academy of Sciences of the United States of America*, 108, 7601-7606.

- MIKAELIAN, D. R., R. J. 1965. Development of hearing in the normal CBA-J mouse: correlation of physiological observations with behavioral responses and with cochlear anatomy. *Acta Otolaryngol.*, 451–461.
- MILLER JD, W. C., COVELL WP. 1963. Deafening effects of noise on the cat. *Acta Oto-Laryngol Suppl*, 176.
- MILLS, A. W. 1960. Lateralization of high-frequency tones. *J Acoust Soc Am*, 32, 132-134.
- MOHRLE, D., NI, K., VARAKINA, K., BING, D., LEE, S. C., ZIMMERMANN, U., KNIPPER, M. & RUTTIGER, L. 2016. Loss of auditory sensitivity from inner hair cell synaptopathy can be centrally compensated in the young but not old brain. *Neurobiol Aging*, 44, 173-84.
- MOLLEMAN, A. 2003. *Patch Clamping: An Introductory Guide To Patch Clamp Electrophysiology*, John Wiley and Sons.
- MOLLER, A. R. 2006. *HEARING: ANATOMY, PHYSIOLOGY, AND DISORDERS OF THE AUDITORY SYSTEM*, Elsevier.
- MOORE, B. C. 2016. A review of the perceptual effects of hearing loss for frequencies above 3 kHz. *Int J Audiol*, 55, 707-714.
- MOREST, D. K. 1968. The collateral system of the medial nucleus of the trapezoid body of the cat, its neuronal architecture and relation to the olivo-cochlear bundle. *Brain Res*, 9, 288-311.
- MOSBACHER, J., SCHOEPFER, R., MONYER, H., BURNASHEV, N., SEEBURG, P. H. & RUPPERSBERG, J. P. 1994. A molecular determinant for submillisecond desensitization in glutamate receptors. *Science*, 266, 1059-62.
- MOSER, T. & BEUTNER, D. 2000. Kinetics of exocytosis and endocytosis at the cochlear inner hair cell afferent synapse of the mouse. *Proceedings of the National Academy of Sciences of the United States of America*, 97, 883-888.
- MULDERS, W. H. & ROBERTSON, D. 2009. Hyperactivity in the auditory midbrain after acoustic trauma: dependence on cochlear activity. *Neuroscience*, 164, 733-46.
- MUONA, M., BERKOVIC, S. F., DIBBENS, L. M., OLIVER, K. L., MALJEVIC, S., BAYLY, M. A., JOENSUU, T., CANAFOGLIA, L., FRANCESCHETTI, S., MICHELUCCI, R., MARKKINEN, S., HERON, S. E., HILDEBRAND, M. S., ANDERMANN, E., ANDERMANN, F., GAMBARDELLA, A., TINUPER, P., LICCHETTA, L., SCHEFFER, I. E., CRISCUOLO, C., FILLA, A., FERLAZZO, E., AHMAD, J., AHMAD, A., BAYKAN, B., SAID, E., TOPCU, M., RIGUZZI, P., KING, M. D., OZKARA, C., ANDRADE, D. M., ENGELSEN, B. A., CRESPEL, A., LINDENAU, M., LOHMANN, E., SALETTI, V., MASSANO, J., PRIVITERA, M., ESPAY, A. J., KAUFFMANN, B., DUCHOWNY, M., MOLLER, R. S., STRAUSSBERG, R., AFAWI, Z., BEN-ZEEV, B., SAMOCHA, K. E., DALY, M. J., PETROU, S., LERCHE, H., PALOTIE, A. & LEHESJOKI, A. E. 2015. A recurrent de novo mutation in KCNC1 causes progressive myoclonus epilepsy. *Nat Genet*, 47, 39-46.
- MUSICANT, A. D. & BUTLER, R. A. 1984. The influence of pinnae-based spectral cues on sound localization. *J Acoust Soc Am*, 75, 1195-200.
- MUSIEK, F. E. 2006. *The Auditory System: Anatomy, Physiology and Clinical Correlates*, Pearson.
- MYINT, A., WHITE, C. H., OHMEN, J. D., LI, X., WANG, J., LAVINSKY, J., SALEHI, P., CROW, A. L., OHYAMA, T. & FRIEDMAN, R. A. 2016. Large-scale phenotyping of noise-induced hearing loss in 100 strains of mice. *Hear Res*, 332, 113-20.
- NAYAGAM, B. A., MUNIAK, M. A. & RYUGO, D. K. 2011. The spiral ganglion: Connecting the peripheral and central auditory systems. *Hearing Research*, 278, 2-20.
- NISHIMURA, Y. & KUMOI, T. 1992. The embryologic development of the human external auditory meatus. Preliminary report. *Acta Otolaryngol*, 112, 496-503.
- NORENA, A. J. & EGGERMONT, J. J. 2003. Changes in spontaneous neural activity immediately after an acoustic trauma: implications for neural correlates of tinnitus. *Hear Res*, 183, 137-53.
- NOWAK, L., BREGESTOVSKI, P., ASCHER, P., HERBET, A. & PROCHIANTZ, A. 1984. Magnesium gates glutamate-activated channels in mouse central neurones. *Nature*, 307, 462-5.

- OERTEL, D. 1983. Synaptic Responses and Electrical-Properties of Cells in Brain-Slices of the Mouse Anteroventral Cochlear Nucleus. *Journal of Neuroscience*, 3, 2043-2053.
- OHLEMILLER, K. K., DAHL, A. R. & GAGNON, P. M. 2010. Divergent aging characteristics in CBA/J and CBA/CaJ mouse cochleae. *J Assoc Res Otolaryngol*, 11, 605-23.
- OLESKEVICH, S., YOUSOUFIAN, M. & WALMSLEY, B. 2004. Presynaptic plasticity at two giant auditory synapses in normal and deaf mice. *Journal of Physiology-London*, 560, 709-719.
- OLIVER, D. & FAKLER, B. 1999. Expression density and functional characteristics of the outer hair cell motor protein are regulated during postnatal development in rat. *J Physiol*, 519 Pt 3, 791-800.
- OLIVER, D. L., BECKIUS, G. E. & SHNEIDERMAN, A. 1995. Axonal projections from the lateral and medial superior olive to the inferior colliculus of the cat: a study using electron microscopic autoradiography. *J Comp Neurol*, 360, 17-32.
- OLLO, C. & SCHWARTZ, I. R. 1979. The superior olivary complex in C57BL/6 mice. *Am J Anat*, 155, 349-73.
- OPSTAL, J. V. 2016. *The Auditory System and Human Sound-Localization Behavior*, Academic Press.
- OVERHOLT, E. M., RUBEL, E. W. & HYSON, R. L. 1992. A circuit for coding interaural time differences in the chick brainstem. *J Neurosci*, 12, 1698-708.
- OXENHAM, A. J. & BACON, S. P. 2003. Cochlear compression: Perceptual measures and implications for normal and impaired hearing. *Ear and Hearing*, 24, 352-366.
- OZAITA, A., MARTONE, M. E., ELLISMAN, M. H. & RUDY, B. 2002. Differential subcellular localization of the two alternatively spliced isoforms of the Kv3.1 potassium channel subunit in brain. *Journal of Neurophysiology*, 88, 394-408.
- PARK, T. J., GROTHE, B., POLLAK, G. D., SCHULLER, G. & KOCH, U. 1996a. Neural delays shape selectivity to interaural intensity differences in the lateral superior olive. *Journal of Neuroscience*, 16, 6554-6566.
- PARK, T. J., GROTHE, B., POLLAK, G. D., SCHULLER, G. & KOCH, U. 1996b. Neural delays shape selectivity to interaural intensity differences in the lateral superior olive. *J Neurosci*, 16, 6554-66.
- PARK, T. J., KLUG, A., HOLINSTAT, M. & GROTHE, B. 2004. Interaural level difference processing in the lateral superior olive and the inferior colliculus. *Journal of Neurophysiology*, 92, 289-301.
- PARKS, T. N. 2000. The AMPA receptors of auditory neurons. *Hearing Research*, 147, 77-91.
- PERFILOVA, V. N. & TYURENKOV, I. N. 2016. [Glutamate Ionotropic Receptors: Structure, Localisation, Function]. *Usp Fiziol Nauk*, 47, 80-96.
- PILATI, N., ISON, M. J., BARKER, M., MULHERAN, M., LARGE, C. H., FORSYTHE, I. D., MATTHIAS, J. & HAMANN, M. 2012. Mechanisms contributing to central excitability changes during hearing loss. *Proc Natl Acad Sci U S A*, 109, 8292-7.
- PILATI, N., LINLEY, D. M., SELVASKANDAN, H., UCHITEL, O., HENNIG, M. H., KOPPSCHEINPFLUG, C. & FORSYTHE, I. D. 2016. Acoustic trauma slows AMPA receptor-mediated EPSCs in the auditory brainstem, reducing GluA4 subunit expression as a mechanism to rescue binaural function. *J Physiol*, 594, 3683-703.
- PLATZER, J., ENGEL, J., SCHROTT-FISCHER, A., STEPHAN, K., BOVA, S., CHEN, H., ZHENG, H. & STRIESSNIG, J. 2000. Congenital deafness and sinoatrial node dysfunction in mice lacking class D L-type Ca<sup>2+</sup> channels. *Cell*, 102, 89-97.
- POLLAK, G. D. 1988. Time Is Traded for Intensity in the Bats Auditory-System. *Hearing Research*, 36, 107-124.
- PURVES D, A. G., FITZPATRICK D, ET AL 2002. *Neuroscience*.
- QUIRK, J. C., SIUDA, E. R. & NISENBAUM, E. S. 2004. Molecular determinants responsible for differences in desensitization kinetics of AMPA receptor splice variants. *J Neurosci*, 24, 11416-20.

- R.G. KLUMPP, H. R. E. 1956. Some measurements of interaural time difference thresholds. *J Acoust Soc Am*, 28, 859-860.
- RAVINDRANATHAN, A., DONEVAN, S. D., SUGDEN, S. G., GREIG, A., RAO, M. S. & PARKS, T. N. 2000. Contrasting molecular composition and channel properties of AMPA receptors on chick auditory and brainstem motor neurons. *J Physiol*, 523 Pt 3, 667-84.
- RAYLEIGH, L. 1907. On our perception of sound direction. *Philos Mag*, 13, 214-232.
- RICCI, A. J. & FETTIPLACE, R. 1998. Calcium permeation of the turtle hair cell mechanotransducer channel and its relation to the composition of endolymph. *J Physiol*, 506 ( Pt 1), 159-73.
- RIETZEL, H. J. & FRIAUF, E. 1998. Neuron types in the rat lateral superior olive and developmental changes in the complexity of their dendritic arbors. *J Comp Neurol*, 390, 20-40.
- ROBLES, L. & RUGGERO, M. A. 2001. Mechanics of the mammalian cochlea. *Physiol Rev*, 81, 1305-52.
- ROCHE, K. W., STANDLEY, S., MCCALLUM, J., LY, C. D., EHLERS, M. D. & WENTHOLD, R. J. 2001. Molecular determinants of NMDA receptor internalization. *Nature Neuroscience*, 4, 794-802.
- RODRIGUEZ-MENCHACA, A. A., ADNEY, S. K., TANG, Q. Y., MENG, X. Y., ROSENHOUSE-DANESKER, A., CUI, M. & LOGOTHETIS, D. E. 2012. PIP2 controls voltage-sensor movement and pore opening of Kv channels through the S4-S5 linker. *Proceedings of the National Academy of Sciences of the United States of America*, 109, E2399-E2408.
- ROGALSKI, S. L., APPELYARD, S. M., PATTILLO, A., TERMAN, G. W. & CHAVKIN, C. 2000. TrkB activation by brain-derived neurotrophic factor inhibits the G protein-gated inward rectifier Kir3 by tyrosine phosphorylation of the channel. *J Biol Chem*, 275, 25082-8.
- RUBIO, M. E. & WENTHOLD, R. J. 1999. Differential distribution of intracellular glutamate receptors in dendrites. *J Neurosci*, 19, 5549-62.
- RUDY, B., CHOW, A., LAU, D., AMARILLO, Y., OZAITA, A., SAGANICH, M., MORENO, H., NADAL, M. S., HERNANDEZ-PINEDA, R., HERNANDEZ-CRUZ, A., ERISIR, A., LEONARD, C. & VEGA-SAENZ DE MIERA, E. 1999. Contributions of Kv3 channels to neuronal excitability. *Ann N Y Acad Sci*, 868, 304-43.
- RUDY, B. & MCBAIN, C. J. 2001. Kv3 channels: voltage-gated K<sup>+</sup> channels designed for high-frequency repetitive firing. *Trends Neurosci*, 24, 517-26.
- RUGGERO, M. A., RICH, N. C., RECIO, A., NARAYAN, S. S. & ROBLES, L. 1997. Basilar-membrane responses to tones at the base of the chinchilla cochlea. *Journal of the Acoustical Society of America*, 101, 2151-2163.
- RUGGERO, M. A., ROBLES, L. & RICH, N. C. 1992. Two-tone suppression in the basilar membrane of the cochlea: mechanical basis of auditory-nerve rate suppression. *J Neurophysiol*, 68, 1087-99.
- RUPPERSBERG, J. P., SCHROTER, K. H., SAKMANN, B., STOCKER, M., SEWING, S. & PONGS, O. 1990. Heteromultimeric channels formed by rat brain potassium-channel proteins. *Nature*, 345, 535-7.
- SAINT MARIE, R. L., OSTAPOFF, E. M., MOREST, D. K. & WENTHOLD, R. J. 1989. Glycine-immunoreactive projection of the cat lateral superior olive: possible role in midbrain ear dominance. *J Comp Neurol*, 279, 382-96.
- SALVI, R. J., WANG, J. & DING, D. 2000. Auditory plasticity and hyperactivity following cochlear damage. *Hear Res*, 147, 261-74.
- SANCHEZ, J. T., GHELANI, S. & OTTO-MEYER, S. 2015. From development to disease: diverse functions of NMDA-type glutamate receptors in the lower auditory pathway. *Neuroscience*, 285, 248-59.
- SANES, D. H. 1993. The development of synaptic function and integration in the central auditory system. *J Neurosci*, 13, 2627-37.

- SANES, D. H., MARKOWITZ, S., BERNSTEIN, J. & WARDLOW, J. 1992. The influence of inhibitory afferents on the development of postsynaptic dendritic arbors. *J Comp Neurol*, 321, 637-44.
- SANES, D. H. & RUBEL, E. W. 1988. The ontogeny of inhibition and excitation in the gerbil lateral superior olive. *J Neurosci*, 8, 682-700.
- SANES, D. H. & TAKACS, C. 1993. Activity-dependent refinement of inhibitory connections. *Eur J Neurosci*, 5, 570-4.
- SATZLER, K., SOHL, L. F., BOLLMANN, J. H., BORST, J. G., FROTSCHER, M., SAKMANN, B. & LUBKE, J. H. 2002. Three-dimensional reconstruction of a calyx of Held and its postsynaptic principal neuron in the medial nucleus of the trapezoid body. *J Neurosci*, 22, 10567-79.
- SCHAETTE, R. & MCALPINE, D. 2011. Tinnitus with a Normal Audiogram: Physiological Evidence for Hidden Hearing Loss and Computational Model. *Journal of Neuroscience*, 31, 13452-13457.
- SCHMID, S., GUTHMANN, A., RUPPERSBERG, J. P. & HERBERT, H. 2001. Expression of AMPA receptor subunit flip/flop splice variants in the rat auditory brainstem and inferior colliculus. *J Comp Neurol*, 430, 160-71.
- SCHWARTZ, I. R. & EAGER, P. R. 1999. Glutamate receptor subunits in neuronal populations of the gerbil lateral superior olive. *Hear Res*, 137, 77-90.
- SHAW, E. A. 1974. Transformation of sound pressure level from the free field to the eardrum in the horizontal plane. *J Acoust Soc Am*, 56, 1848-61.
- SHERA, C. A. & GUINAN, J. J., JR. 1999. Evoked otoacoustic emissions arise by two fundamentally different mechanisms: a taxonomy for mammalian OAEs. *J Acoust Soc Am*, 105, 782-98.
- SLEPECKY, N. 1986. Overview of Mechanical Damage to the Inner-Ear - Noise as a Tool to Probe Cochlear Function. *Hearing Research*, 22, 307-321.
- SLIWINSKA-KOWALSKA, M. & DAVIS, A. 2012. Noise-induced hearing loss. *Noise Health*, 14, 274-80.
- SMART, S. L., LOPANTSEV, V., ZHANG, C. L., ROBBINS, C. A., WANG, H., CHIU, S. Y., SCHWARTZKROIN, P. A., MESSING, A. & TEMPEL, B. L. 1998. Deletion of the K(v)1.1 potassium channel causes epilepsy in mice. *Neuron*, 20, 809-819.
- SMITH, A. J., OWENS, S. & FORSYTHE, I. D. 2000. Characterisation of inhibitory and excitatory postsynaptic currents of the rat medial superior olive. *J Physiol*, 529 Pt 3, 681-98.
- SMITH, K. E., BROWNE, L., SELWOOD, D. L., MCALPINE, D. & JAGGER, D. J. 2015. Phosphoinositide Modulation of Heteromeric Kv1 Channels Adjusts Output of Spiral Ganglion Neurons from Hearing Mice. *Journal of Neuroscience*, 35, 11221-11232.
- SMITH, P. H., JORIS, P. X. & YIN, T. C. 1993. Projections of physiologically characterized spherical bushy cell axons from the cochlear nucleus of the cat: evidence for delay lines to the medial superior olive. *J Comp Neurol*, 331, 245-60.
- SMITH, P. H., JORIS, P. X. & YIN, T. C. 1998. Anatomy and physiology of principal cells of the medial nucleus of the trapezoid body (MNTB) of the cat. *J Neurophysiol*, 79, 3127-42.
- SOMMER, B., KEINANEN, K., VERDOORN, T. A., WISDEN, W., BURNASHEV, N., HERB, A., KOHLER, M., TAKAGI, T., SAKMANN, B. & SEEBURG, P. H. 1990. Flip and flop: a cell-specific functional switch in glutamate-operated channels of the CNS. *Science*, 249, 1580-5.
- SOMMER, I., LINGENHOHL, K. & FRIAUF, E. 1993. Principal cells of the rat medial nucleus of the trapezoid body: an intracellular in vivo study of their physiology and morphology. *Exp Brain Res*, 95, 223-39.
- SONG, P., YANG, Y., BARNES-DAVIES, M., BHATTACHARJEE, A., HAMANN, M., FORSYTHE, I. D., OLIVER, D. L. & KACZMAREK, L. K. 2005. Acoustic environment determines phosphorylation state of the Kv3.1 potassium channel in auditory neurons. *Nat Neurosci*, 8, 1335-42.

- SPOENDLIN, H. 1972. Innervation densities of the cochlea. *Acta Otolaryngol*, 73, 235-48.
- SPOENDLIN, H. & BRUN, J. P. 1973. Relation of structural damage to exposure time and intensity in acoustic trauma. *Acta Otolaryngol*, 75, 220-6.
- STARR, A., MICHALEWSKI, H. J., ZENG, F. G., FUJIKAWA-BROOKS, S., LINTHICUM, F., KIM, C. S., WINNIER, D. & KEATS, B. 2003. Pathology and physiology of auditory neuropathy with a novel mutation in the MPZ gene (Tyr145->Ser). *Brain*, 126, 1604-19.
- STEINERT, J. R., POSTLETHWAITE, M., JORDAN, M. D., CHERNOVA, T., ROBINSON, S. W. & FORSYTHE, I. D. 2010. NMDAR-mediated EPSCs are maintained and accelerate in time course during maturation of mouse and rat auditory brainstem in vitro. *J Physiol*, 588, 447-63.
- STERENBORG, J. C., PILATI, N., SHERIDAN, C. J., UCHITEL, O. D., FORSYTHE, I. D. & BARNES-DAVIES, M. 2010. Lateral olivocochlear (LOC) neurons of the mouse LSO receive excitatory and inhibitory synaptic inputs with slower kinetics than LSO principal neurons. *Hear Res*, 270, 119-26.
- STUART, G. J. & SAKMANN, B. 1994. Active Propagation of Somatic Action-Potentials into Neocortical Pyramidal Cell Dendrites. *Nature*, 367, 69-72.
- SVIRSKIS, G., KOTAK, V., SANES, D. H. & RINZEL, J. 2002. Enhancement of signal-to-noise ratio and phase locking for small inputs by a low-threshold outward current in auditory neurons. *Journal of Neuroscience*, 22, 11019-11025.
- TAGOE, T., BARKER, M., JONES, A., ALLCOCK, N. & HAMANN, M. 2014. Auditory nerve perinodal dysmyelination in noise-induced hearing loss. *J Neurosci*, 34, 2684-8.
- TAKAHASHI, T., FELDMAYER, D., SUZUKI, N., ONODERA, K., CULLCANDY, S. G., SAKIMURA, K. & MISHINA, M. 1996. Functional correlation of NMDA receptor epsilon subunits expression with the properties of single-channel and synaptic currents in the developing cerebellum. *Journal of Neuroscience*, 16, 4376-4382.
- TAKAHASHI, T., MOMIYAMA, A., HIRAI, K., HISHINUMA, F. & AKAGI, H. 1992. Functional correlation of fetal and adult forms of glycine receptors with developmental changes in inhibitory synaptic receptor channels. *Neuron*, 9, 1155-61.
- TANSEY, E. P., CHOW, A., RUDY, B. & MCBAIN, C. J. 2002. Developmental expression of potassium-channel subunit Kv3.2 within subpopulations of mouse hippocampal inhibitory interneurons. *Hippocampus*, 12, 137-48.
- TASCHENBERGER, H., LEAO, R. M., ROWLAND, K. C., SPIROU, G. A. & VON GERSDORFF, H. 2002. Optimizing synaptic architecture and efficiency for high-frequency transmission. *Neuron*, 36, 1127-43.
- TASCHENBERGER, H. & VON GERSDORFF, H. 2000. Fine-tuning an auditory synapse for speed and fidelity: developmental changes in presynaptic waveform, EPSC kinetics, and synaptic plasticity. *J Neurosci*, 20, 9162-73.
- THOMPSON, A. M. & SCHOFIELD, B. R. 2000. Afferent projections of the superior olivary complex. *Microsc Res Tech*, 51, 330-54.
- TOESCA, A. 1996. Central and peripheral myelin in the rat cochlear and vestibular nerves. *Neurosci Lett*, 221, 21-4.
- TOLLIN, D. J. 2003. The lateral superior olive: a functional role in sound source localization. *Neuroscientist*, 9, 127-43.
- TOLLIN, D. J. & HENNING, G. B. 1998. Some aspects of the lateralization of echoed sound in man. I. The classical interaural-delay based precedence effect. *J Acoust Soc Am*, 104, 3030-8.
- TOLLIN, D. J. & YIN, T. C. 2002a. The coding of spatial location by single units in the lateral superior olive of the cat. I. Spatial receptive fields in azimuth. *J Neurosci*, 22, 1454-67.
- TOLLIN, D. J. & YIN, T. C. 2002b. The coding of spatial location by single units in the lateral superior olive of the cat. II. The determinants of spatial receptive fields in azimuth. *J Neurosci*, 22, 1468-79.

- TONG, G., SHEPHERD, D. & JAHR, C. E. 1995. Synaptic desensitization of NMDA receptors by calcineurin. *Science*, 267, 1510-2.
- TONG, H., KOPP-SCHEINPFLUG, C., PILATI, N., ROBINSON, S. W., SINCLAIR, J. L., STEINERT, J. R., BARNES-DAVIES, M., ALLFREE, R., GRUBB, B. D., YOUNG, S. M., JR. & FORSYTHE, I. D. 2013. Protection from noise-induced hearing loss by Kv2.2 potassium currents in the central medial olivocochlear system. *J Neurosci*, 33, 9113-21.
- TONG, H., STEINERT, J. R., ROBINSON, S. W., CHERNOVA, T., READ, D. J., OLIVER, D. L. & FORSYTHE, I. D. 2010. Regulation of Kv channel expression and neuronal excitability in rat medial nucleus of the trapezoid body maintained in organotypic culture. *J Physiol*, 588, 1451-68.
- TRAYNELIS, S. F., WOLLMUTH, L. P., MCBAIN, C. J., MENNITI, F. S., VANCE, K. M., OGDEN, K. K., HANSEN, K. B., YUAN, H., MYERS, S. J. & DINGLEDINE, R. 2010. Glutamate receptor ion channels: structure, regulation, and function. *Pharmacol Rev*, 62, 405-96.
- TRUSSELL, L. 1998. Control of time course of glutamatergic synaptic currents. *Glutamate Synapse as a Therapeutical Target: Molecular Organization and Pathology of the Glutamate Synapse*, 116, 59-69.
- TRUSSELL, L. O. 1999. Synaptic mechanisms for coding timing in auditory neurons. *Annual Review of Physiology*, 61, 477-496.
- TSUCHITANI, C. & BOUDREAU, J. C. 1966. Single unit analysis of cat superior olive S segment with tonal stimuli. *J Neurophysiol*, 29, 684-97.
- TSUCHITANI, C. & BOUDREAU, J. C. 1969. Stimulus level of dichotically presented tones and cat superior olive S-segment cell dcharge. *J Acoust Soc Am*, 46, 979-88.
- VEGA-SAENZ DE MIERA E, WEISER M, KENTROS C, LAU D, MORENO H, SERODIO P & B, R. 1994. *Shaw-related K<sup>+</sup> channels in mammals*, Academic, Orlando.
- VETTER, D. E. & MUGNAINI, E. 1992. Distribution and dendritic features of three groups of rat olivocochlear neurons. A study with two retrograde cholera toxin tracers. *Anat Embryol (Berl)*, 185, 1-16.
- VISSEL, B., KRUPP, J. J., HEINEMANN, S. E. & WESTBROOK, G. L. 2001. A use-dependent tyrosine dephosphorylation of NMDA receptors is independent of ion flux. *Nature Neuroscience*, 4, 587-596.
- VON HEHN, C. A., BHATTACHARJEE, A. & KACZMAREK, L. K. 2004. Loss of Kv3.1 tonotopicity and alterations in cAMP response element-binding protein signaling in central auditory neurons of hearing impaired mice. *J Neurosci*, 24, 1936-40.
- VYKLYCKY, V., KORINEK, M., SMEJKALOVA, T., BALIK, A., KRAUSOVA, B., KANIAKOVA, M., LICHNEROVA, K., CERNY, J., KRUSEK, J., DITTERT, I., HORAK, M. & VYKLYCKY, L. 2014. Structure, function, and pharmacology of NMDA receptor channels. *Physiol Res*, 63 Suppl 1, S191-203.
- WANG, H., YIN, G., ROGERS, K., MIRALLES, C., DE BLAS, A. L. & RUBIO, M. E. 2011. Monaural conductive hearing loss alters the expression of the GluA3 AMPA and glycine receptor alpha1 subunits in bushy and fusiform cells of the cochlear nucleus. *Neuroscience*, 199, 438-51.
- WANG, L. Y., GAN, L., FORSYTHE, I. D. & KACZMAREK, L. K. 1998. Contribution of the Kv3.1 potassium channel to high-frequency firing in mouse auditory neurones. *J Physiol*, 509 ( Pt 1), 183-94.
- WANG, Y., HIROSE, K. & LIBERMAN, M. C. 2002. Dynamics of noise-induced cellular injury and repair in the mouse cochlea. *JARO*, 3, 248-268.
- WARR, W. B. 1975. Olivocochlear and vestibular efferent neurons of the feline brain stem: their location, morphology and number determined by retrograde axonal transport and acetylcholinesterase histochemistry. *J Comp Neurol*, 161, 159-81.
- WASHBURN, M. S., NUMBERGER, M., ZHANG, S. & DINGLEDINE, R. 1997. Differential dependence on GluR2 expression of three characteristic features of AMPA receptors. *J Neurosci*, 17, 9393-406.

- WEISER, M., VEGA-SAENZ DE MIERA, E., KENTROS, C., MORENO, H., FRANZEN, L., HILLMAN, D., BAKER, H. & RUDY, B. 1994a. Differential Expression of Shaw-Related K<sup>+</sup> Channels in the Rat Central-Nervous-System. *Journal of Neuroscience*, 14, 949-972.
- WEISER, M., VEGA-SAENZ DE MIERA, E., KENTROS, C., MORENO, H., FRANZEN, L., HILLMAN, D., BAKER, H. & RUDY, B. 1994b. Differential expression of Shaw-related K<sup>+</sup> channels in the rat central nervous system. *J Neurosci*, 14, 949-72.
- WEISZ, C. J., RUBIO, M. E., GIVENS, R. S. & KANDLER, K. 2016. Excitation by Axon Terminal GABA Spillover in a Sound Localization Circuit. *J Neurosci*, 36, 911-25.
- WIGHTMAN FL, K. D. *Sound localization. In: Human psychophysics*, New York, Springer.
- WILD, A. R., JONES, S. & GIBB, A. J. 2014. Activity-dependent regulation of NMDA receptors in substantia nigra dopaminergic neurones. *J Physiol*, 592, 653-68.
- WIMMER, V. C., HORSTMANN, H., GROH, A. & KUNER, T. 2006. Donut-like topology of synaptic vesicles with a central cluster of mitochondria wrapped into membrane protrusions: A novel structure-function module of the adult calyx of Held. *Journal of Neuroscience*, 26, 109-116.
- WRIGHT, A. & VISSEL, B. 2012. The essential role of AMPA receptor GluR2 subunit RNA editing in the normal and diseased brain. *Front Mol Neurosci*, 5, 34.
- WU, S. H. & KELLY, J. B. 1993. Response of Neurons in the Lateral Superior Olive and Medial Nucleus of the Trapezoid Body to Repetitive Stimulation - Intracellular and Extracellular Recordings from Mouse-Brain Slice. *Hearing Research*, 68, 189-201.
- WU SH, K. J. 1993. Response of neurones in the lateral superior olive and medial nucleus of the trapezoid body to repetitive stimulation: intracellular and extracellular recordings from the mouse brain slice. *Hearing Reserch*, 189 - 201.
- YANG, H., XIONG, H., OU, Y., XU, Y., PANG, J., LAI, L. & ZHENG, Y. 2016. Effect of repetitive transcranial magnetic stimulation on auditory function following acoustic trauma. *Neurol Sci*, 37, 1511-6.
- YANG, Y. M., AITOUBAH, J., LAUER, A. M., NURIYA, M., TAKAMIYA, K., JIA, Z. P., MAY, B. J., HUGANIR, R. L. & WANG, L. Y. 2011. GluA4 is indispensable for driving fast neurotransmission across a high-fidelity central synapse. *Journal of Physiology-London*, 589, 4209-4227.
- YLIKOSKI, M. E. & YLIKOSKI, J. S. 1994. Hearing loss and handicap of professional soldiers exposed to gunfire noise. *Scand J Work Environ Health*, 20, 93-100.
- YOUSOUFIAN, M., COUCHMAN, K., SHIVDASANI, M. N., PAOLINI, A. G. & WALMSLEY, B. 2008. Maturation of auditory brainstem projections and calyces in the congenitally deaf (dn/dn) mouse. *Journal of Comparative Neurology*, 506, 442-451.
- YOUSOUFIAN, M., OLESKEVICH, S. & WALMSLEY, B. 2005. Development of a robust central auditory synapse in congenital deafness. *Journal of Neurophysiology*, 94, 3168-3180.
- YOUSOUFIAN, M. & WALMSLEY, B. 2007. Brain-derived neurotrophic factor modulates cell excitability in the mouse medial nucleus of the trapezoid body. *European Journal of Neuroscience*, 25, 1647-1652.
- ZAGHA, E., LANG, E. J. & RUDY, B. 2008. Kv3.3 channels at the Purkinje cell soma are necessary for generation of the classical complex spike waveform. *Journal of Neuroscience*, 28, 1291-1300.
- ZHANG, S., EDELMANN, L., LIU, J., CRANDALL, J. E. & MORABITO, M. A. 2008a. Cdk5 regulates the phosphorylation of tyrosine 1472 NR2B and the surface expression of NMDA receptors. *J Neurosci*, 28, 415-24.
- ZHANG, S., EDELMANN, L., LIU, J. N., CRANDALL, J. E. & MORABITO, M. A. 2008b. Cdk5 regulates the phosphorylation of tyrosine 1472 NR2B and the surface expression of NMDA receptors. *Journal of Neuroscience*, 28, 415-424.
- ZHANG, Y. & KACZMAREK, L. K. 2015. Kv3.3 potassium channels and spinocerebellar ataxia. *J Physiol*.

ZHENG, Q. Y., JOHNSON, K. R. & ERWAY, L. C. 1999. Assessment of hearing in 80 inbred strains of mice by ABR threshold analyses. *Hear Res*, 130, 94-107.